Secondary Circulation in Partially Vegetated Flows

Stefania Unigarro Villota

ORCID: 0000-0002-8453-7168

Master of Science in Civil Engineering for Risk Mitigation, 2017

Bachelor in Civil Engineering, 2014

A thesis submitted for the degree of

Doctor of Philosophy

Oct 2022

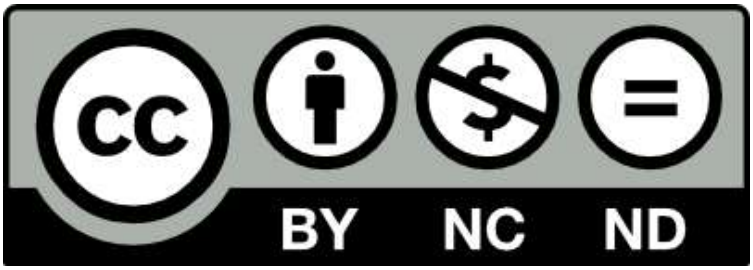
Department of Civil Engineering

School of Engineering

Submitted in total fulfilment for the jointly awarded degree of Doctor of Philosophy at the University of Melbourne and the University of Birmingham

UNIVERSITY OF BIRMINGHAM

University of Birmingham Research Archive
e-theses repository



This unpublished thesis/dissertation is under a Creative Commons Attribution-NonCommercial-NoDerivatives 4.0 International (CC BY-NC-ND 4.0) licence.

You are free to:

Share — copy and redistribute the material in any medium or format

The licensor cannot revoke these freedoms as long as you follow the license terms.

Under the following terms:

Attribution — You must give appropriate credit, provide a link to the license, and indicate if changes were made. You may do so in any reasonable manner, but not in any way that suggests the licensor endorses you or your use.

NonCommercial — You may not use the material for commercial purposes.

NoDerivatives — If you remix, transform, or build upon the material, you may not distribute the modified material.

No additional restrictions — You may not apply legal terms or technological measures that legally restrict others from doing anything the license permits.

Notices:

You do not have to comply with the license for elements of the material in the public domain or where your use is permitted by an applicable exception or limitation.

No warranties are given. The license may not give you all of the permissions necessary for your intended use. For example, other rights such as publicity, privacy, or moral rights may limit how you use the material.

Unless otherwise stated, any material in this thesis/dissertation that is cited to a third-party source is not included in the terms of this licence. Please refer to the original source(s) for licencing conditions of any quotes, images or other material cited to a third party.

Abstract

Partially vegetated flows like those over rivers with riparian vegetation are common in natural environments. In these flows, vegetation acts as a porous obstruction for the flow. Thus, the slow interstitial fluid inside the vegetation and the rapid free streams above and next to it, lead to large gradients of shear at the vegetation patch boundaries, where shear layers are created. These shear layers are characterised by large turbulent coherent structures that interact with secondary circulations developed due to the differential roughness between the vegetation and the adjacent unobstructed flow. This hydrodynamic interaction dictates the interfacial mass and momentum transport in aquatic environments. As vegetation provides important ecosystem services, such as water quality improvement through nutrients and heavy metals retention, sediment trapping, and oxygen flux, the hydrodynamic transport occurring at the interface can significantly impact many physical, chemical and ecological processes. Therefore, flow characterisation through patchy vegetation is important for a system-level understanding of vegetated flows and management of river and coastal systems. However, the characterisation of these flows is complex, owing to their three-dimensionality, which is not yet fully understood. This thesis presents the characterisation of the three-dimensional flow developed on a partially vegetated channel, focussing upon the role of secondary circulation on mass and momentum transport. Firstly, an experimental approach was employed to determine the flow properties, taking 3D-point velocity measurements, using an Acoustic Doppler Velocimeter (ADV), in the cross-sectional plane on a partially vegetated flume. Experiments were configured to examine the influence of vegetation density, over a range of reported realistic field conditions, and shallowness on the mean and turbulent flow. Subsequently, an analytical model was used to predict depth-averaged streamwise velocities, modelling the effects of secondary circulation on the momentum equation.

The results reveal that secondary circulation cells scale with the vertical shear layer thickness within the vegetation and the water depth beside the canopy patch. The rotational direction of the major pair of cells located at the lateral canopy-water interface inverts, either at high densities due to the growth of an emergent rotating pair of cells, or at reduced water depths. Secondary circulation contributions to vertical mass transport, for the higher submergence condition,

are estimated to be of the same order of magnitude as that of turbulent diffusion. Advective dispersive stresses arising due to mean flow fluctuations are found to be up to 21% of the total vertical shear stress and the main contributors to lateral shear stress within the vegetation and in the main channel outside the mixing layer. Additionally, this work presents the first attempt at using the Shiono and Knight Method, an analytical model based on the depth-averaged Navier-Stokes equation, to model depth-averaged streamwise velocities in submerged partially vegetated channels. Appropriate advice on the values of calibration parameters and cross-section discretisation is given. The combined experimental and modelling approaches provide and insight into the 3D flow structure and highlights the importance of secondary circulation when evaluating mass and momentum transport in submerged partially vegetated flows.

Key words: turbulent open-channel flows, partially vegetated channel, secondary circulation, advective dispersive stress, vertical scalar transport, predictive depth-averaged velocity model, SKM, conveyance in partially vegetated flows.

Thesis declaration

I, Stefania Unigarro Villota, certify that:

- This thesis comprises only my original work and it has been substantially accomplished during enrolment in the degree.
- No part of this work will, in the future, be used in a submission in my name, for any other degree or diploma in any university or other tertiary institution without the prior approval of The University of Melbourne, and The university of Birmingham, UK as partner institution responsible for the joint-award of this degree.
- Due acknowledgement has been made in the text to all other material used.
- This thesis contains work published or prepared for publication, some of which has been co-authored.
- This thesis is fewer than the 100,000 words in length, exclusive of tables, maps, bibliography and appendices.

Acknowledgements

To my supervisors in Australia, Dr Jimmy Philip and Dr Marco Ghisalberti, thank you for believing in this project, for the support, the extensive discussions, and the continuous feedback and advice on my experimental work. Thank you, Marco, for making this possible and thank you, Jimmy, for your patience and for always being willing to share your knowledge. I extend my gratitude to my supervisors in the UK, Dr Soroosh Sharifi and Dr Michael Jesson for the discussions and feedback on the modelling part of this study. Thank you to my advisor, Prof Michael Stewardson for the support and advice throughout my candidature. I would also like to thank Dr Paul Branson for his interest in the project, for bringing additional scientific support to this work and for the help in all technical aspects in the lab. Special thanks to my mentor, Dr Lauren Thomas-Seale for her encouragement, emotional support and advice during the last stage of this journey.

Many thanks to the Oceans Graduate School at the University of Western Australia for having me as a graduate visitor. I greatly benefited from the use of the Geophysical Fluid Dynamics Laboratory in which I performed the experimental work for this project. Thank you to my fellow experimentalists Dr Maryam Abdolahpour, Mario Conde Frias and Fei He.

Thank you to my family and the Montenegro-Johnson family for their encouragement and immense and continuous support throughout this experience. Thank you to my friends, specially to Veronica Herrera, Maura DeGiovanni, Luz Castro and Paula Rodriguez, who have been of great emotional support and helped me thrive in challenging circumstances. I would also like to thank my partner for his help, his love and the continuous support and encouragement.

I gratefully acknowledge the financial support of the Priestley scholarship granted by The University of Melbourne and The University of Birmingham as part of their joint PhD programme. Thank you to Kate Hale, Cloe Jakel, Petra Van Nieuwenhoven and Tim Baldwin at UoM, and Kate Sterne at UoB for their support in all the joint PhD matters.

To Mom

remembered with love

Contents

Contents iv

List of Figures xii

List of Tables xiii

List of Symbols xiv

1 Introduction 1

1.1 Motivation and significance 1

1.1.1 Main flow and shear-induced structures in channels with vegetation 2

1.1.2 Secondary flow and vortical structures over heterogeneous beds 5

1.1.3 Momentum and mass exchange in partially vegetated flows 6

1.2 Research Objectives 8

1.2.1 Characterise the three-dimensional flow in submerged partially vegetated channels 8

1.2.2 Investigate the effects of vegetation density and shallowness on the flow structure of patchy vegetation 8

1.2.3 Model spanwise depth-averaged velocity distributions in submerged partially vegetated channels 9

1.3 Thesis Outline 9

2 Background 11

2.1 Vegetated flows 12

2.1.1 Structures and scales 12

2.1.2 Quantitative information of key dimensionless parameters in the field 16

2.1.3 Momentum and mass exchange . . . 19
2.2 Secondary circulation . . . 21
2.2.1 Corner secondary circulation . . . 22
2.2.2 Secondary circulation over heterogeneous surfaces . . . 24
2.3 Conveyance estimation . . . 30
2.3.1 The Shiono-Knight Method (SKM) . . . 32

3 Experimental Methodology 40
3.1 Open-channel flume facility . . . 40
3.2 Velocity measurements and data processing . . . 44
3.2.1 Filtering and despiking . . . 45
3.2.2 Rotation correction . . . 47

4 Characterising the three-dimensional flow in partially vegetated channels 49
4.1 Introduction . . . 50
4.2 Methodology . . . 50
4.2.1 Time-space averaging . . . 50
4.2.2 Shear layer thickness . . . 54
4.2.3 Peclet number and vertical scalar transport . . . 57
4.3 Streamwise flow structure . . . 58
4.3.1 Streamwise velocity scaling and shear layer structure . . . 62
4.3.2 Shear layer thickness . . . 66
4.4 Secondary circulation . . . 67
4.5 Turbulent and dispersive shear stresses . . . 71
4.6 Impact of flow structure on vertical scalar transport . . . 77
4.7 Discussion . . . 78
4.8 Conclusions . . . 81

5 Effects of vegetation density and shallowness on the flow structure 84
5.1 Introduction . . . 85
5.2 Methodology . . . 85
5.2.1 Shear stress over heterogeneous beds . . . 85
5.2.2 Shear layer thickness . . . 86
5.2.3 Secondary circulation strength . . . 87
5.3 Impact of varying vegetation density ϕ on streamwise velocity structure . . . 88

5.3.1 Streamwise velocity profiles and shear-layer structure . . . 92
5.3.2 Shear layer thickness . . . 96
5.4 Impact of varying vegetation density on the structure of Secondary circulation . . . 97
5.5 Impact of varying vegetation density - relationship between shear stress and secondary circulation . . . 102
5.6 Impact of shallowness H/h on the streamwise velocity structure . 106
5.6.1 Streamwise velocity profiles and shear layer structure . . . 108
5.6.2 Shear layer thickness . . . 111
5.7 Impact of shallowness - characteristics of secondary circulation . . 112
5.8 Impact of shallowness - relationship between shear stress and secondary circulation . . . 116
5.8.1 Conclusions . . . 122

6 Turbulent kinetic energy production and transport, and energy spectra 125
6.1 Introduction . . . 125
6.1.1 Energy balance within the secondary circulation . . . 126
6.2 1D streamwise turbulence energy spectra . . . 131
6.3 Conclusions . . . 136

7 Modelling spanwise depth-averaged velocity distributions in submerged partially vegetated channels 138
7.1 Introduction . . . 139
7.2 Physical modelling . . . 139
7.2.1 Velocity distribution and Reynolds shear stress . . . 139
7.3 Predicting depth-averaged velocities using the Shiono-Knight Method . . . 143
7.3.1 Input model parameters . . . 146
7.3.2 Modelling depth-average streamwise velocity . . . 147
7.4 Conclusions . . . 153

8 Conclusions and future work 155
8.1 Conclusions . . . 155
8.2 Future work . . . 158

References 161

Appendix A **175**

List of Figures

1.1 Vortices observed in fully-developed flow conditions in a) a channel partially containing emergent vegetation and b) a channel full of submerged vegetation. c) vortices expected to develop in a submerged partially vegetated channel as in the present work. Secondary circulation over alternating longitudinal d) elevated-recessed surfaces or ridge-type roughness and e) smooth-rough surfaces or strip-type roughness. 4

2.1 Time-averaged streamwise velocity profiles in a (a) boundary layer flow (b) submerged canopy flow with dense vegetation (c) submerged canopy flow with slightly dense vegetation (d) emergent canopy flow. 13

2.2 Diagram of the shear layer variables from Ghisalberti & Nepf (2006). 14

2.3 Top view of a partially vegetated channel with the vegetation patch located in the middle of the channel. 16

2.4 Data, $C_D ab$ vs H/h, reported in field studies (grey area), and collected from experimental studies that analysed the secondary flow in submerged vegetated-porous patches (△) Nezu & Onitsuka (2001), (□) Hopkinson & Wynn (2009), (◁) Folorunso (2015). . . 19

2.5 Secondary circulation streamlines in rectangular-straight open-channels of different width-to-depth ratios. Adapted from Naot & Rodi (1982). 23

2.6 Schematic drawing of the distribution of time-averaged streamwise and spanwise velocities, $\overline{u}$ and $\overline{v}$, respectively, by Knight et al. (2007). 37

2.7 Schematic drawing of the secondary flow in a rectangular channel, representing the distribution of $\langle\overline{u}\rangle_d\langle\overline{v}\rangle_d$, the panel divisions and the sign of the rotating cells (Omran, 2005). 38

3.1 Schematic of the experimental set-up in a wide non-tilting recirculating flume of the long patch of vegetation aligned in the streamwise direction. a) Top view. b) A photograph of the flume taken from the downstream end. c) The spanwise cross-section (Section A-A) of the flow where measurements of the velocity field were obtained using a 3D downward-looking ADV. 41

3.2 Pictures of the top view of the different vegetation densities studied. 42

3.3 Data, $C_D ab$ vs H/h, reported in field studies (grey area), and collected from experimental studies that analysed the secondary flow in submerged vegetated-porous patches (△) Nezu & Onitsuka (2001), (□) Hopkinson & Wynn (2009), (◁) Folorunso (2015). . . 44

4.1 Typical vertical and lateral time-averaged streamwise velocity profiles within the patch of vegetation and lateral Reynolds shear stress distribution. a) Representative vertical velocity profile $\overline{u}\ (z)$ with mixing-layer variables defined. b) Lateral velocity profile $\overline{u}\ (y)$ with characteristic mixing-layer variables, and lateral Reynolds shear stress $\overline{u'v'}$ 56

4.2 Contour maps of the normalised time-averaged streamwise velocity $\overline{u}$ in the cross (yz) plane centred on the lateral edge of the canopy for, a) the sparser ($\phi = 0.025$), and b) denser ($\phi = 0.10$) canopies. The (in plane) secondary flow is indicated by velocity vectors. c) Normalised $\overline{u}(z)$ profiles at four spanwise locations. d) Normalised $\overline{u}(y)$ profiles at four depths. 60

4.3 Vertical scaling of time-averaged streamwise velocity, within the canopy, for the two solid volume fractions $\phi = 0.025$ (▲) and $\phi = 0.10$ (•). a) Normalised streamwise velocity horizontally-averaged over the canopy width $\overline{u}\ |_{y>0}/U_2$. b) Normalised inner-layer profiles with the hyperbolic tangent profile fit for reference (red line). (c) Normalised outer-layer profiles with the canopy-boundary-layer profile fit for reference (red line). 63

4.4 Lateral scaling of time-averaged streamwise velocity $\overline{u}$ within the canopy for the two solid volume fractions $\phi = 0.025$ (▲) and $\phi = 0.10$ (•). a) Normalised time-space-averaged streamwise velocity. b) Normalised inner-layer profiles with the fitted hyperbolic tangent profile for reference (red line). 65

4.5 Normalised average thickness of the shear layer in the vertical and lateral directions for the two vegetation densities. 66
4.6 Normalised time-averaged velocities in the cross-plane for a) $\phi = 0.025$ and b) $\phi = 0.10$. Upper plots represent streamlines coloured by the normalised time-averaged vertical velocity $\overline{w}/U_b$. Lower plots show normalised time-averaged spanwise velocities $\overline{v}/U_b$. 69
4.7 Effect of the vegetation patch on the normalised dispersive (left panels), advective dispersive (middle-left panels) turbulent Reynolds (middle-right panels) and total (right panels) shear stresses for a) $\phi = 0.025$ and b) $\phi = 0.10$. 72
4.8 Normalised vertical dispersive $-\langle\overline{u}''\overline{w}''\rangle$, advective dispersive $-\langle\tilde{\overline{u}}\tilde{\overline{w}}\rangle$, turbulent Reynolds $-\langle\overline{u'w'}\rangle$ and total $-\langle\overline{\tau_{zx}}\rangle$ shear stresses for the two canopy densities $\phi = 0.025$ ($\triangle$) and $\phi = 0.10$ ($\circ$). The spanwise average was done over a) the spanwise velocity wavelength λ_V, and b) part of the wavelength λ_V that lies within the canopy denoted as λ_{Vc}. 75
4.9 Normalised depth-averaged lateral dispersive $\langle\overline{u}''\overline{v}''\rangle_d$, advective dispersive $\langle\tilde{\overline{u}}\tilde{\overline{v}}\rangle_d$, turbulent Reynolds $\langle\overline{u'v'}\rangle_d$ and total $\langle\overline{\tau_{xy}}\rangle_d$ shear stresses for the two vegetation densities $\phi = 0.025$ ($\triangle$) and $\phi = 0.10$ ($\circ$). 76
4.10 Normalised vertical profile of horizontally-averaged eddy viscosity within the mixing layer for the two densities, $\phi = 0.025$ ($\blacktriangle$) and $\phi = 0.10$ ($\bullet$). 77
4.11 The three-dimensional flow structure in a partially vegetated channel. 79

5.1 Contour maps of the normalised time-averaged streamwise velocity $\overline{u}$ in the cross (yz) plane of five canopy densities: $\phi = 0.0125$, $\phi = 0.025$, $\phi = 0.05$, $\phi = 0.10$, and $\phi = 0.20$. 90
5.2 Vertical scaling of streamwise velocity profiles for varying densities represented by symbols as in Table 5.1. a) Normalised time-averaged and horizontally averaged within the canopy ($y > 0$) streamwise velocity $\overline{u}|_{y>0}/U_2$. b) Normalised inner-layer profiles with the hyperbolic tangent profile fit for reference (red line). c) Normalised outer-layer profiles with the canopy-boundary-layer profile fit for reference (red line). 93

5.3 Lateral scaling of streamwise velocity profiles for varying densities represented by symbols as in Table 5.1. a) Lateral time-averaged and vertically-averaged over heights $z < h$ streamwise velocity profiles $\overline{u}|_{z<h}$. b) Normalised lateral streamwise velocity with inner- and outer-layers for $\phi = 0.0125$. The inner-layer profile scales with a hyperbolic-tangent profile. The outer layer profile scales with a sinusoidal function. c) Normalised inner-layer profiles with the hyperbolic-tangent profile fit for reference (red line). d) Normalised outer-layer profiles. 95

5.4 Lateral streamwise velocity profiles for the denser patch of vegetation ($\phi = 0.20$) of widths B and $2B$ and a *step*. A dense patch of vegetation causes the same effects on the lateral streamwise velocity profiles in the main channel near the drag discontinuity as a solid step. 96

5.5 Vertical and lateral mixing layer thickness, t_{ml_z} and t_{ml_y}, respectively, normalised by the water depth (H). 97

5.6 Secondary circulation illustrated by the normalised swirl strength multiplied by the sign of vorticity for a) $\phi = 0.0125$ b) $\phi = 0.025$, c) $\phi = 0.05$, d) $\phi = 0.10$, and e) $\phi = 0.20$. f) a step and g) a wider (i.e. double the width for cases (a-e)) patch of density $\phi = 0.20$. . 99

5.7 Variation of the normalised circulation of streamwise vorticity with vegetation density. 102

5.8 Normalised vertical shear stress distribution in the cross-sectional plane with the locations of upward ⓤ and downward ⓓ motions. 104

5.9 Shear stresses and their relationship with upward and downward flows. Normalised depth-averaged streamwise velocity, total lateral shear stress, and lateral Reynolds shear stress for a) $\phi = 0.05$ and b) $\phi = 0.10$. 106

5.10 Contour maps of the normalised time-averaged streamwise velocity $\overline{u}$ in the cross (yz) plane centred on the lateral canopy-water interface for shallowness conditions of $H/h = 3.0$, $H/h = 2.5$, and $H/h = 2.0$ (in columns) and canopy densities $\phi = 0.025$, $\phi = 0.10$, and $\phi = 0.20$ (in rows). Dashed lines represent patch boundaries. The (in plane) secondary flow is indicated by scaled overlying velocity vectors $[\overline{v}, \overline{w}]/0.15U_b$. Decreasing H/h reverts the direction of the vertical flow observed at the lateral-canopy water interface, and suppress secondary circulations above the canopy. 107

5.11 Vertical scaling of time-averaged streamwise velocity within the canopy for various shallowness conditions. a) Streamwise velocity profiles for $H/h = 2.0$ normalised by mixing layer parameters, with the hyperbolic tangent profile fit for reference (red line). b) Normalised inner-layer profiles for canopies in a submerged condition of $H/h = 2.5$. The hyperbolic tangent profile appears in red for reference. c) Normalised outer-layer profiles at $H/h = 2.5$ with the canopy-boundary-layer profile fit for reference (red line). 109

5.12 Lateral distribution of streamwise velocity profiles below the canopy top. a) Time-averaged and vertically-averaged over $z < h$ streamwise velocity profiles for three canopy densities at $H/h = 2.0$. b) Normalised inner-layer profiles for canopies in a submerged condition of $H/h = 2.0$. The inner-layer profile scales with a hyperbolic-tangent profile (red line) described by (4.15) c) Time-averaged and vertically-averaged over $z < h$ streamwise velocity profiles of the patch of density $\phi = 0.10$ for the three submergence conditions. The change in concavity of profiles near the LCWI as water depth decreases reflects the sign reversal of the vertical flow at the lateral drag discontinuity. Markers as in Table 5.1. 111

5.13 Vertical, t_{mlz}, and lateral, t_{mly}, mixing layer thickness normalised by the array height h. 112

5.14 Normalised swirl strength multiplied by the sign of streamwise vorticity illustrating the secondary circulation for shallowness conditions of $H/h = 3.0$, $H/h = 2.5$, and $H/h = 2.0$ (in columns) and canopy densities $\phi = 0.025$, $\phi = 0.10$, and $\phi = 0.20$ (in rows). Lower water depths strengthen the counter clockwise cell next to the patch of vegetation, changing the direction of the vertical flow at the LCWI. Secondary flow is indicated by (s) and tertiary flow by (t). 114

5.15 Variation of the normalised circulation of streamwise vorticity with shallowness. 116

5.16 Colourmaps of the normalised vertical shear stress, $-\overline{u'w'}/{U_b}^2$, and profiles of the normalised depth-averaged lateral shear stress, $\langle\overline{u'v'}\rangle_d/{U_b}^2$, and dispersive stress due to mean flow fluctuations,$\langle\tilde{\bar{u}}\tilde{\bar{v}}\rangle_d/{U_b}^2$, at $H/h = 2.5$ for densities a) $\phi = 0.10$, b) $\phi = 0.20$. 118

5.17 Colourmaps of the normalised vertical shear stress, $-\overline{u'w'}/{U_b}^2$, and profiles of the normalised depth-averaged lateral shear stress, $\langle\overline{u'v'}\rangle_d/{U_b}^2$, and dispersive stress due to mean flow fluctuations,$\langle\tilde{\bar{u}}\tilde{\bar{v}}\rangle_d/{U_b}^2$, at $H/h = 2.0$, for densities a) $\phi = 0.025$, b) $\phi = 0.10$, and c) $\phi = 0.20$. 120

5.18 Pictures of the longitudinal sediment streaks seen during experiments with a patch of density $\phi = 0.20$ at $H/h = 2.0$ (left picture), and $\phi = 0.13$ at 1.6 (right picture). 122

6.1 Colourmaps of the production terms a) $P_{u'v'}$, b) $P_{u'w'}$, c) $P_{v'v'}$ and d) $P_{w'w'}$ for the patch of density $\phi = 0.10$ and $H/h = 3.0$. Production terms $P_{u'v'}$ and $P_{u'w'}$ are dominant and larger at the canopy patch boundaries. Note that colourbars are different for colourmaps in the first row and the second row. 128

6.2 Colourmaps of TKE transport equation terms for a patch of density $\phi = 0.10$ and $H/h = 3.0$: a) $\mathcal{P}$, b) $\mathcal{C}_y + \mathcal{C}_z$, c) $\mathcal{T}$, d) $P + T$ and e) $-\varepsilon_{est}$; and f) the vertical gradient of TKE. 129

6.3 Premultiplied streamwise energy spectrograms for a canopy patch of $\phi = 0.10$ and $H/h = 3.0$ in the main channel at a) $y/H = -0.5$ and b) $y/H = -0.11$; and within the vegetation at c) $y/H = 0.61$ and $y/H = 1.17$. Turbulence intensity profiles are presented next to the spectrograms. The red dashed lines mark the height at which maximum energy is observed. In c) and d), the red dashed line also coincides with the top of the canopy. The green line represents a point of large energy level above the canopy, at $z/H = 0.55$. Note that the colorbar for a) is different from that of (b-d) 132

6.4 Premultiplied 1D streamwise energy spectra $k_x\Phi_{u'u'}/{U_b}^2$ as a function of streamwise wavelength λ_x and vertical location z of all canopy densities (in columns) at $H/h = 3.0$. Cases on the first row are spectrograms at the centre of the patch width (i.e. $y = B/2$). The second row illustrates spectrograms in the main channel, next to the vegetation patch at $y = -B/4$. 134

6.5 Premultiplied 1D streamwise energy spectra $k_x\Phi_{u'u'}/{U_b}^2$ as a function of streamwise wavelength λ_x and vertical location z for a dense canopy, $\phi = 0.20$, at a) $H/h = 3.0$, b) $H/h = 2.5$, and c) $H/h = 2.0$. 136

7.1 Distribution of normalised time-averaged streamwise velocity $\overline{u}$ in the cross (yz) plane for a) $\phi = 0.0125$, b) $\phi = 0.05$, and c) $\phi = 0.10$. The (in plane) secondary flow is indicated by velocity vectors $[\overline{u}, \overline{w}]/0.4U_b$. Black dashed lines represent patch boundaries. Locations of channel subdivisions for the SKM panels are shown by vertical white dashed lines. 140

7.2 Normalised time-averaged vertical turbulent Reynolds stress for a) $\phi = 0.0125$, b) $\phi = 0.05$, and c) $\phi = 0.10$. Secondary circulations are represented by in-plane streamlines. Black dashed lines represent patch boundaries. The maximum shear occurs at the top of the canopies, being larger in regions of downward flow than in those of upward flow. Be aware that the white space in the figure does not represent zero vertical Reynolds stress but it is much smaller than the stress caused by the vegetation patch. . . . 142

7.3 a) Contributions of turbulent Reynolds, dispersive and advective dispersive stresses to the depth-averaged lateral shear stress for $\phi = 0.10$. b) Total depth-averaged lateral shear stress for the three canopy densities. Contributions of the secondary circulation through the advective shear stress are significant and should be taken into account when considering the depth-average lateral shear stress. 143
7.4 Distribution of the non-dimensional eddy viscosity λ (a-c) and secondary circulation term Γ (d-f) across the partially vegetated channel for three canopy densities $\phi = 0.0125$, $\phi = 0.05$, and $\phi = 0.10$. Large variations in lambda are observed close to the lateral canopy-water interface (i.e. $y/H = 0$) with increasing canopy density as momentum transport is enhanced there. Positive peaks of Γ occur at locations of strong upward flow while negative peaks are associated to downward flows. 148
7.5 Panel-averaged secondary circulation term Γ (a-c) and lateral distribution of the depth-averaged streamwise velocity (d-f) across the partially vegetated channel for three canopy densities $\phi = 0.0125$, $\phi = 0.05$, and $\phi = 0.10$. Error bars represent the standard deviation of measured Γ values within each panel. The standard deviation of Γ is sometimes larger than the maximum difference between averaged Γ values in the channel. Modelled depth-averaged velocities agree well with experimental data. . . . 151
7.6 Distribution of the depth-averaged streamwise velocity for $\phi = 0.025$. Predicted velocities represent measured data with a maximum relative error of 12%. 153

List of Tables

2.1 Aquatic vegetation properties reported in some field studies. . . . 18

3.1 Experimental conditions: canopy density ϕ, water depth H (uncertainty of ± 1 mm), canopy height h, shallowness H/h, canopy patch width B, bulk velocity U_b calculated as the integrated mean of measured streamwise velocity profiles extrapolated to the water surface using the log law (uncertainty of ± 0.06 cm/s); and S_0 the water surface slope (uncertainty of ± 0.000001). 43

5.1 Summary of vegetation densities and shallowness conditions studied. 88

7.1 Values of the SKM parameters λ, f and Γ used in the model. The first three rows correspond to panels within the vegetated patch, while the last four rows represent panels in the main channel. . . 152

List of Symbols

Roman Symbols

A	Contact area between the fluid and obstruction elements inside the averaging volume.
A_{cs}	Cross-sectional area of flow.
A_1	SKM constant.
A_2	SKM constant.
a	Canopy frontal area per unit volume.
b	Major axis for $\Delta^2 u_i$ versus u_i.
B	Canopy patch width.
B_{ch}	Channel width.
c	Minor axis for $\Delta^2 u_i$ versus u_i.
C_D	Canopy drag coefficient.
$\mathcal{C}_y$	Turbulent kinetic energy advection term ($= \overline{v}(\partial K/\partial y)$).
$\mathcal{C}_z$	Turbulent kinetic energy advection term ($= \overline{w}(\partial K/\partial z)$).
c_f	Fanning friction factor ($= f/4$).
D	Two-dimensional velocity gradient of the time-space averaged velocity gradient tensor.
D_r	Depth ratio in compound channels ($= (H_{mc} - H_{fp})/H_{mc}$).
D_{tz}	Turbulent diffusivity in the z-direction.
$\langle D_x \rangle_d$	depth-averaged drag force in the main flow direction.
d_v	Canopy element diameter.
f	Darcy-Weisbach friction coefficient.
f_s	Sampling frequency.
f_v	Friction coefficient for the vegetated region.

g	Acceleration due to gravity.
H	Water depth.
H_{fp}	Water depth in the floodplain.
H_{mc}	Water depth in the main channel.
h	Canopy height.
h_d	Canopy displacement height or mean level of momentum absorption.
k	SKM constant.
k_x	Streamwise wavenumber.
L_D	Canopy drag length scale.
l_z	Vertical characteristic length over which scalar transport occurs.
N_v	Number of canopy elements per unit bed area.
n	Manning coefficient.
$\hat{n}$	Unit normal vector pointing from the solid to the fluid region.
P	Spanwise spacing between consecutive rough/elevated regions.
$\mathcal{P}$	Production of turbulent kinetic energy.
Pe	Peclet number.
p	Pressure.
Re	Hydraulic Reynolds number ($= U_b H/\nu$).
R_H	Hydraulic Radius.
S	Roughness width.
S_0	Longitudinal water surface slope.
s	Centre-to-centre distance between canopy elements.
$\mathcal{T}$	Transport of turbulent kinetic energy.
t_{ml}	Nominal vegetated shear layer thickness.
t_{ml_y}	Shear layer thickness in the y-direction.
t_{ml_z}	Shear layer thickness in the z-direction.
U_b	Cross-sectional time-averaged streamwise velocity.
U_c	Convection velocity.
U_{mean}	Arithmetic mean of U_1 and U_2.
U_{m_y}	Matching streamwise velocity between the inner and outer layers in the y-direction.
U_{m_z}	Matching streamwise velocity between the inner and outer layers in the z-direction.
U_s	Slip velocity ($U_0 - U_1$).

U_v	Bulk streamwise velocity inside the canopy.
$U_{z=H}$	Velocity at the water surface.
U_h	Velocity at the top of the canopy.
U_0	Time-averaged streamwise velocity at the inflection point.
U_1	Time-averaged streamwise velocity deep inside the patch.
U_2	The largest (constant) time-averaged streamwise velocity in the open channel.
$U_{2_{tanh}}$	Maximum time-averaged streamwise velocity of a hyperbolic tangent profile fitted to the experimental data recorded inside the canopy.
$U^*{}_{in}$	Rescaled velocity in the inner region.
$U^*{}_{out}$	Rescaled velocity in the outer region.
$\overline{u}$	Time-averaged streamwise velocity.
$\overline{u}_{max-y}$	Maximum time-averaged streamwise velocity within $-B < y < B$ in the y-direction.
$\overline{u} \mid_{y>0}$	Time-averaged streamwise velocity spatially averaged over the patch width B in the y-direction.
$\overline{u} \mid_{z<h}$	Time-averaged streamwise velocity profile averaged in z over depths below the canopy height.
$\langle \tilde{\tilde{u}}\tilde{\tilde{v}} \rangle_d$	Depth-averaged advective (due to mean flow heterogeneities) dispersive shear stress.
$\langle \overline{u'v'} \rangle_d$	Depth-averaged lateral Reynolds shear stress.
$\langle \overline{u}''\overline{v}'' \rangle_d$	Depth-averaged dispersive stress from the spatial fluctuations of the flow near a porous medium (i.e. the canopy patch).
$\langle \tilde{\tilde{u}}\tilde{\tilde{w}} \rangle_{\lambda_V}$	Spanwise-averaged (over λ_V) advective (due to mean flow heterogeneities) dispersive shear stress.
$\langle \overline{u'w'} \rangle_{\lambda_V}$	Spanwise-averaged (over λ_V) vertical Reynolds shear stress.
$\langle \overline{u}''\overline{w}'' \rangle_{\lambda_V}$	Spanwise-averaged (over λ_V) dispersive stress from the spatial fluctuations of the flow near a porous medium (i.e. the canopy patch).
u_*	Friction velocity.
V_b	Cross-sectional time-averaged spanwise velocity.
$\overline{v}$	Time-averaged spanwise velocity.
W_b	Cross-sectional time-averaged vertical velocity.
W_{lz}	Representative time-averaged vertical velocity within l_z.
$\overline{w}$	Time-averaged vertical velocity.

x	Streamwise coordinate.
y	Spanwise coordinate.
y_m	Lateral (in y) position of the matching streamwise velocity between the hyperbolic-tangent and the canopy log-law profiles.
y_0	Location, in the y-direction, of the inflection point of a fitted hyperbolic tangent profile.
y_1	Location of U_1 in the y-direction.
y_2	Location of U_2 in the y-direction.
${y^*}_{in}$	Rescaled lateral coordinate in the inner region.
z	Coordinate normal to the channel bed.
z_b	Bottom roughness length scale.
z_m	Vertical (in z) position of the matching streamwise velocity between the hyperbolic-tangent and the canopy log-law profiles.
z_{mean}	Height at which the time-averaged streamwise velocity is equal to U_{mean}.
z_1	Location of U_1 in the z-direction.
z_2	Location of U_2 in the z-direction.
${z^*}_{in}$	Rescaled vertical coordinate in the inner region.
${z^*}_{out}$	Rescaled coordinate in the outer region.

Greek Symbols

α	Degree-angle representing rotation about the x axis.
β	Degree-angle representing rotation about the y axis.
Γ	Advection term representing the streamwise momentum exchange due to the averaged secondary flow structures.
γ	SKM constant.
Δu_i	First derivative of a velocity u_i.
$\Delta^2 u_i$	Second derivative of a velocity u_i.
ΔU	Overall velocity difference ($= U_2 - U_1$).
ΔU_{tanh}	Internal time-averaged streamwise velocity difference ($= U_{2_{tanh}} - U_1$).
δ	Turbulent boundary layer thickness.
δ_I	Inner-mixing-layer thickness.
δ_O	Outer-mixing-layer thickness.
ϵ	Circulation of streamwise vorticity.
ϵ^*	Normalised circulation of streamwise vorticity ($= \epsilon / HU_b$).

ε	Dissipation of turbulent kinetic energy.
ε_{est}	Estimated dissipation of turbulent kinetic energy assuming homogeneous isotropic turbulence.
θ	Momentum thickness.
θ_y	Momentum thickness in the y-direction.
$\theta_{y_{tanh}}$	Momentum thickness in the y-direction from $-\infty$ to y_0.
θ_z	Momentum thickness in the z-direction.
$\theta_{z_{tanh}}$	Momentum thickness in the z-direction from $-\infty$ to z_0.
θ_{PST}	Rotation angle of the principal axes of $\Delta^2 u_i$ versus u_i.
κ	von-Karman constant.
λ	Dimensionless Eddy viscosity.
λ_{ci}	Swirl strength.
λ_U	Universal threshold.
λ_V	Time-averaged spanwise velocity wavelength.
λ_{Vc}	Part of the spanwise velocity wavelength that lies within the canopy.
λ_x	Streamwise wavelength.
μ	Dynamic viscosity.
μ_{bc}	SKM boundary condition parameter.
ν	Kinematic viscosity.
ν_{tz}	Turbulent eddy viscosity in the z-direction.
ρ	Fluid density.
σ_u	Standard deviation of u_i.
σ_{Δ_u}	Standard deviation of Δu_i.
σ_u	Standard deviation of $\Delta^2 u_i$.
τ_b	Bed shear stress.
$\langle\overline{\tau_{xy}}\rangle_d$	Depth-averaged lateral total shear stress.
$\langle\overline{\tau_{zx}}\rangle_{\lambda_V}$	Spanwise-averaged vertical total shear stress.
$\Phi_{u'u'}$	1D power spectral density of the streamwise turbulent velocity fluctuation.
ϕ	Canopy density or solid volume fraction ($= N_v \pi {d_v}^2/4$ for a cylinder array).
ϕ_f	Porosity of the patch of vegetation ($= 1 - \phi$).
ψ	Degree-angle representing rotation about the z axis.
Ω_x	Streamwise vorticity.

Chapter 1

Introduction

1.1 Motivation and significance

In aquatic ecosystems, the spatial distribution of vegetation is not always ideally homogeneous, but instead develops in self-organised patches that emerge from scale-dependent feedbacks between plant growth, water flow and local erosion/deposition rates (K. van Wesenbeeck et al., 2008; Schoelynck et al., 2012). These patches often grow over a wide range of size scales forming clustered groups of one or more species (Schoelynck et al., 2012) that rearrange at different timescales (A. Murray et al., 2008). Thus, feedbacks define discrete arrays, but may also explain landscape colonization by patchy vegetation growing dynamically in time (A. Murray et al., 2008). In braided rivers, for instance, vegetation encroachment is enhanced at inactive low-flow channels, transforming the entire system from braided to single-thread (Tal & Paola, 2007). Similarly, floodplain landscapes may be formed when vegetation expands and becomes dense enough to divert the flow away from cutoff closed loops in meandering rivers (Perucca et al., 2007). Furthermore, floodplain fertile alluvial soils are often used as agricultural fields where crops are planted in regular rows creating human-built patches next to freshwater streams.

Vegetated patches act as porous obstructions for the flow, representing an abrupt spanwise variation in roughness, which results in the development of shear across the canopy patch boundaries. These shear flows are often characterised by the

formation of large coherent structures (i.e. shear-induced vortices) in the horizontal (White & Nepf, 2007) and vertical planes (Ghisalberti & Nepf, 2002), at the canopy-water interface, and generate cross-channel secondary circulations (e.g. Nezu & Onitsuka, 2001; Anderson et al., 2015) that actively enhance mass and momentum exchange between different regions of the flow (e.g. Shiono & Knight, 1991; Ghisalberti & Nepf, 2005; Van Prooijen et al., 2005; Vermaas et al., 2011).

The mass and momentum exchange in partially vegetated flows is important for many hydrological, ecological, hydraulic and morphodynamic processes. While the faster flowing water in the main channel carries sediment and nutrient loads, the vegetation zone presents the ecological diversity and the capacity for hydrological storage and sediment retention. This highlights the importance of flow circulation between the vegetation and the main channel. Vegetation helps regulate water quality (Moore, 2004) and promotes retention of nutrients and heavy metals (e.g. Bal et al., 2013; Cornacchia et al., 2019), which are crucial processes for community primary productivity and ecosystem function (A. Murray et al., 2008). Vegetation also increases bed roughness and decreases near-bed turbulent stress (e.g. López & García, 1998; Carollo et al., 2005) promoting local sedimentation (Nepf, 2012) but can also lead to rising water levels and increasing flood risk (e.g. Benifei et al., 2015). Vegetation coverage increases soil strength, preventing erosion (A. Murray et al., 2008), and favours the establishment and survival of new vegetation, which is a key factor for the creation of new floodplains and morphological changes of rivers, such as the reduction of braiding and meandering (e.g. Tal & Paola, 2007; Bertoldi et al., 2011). Therefore, the characterisation of flow through patchy vegetation is important for a system-level understanding of vegetated environments and management of river and coastal systems.

1.1.1 Main flow and shear-induced structures in channels with vegetation

Although the necessity for a better understanding of the hydrodynamics relating to submerged partially vegetated flows is evident, their practical investigation is complex due to the three-dimensional nature of the flow. Due to this complexity, the impact of patchy vegetation on riverine and coastal flows has not been fully characterised (e.g. Shiono & Knight, 1991; Nezu & Onitsuka, 2001). Previous studies have utilised simplified 2D models to elaborate on the fluid dynamics, as well as on the mass and momentum exchange (e.g. Ikeda & Kanazawa, 1996;

Raupach et al., 1996; Nepf & Vivoni, 2000; Ghisalberti & Nepf, 2002; White & Nepf, 2007; Caroppi et al., 2021). Typical 2D models are used in cases either where horizontal flows dominate over vertical flows, e.g. emergent partially vegetated channels, i.e. flows over vegetation patches where their height exceeds the water depth (Figure 1.1a) or, where vertical motions are stronger compared to horizontal motions, as in fully vegetated flows, i.e flows in which the (submerged) vegetation and the open water share only one interface located at the top of the canopy (Figure 1.1b). However, these 2D models neglect contributions from the secondary flow, which may be significant.

In the flows of the aforementioned 2D models, the roughness layer (i.e. canopy) is porous/permeable and imposes resistance to the flow, creating strong shear in the horizontal (Figure 1.1a) or vertical (Figure 1.1b) planes, and an inflection point appears in the mean velocity profile at the canopy-open water interface. Note that the inflection point in a mean velocity profile is sign of emerging Kelvin-Helmholtz instability and subsequently coherent structures leading to strong turbulence. Thus, the flow is characterised by two regions of constant velocity, separated by a confined mixing layer containing coherent vortex structures (Ghisalberti & Nepf, 2004) in either the horizontal (Figure 1.1a) or vertical (Figure 1.1b) plane (Ghisalberti & Nepf, 2002; White & Nepf, 2007). In fully vegetated flows where the canopy-scale vortices dominate the turbulence, the vertical velocity profile of the mixing layer is symmetric and has a roughly hyperbolic tangent form (Ghisalberti & Nepf, 2002). However, in partially vegetated flows with emergent vegetation, the spanwise velocity distribution suggests an asymmetric vegetated mixing layer structure (which takes a hyperbolic tangent-like shape) within the canopy and a laminar boundary layer structure outside the patch (White & Nepf, 2007; Caroppi et al., 2021). This difference in the velocity distribution between the horizontal and vertical shear layers in 2D systems leaves room for ambiguity in understanding how submerged vegetation will affect the 3D mean and turbulent structures; in particular, how shear layers will behave in both the horizontal and vertical planes as they simultaneously develop (Figure 1.1c).

Vegetation characteristics, such as canopy morphology, density and flexibility, have been shown to govern the extent of the vertical shear layer in fully vegetated flows. Canopies with higher vegetation density generate a thinner vertical shear layer, which results in narrower zones of mass and momentum exchange (e.g. Nepf & Vivoni, 2000; Ghisalberti & Nepf, 2004). Conversely, foliated and

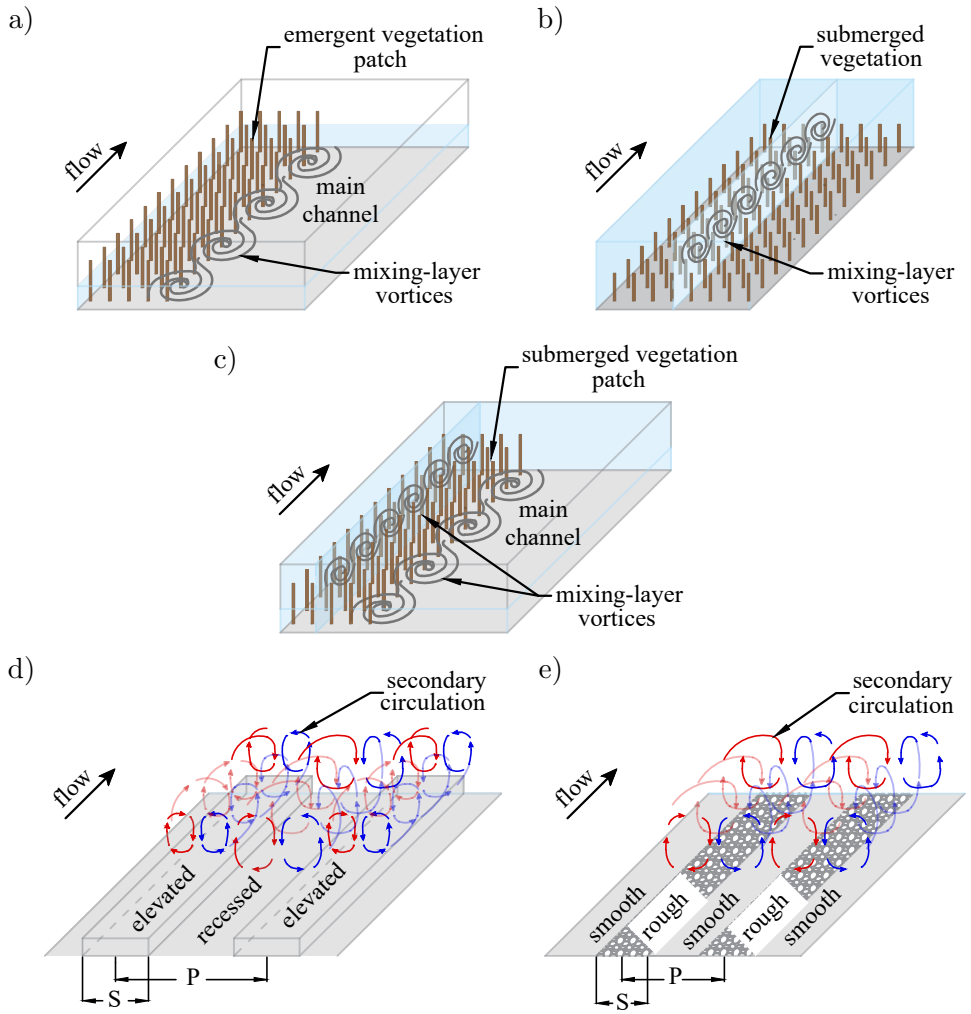


Figure 1.1: Vortices observed in fully-developed flow conditions in a) a channel partially containing emergent vegetation and b) a channel full of submerged vegetation. c) vortices expected to develop in a submerged partially vegetated channel as in the present work. Secondary circulation over alternating longitudinal d) elevated-recessed surfaces or ridge-type roughness and e) smooth-rough surfaces or strip-type roughness. Upward flow occurs over the smooth surface in flows over smooth-rough surfaces, and at the lateral edge of the elevation in flows over elevated-recessed surfaces.

flexible vegetation allows a greater penetration of the shear-induced vortices into the canopy leading to a thicker mixing layer, and consequently a wider exchange zone (e.g. Ghisalberti & Nepf, 2002). The depth of canopy submergence also plays a key role in the development of the vertical shear layer as shallow conditions restrict their growth (Nepf & Vivoni, 2000). In emergent partially vegetated flows, although foliated vegetation allows for a greater lateral shear-induced vortex penetration inside the patch (Caroppi et al., 2021), the coherent vortex size was suggested to be set by water depth and bottom friction in the main channel

(White & Nepf, 2007). Therefore, it is important to study the 3D flow of a submerged partially vegetated channel under changes of vegetation characteristics and submergence conditions.

1.1.2 Secondary flow and vortical structures over heterogeneous beds

Besides the shear-induced vortices and associated mixing layers developing on the horizontal and vertical planes (§1.1.1), cross-channel vortical structures are also expected to develop in 3D flows such as those over submerged patchy vegetation. Secondary circulation has been widely and independently studied in flows over spanwise changes in bed elevation (i.e. topographical variation with alternating elevated and recessed regions, also known as ridge-type roughness - Figure 1.1d) or bed roughness (i.e. skin-friction variation with alternating low and high shear stress strips, known as strip-type roughness - Figure 1.1e) representative of many natural and engineered systems. Some common examples are bedforms and topographical sediment distributions (Colombini, 1993; Wang & Cheng 2006; Jesson et al., 2013b), wind farms (Vanderwel et al., 2017), super-hydrophobic surfaces (Türk et al., 2014), urban-like configurations (Cheng & Castro, 2002; Coceal et al., 2006) or aerodynamic surfaces with simple changes in transverse roughness (Willingham et al., 2014; Anderson et al., 2015; Hwang & Lee, 2018; Medjnoun et al., 2020).

It is evident that there exists a close link between the spanwise locations of the upward and downward motions characterising secondary cells and the surface type. For topographical heterogeneities, upwash and downwash motions usually occur at the edge of the elevated region and above the recessed region, respectively (e.g. Vanderwel et al., 2017; Hwang & Lee, 2018; Medjnoun et al., 2020, and see Figure 1.1d). For alternating smooth-rough surfaces, the converging (diverging) motion is observed over high (low) drag regions as in Figure 1.1e (e.g. Wang & Cheng, 2006; Anderson et al., 2015; Willingham et al., 2014). In this context, the characterisation of secondary circulation in partially vegetated channels, which is the focus of the present work, is not straightforward. This is primarily because partially vegetated channels not only present a topographical variation of the bed surface (represented by the canopy height) but also a change in bed roughness between a porous medium and the main channel.

Several parametric studies have been undertaken to identify the bed properties that govern the structure of the secondary cells in ridge- and strip-type roughness flows. It has been shown that parameters such as increasing differential roughness on strip-type roughness flows (Türk et al., 2014; Willingham et al., 2014) (Figure 1.1e), and the shape and width of the elevations of ridge-type roughness flows (Wang & Cheng 2006; Medjnoun et al., 2020) (Figure 1.1d) have an influence on the secondary flow structure and its strength. The spanwise spacing between adjacent rough strips or elevated regions for strip- and ridge-type roughness flows, respectively (Anderson et al., 2015; Hwang & Lee, 2018; Yang & Anderson, 2018; Wang & Cheng 2006) has also been related to size changes of the secondary cells, as well as variations in their strength. However, it is difficult to draw direct conclusions on the connection between submerged partially vegetated channels and features of secondary cells due to the porous nature of vegetation canopies.

Studies investigating secondary circulations in partially vegetated flows are scarce. For instance, Naot et al. (1996) studied the hydrodynamics of partially vegetated flows with varying density, but they did not directly report the secondary flow structure, rather only its impact on the streamwise velocity field. Nezu & Onitsuka (2001) observed the secondary circulation in a partially vegetated channel with a single plant density under confined flow conditions (of water depth to canopy height ratio of approximately 1.4) where the development of the vertical streamwise velocity profiles is restricted by water depth (Nepf & Vivoni, 2000). They demonstrated that the secondary cells differ from those in compound open channel flows such as a river and its floodplain (which is a form of ridge-type roughness flow similar to that seen in Figure 1.1d), and resembled the patterns of strip-type roughness flows (shown in Figure 1.1e) where upward flow was observed in the main channel and descending motion in the vegetated zone. However, there is still a lack of understanding of the secondary cells' features in unconfined flow conditions and the influence of canopy density.

1.1.3 Momentum and mass exchange in partially vegetated flows

It has been demonstrated that both coherent mixing layer vortices and secondary circulations can contribute significantly to streamwise momentum exchange in 3D partially obstructed shear flows (e.g. Vermaas et al., 2011; Vanderwel et al., 2019; Medjnoun et al., 2020). In fact, various numerical and experimental studies on

ridge-type roughness flows have reported that dispersive stresses due to mean flow heterogeneities, i.e. secondary circulation, (to be defined in §4.2.1) can contribute up to 55% of the total shear stress (Vanderwel et al., 2019; Medjnoun et al., 2020). These results encourage the investigation of the 3D nature of partially vegetated flows to reveal the relevant mechanisms of momentum exchange in these systems. The understanding of these mechanisms allows the correct use of, for instance, predictive velocity models, essential for estimating flow conveyance which, in turn, advise flood alleviation schemes, flood warning and emergency evacuation plans and river restoration studies.

Along with momentum exchange, mass exchange is also worthy of investigation due to the potential of vegetation for improving water quality through the removal of nutrients, particulates and heavy metals (Moore, 2004; Bal et al., 2013; Cornacchia et al., 2019). In submerged fully vegetated flows (Figure 1.1b), the efficiency of this removal depends on the rate of material exchange between the canopy and the overlying water and consequently the residence time in aquatic canopies. Since the turbulent structure of a vegetated flow is typically dominated by the turbulence generated in the vegetated shear layer, vertical turbulent diffusion is believed to be the dominant process controlling vertical mass transport (Ghisalberti & Nepf, 2005). However, Ghisalberti (2010) found that a small (5% to 10%) gradient in canopy density in a vegetated flow creates secondary circulations that can contribute significantly to vertical scalar transport by means of vertical advection. Thus, both turbulent diffusion and advection due to secondary flows could actively contribute to mass exchange in submerged partially vegetated flows.

1.2 Research Objectives

The aim of this study is to investigate the secondary flow as a relevant key feature of the three-dimensionality of partially vegetated flows, in particular the contribution of secondary circulation to interfacial mass and momentum exchange. To achieve this aim, three specific objectives are proposed:

1.2.1 Characterise the three-dimensional flow in submerged partially vegetated channels

The importance of the flow three-dimensionality in a submerged partially vegetated channel, in particular the spatial extent of the characteristic large coherent structures and their role in mass and momentum exchange, may be tightly linked to the type of surface heterogeneity represented by the canopy. In this matter, a vegetation patch can be seen as a large porous obstruction where the flow across patch boundaries may represent a mixture of flow characteristics in a permeable medium and free shear flow. Additionally, the spanwise inhomogeneity that the vegetation represents may be of a different nature than that of the widely studied strip- and ridge-type roughness flows. Hence, relevant length scales and secondary flow strength may differ from the existing knowledge. A detailed and systematic experimental study is undertaken, which allows flow observations in a plane orthogonal to the main flow direction. Chapter 4 discusses these results and the characterisation of the hydrodynamics of the flow and their impact on mass and momentum exchange. Two submerged canopies, one sparse and one dense, are studied. This, as the first step, will allow a better understanding of flow through submerged patchy vegetation.

1.2.2 Investigate the effects of vegetation density and shallowness on the flow structure of patchy vegetation

While the characteristics of the three-dimensional flow in patchy vegetation evaluated in Chapter 4 show a generalised framework of the flow structure, parametric studies are of great importance to identify the effects of (in this case) key bed properties or flow conditions that may govern the size and strength of the flow structures previously identified. Riverine vegetation comprises different species and consequently is of varying density, while water levels fluctuate throughout

the year due to, for instance, periods of intense rainfall. Thus, the effects of vegetation density (spanning over a wide range of solid volume fractions) and shallowness conditions (i.e. how submerged the patch of vegetation is) are investigated in Chapter 5.

To further investigate the nature of turbulence under the imposed spanwise heterogeneity, (i.e. the vegetation patch), for the different cases studied, the energy balance using the turbulent kinetic energy (TKE) equation and streamwise velocity spectrograms are presented and discussed in Chapter 6.

1.2.3 Model spanwise depth-averaged velocity distributions in submerged partially vegetated channels

Results from Chapters 4, 5 and 6 provide the necessary information for calibrating numerical/analytical models for predictive purposes. The quasi-2D Shiono and Knight method, adopted by the UK Environment Agency for use in its 'Conveyance and Afflux Estimation System' (CES) software (www.river-conveyance.net), is a simple but effective method to predict depth-averaged streamwise velocity. Due to its successful application in many laboratory and field cases, the SKM has been adopted in the present work as a first attempt to model submerged partially vegetated channels, providing a basis for estimating flow conveyance that may be useful to environmental regulators and river managers.

1.3 Thesis Outline

This thesis contains 8 Chapters. Chapter 1 introduces the significance and motivation, and presents the aims to be achieved in the present work. Chapter 2 provides a further review of previous relevant research findings in vegetated flows, secondary circulation and spanwise velocity modelling using the SKM. Detailed description of the experimental set-up used for this work, and velocity data processing are presented in Chapter 3. The characterisation of the three-dimensional flow in a partially vegetated channel and the importance of the secondary flow for mass and momentum transport are presented in Chapter 4. This is followed by a parametric analysis of the impact of vegetation density and submergence conditions on the flow structures, which is discussed in Chapter 5. In Chapter 6,

the generation of the cross-plane flow structures and their imprint on the nature of turbulence in the streamwise direction are investigated through the analysis of the terms in the TKE equation and the 1D energy spectra of the streamwise turbulent velocity fluctuations, respectively. Chapter 7 presents the results of the application of the Shiono-Knight Model for the prediction of depth-averaged streamwise velocities in submerged partially vegetated channels. A summary of the present work, along with some comments and recommendations for future work, are provided in Chapter 8.

Chapter 2

Background

This chapter provides a background on the three main topics involved in the present research: vegetated flows, secondary circulation, and conveyance estimation; giving an overview of the key concepts and the current state of research within closely related fields. It starts with the conceptualization and the simplified (widely-adopted) representation of vegetated flows for laboratory investigations. An overview of the mean streamwise structure in fully vegetated flows, and the turbulent features and their scales is given afterwards. A discussion about the impact of vegetation submergence on fully vegetated flows and canopy density on both, fully vegetated flows and emergent partially vegetated flows is also introduced. Towards the end of this first section, vegetation densities and submergence conditions reported in field studies are presented and compared with the few experimental studies on submerged partially vegetated flows (i.e. the case studied here). Observed contributions of the mean and turbulent flow structures developed in vegetated flows to streamwise mass and momentum exchange are also presented.

Later, a brief introduction to early observations of secondary circulation of Prandtl's second kind in various flows is given, followed by the characteristics reported for those caused by corner effects, and heterogeneous surfaces. As the latter is more relevant to the present study, results from several parametric studies are discussed, including observations on the direction of rotation, scaling and strength of the secondary cells. Discussion of the two previous topics leads into their ap-

plication in a flow conveyance estimator. The development and application of the Shiono and Knight method (SKM), an effective model for engineering design purposes, is described in detail, as well as the research on the SKM applied to channels with emergent vegetated floodplains. This background section is intended to show the foundation of knowledge which this thesis builds upon. Here, the streamwise, spanwise and vertical directions are denoted by x, y and z, respectively, with the corresponding instantaneous velocities u, v and w.

2.1 Vegetated flows

2.1.1 Structures and scales

Aquatic vegetation can be conceptualised as a porous medium, usually represented as homogeneous arrays of discrete and rigid canopy elements or stems. Thus, the geometry of the canopy (i.e. community of these elements) is defined by the characteristics of the canopy elements, e.g. the diameter or width of stems or branches d_v, and the spacing between them s. These two parameters are useful for describing the canopy density by, for instance, the frontal area per canopy volume, $a(\mathrm{m}^{-1}) = d_v/s^2$, the solid volume fraction ϕ occupied by canopy elements (for cylinders $\phi \approx (\pi/4)d_v^2/s^2$) or the porosity $\phi_f = 1 - \phi$. Aquatic canopies exhibit a wide range of diameters ranging from $d_v = 0.1 - 9$ cm and solid volume fractions ϕ as high as 0.45 (e.g. Luhar et al., 2008; Nepf, 2011; Tanino, 2012, and further discuss in §2.1.2). Within the vegetation array (i.e. canopy elements), the flow is spatially heterogeneous as it moves around stems. Therefore, flow quantities such as velocities are commonly obtained by applying a double-averaging procedure in which Reynolds' decomposition for an instantaneous variable is followed by a decomposition of the time-averaged variables to eliminate variations due to the canopy structure (Raupach & Shaw, 1982). Details on the time and spatial averaging procedure and further averaging methods are given in §4.2.1.

In this context, submerged vegetation represents a porous obstruction for the flow, leading to velocity heterogeneity caused by variations in vegetation density and morphology (Ghisalberti & Nepf, 2002; Nepf, 2011). In addition to reconfiguring mean flow patterns, the presence of vegetation can also impact turbulence structures. In open-channel flows, largest turbulent features scale with flow depth and channel width (e.g. Tominaga & Nezu, 1991; Vermaas et al., 2011; Jesson, 2012). However, vegetation drag damps the turbulence within the flow changing

the turbulent length scales which would now depend on the average flow resistance exerted by the canopy (Ghisalberti & Nepf, 2004). Thus, transport and circulation of water within the vegetation is largely dictated by the spatial variability of vegetation density. The depth of canopy submergence also plays a key role in water circulation. In fully vegetated channels (as in Figure 1.1b), the vertical profile of streamwise velocity changes form depending on the relative depth of submergence given by the water depth H to canopy height h, i.e. the ratio H/h (Nepf, 2011) (Figure 2.1(a-d)). Thus, a canopy flow is deeply submerged for $H/h > 10$, has a shallow submergence for ratios $H/h < 5$ and it is emergent when $H/h \leq 1$ (Nepf, 2011). Deeply submerged flows or unconfined flows experience large turbulent stress at the top of the canopy and are dominated by large-scale boundary-layer turbulence. This is the case for terrestrial canopies (e.g. Raupach et al., 1996). In emergent canopies (i.e. vegetation height occupies the entire water depth), the flow is controlled by potential gradients from bed and water surface slopes, while for ratios of $H/h < 5$ (very common in aquatic systems), there is an overflow above the canopy and the flow is controlled by both potential gradients and turbulent stress (Nepf & Vivoni, 2000).

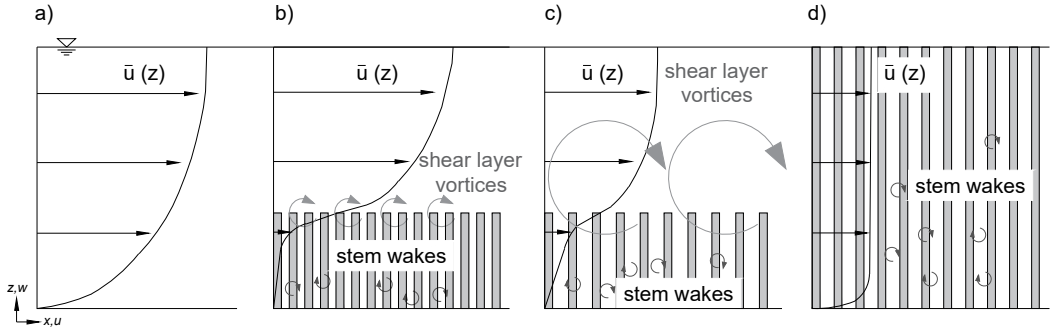


Figure 2.1: Time-averaged streamwise velocity profiles in a (a) boundary layer flow (b) submerged canopy flow with dense vegetation (c) submerged canopy flow with slightly dense vegetation (d) emergent canopy flow.

For submerged canopies of $H/h < 5$, the flow resistance exerted by the canopy causes a differential velocity between the slow moving fluid inside the vegetation and the faster moving fluid outside the canopy, such that at the canopy interface there is a region of shear similar to that observed in free shear layers but of finite width (Ghisalberti & Nepf, 2004). In fact, the canopy shear layer may not extend to the water surface nor the bed, dividing the flow into a lower and an upper region, identified by Nepf & Vivoni (2000) as the *longitudinal exchange zone*, and the *vertical exchange zone*, respectively. In the former, the exchange is

similar as in emergent canopies, and the scalar transport is driven by longitudinal advection. In the vegetated shear layer or vertical exchange zone, turbulent stress significantly contributes to the momentum and scalar transport, and pressure gradient wanes with increasing depth ratios. For unconfined shallow flows ($H/h \geq 2$) with rigid vegetation, the separation of these two zones occurs at a depth z_1. The vertical shear layer is defined by the limits z_1 (where the mean streamwise velocity is U_1), and z_2 (where the velocity is U_2), and has a thickness t_{ml} with a total shear defined by $\Delta U = U_2 - U_1$ (Figure 2.2). In the upper and lower limits of the vertical shear layer the velocity gradient and stress are approximately zero (Figure 2.2).

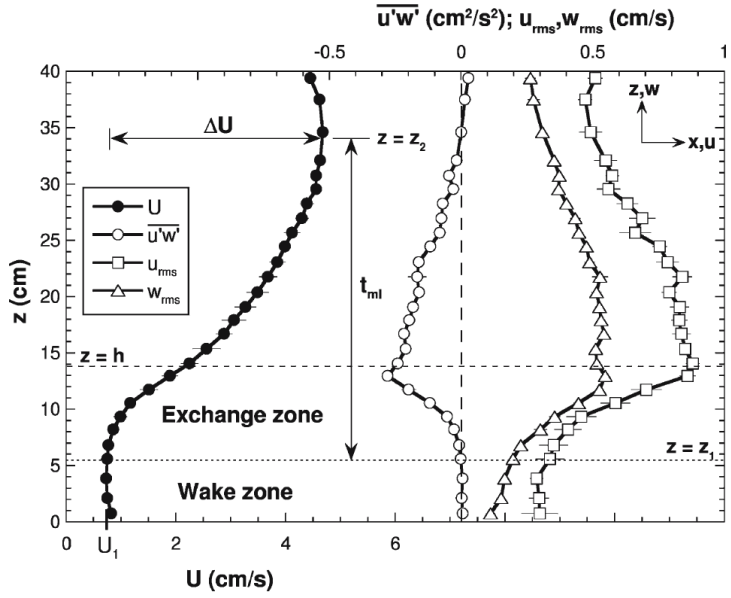


Figure 2.2: Diagram of the shear layer variables from Ghisalberti & Nepf (2006). Here the wake zone refers to the so called longitudinal exchange zone. The presence of vegetation generates the shear layer at the top of the canopy, which transforms the velocity profiles and so the turbulence intensities. U is the time-averaged streamwise velocity, $\overline{u'w'}$ is the vertical Reynolds stress and u_{rms} and w_{rms} represent turbulence strength in the streamwise and vertical directions.

Raupach et al. (1996) established the analogy between the canopy shear layer and a free shear layer, providing explanation to distinctive features of turbulence in canopy flows. As they identified an inflection point in the streamwise velocity profile, which can trigger a flow instability of the Kelvin-Helmholtz type that led to the formation of large coherent structures, they were able to explain the behaviour of the turbulent length scales of such coherent motions responsible for vertical transport near the canopy top. However, this analogy only holds when the canopy drag is sufficient to cause an inflection point in the velocity pro-

file. According to the experimental results by Poggi et al. (2004), large coherent structures only develop for sufficiently dense canopies with a frontal area index $ah \gtrsim 0.1$. Hence, flow in dense vegetation may develop at three different length scales (Raupach et al., 1996; Poggi et al., 2004): deeper in the canopy ($z/h \ll 1$), *Region I*, the length scale is linked to the size of the von Karman vortex streets equal to $d_v/0.21$; in the shear layer, *Region II*, the coherent vortices scale with the canopy drag length scale $(C_D a)^{-1}$ and the distribution of u_*/U_h, where U_h is the time-averaged streamwise velocity at the top of the canopy and the friction velocity $u_* = \sqrt{\max(-\overline{u'w'})}$, where $\overline{u'w'}$ is the vertical Reynolds stress (further discussed in §4.2.2). *Region III* sits well above the canopy ($z/h \gg 2$), in which the shear layer converges to rough-wall boundary characteristics dominated by vortices with length scales $(z - h_d)$ where h_d is the zero-plane displacement of the logarithmic structure, corresponding to the mean level of momentum absorption (e.g. Thom, 1971, and further discussed in §4.2.2). On the other hand, the velocity profile of sparse canopies for which $ah < 0.1$, resembles that of a turbulent boundary layer.

Similar coherent structures and canopy shear layers have also been observed in *emergent partially* vegetated canopies, where canopies do not occupy the entire channel width. In this flow the shear forms at the lateral interface between the vegetation and the free-flow (as shown in Figure 1.1a) (e.g. White & Nepf, 2007), and flow deceleration associated with the porous obstruction (i.e. canopy), will not only depend on the canopy drag length scale, but also on the width of the array, B, that may restrict the spanwise shear layer growth. If the vegetation patch is located within the channel and far from the flume walls, the vortices generated at the canopy lateral boundaries may interact across the canopy width. Hence, the non-dimensional flow-blockage of the array $C_D ab$ (b being half canopy width, where $B = 2b$) may determine the hydrodynamics (Rominger & Nepf, 2011) (Figure 2.3). This spanwise shear layer, as in vegetated flows, exhibits an inflection point that enhances the growth of large coherent structures (i.e. Kelvin-Helmholtz vortices) (White & Nepf, 2007) which may penetrate into the canopy and dominate mass and momentum exchange between vegetated and non-vegetated zones. The influence of the vortices on the canopy interior flow is determined by the vortex penetration length, differentiating low-flow blockage canopies $C_D ab < 2$ from high-flow blockage canopies $C_D ab \geq 2$. Previous descriptions of the flow structure highlight the importance of the submergence ratio H/h and the canopy density as key impact factors influencing the flow behaviour

over vegetated and partly vegetated channels.

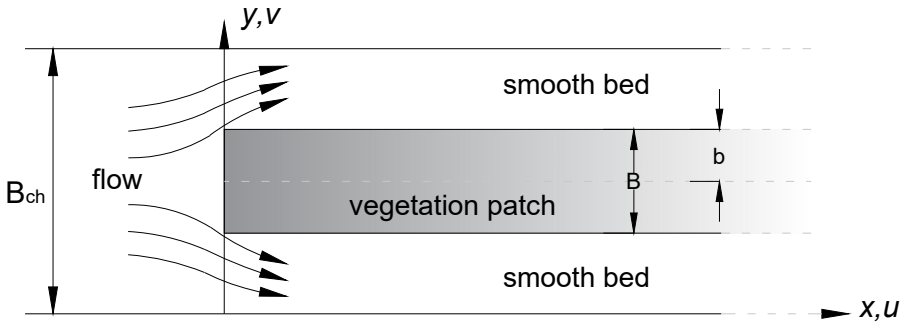


Figure 2.3: Top view of a partially vegetated channel with the vegetation patch located in the middle of the channel.

2.1.2 Quantitative information of key dimensionless parameters in the field

Field measurements have shown the large range of vegetation densities characterising aquatic environments. Canopy-elements such as stems, shoots and clusters of shoots (commonly seen in seagrass or saltmarsh species), or trunks and roots of mangroves have different widths (i.e diameters d_v) and colonize forming finite vegetation patches within rivers, wetlands, estuaries and coastal areas. In seagrass, for instance, blade densities range from $N_v \approx \mathcal{O}(400)$ to $\mathcal{O}(6000)$ m^{-2}, with a blade width between $d_v = 2.5$ and 5 mm (measured by Worcester (1995), reported by Vivoni-Gallart (1998)). Similar characteristics are present in salt marshes, in which the stem density ranges from $N_v \approx \mathcal{O}(27)$ to $\mathcal{O}(3000)$ m^{-2}, and the characteristic plant width can reach up to $d_v = 10$ mm (Leonard & Luther, 1995; Asaeda et al., 2005; Huang et al., 2008; Neumeier & Amos, 2006; Ozeren et al., 2014). In contrast, trunk and roots densities in mangroves are smaller, with $N_v \approx 0.08 - 1$ trunks m^{-2} (Mazda et al., 1997; Mazda et al., 2006), and $N_v \approx 22 - 122$ roots m^{-2} (Mazda et al., 1997, 2006; Osorio et al., 2019) with reported trunk and root diameters as large as $d_v = 12$ cm and $d_v = 4$ cm, respectively. These values suggest a canopy frontal area a that can be as high as $a \approx 20$ m^{-1}. Moreover, the values of the canopy half width b reported in some of these studies vary from nearly 0.3 m to 50 m, leading to approximate values of the flow-blockage factor $C_D ab$ from 0.2 to 55 (Table 2.1). In addition, solid volume fractions reported are of roughly $\phi \approx 0.0002$ to 0.45. Submergence ratios H/h measured in the field, although highly variable due to seasonal changes and

tides, range from emergent $H/h \approx 0.2$ to submerged conditions $H/h \approx 6.5$ (Table 2.1).

Although experimental studies in vegetated open-channel flows have been performed to understand their hydrodynamics, for a wide range of canopy densities and submergence ratios observed in nature (see for example the review of Nepf (2012)), these have not focused on the role of secondary circulation. In fact, secondary circulation in open-channel flows has been a field of research mostly devoted to the understanding of the creation of bedforms such as sand ribbons (see, for instance, references in Nikora & Roy, 2012), and the behaviour of the cell structure in compound open-channels to characterise their influence in quasi-2D flow models like the Shiono-Knight model (e.g. Shiono & Knight, 1991; Omran & Knight, 2006; Knight et al., 2007). Thus, studies on secondary circulation over granular bed patches are few in number (e.g. McLelland et al., 1999; Wang & Cheng, 2006; Vermaas, 2008; Vermaas et al., 2011; Jesson, 2012), but even more rare on partially vegetated flows (Nezu & Onitsuka, 2001; White & Nepf, 2007; Hopkinson & Wynn, 2009; Folorunso, 2015) (Figure 2.4).

Table 2.1: Aquatic vegetation properties reported in some field studies.

Specie	Density [m^{-2}]	d [mm]	$C_D ab$	H/h	Reference
Zostera marina	242 - 330	2.8	n/a	2.0 - 4.4	Worcester (1995)
Zostera marina	133 - 173	2.8	9.5 - 17.7	0.2 - 1.3	
Spatina maritima	2340 - 3030	3.0 - 6.0	n/a	3.0	Neumeier & Amos (2006)
Spartina anglica	1450 - 1850	3.0 - 6.0	10.6 - 55.5	1.8 - 2.7	
Bacopa caroliniana	27.8	3.6	0.3	n/a	Huang et al. (2008)
Cladium jamaicense	317.3	10.4	8.3	n/a	
Eleocharis cellulosa	41.7	2.4	n/a	n/a	
Eleocharis elongata	2100	1.0	n/a	n/a	
Typha augustifolia	48 - 286	21 - 29*	0.4 - 3.5	n/a	Asaeda et al. (2005)
Zizania latifolia	46 - 721	20 - 42*	0.4 - 14.4	n/a	
S. alterniflora	405 - 545	5.1 - 6.5	3.3 - 4.2**	0.81 - 0.85	Ozeren et al. (2014)
J. roemerianus	2857	2.4	4.20 - 5.7**	0.5 - 0.8	
Sonnerita sp.(trunk)	0.08	117	0.22	1.1	Mazda et al. (2006)
Sonnerita sp.(pneumatophores)	131	7.3	22.2	6.5	

* These values refer to shoots. For all the other studies on seagrass and saltmarsh species, canopy-elements are stems.

** These values were calculated using the drag coefficient specified in the reference. For all the other studies, C_D was assumed to be 1.

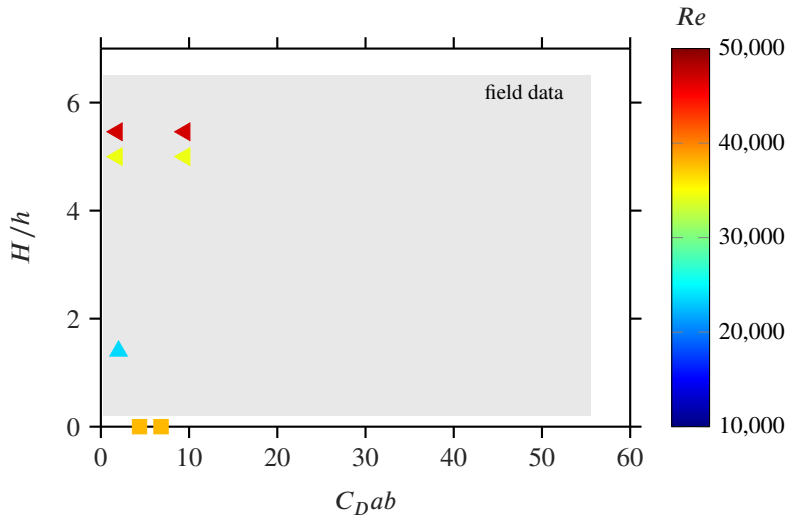


Figure 2.4: Data, $C_D ab$ vs H/h, reported in field studies (grey area), and collected from experimental studies that analysed the secondary flow in submerged vegetated-porous patches (△) Nezu & Onitsuka (2001), (□) Hopkinson & Wynn (2009), (◁) Folorunso (2015). In the study by Hopkinson & Wynn (2009) vegetation is placed on the streambank, consequently no H/h value was assigned.

Experimental flows in Figure 2.4 are in turbulent subcritical regime as in natural rivers. The contrast between field and experimental data reveals the fact that the nature of secondary circulations and their role on mass and momentum transport in partially vegetated flows remains largely unknown. Yet, fundamental knowledge of their dynamics is required before any attempt to develop predictive formulae for secondary velocities.

2.1.3 Momentum and mass exchange

In flows over heterogeneous beds such as compound channels or emergent partially vegetated channels, the flow over the shallower floodplain or within the vegetation, respectively, is slower than that in the main open channel due to the difference in roughness. As a result, a horizontal shear (or mixing) layer develops at the interface where there is a large gradient in velocities (Van Prooijen et al., 2005). This horizontal shear layer is characterised by self-organised flow structures, which has a horizontal length scale (in shallow flows) that is larger than the water depth (White & Nepf, 2007). In compound channels, the differences in bed height in the spanwise direction sustains the velocity difference and the mixing layer growth is limited by the bed friction, achieving an equilibrium width. In emergent partially vegetated channels a similar horizontal shear layer is generated. However, vegetation greatly dampens the flow, generating turbulence and

adding drag force which significantly increases the velocity gradient between the vegetation and the main channel. As a consequence, the horizontal vortices are stronger compared to those in cases without vegetation, promoting more transverse momentum transport into the canopy (White & Nepf, 2007; Truong et al., 2019). Furthermore, the transverse momentum exchange in compound channels significantly depends on the transitional slope; for example, in steep slopes the secondary circulation plays an important role in momentum transport (Truong et al., 2019).

It has been demonstrated that both coherent mixing layer vortices and secondary circulations can contribute significantly to streamwise momentum exchange in 3D, partially obstructed shear flows (e.g. Vermaas et al., 2011; Vanderwel et al., 2019; Medjnoun et al., 2020). Results from an experimental study on flow over a longitudinal surface composed of rough and smooth strips revealed that the momentum exchange contributions from the secondary circulation and from mixing layer vortices are of the same order of magnitude (Vermaas et al., 2011). In fact, the former was observed to exceed the contribution of the latter as water depth increased. Vanderwel et al. (2019) studied, numerically and experimentally, the development of secondary circulation in turbulent boundary layers on ridge-type roughness flows and observed that dispersive stresses due to mean flow heterogeneities contribute up to 28% of the total shear stress. Medjnoun et al. (2020) investigated the effects of roughness geometry on secondary circulation in turbulent boundary layers. Dispersive stresses arising due to the spatial heterogeneity of the mean flow were shown to be significant in magnitude over a large portion of the boundary layer, contributing between 15 and 55% of the total shear stress. It is yet to be explored how significant secondary circulation is for momentum exchange in submerged partially vegetated flows (i.e. this study), as these flows are expected to be highly three-dimensional.

In addition, submerged aquatic vegetation has the potential to improve water quality via, for instance, nutrient uptake and oxygen production (e.g. Moore, 2004; Bal et al., 2013; Cornacchia et al., 2019). The efficiency of these processes depend on the rate of exchange of particulates between vegetated and non-vegetated zones. As fully vegetated flows are shear-driven turbulent flows in which large scale coherent vortices dominate the exchange of scalars and momentum between the canopy and the overlying flow, mass exchange is enhanced within a finite shear layer (Ghisalberti & Nepf, 2004) through mainly turbulent

diffusivity, D_{tz} (Ghisalberti & Nepf, 2005). The vertical variability of D_{tz} is significant and scales with the mixing layer width having a peak at $D_{tz} = 0.032\Delta U t_{ml}$ (Ghisalberti & Nepf, 2005). However, a vertical advective flux coming from secondary circulation could make a significant contribution to water replacement above the canopy, highlighting the importance of secondary circulation in vertical mass transport (Ghisalberti & Nepf, 2005; Ghisalberti, 2010). A rather simple quantification of this contribution is given by the Peclet number Pe, which is the ratio of vertical advection to turbulent diffusion (further explored in §4.6). Evaluation of the Peclet number under different vegetation densities and submergence ratios will provide an understanding of the dominant mechanisms controlling vertical mass transport. When $Pe \ll 1$ the flow is vertical mixing dominated. In contrast, when $Pe \gg 1$ the flow is controlled by advection and the water renewal will be primarily dominated by the secondary circulation flux carrying nutrients, sediments, and contaminants from above the canopy. Finally, when $Pe \approx \mathrm{O}(1)$ both advection and diffusion are equally significant.

2.2 Secondary circulation

Historically, observations of sediment agglomeration in distinct patterns on open-channel flow beds present evidence of flow circulation orthogonal to the main flow direction. For example, Vanoni (1946) observed the formation of several sediment streaks along an open channel after introducing fine sediments in circulating clear water. Artificial bedforms, such as sand ribbons, were also experimentally observed on beds of straight channels where flow-bed sediment interactions occurred (e.g. McLean, 1981; Nezu & Nakagawa, 1993). However, the first classification of this orthogonal flow in fluid mechanical terms was proposed by Prandtl 1952. The first category suggested by Prandtl, is related to mean flow skewness due to heterogeneities in the streamwise direction caused by, for instance, meanders in rivers or curved pipes. The second class, known as Prandtl's secondary flow of the second kind, corresponds to the secondary circulation induced by turbulence anisotropy, which manifests in the form of streamwise rotating motions embedded within a primary flow (Einstein & Li, 1958; Hinze, 1967). Only the latter kind is of importance to this work as it is restricted to turbulent flows in straight channels.

Prandtl's secondary flow of the second kind has been observed in the corners of

prismatic channels as a fluid motion going from regions close to the corner bisector to the walls (Nezu & Nakagawa, 1993, and the references therein). It has also been observed over beds with differential roughness or varying topography as cross-sectional plane spiral motions with upflows and downflows near the junction between different bed roughnesses. Two of the most studied flows over non-homogeneous beds in open-channels comprise: compound channels, consisting of a main channel and adjacent floodplains, (e.g. Shiono & Knight, 1988, 1991; Tominaga & Nezu, 1991) and flows over bimodal sediment beds (e.g. McLean, 1981; Colombini, 1993; Colombini & Parker, 1995; Nezu & Nakagawa, 1993). However, relatively fewer studies exist on secondary flows of Prandtl's second kind in patchily vegetated channels (Naot & Rodi, 1982; Nezu & Onitsuka, 2001). These secondary flows enhance the transport of transferable quantities associated with turbulent motion, momentum and energy as they distort the local flow structure, in particular, contour lines of mean streamwise velocity on a plane orthogonal to the primary flow direction. This distortion modifies the wall shear stress that ends up redistributing turbulence intensities (Nezu & Nakagawa, 1993).

2.2.1 Corner secondary circulation

Velocity contour lines in open-channels bulge toward the side walls reflecting the influence of the free surface and/or the aspect ratio (i.e. channel width to water depth ratio, B_{ch}/H) (Naot & Rodi, 1982; Nezu & Onitsuka, 2001). The free surface damps velocity fluctuations perpendicular to it, consequently, the maximum velocity occurs below the free surface. The aspect ratio affects the secondary flow size, so secondary cells may occupy the entire channel width or be restricted to small distances from the walls. According to the extensive studies reported on Nezu & Nakagawa (1993), a central part unaffected by corner secondary circulation can be defined by:

$$\left|\frac{y'}{H}\right| \leq \frac{\dfrac{B_{ch}}{H} - \left(\dfrac{B_{ch}}{H}\right)_{cr}}{2} \tag{2.1}$$

where y' is the spanwise distance from the centre of the channel, and $(B_{ch}/H)_{cr}$ is the critical aspect ratio below which secondary flows affect the whole channel, $(B_{ch}/H)_{cr} = 5$. In narrow channels, where $(B_{ch}/H)_{cr} < 5$, the secondary circu-

lation cells appear with one stronger near the bed, transporting low momentum toward the channel centre, and another weaker near the free surface, transporting high momentum from the water surface downwards (Naot & Rodi, 1982) (Figure 2.5). As a consequence of the secondary flow, a "velocity-dip" appears, where the maximum velocity in the vertical direction is seen just below the free surface (Nezu & Nakagawa, 1993). The velocity-dip disappears in wide open-channels (i.e. $(B_{ch}/H)_{cr} < 5$) with the strengthening of the free surface cell. In some cases, the free surface cell may even suppress the bottom cell (Naot & Rodi, 1982) (Figure 2.5). Corner secondary flow patterns in smooth open-channels remained similar for aspect ratios between four and six (Nezu & Nakagawa, 1993).

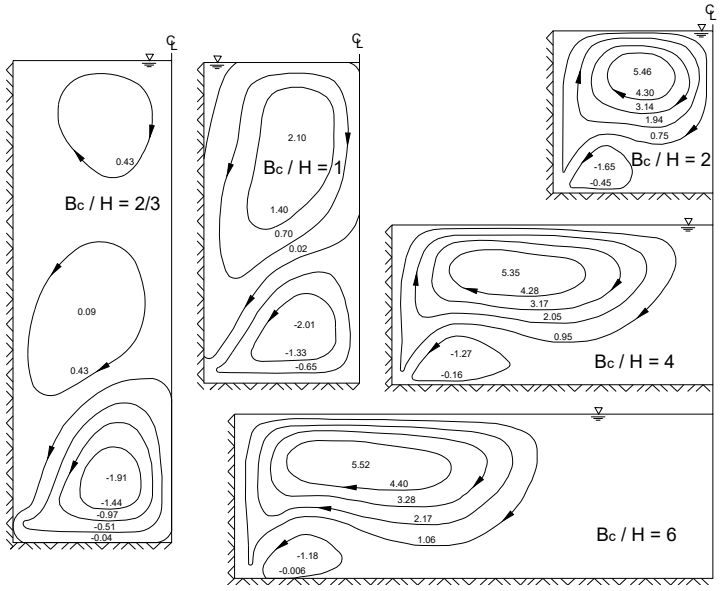


Figure 2.5: Secondary Circulation streamlines in rectangular-straight open-channels of different width-to-depth ratios. Adapted from Naot & Rodi (1982).

At larger aspect ratios of 6.3 and 8.5, the surface and bottom cells were seen to occupy a spanwise distance equal to the water depth, followed by a cross-sectional cell of size H right next to them (Rodríguez & García, 2008). For uniform smooth beds, the bottom cell dominates, thus the adjacent cell rotates clockwise. However, for uniform rough beds, the surface cell is predominant; consequently, the adjacent cell rotates counterclockwise (Rodríguez & García, 2008). Therefore, sidewall effects are usually restricted to a region of approximately $2H$ in very wide open-channel flows over uniform beds. Although the corner secondary cell structure over heterogeneous surfaces may be the same, there is no characterisation of the relationship between the aspect ratio and the corner secondary cell patterns in vegetated flows or partially vegetated flows. Nezu & Onitsuka (2001)

experimentally studied secondary circulations in a submerged partially vegetated channel. They reported that wall effects were limited to approximately 20% of the channel width, but a final conclusion cannot be drawn from a single study in which only one vegetation density and submergence condition were investigated.

2.2.2 Secondary circulation over heterogeneous surfaces

Secondary circulation over surfaces with differential roughness was probably first investigated by Hinze (1967), who experimentally observed these vortical structures in a rectangular duct with partially corrugated walls. Hinze used the turbulent kinetic energy (TKE) equation to analyse the secondary flow mechanics, suggesting that secondary circulation is induced by the imbalance between turbulent production and viscous dissipation. The study showed that the imbalance was due to turbulence anisotropy in the shear stresses caused, in turn, by the spanwise heterogeneity of the wall. Downward motions were observed over the rough (corrugated) surfaces, i.e. strips of higher drag, and upward motions over the smooth, low drag strips (c.f. Figure 1.1d).

In open-channel flows, observations of secondary flow structures over heterogeneous mobile beds attracted the interest of researchers in the river hydraulics community, as these cross-plane motions were often associated with bed-forms formation and sediment transport (McLean, 1981; Colombini, 1993; Nezu & Nakagawa, 1993). Several laboratory and field studies on secondary flows over heterogeneous beds in open channels were performed by Nezu and co-workers during the last decades of the 20th century (Nezu & Nakagawa, 1993). In the 1980s, their studies on movable sand beds concluded that the organised fluid motions were associated with sediment transport, and occurred intermittently until sand ribbons were observed and seemed to stabilise. At this time the secondary circulations also appeared to be stable across the channel. Experimental studies on secondary flow also comprised artificial ridge elements. Nezu & Nakagawa (1984) created rigid ridges with a trapezoidal cross-section and placed them over a conduit surface at regular intervals. They observed relatively strong upflows over the ridges compared to the downflows over the troughs. Their results showed that strong secondary cells, of the size of the water depth, were produced when the spacing between ridge elements was equivalent to the water depth, inducing significant spanwise mean flow and turbulence heterogeneity. Later, McLelland et al. (1999) used a bimodal sediment bed composed of a sand and gravel mixture

to shed some light on the structure and intensity of the secondary circulation generated and the selective transport of the sediment mixture. They observed a self-organisation of the grains in an alternating pattern of coarse and fine sediments strips in the spanwise direction. It was reported that the secondary flow generated, re-distributed the cross-stream bed shear stress. Finer sediments were entrained from high shear stress regions and deposited in regions of lower shear stress, enhancing lateral fluctuations, which, in turn, lead to higher shear stress heterogeneity and turbulence anisotropy. The non-homogenitity of the shear stress contributed to sediment sorting, generating a loop of self-sustained feedback.

In the last two decades, significant effort has been devoted to characterise secondary circulation over heterogeneous surfaces due to the advancements in computational resources and experimental apparatus. These advancements have allowed for deeper investigations on the cross-plane vortical structures and their formation, but also put into question previously established concepts and their applicability. Since then, heterogeneous surfaces, present in both natural systems and engineering systems (such as aerodynamic surfaces, wind farms, urban-like configurations, among others), have been studied under two different conditions: ridge-type, where the surface presents solely changes in elevation or topography (e.g. compound channels) (Figure 1.1d), and strip-type, where the spanwise heterogeneity is represented by variations in wall drag or skin-friction (e.g. bimodal sediment beds) (Figure 1.1e). Wang & Cheng (2006) performed an experimental study in an open channel under both bed roughness types. Similarly to previous findings, the study noticed a pair of counter-rotating cells developing at the bed discontinuity. In their experiment, the location of upward and downward motions differed from one roughness type to the other. In strip-type roughness flows, they observed upward (downward) motions over the smooth (rough) strip. For ridge-type roughness flows, the upwash occurred either above the elevated regions or at the discontinuity depending on the shape of the ridge. Vermaas (2008) experimentally studied a strip-type roughness flow in an open-channel, where the channel width was split into two strips, one smooth and one rough. The latter composed of fixed sediments. A pair of secondary flow cells was observed in the cross-plane, the centre of which was located above the smooth side near the bed discontinuity. The results showed that secondary cells scaled with the water depth, having their centre slightly below half of the water depth, and had a width of twice the water depth. Jesson et al. (2013b) also investigated

secondary flows over parallel rough-smooth strips in an open-channel. The study reported bulging of the streamwise velocity contours as a consequence of the bed heterogeneity and the secondary circulation formation. Downflow over the rough bed and upflow above the smooth bed were observed, which is in agreement with the studies by Wang & Cheng (2006) and Vermaas (2008).

Ridge-type roughness flows in open-channels have been mainly studied in compound channels, representing a main stream and the adjacent elevated floodplains. Tominaga & Nezu (1991) carried out one of the first experimental works showing the three-dimensional distribution of mean velocity and the corresponding turbulent components in compound channels. They showed that secondary cells were generated at both sides of the main channel-floodplain discontinuity, sharing a strong upward flow at the junction. The magnitude of the rotating cells reached maximum when the floodplain height to water depth ratio was of 0.5. As this ratio became larger, the cell above the floodplain became bigger, occupying the entire water depth, and the cell over the main channel almost disappeared. However, smaller ratios led to a bigger main channel secondary cell and no secondary cell on the floodplain . They also investigated the effects of a rough bed on the floodplain, but no significant differences between smooth and rough floodplains were found. These results coincided with later studies reported in Nezu & Nakagawa (1993) where trapezoidal and rectangular channels, as well as different bed roughness were studied. A highlight of the studies by Nezu & Nakagawa (1993) was the explanation given to the vertical flow seen at the discontinuity pointing towards the free surface, which they showed to be caused by turbulence anisotropy between the main channel and the floodplains. Kara et al. (2012) performed a computational study, Large Eddy Simulations - LES, on the turbulent flow of compound channels of different floodplain depths. The secondary circulation structure and rotation observed were in good agreement with the experimental work performed by the authors and previous studies by Tominaga & Nezu (1991) and Nezu & Nakagawa (1993). However, the simulations allowed an accurate statistical turbulent flow analysis showing that as a consequence of the secondary circulation, spanwise Reynolds stresses were of the same order of magnitude as vertical Reynolds stresses. The importance of the spanwise Reynolds stresses became less significant in the shallow condition where the floodplain to water depth ratio was of 0.25. They reported that turbulence anisotropy of the bed-normal Reynolds stress was responsible for the generation of the secondary circulation.

Despite channels having riparian vegetation, studies investigating secondary circulations in partially vegetated flows are scarce. Naot et al. (1996) studied the hydrodynamics of patches of vegetation of varying density and focused their analysis on the impact of these cross-sectional cells on the streamwise velocity field. Nezu & Onitsuka (2001) observed secondary circulation for a single patch of vegetation, with a sparse density and under confined flow conditions (of water depth to canopy height ratio of approximately 1.4), which could restrict the secondary cells growth. They demonstrated that the secondary cells resembled the patterns of strip-type roughness flows (shown in Figure 1.1e) as opposed to the ridge-type roughness flows. However, there remains a lack of understanding of the scale of the secondary cells, and their structure and strength in unconfined flow conditions. Furthermore, the influence of canopy density in flows over patchy vegetation is unknown.

Secondary flows have also earned great interest in the mechanical engineering community, which have devoted particular attention to investigating the effects of the heterogeneous surface characteristics on the secondary circulation structure and formation mechanism. Mejia-Alvarez & Christensen (2013) experimentally investigated secondary flows in a turbulent boundary layer on a replica of a damaged turbine blade. They reported that the ensemble-averaged streamwise velocity was heterogeneous in the spanwise direction and formed flow channels of high- and low- momentum pathways (HMPs and LMPs, respectively). These pathways enhanced turbulent, vortical motions, forming at their boundaries. Barros & Christensen (2014), further investigated the flow over this highly irregular surface, showing the presence of secondary flows. They identified LMPs with upward motions and HMPs with downward motions, occurring above the recessed and elevated regions, respectively. Turbulent Kinetic Energy (TKE) and Reynolds shear stresses were observed to be particularly enhanced in regions of LMPs. Although LMPs are associated with upflows and HMPs with downward motions, recent studies showed that the spanwise location of the momentum pathways were different for ridge- and strip-type roughness flows, which could be linked to the reversal of the direction of rotation of the secondary motion.

Direction of rotation

For the strip-type roughness, the converging motion associated with a HMP has been observed over high drag regions, but also low drag regions depending on

the specific configuration of the spanwise heterogeneity. Willingham et al. (2014) modelled a strip-type roughness flow and studied the effects of increasing ratios of high-to-low roughness, and reducing the width of the high roughness strip, keeping a constant separation between high roughness strips, S (Figure 1.1e). For all cases, they observed LMPs and HMPs over low and high roughness regions, respectively. Anderson et al. (2015) performed LES for a broad parametric range over which the high roughness strip width, S, to boundary layer thickness, δ, ratio and the high-to-low roughness ratio were varied. The LMP and HMP formation occurred over the low and high roughness strips, respectively, which is in agreement with the results by Wang & Cheng (2006) and Willingham et al. (2014).

However, some studies have shown that LMPs (HMPs) can also manifest over high (low) roughness strips. Stroh et al. (2016) performed a series of Direct Numerical Simulations (DNS) in a fully turbulent channel flow varying two parameters: the ratio of the distance over consecutive smooth regions, P, to the rough strip width, S (see Figure 1.1e), and friction Reynolds numbers. They showed that increasing the distance between smooth strips, while keeping the P/S ratio constant, led to the formation of a new counter-rotating pair with the opposite direction of rotation, which eventually replaced the initial pair of cells. Thus, the location of LMPs (HMPs) passed from being above the rough (smooth) to manifest over the low (high) roughness regions. They also reported that increasing the width of the rough strip for the same distance between smooth strips had the same effect on the location of the HMPs and LMPs. Recent investigations over super-hydrophobic surfaces, characterised by spanwise-aligned grooves, representing regions of high and low drag with a no-slip surface and a shear-free surface, have shown similar behaviours to those observed by Stroh et al. (2016). Large widths of the no-slip region presented downward flows over the no-slip region. In contrast, small widths of the no-slip region reversed the sense of rotation of the secondary circulation due to the growth of an emergent new pair of cross-sectional vortical structures (Türk et al., 2014). Furthermore, Chung et al. (2018) performed numerical experiments varying the spanwise spacing of high and low shear stress strips. Their results showed that for very large roughness wavelengths, HMPs were seen over low stress regions.

On ridge-type roughness flows, downward motions have been observed over the lower drag, or recessed, regions. Vanderwel & Ganapathisubramani (2015), ex-

perimentally studied a ridge-type roughness flow using LEGO baseboards and bricks to evaluate the effect of spanwise spacing between ridge elements on the secondary flow structure and strength. By systematically varying the ratio of spanwise spacing to boundary layer thickness, they demonstrated that upwelling (associated with LMPs) was located over the elevated regions and downdraughts (associated with HMPs) in the recessed regions. This is consistent with previous findings by Nezu & Nakagawa (1984) and Wang & Cheng (2006), and the follow-up experimental and numerical studies over elevated spanwise-aligned ridges created by LEGO bricks by Vanderwel & Ganapathisubramani (2015). Furthermore, Hwang & Lee (2018) investigated the effects of ridge width (S in Figure 1.1d) and the spanwise wavelength (P in Figure 1.1d), using DNS. They argued that as the value of S increased, a new pair of rotating cells, called tertiary flow, emerged over the elevated region. They also showed that further increments of S led to the formation of a quaternary flow over the crest. However, the rotational direction of the secondary flow remained unchanged. The location of HMPs and LMPs that occurred over the recessed and elevated regions, respectively, also remained unaltered.

These parametric studies, despite the heterogeneous surface type, have also demonstrated the importance of the spanwise spacing P and roughness width S (illustrated in Figures 1.1d and 1.1e) in the scaling of the secondary cells over both, strip- and ridge-type roughness flows. In fact, some limiting cases can be identified when comparing S to the dominant length scale of the flow, i.e. the boundary layer thickness δ.

Scaling

Studies of secondary flows in turbulent boundary layers over heterogeneous surfaces have evaluated the effects of varying S (the rough/elevated region width) and δ (the turbulent boundary layer thickness) to correlate the surface properties with the hydrodynamic properties of the flow. Note that for open-channel flows $\delta \approx H$. As the ratio S/δ becomes significantly larger than 1, S is sufficiently large to contain the secondary flow cells within the areas close to the spanwise heterogeneity. Hence, in the areas far from the discontinuity, the flow behaves according to the local surface conditions (e.g. Vanderwel & Ganapathisubramani, 2015; Chung et al., 2018; Medjnoun et al., 2018; Yang & Anderson, 2018). In ridge-type roughness flows where $S/\delta \gg 1$, a new pair of counter-rotating

cells (also known as tertiary flow) has been observed to emerge at the roughness discontinuity. This new pair had a smaller size and was weaker than the secondary flow (Vanderwel & Ganapathisubramani, 2015) However, a tertiary flow also manifested for increasing ridge width values (Hwang & Lee, 2018). For the cases where $S/\delta \ll 1$, the size of the secondary circulation is limited by the smaller spacing, P, or roughness width, S, and it is confined near the heterogeneous surface. Hence, the flow remains relatively homogeneous (Vanderwel & Ganapathisubramani, 2015; Chung et al., 2018; Yang & Anderson, 2018).

The size and strength of the secondary circulation were maximised when the S/δ ratio was ≈ 1. The secondary cells filled the entire space within the boundary layer and the channel, and the strength was relatively large compared to smaller or larger S/δ ratios (Nezu & Nakagawa, 1984; Vanderwel & Ganapathisubramani, 2015; Medjnoun et al., 2018). Interestingly, Yang & Anderson (2018) observed the reversal of the direction of rotation of the secondary flow at this limiting case, which is thought to be the result of the competing effect between the δ-scaled secondary flow (caused by surface heterogeneity) and the roughness-scaled secondary circulation induced by the roughness elements of the ridge-type roughness flow.

Both the understanding of the hydrodynamics of vegetated flows presented in §2.1.1 and the secondary circulation characteristics over heterogeneous surfaces given in §2.2 are essential to modelling complex three-dimensional river systems. The impact of the three-dimensional flow structures is reflected on the lateral distribution of the mean streamwise velocity, and the (discharge) conveyance capacity of rivers. Conveyance estimation informs authorities, enabling them to make better decisions on a variety of technical aspects relating to river engineering including, but not not limited to, open-channel flow engineering design and flood risk assessment.

2.3 Conveyance estimation

Riverine vegetation growing alongside river banks and in floodplains creates additional hydraulic resistance to the flow, reducing the local velocity within the vegetation; thereby increasing the mean flow velocity difference between the vegetated region and the adjacent free flow. The spanwise variations in roughness

result in shear layers developing at the vegetation boundaries, characterised by the formation of large turbulence-induced vortices (e.g. Ikeda & Kanazawa, 1996; Ghisalberti & Nepf, 2002; White & Nepf, 2007), and cross-channel secondary circulation structures (e.g. Naot et al., 1996; Nezu & Onitsuka, 2001). These coherent structures enhance not only mass but also momentum exchange between the vegetated and non-vegetated regions, affecting the lateral distribution of the streamwise velocity, and modifying the (discharge) conveyance capacity of rivers (e.g. Rameshwaran & Shiono, 2007; Tang & Knight, 2009; Tang et al., 2011). Therefore, prediction of the lateral distribution of streamwise velocity is essential in estimating flood capacity which, in turn, advises flood alleviation schemes, flood warning and emergency evacuation plans, and river restoration studies.

The superposition and interaction of the highly turbulent shear, the bed-generated turbulence and the secondary circulation structures, and their contributions to streamwise momentum exchange and flow conveyance, are complex and a subject of contention in fluid mechanics. Various three-dimensional models, based on the three-dimensional form of the Navier-Stokes equations, have been developed to predict streamwise velocities in non-vegetated compound channels (i.e. river channels with non-vegetated floodplains) (e.g. Pezzinga, 1994; Kang & Choi, 2006; Rodi et al., 2013). However, these 3D models rely on several empirical constants and are computationally expensive. As a result one-dimensional models are very popular in practice. Two of the most widely used 1D conveyance estimators are the Manning and Darcy-Weisbach empirical equations, respectively,

$$Q = \frac{A_{cs} {R_H}^{2/3}}{n} {S_0}^{1/2} \tag{2.2}$$

$$Q = \left(\frac{8g}{f}\right)^{1/2} A_{cs} {R_H}^{2/3} {S_0}^{1/2} \tag{2.3}$$

where A_{cs} is the cross-sectional area of flow, R_H is the hydraulic radius, S_0 is the channel bed slope, g is the acceleration due to gravity, and n and f are the Manning and Darcy-Weisbach friction coefficients, respectively. The friction factor includes energy loss mechanisms such as turbulence, vegetation, bed roughness, channel geometry, etc, which determine the frictional resistance of the channel to a

given flow. For over-bank channels, the cross-section is divided into sub-channels of homogeneous streamwise velocity and the discharge is computed as the sum of the discharges in each sub-section. However, these 1D models are empirical, fit specific experimental datasets, and treat the channel as a unit ignoring certain components of the 3D equations (e.g. Wormleaton & Merrett, 1990; Bousmar & Zech, 1999). Furthermore, these do not describe the distribution of the lateral mean velocity, which is important for the applications stated above.

Recently, physically derived models, or quasi-two-dimensional formulae, based on depth-averaged parameters have been found to be a suitable compromise between one and three-dimensional models, and have proved effective for engineering design purposes. One such approach was proposed by Shiono & Knight (1988), who developed an analytical model for the depth-averaged streamwise velocity and bed shear stress in non-vegetated compound channels, based on the effects of bed shear stress and laterally generated turbulence on momentum exchange. This model was later improved to include the effects of the secondary circulation through an advective term, as secondary flow was found to be of great importance at the main channel-floodplain interface (Shiono & Knight, 1991). The model, known as the Shiono and Knight Model (SKM), was proven to be capable of reproducing velocities and bed shear stresses in non-vegetated compound channels (e.g. Omran & Knight, 2006; Rameshwaran & Shiono, 2007; Tang & Knight, 2009) and in-bank flows with differential roughness (e.g. Jesson et al., 2013c), and has been successfully applied to real cases (e.g. McGahey et al., 2006). Due to its efficacy, it was adopted by the UK Environment Agency for use in its 'Conveyance and Afflux Estimation System' (CES) software (www.river-conveyance.net).

2.3.1 The Shiono-Knight Method (SKM)

The Shiono and Knight method is a quasi two-dimensional theoretical model based on the depth-averaged form of the Reynolds-Averaged-Navier-Stokes (RANS) equation. It was initially proposed to model the interaction between a main channel and its adjacent floodplains in compound channels (Shiono & Knight, 1988), and it was later extended to include secondary circulation effects (Shiono & Knight, 1991). The depth-averaging gives a differential equation, which can be solved analytically, and takes into account the effects of bed friction, lateral turbulent exchange and secondary circulation (Shiono & Knight, 1991).

The mathematical expression for rectangular channels will be outlined in the following paragraphs but more detail can be found in Shiono & Knight (1988, 1991). Assuming a steady ($\partial/\partial t = 0$), uniform flow ($\partial/\partial x = 0$) and neglecting friction viscosity, the streamwise momentum Navier-Stokes equation is given by (Shiono & Knight, 1988),

$$\rho\left(\frac{\partial}{\partial y}\overline{u}\ \overline{v} + \frac{\partial}{\partial z}\overline{u}\ \overline{w}\right) = \rho g S_0 + \frac{\partial}{\partial y}(-\rho\overline{u'v'}) + \frac{\partial}{\partial z}(-\rho\overline{u'w'}) \tag{2.4}$$

where, $\overline{u}$, $\overline{v}$ and $\overline{w}$ are the time-averaged streamwise, spanwise and vertical velocities corresponding to x, y and z; u', v' and w' are the turbulent velocity fluctuations, or deviations from the time-averaged values. The water density is represented by ρ, g is the acceleration due to gravity and S_0 is the bed slope. The expression in (2.4) exhibits the balance between the gravitational driving forces (first term in the right-hand-side (RHS)) and the momentum transfer from secondary circulation (left-hand-side (LHS)) and turbulent Reynolds stresses (second and third terms in the RHS). The depth-averaged form of (2.4) is obtained by integrating (2.4) in depth (i.e the z-direction), from the bed level z_{bed} to the water surface level z_s. Thus, applying the Leibnitz integral rule to the first term on the LHS of (2.4) gives,

$$\begin{aligned}\int_{z_{bed}}^{z_s}\rho\frac{\partial}{\partial y}(\overline{u}\ \overline{v})dz = &\ \frac{\partial}{\partial y}\int_{z_{bed}}^{z_s}\rho(\overline{u}\ \overline{v})dz - \rho(\overline{u}\ \overline{v})|_{z_s}\frac{\partial z_s}{\partial y} + \rho(\overline{u}\ \overline{v})|_{z_{bed}}\frac{\partial z_{bed}}{\partial y} \\ = &\ \frac{\partial}{\partial y}H\rho\langle\overline{u}\ \overline{v}\rangle_d - \rho(\overline{u}\ \overline{v})|_{z_s}\frac{\partial z_s}{\partial y} + \rho(\overline{u}\ \overline{v})|_{z_{bed}}\frac{\partial z_{bed}}{\partial y}\end{aligned} \tag{2.5}$$

where H is the water depth and $\langle\ \rangle_d$ denotes a depth-averaged quantity. Assuming that: (i) the velocity at the bed is zero, then $\overline{u} = \overline{v} = 0$; and (ii) the water surface remains horizontal in the y-direction, then $\partial z_s/\partial y = 0$. Thus, the last two terms on (2.5) are equal to zero. The second term on the LHS of (2.4) is also zero as it is assumed that the vertical mean component of the velocity $\overline{w}$ is zero at the bed and water surface.

On the RHS of (2.4), the first term becomes $\rho g H S_0$, and the second term is

handled using the Leibniz's rule and assumptions (i) and (ii), as before. Therefore, the integral for the second term on the RHS of (2.4) can be expressed as,

$$\int_{z_{bed}}^{z_s} \frac{\partial}{\partial y}(-\rho\overline{u'v'})dz = \frac{\partial}{\partial y}\int_{z_{bed}}^{z_s}(-\rho\overline{u'v'})dz = \frac{\partial}{\partial y}H\langle\tau_{xy}\rangle_d \tag{2.6}$$

where $\langle\tau_{xy}\rangle_d = (1/H)\int_0^H(-\rho\overline{u'v'})dz$ is the depth-averaged lateral Reynolds shear stress. Finally, the integration in depth of the third term on the RHS of (2.4) representing the vertical variation of the vertical Reynolds shear stress can be expressed as,

$$\int_{z_{bed}}^{z_s} \frac{\partial}{\partial z}(-\rho\overline{u'w'})dz = \tau_s - \tau_b \tag{2.7}$$

where τ_s and τ_b are the vertical Reynolds shear stresses at the water surface and the bed, respectively. However, $-\rho\overline{u'w'}$ is assumed to vary linearly following the equation,

$$(-\rho\overline{u'w'}) = \tau_b\left(1 - \frac{z}{H}\right) \tag{2.8}$$

Hence, replacing equations (2.5) to (2.8) into (2.4), the depth-averaged streamwise momentum equation can be written as,

$$\frac{\partial H\rho\langle\overline{u}\ \overline{v}\rangle_d}{\partial y} = \rho g H S_0 + \frac{\partial H\langle\tau_{xy}\rangle_d}{\partial y} - \tau_b \tag{2.9}$$

The term on the LHS of (2.9) is attributed to secondary flow effects, commonly represented with the Greek letter Γ; the bed shear stress τ_b, in the SKM, is expressed using the Darcy-Weisbach friction law,

$$f = \frac{8\tau_b}{\rho\langle\overline{u}\rangle_d{}^2} \tag{2.10}$$

The depth-mean transverse Reynolds shear stress $\langle\tau_{xy}\rangle_d$, was modelled by Shiono & Knight (1988) using a Boussinesq eddy viscosity model. The model assumes that the eddy viscosity is proportional to the water depth, H, and the friction

velocity, u_*, as follows,

$$\langle \tau_{xy} \rangle_d \equiv \rho \nu_{t_{xy}} \frac{\partial \langle \overline{u} \rangle}{\partial y} \equiv \rho \lambda H u_* \frac{\partial \langle \overline{u} \rangle}{\partial y} \tag{2.11}$$

In (2.11), λ is the non-dimensional eddy viscosity coefficient. Therefore, substituting (2.11) and (2.10) into (2.9) gives (Shiono & Knight, 1991),

$$\rho g H S_0 + \frac{\partial}{\partial y}\left(\rho \lambda H^2 \left(\frac{f}{8}\right)^{1/2} \langle \overline{u} \rangle_d \frac{\partial \langle \overline{u} \rangle_d}{\partial y}\right) - \frac{\rho f \langle \overline{u} \rangle_d^{\,2}}{8} = \Gamma \tag{2.12}$$

Equation (2.12) is a function of three parameters f, λ and Γ, and is the basis of the SKM. These parameters require careful calibration, but once prescribed, (2.12) can be numerically solved for $\langle \overline{u} \rangle_d$. The bed shear stress distribution can also be obtained via (2.10).

Analytical solution and SKM parameters

For a constant depth domain, Shiono & Knight (1991) showed that the model represented by (2.12) has an analytical solution for $\langle \overline{u} \rangle_d$. As the SKM parameters are not constant along the spanwise direction, and to improve the accuracy of the model, the cross-section of the channel was divided into sub-areas, where the i^{th} panel is in a constant depth region. Then, $\langle \overline{u} \rangle_d$ is given by,

$$\langle \overline{u} \rangle_d = [A_{i1} e^{\gamma y} + A_{i2} e^{-\gamma y} + k]^{1/2} \tag{2.13}$$

The unknown coefficients A_{i1} and A_{i2} are evaluated from the boundary conditions of the system (Shiono & Knight, 1991). Details of the evaluation of these unknowns and constants γ and k are further explained in Chapter 7. Derivation of the analytical solution of the SKM can be found in Appendix C of Jesson (2012).

Parameters f, λ and Γ, must be known to solve (2.13). It has been shown that f is the most influential parameter in the model, followed by the secondary circulation term, Γ, and the non-dimensional eddy viscosity, λ (Omran, 2005; Jesson, 2012). Shiono & Knight (1991) investigated the distribution of the friction factor, f, in compound channels of trapezoidal cross-section. They found that f was relatively

constant in the main channel and the floodplain, but increased for the floodplain when the relationship between water depth in the main channel, H_{mc}, and the floodplain, H_{fp}, $D_r = (H_{mc} - H_{fp})/H_{mc}$ decreased, due to the difference in Reynolds number. Tominaga et al. (1989) and Abril & Knight (2004) reported that higher f values on the floodplain required higher values of Γ/H_{fp} for model calibration, suggesting a link between f and Γ.

The distribution of the non-dimensional eddy viscosity, λ, representing the effects of turbulence on momentum exchange was investigated by Shiono & Knight (1991) in overbank channels. They demonstrated that within the main channel, λ remained constant at 0.07, and in the floodplain it varied from a minimum near the main channel-floodplain interface to a maximum towards the floodplain sidewall. The rate of increase of this parameter was found to depend on the aspect ratio and the depth ratio, D_r. As λ depends on the transverse shear stress (see (2.11)), Shiono & Knight (1991) found that λ values that included the secondary flow effects were of the order of ten times larger than those due to turbulence alone. However, further research on the SKM parameters has shown that variations of λ has a relatively small effect on the results of $\langle\overline{u}\rangle_d$ (e.g. Omran, 2005; Knight et al., 2007; Tang & Knight, 2008). Although this common value of 0.07 is not physically unreasonable, there is no explanation as to why the impact of varying λ is negligible and why it is still an input parameter.

In adapting secondary flow effects to the model, Shiono & Knight (1991) assumed pre-defined transverse points in which the secondary flow was maximum, and decreased linearly on either side. Omran (2005) and Knight et al. (2007), refined the secondary circulation model based on experimental work and observations of the distribution of the time-averaged streamwise and spanwise velocities in depth. They observed that streamwise velocity is always positive, but the transverse velocity alternates between positive and negative in the vertical direction as shown in Figure 2.6. Thus, the sign of the product $\langle\overline{u}\rangle_d\langle\overline{v}\rangle_d$ depends on the sign of $\overline{v}$. This means that the maximum value of $\langle\overline{u}\rangle_d\langle\overline{v}\rangle_d$ occurs at the centreline of a secondary circulation cell that rotates clockwise, while the minima occurs at the centreline of the secondary cell rotating anticlockwise (Figure 2.7). Therefore, they suggested linearly varying $\langle\overline{u}\rangle_d\langle\overline{v}\rangle_d$ from its maxima to its minima, splitting the channel into panels for which the secondary flow term, Γ, was constant.

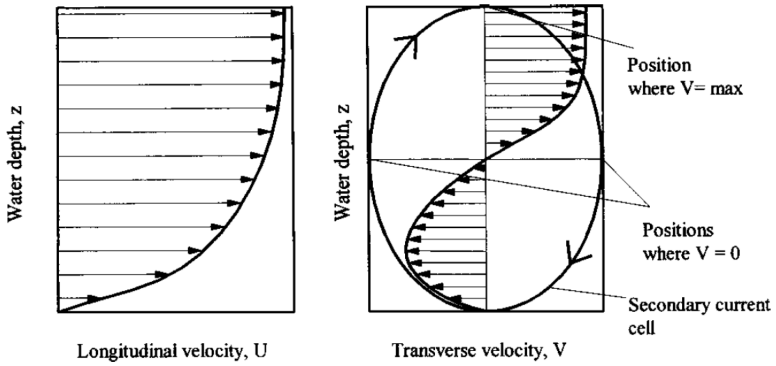


Figure 2.6: Schematic drawing of the distribution of time-averaged streamwise and spanwise velocities, $\overline{u}$ (U in the drawing) and $\overline{v}$ (V in the drawing), respectively, by Knight et al. (2007).

Although Γ, λ and f have a physical meaning, they can be considered tuning parameters for calibration. Omran (2005), for instance, investigated the issues arising from the boundary shear stress distribution. For his study, he calculated f via (2.10), used the standard value of $\lambda = 0.07$ and left Γ as a tuning parameter, albeit keeping the sign given by the secondary circulation cells. Chlebek & Knight (2006) calibrated the SKM in rectangular channels. Their technique consisted on holding two parameters constant while varying the third parameter obtained from the comparison of theoretical results and available flow data. They developed relationships between the SKM parameters and the aspect ratio of the channels. Such relationships delivered successful results after being tested using additional experimental data. Sharifi et al. (2009) used a multi-objective evolutionary algorithm to find values for Γ, λ and f, within physically realistic ranges, keeping the sign of the secondary circulation cells. He showed that multiple solutions exist and ranked the solutions comparing the results with experimental data.

Application of the SKM

The SKM has been shown to be capable of predicting depth-averaged streamwise velocity and bed shear stress with sufficient accuracy for engineering design purposes. McGahey et al. (2006), for instance, used 24 datasets ranging from laboratory experiments to large natural rivers, to compare the performance of the SKM within the CES to other one-dimensional hydrodynamic modelling software. His results showed that the SKM outperformed other industrially used models, obtaining more accurate velocity predictions and bed shear stress.

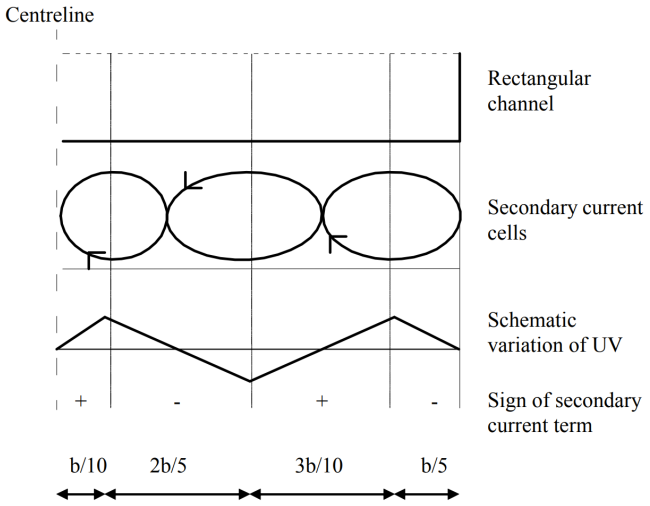


Figure 2.7: Schematic drawing of the secondary flow in a rectangular channel, representing the distribution of $\langle\overline{u}\rangle_d\langle\overline{v}\rangle_d$ (UV in the drawing), the panel divisions and the sign of the rotating cells (Omran, 2005). b in the drawing is the channel width.

Despite the fact that natural riverine systems commonly have riparian vegetation and vegetated floodplains, relatively little work has been undertaken to predict depth-averaged velocities in channels with vegetation, using the SKM. Rameshwaran & Shiono (2007) applied the SKM to a compound channel with emergent vegetation on the floodplain. The original SKM parameters were adapted to account for the effects of vegetation, modelling the canopy as an additional momentum sink term in the time-volume-averaged Navier-Stokes equation. Results showed good agreement between the model and experimental data. Tang et al. (2011) applied the modified version of the SKM to the experimental data obtained by White & Nepf (2007) in a partially vegetated channel with emergent vegetation for a range of canopy densities. Their results demonstrated the great capabilities of the modified SKM for predicting the lateral depth-averaged velocity distribution in emergent patchy vegetation. However, the degree of submergence of the vegetation determines the hydrodynamics of the flow, as low submergence can restrict the growth and strength of vertical mixing layer vortices (Nepf & Vivoni, 2000), as well as hinder the appearance of roughness-induced secondary circulation (Naot et al., 1996). Thus, momentum exchange in submerged partially vegetated channels differs from that in emergent patchy vegetation. It remains to be seen how well the SKM model performs for submerged partially vegetated channels and what the effects of vegetation density on the SKM parameters are. These results will be discussed in Chapter 7.

In light of the current knowledge on fully vegetated flows, emergent partially vegetated flows, secondary circulation over heterogeneous surfaces and the successful application of the SKM model to three-dimensional flows, the present study on submerged partially vegetated channels seeks to investigate the following questions: i) What does the three-dimensional flow (i.e. the turbulence-induced vortices and cross-plane rotating motions) look like in a submerged partially vegetated channel? Although some general inferences can be drawn from previous studies, the flow in a submerged partially vegetated channel has not been characterised yet. ii) How do flow structures change with key impact parameters such as vegetation density and submergence ratio?. iii) What are the relevant length scales carrying the information of the heterogeneous surface represented by a patch of vegetation? This question needs to be answered by keeping in mind that vegetation is a porous medium, which is characterised by both a topographical and a bed roughness variation. iv) How are the upwash and downwash motions distributed within the channel cross-section? v) Is it possible to predict the direction of rotation of secondary cells at the roughness discontinuity? vi) What parameters contribute to the strength of the secondary cells? Lastly, vii) Does the SKM allow for an accurate representation of the effects of the three-dimensional flow on the lateral distribution of depth-averaged velocity in partially vegetated channels? This will lead to better estimations of the discharge conveyance capacity of these systems. Note that this is usually obtained through the knowledge of streamwise velocity and bed shear stress but, in the present study, their profiles are complicated to predict due to, amongst other things, the presence and location of secondary circulation cells. Questions i, iii and iv are directly linked to objective 1.2.1; ii to vi to objective 1.2.2 and viii to objective 1.2.3.

Chapter 3

Experimental Methodology

3.1 Open-channel flume facility

Experiments were conducted in a 184.3 cm wide, 550.0 cm long and 32.0 cm deep non-tilting, recirculating flume in the Geophysical Fluid Dynamics Laboratory at the University of Western Australia. Water was recirculated by a centrifugal pump and the discharge was adjusted by setting the rotational speed of the motor-impeller. A long patch of model submerged vegetation was built on one side of the channel using a staggered array of rigid wooden dowels placed in perforated PVC boards as shown in Figure 3.1(a-c). Canopy elements had diameter d_v =0.64 cm and height $h = 9$ cm. The patch was 406 cm long (in the streamwise direction) and had a spanwise width of $B = 61.5$ cm (approximately one-third of the flume width) allowing free development of the turbulence-induced secondary circulation far from the influence of corner effects (Naot & Rodi, 1982) (Figure 3.1a and Figure 3.1c). The cylinder array density is described by the solid volume fraction $\phi = N_v \pi d_v^2/4$, where N_v is the number of cylinders per unit bed area. Solid volume fractions of $\phi = 0.0125$, $\phi = 0.025$, $\phi = 0.05$, $\phi = 0.10$, and $\phi = 0.20$ were studied (Figure 3.2), which correspond to realistic field conditions reported for aquatic shrubs and meadows, widely used to represent generic aquatic vegetation (e.g. Luhar et al., 2008; Nepf, 2011; Tanino, 2012). Two additional configurations were also studied, a stainless steel *step* of width B and height h, representing the densest condition possible; and a dense patch of vegetation, $\phi = 0.20$, of double the initial width, i.e. $2B = 123$ cm.

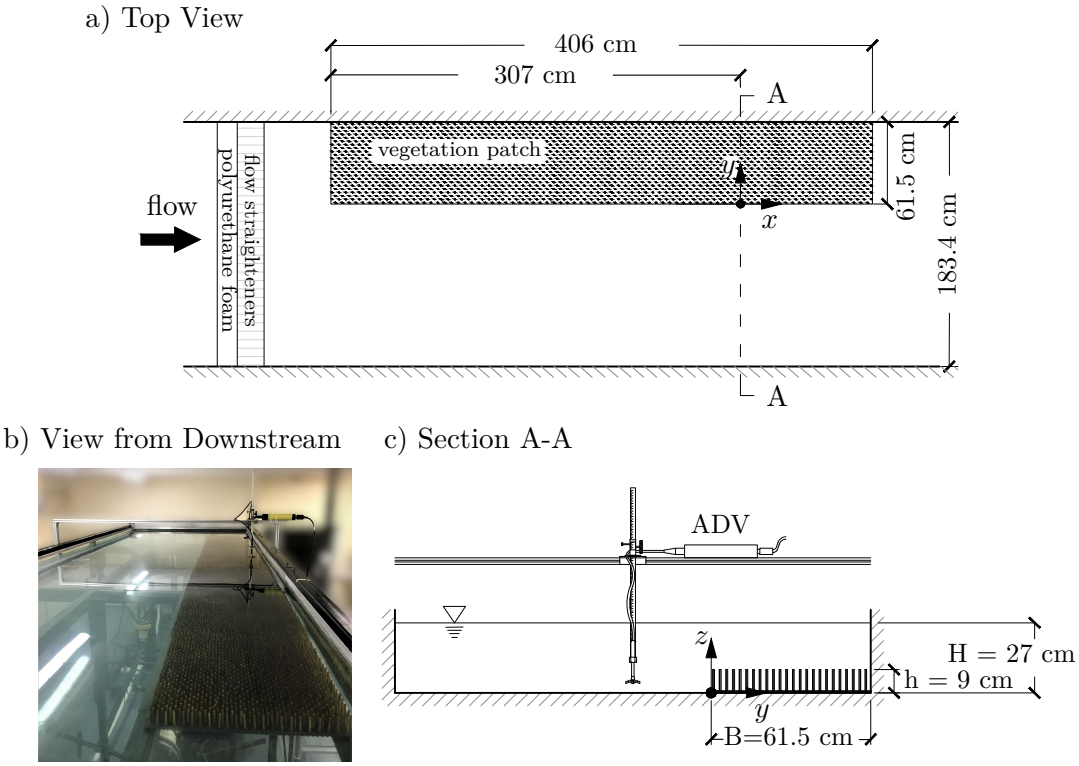


Figure 3.1: Schematic of the experimental set-up in a wide non-tilting recirculating flume of the long patch of vegetation aligned in the streamwise direction. a) Top view. b) A photograph of the flume taken from the downstream end. c) The spanwise cross-section (Section A-A) of the flow where measurements of the velocity field were obtained using a 3D downward-looking ADV.

Turbulence coming from the upstream tank was dampened by placing a 10 cm thick (in the streamwise direction) polyurethane foam sheet occupying the entire channel cross-section at the upstream end. Polycarbonate flow straighteners were placed immediately downstream of the foam to help laterally disperse and minimise inlet swirl (Figure 3.1a). Initially, flow dynamics were observed in a shallow submergence condition of $H/h = 3$ (Nepf, 2012), where H is the water depth, for all canopy densities and the *step*. Due to the physical nature of the experimental set-up, the flow was gradually-varied but the flow depth was kept constant at $H = 27$ cm (± 1 mm) at the test section located 307 cm far downstream of the canopy leading edge (Figures 3.1a and 3.1c). This streamwise location far exceeds the 10 drag lengths $L_D = (C_D a)^{-1}$, for all canopy densities, for which fully-developed flow conditions are expected to hold in vegetated flows (e.g. Morse et al., 2002; Moltchanov et al., 2011). Here, C_D is the drag coefficient calculated using the density-dependent model proposed by van Rooijen et al. (2018), and

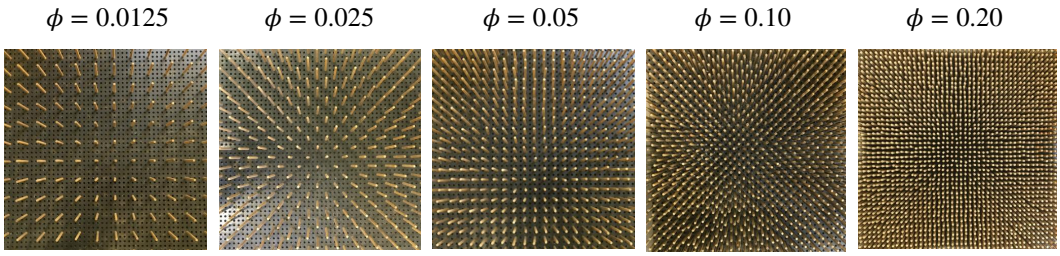


Figure 3.2: Pictures of the top view of the different vegetation densities studied.

a is the canopy frontal area per unit volume. In addition, Rominger & Nepf (2011) found that shear vortices in patchy vegetation fully develop at distances larger than the flow adjustment length L. For canopies imposing a high flow-blockage on the flow, i.e. $C_D a(B/2) \leq 2$ such in the present study, this length $L = (7.0 \pm 0.4)B/2$. Hence, the measurement location from the front of the canopy, here $L = 307$ cm, was chosen such that it exceeded $7.4B/2 = 227.55$ cm. A final check on the canopy flow conditions was undertaken by performing a preliminary experiment with a vegetation array of $\phi = 0.0125$. Velocity profiles taken in the cross-sectional plane 307 cm from the canopy leading edge were compared with those taken 73 cm further downstream. The maximum time-averaged streamwise velocity difference between profiles at these two locations was less than 3%, suggesting the flow was well-developed within 307 cm of the front of the canopy.

Two piezometer tubes were installed 311 cm apart (in the x direction) and 15 cm away from the non-vegetated wall to measure water levels and calculate the longitudinal water surface slope, which is assumed to be bed slope S_0. A fixed camera was used to get frames of the water levels in the piezometer tubes. The difference in water depth was calculated using image pixels, after applying a rotation correction to the images, giving S_0 values of 0.000013, 0.000015, 0.000018 and 0.000020 ($\pm$ 0.000001) for increasing solid volume fractions of $\phi = 0.0125$, $\phi = 0.025$, $\phi = 0.05$, and $\phi = 0.10$, respectively at $H/h = 3.0$. The cross-sectional channel streamwise velocity U_b was 7.11 ± 0.06 cm/s for all densities at $H/h = 3.0$. The uncertainty of U_b was determined by the variations in two methods used to extrapolate the velocity profiles outside the measurement window (see §3.2). Vertical velocity profiles were extrapolated using the log-law and assuming the uppermost measured velocity constant up to the water surface. These velocities correspond to turbulent flow conditions with a hydraulic Reynolds number $Re \equiv$

$U_b H/\nu \approx 19000$.

To investigate the effects of shallowness on the flow properties and structure, flow dynamics were also observed at submergence ratios of $H/h = 2.5$ for the patches of density $\phi = 0.10$, and $\phi = 0.20$; and $H/h = 2.0$ for vegetation densities $\phi = 0.025$, $\phi = 0.10$, and $\phi = 0.20$. Velocity measurements for these cases were also taken at the cross-section located 307 cm far downstream of the canopy leading edge. Table 3.1 describes all the experimental conditions studied. Figure 3.3 shows the extension of the present experimental work on submerged partially vegetated channels compared to reported realistic field conditions and previous similar studies. Note that as H/h and $C_D ab$ become larger, the flow will tend to perceive the vegetation patch as a rough-homogeneous surface rather than an heterogeneous one; this assuming that vegetation density does not change within the same patch.

Table 3.1: Experimental conditions: canopy density ϕ, water depth H (uncertainty of ± 1 mm), canopy height h, shallowness H/h, canopy patch width B, bulk velocity U_b calculated as the integrated mean of measured streamwise velocity profiles extrapolated to the water surface using the log law (uncertainty of ± 0.06 cm/s); and S_0 the water surface slope (uncertainty of ± 0.000001).

ϕ	**h** (cm)	**H** (cm)	**H/h**	**B** (cm)	U_b (cm/s)	S_0
No canopy	-	27	-	-	7.13	-
0.0125	9	27		61.5	7.11	0.000013
0.025	9	27		61.5	7.11	0.000015
0.05	9	27		61.5	7.08	0.000018
0.10	9	27	3.0	61.5	7.05	0.000020
0.20	9	27		61.5	6.92	-
0.20	9	27		123.0	7.47	-
1.00 (step)	9	27		61.5	-	-
0.10	9	22.5	2.5	61.5	8.55	-
0.20	9	22.5		61.5	8.53	-
0.025	9	18		61.5	10.41	-
0.10	9	18	2.0	61.5	10.39	-
0.20	9	18		61.5	10.63	-

A schematic diagram of the experimental set-up and measurement plane is shown in Figures 3.1a and 3.1c. The origin of the coordinate system is placed at the test section, coinciding with the lateral canopy-water interface (LCWI), and at the bottom of the flume. The streamwise direction is x taken positive downstream,

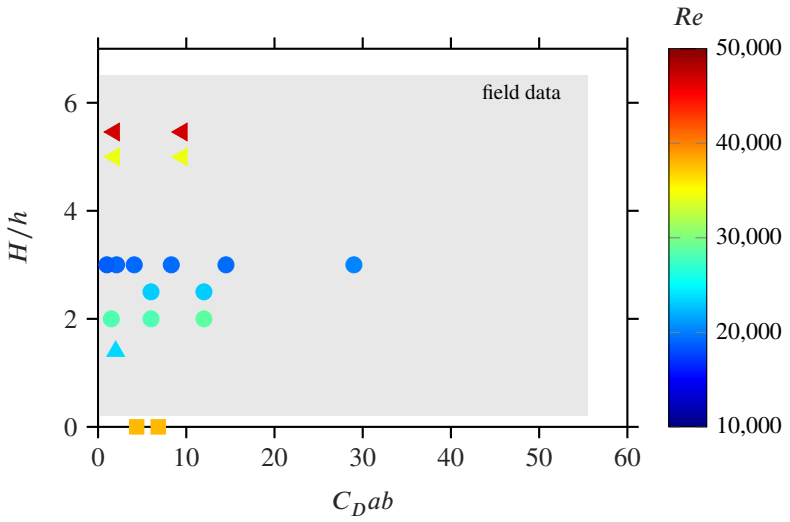


Figure 3.3: Data, $C_D ab$ vs H/h, reported in field studies (grey area), collected from experimental studies that analysed the secondary flow in submerged vegetated-porous patches (△) Nezu & Onitsuka (2001), (□) Hopkinson & Wynn (2009), (◁) Folorunso (2015), and the present work (◯). In the study by Hopkinson & Wynn (2009) vegetation is placed on the streambank, consequently no H/h value was assigned.

the spanwise direction is y taken positive into the canopy and the bed-normal direction is z taken positive upwards. The corresponding velocities are u, v, and w. The LCWI, $y = 0$, was taken at a distance of 0.64 cm ($= d_v$) from the outermost dowel row (Figures 3.1a and 3.1c).

3.2 Velocity measurements and data processing

Instantaneous 3D point velocity measurements (streamwise, spanwise and normal to the bed; u, v, and w respectively) were taken in the cross-sectional plane using a Sontek downward-looking ADV (Acoustic Doppler Velocimeter). *Sphericel 110P8* hollow glass microspheres in the size range of 5 - 25 μm were used as seeding particles. The probe was mounted on a rigid aluminium frame consisting of linear bearings that allowed for precise ($\pm$ 0.5 mm) manual positioning of the probe in the streamwise (x), spanwise (y) and vertical (z) directions. Velocity measurements in the partially vegetated open-channel were recorded at a rate of 25 Hz. To determine the sample length, velocity measurements were taken at 5 positions in the yz-plane (two near the top of the vegetation, one above the canopy patch and 2 next to it) for the patch of density $\phi = 0.10$ at $H/h = 3.0$ for 30 min. A recording time of 8 minutes was found to be sufficiently large to achieve statistically stationary time average velocity and turbulence parameters,

as seen by the level out of the curves representing the standard deviation of these parameters against time length. Therefore, a total of 12.000 data points were recorded in time at each spatial position. The probe was traversed across points spaced at 1.5 cm or 3 cm within the patch and up to a B distance away from the patch lateral edge (i.e. in the spanwise direction), and every 2 cm in the vertical, starting at 1 cm above the bed. The denser spanwise spacing of 1.5 cm was used in the high gradient region of the velocity profile, i.e. around the LCWI. From $2B$ to the wall opposite the vegetation, measurements were taken every 6 cm in the spanwise direction and 2 cm in depth (the grids can be seen by cross-plane velocity vectors on streamwise velocity countour maps in the following three chapters and in Appendix A).

Due to the size of the probe and that the ADV measures at a point approximately 5 cm below the probe tip (this in order to reduce any interference with the flow at the measuring point), measurements were taken from $y/H = -4.38$ to $y/H = 2.28$ and $z/H = 0.04$ to $z/H = 0.78$ for $H/h = 3.0$, $z/H = 0.04$ to $z/H = 0.76$ for $H/h = 2.5$, $z/H = 0.06$ to $z/H = 0.72$ for $H/h = 2.0$. Although side-looking ADVs are sometimes used to take measurements close to the water surface, this instrument was not available in the laboratory. As a result, velocity profiles were extrapolated incurring in uncertainties on the results obtained (further discussed in §4.2.2). For further investigations in partially vegetated flows, it is recommended to use downward-looking ADVs together with side-looking ADVs or the combination with other measurement techniques such as PIV or stereoscopic PIV. To measure velocity within the patch, individual canopy elements were removed in an area of about 50 cm^2 (equivalent to a square of side $3.25s$ for $\phi = 0.025$ and $4s$ for $\phi = 0.10$, where s is the centre-to-centre distance between dowels) to allow unobstructed ADV probe access. As shown by Ikeda & Kanazawa (1996), the removal of canopy elements over a short length ($7s$ in their study) has little impact on the flow statistics. Dowels were replaced after measurements at each spanwise position.

3.2.1 Filtering and despiking

Instantaneous data were pre-filtered using the signal to noise ratio (SNR) and correlation (CORR) values associated with each point in the velocity record. Points with SNR < 15 dB and CORR $< 70\%$ were discarded as suggested by the manufacturer (SonTek, 2001). Spike noise (or corrupted data) was removed by

applying the Phase Space Thresholding method (PST) (Goring & Nikora, 2002) as modified by Wahl (2003), using the software *WinADV* (Wahl, 2000). The method is based on the following facts and successful ideas: i) high-frequency signal components are enhanced when differentiating the signal (e.g. Roy et al., 2000), ii) the maximum of a white noise sequence is given by the Universal threshold (e.g. Katul & Vidakovic, 1998) and iii) the use of phase-space maps to detect spikes in ocean wave records (e.g. McKinney, 1993). In the PST, data points are plotted on a phase-space three-dimensional plot of velocity and approximations of the first and second derivatives. The points cluster on an ellipsoid defined by the Universal criterion and points lying outside the ellipsoid are rejected as spikes. Subsequently, the spikes are replaced using a cubic polynomial best-fit to the first 12 good data points on each side of the spike. The method is iterative as ellipse boundaries change with the replaced spikes; thus, iterations end once the number of spikes is zero (Goring & Nikora, 2002). Given a velocity u_i, each iteration has the following steps (Goring & Nikora, 2002):

1. Calculate the first and second derivatives $\Delta u_i = (u_{i+1} - u_{i-1})/2$ and $\Delta^2 u_i = (\Delta u_{i+1} - \Delta u_{i-1})/2$, respectively.

2. Calculate the standard deviations of the three variables σ_u, $\sigma_{\Delta u}$ and $\sigma_{\Delta^2 u}$ and the expected maxima using the Universal criterion $\lambda_U \sigma = \sqrt{2 \ln n}\sigma$, where λ_U is the Universal threshold, σ standard deviation of the normal, random variable, and n the number of points.

3. Calculate the rotation angle of the principal axes of $\Delta^2 u_i$ versus u_i using the cross correlation,

$$\theta_{PST} = tan^{-1}(\sum u_i \Delta^2 u_i / \sum u_i^2)$$

4. Calculate the ellipse for each pair of variables, namely u_i, Δu_i and $\Delta^2 u_i$. Thus, for Δu_i versus u_i the major axis is $\lambda_U \sigma_u$ and the minor axis is $\lambda_U \sigma_{\Delta u}$; for $\Delta^2 u_i$ versus Δu_i the major and minor axes are $\lambda_U \sigma_{\Delta u}$ and $\lambda_U \sigma_{\Delta^2 u}$, respectively; and for $\Delta^2 u$ versus u_i the major axis b and the minor axis c are the solution of $(\lambda_U \sigma_u)^2 = b^2 \cos^2\theta_{PST} + c^2 \sin^2\theta_{PST}$ and $(\lambda_U \sigma_{\Delta^2 u})^2 = b^2 \sin^2\theta_{PST} + c^2 \cos^2\theta_{PST}$.

5. For each projection in phase-space, identify the points that lie outside the ellipsoid and replace them.

Wahl (2003) suggested that i) the identification of spikes should be done in three-dimensional space rather than using the three projections of the ellipsoid in the two-dimensional space, ii) the use of the Chauvenet's criterion for the Universal threshold and so for excluding outliers, and iii) the change of the classic estimators for location (general position of the data) and scale (spread of the data), i.e. the mean and standard deviation, for estimators known to be insensitive to outliers, such as the sample median and the median of the absolute deviations. However, these changes do not necessarily lead to different results for ADV time series in the range from 10^4 to 10^7 as discussed by Goring & Nikora in the closure of Wahl (2000). Note that the order of magnitude of the time series of this study is 10^4. Additionally, the despiking process followed by Wahl (2003) does not use spike replacement which reduces the length of the time series, changing the structure of the signal. This is appropriate when computing statistical moments but less so for spectra or correlation analysis. Thus, for the spectral analysis, the PST with spikes replacement proposed by Goring & Nikora (2002) and incorporated in the *Velocity Signal Analyser* software (freely downloadable from www.mikejesson.com) (Jesson et al., 2015) was used. The spike detection and replacement methods used in the present study were chosen based on the optimization study by Jesson et al. (2013a) and their suitability for three-dimensional flows over heterogeneous beds demonstrated by Jesson (2012).

3.2.2 Rotation correction

Although efforts were made to align the ADV probe axes to the flume axes when mounted and fixed onto the traversal frame, a small angular offset may persist. Therefore to minimise errors due to misalignment, a 3D rigid-body rotation correction was applied to all point velocity measurements taken in the yz plane, in the channel without vegetation. The roll (α), pitch (β) and yaw (ψ) angles, representing rotations about the x, y, and z axis respectively, were derived from a 3D rotation matrix $\mathbf{R}$ that aligns a unit vector $\mathbf{a}$ onto a unit vector $\mathbf{b}$. Vector $\mathbf{a}$ is a three-element vector that contains the cross-sectional time-averaged streamwise U_b, spanwise V_b and vertical W_b velocities, while $\mathbf{b} = [1\ 0\ 0]$, assuming that V_b and W_b are zero based on continuity at the centreline in the flume without canopies. The 3D rotation matrix according to the Rodrigues' formula is given

by (Murray et al., 2017),

$$\boldsymbol{R} = \boldsymbol{I} + [\boldsymbol{v}]_x + [\boldsymbol{v}]_x{}^2 \, \frac{1-c}{s^2} \tag{3.1}$$

where $\boldsymbol{I}$ is the identity matrix, $[\boldsymbol{v}]_x$ is the antisymmetric matrix of $\boldsymbol{v} = \boldsymbol{a} \times \boldsymbol{b}$, and c and s are shorthand for cosine and sine of θ, the angle between $\boldsymbol{a}$ and $\boldsymbol{b}$. $\cos(\theta) = \boldsymbol{a} \cdot \boldsymbol{b}$ and $\sin(\theta) = ||\boldsymbol{v}||$ by definition of scalar product and cross product, respectively.

Euler angles α, β and ψ were then computed by equating each element in $\mathbf{R}$ to the corresponding element in the matrix product $\mathbf{R}_* = \mathbf{R}_z(\alpha)\mathbf{R}_y(\beta)\mathbf{R}_x(\psi)$; where $\mathbf{R}_*$ represents a sequence of three rotations, one about each axis (x, y and z). Using the right hand rule to define axes orientation (Murray et al., 2017),

$$\begin{aligned} \boldsymbol{R}^* &= \boldsymbol{R}_z(\psi)\boldsymbol{R}_y(\beta)\boldsymbol{R}_x(\gamma) \\ &= \begin{bmatrix} c(\beta)c(\psi) & s(\psi)s(\beta)c(\gamma) - c(\gamma)s(\psi) & c(\gamma)s(\beta)c(\psi) + s(\gamma)s(\psi) \\ c(\beta)s(\psi) & s(\gamma)s(\beta)s(\psi) + c(\gamma)c(\psi) & c(\gamma)s(\beta)s(\psi) - s(\gamma)c(\psi) \\ -s(\beta) & s(\gamma)c(\beta) & c(\gamma)c(\beta) \end{bmatrix} \end{aligned} \tag{3.2}$$

The resulting roll angle α was $\mathcal{O}(10^{-3})$, the pitch angle β was $0.55°$ and the yaw angle ψ was $0.48°$. Measured instantaneous velocities were rotated by these angles before computing flow statistics.

Chapter 4

Characterising the three-dimensional flow in partially vegetated channels[†]

Abstract

Partially obstructed shear flows, such as flows over submerged vegetation patches in river systems, are common in natural environments. Here, a model of a patchily-vegetated river flow, using staggered arrays of rigid wooden dowels, is used to experimentally characterise the flow. Three-component point velocity measurements in the cross sectional plane are used to investigate the highly nonuniform, 3D flow field in patchy vegetation and its effect on mass and momentum exchange. The cross-sectional distribution of mean streamwise velocity varies as a consequence of the bed heterogeneity, being highly dependent on vegetation density. Asymmetric shear layers form at the vertical and lateral edges of the canopy, having different scales within the canopy and in the unvegetated region. Secondary flow cells form in the cross-plane, with a size that decreases with increasing canopy density. The strength of the upward and downward motions is found to be greater for denser canopies. In addition to the secondary flow, additional rotating cells are observed both above the patch and next to it with

[†]Results from this chapter are published on *Water Resources Research*. doi.org/10.1029/2022WR032570

increasing canopy density. A triple-averaging procedure allowed for the quantification of advective dispersive stresses which are up to 21% of the total shear stress. This demonstrates the significant role of secondary circulation generated by patchy vegetation in interfacial momentum exchange. Finally, the secondary circulation contribution to vertical scalar transport is estimated to be of the same order as that due to turbulent diffusion, highlighting the importance of understanding the impact of the secondary flow field on aquatic ecosystem function.

4.1 Introduction

Although efforts have been made towards characterising vegetated and partially vegetated flows, little is known about the impact of the porous obstruction (i.e. canopy patch) on the three-dimensional flow. In fact, there is almost no understanding on the mechanisms that dominate mass and momentum exchange in submerged, partially vegetated flows, despite many natural systems being comprised of submerged, patchy vegetation. Therefore, this chapter seeks to answer the following questions: How does patchy submerged vegetation affect the three-dimensional mean and turbulent flow structure? What are the relevant scales that characterise the main flow features? Do the secondary flows generated by the vegetation significantly contribute to mass and momentum transport?

4.2 Methodology

4.2.1 Time-space averaging

Due to the inhomogeneity of velocity in the spanwise direction in a partially vegetated channel, statistical features of the flow field were expected to be highly three-dimensional. Thus, proper spatial-averaging of flow variables becomes essential in providing reliable estimates of flow properties. First, a double-averaging (in time and space) procedure was employed, whereby the conventional Reynolds decomposition (in time) was accompanied by a spatial decomposition of the time-averaged variable. The spatial extent of the averaging being a small spatial region containing few stationary canopy elements, but within the fluid region (also known as 'intrinsic' spatial average) (e.g. Whitaker, 1969; Breugem et al., 2006; White & Nepf, 2007; Nikora et al., 2019). As such, the instantaneous velocity component $u_i(x, y, z, t)$ is first decomposed into the local time average over the length of the velocity record $\overline{u_i}(x, y, z)$ and instantaneous deviations from it

$u_i'(x,y,z,t)$, i.e.,

$$u_i(x,y,z,t) = \overline{u_i}(x,y,z) + u_i'(x,y,z,t) \tag{4.1}$$

leading to the time-averaged momentum equation for a steady flow,

$$\frac{\partial \overline{u_i}\,\overline{u_j}}{\partial x_j} + \frac{\partial \overline{u_i' u_j'}}{\partial x_j} = -\frac{1}{\rho}\frac{\partial \overline{p}}{\partial x_i} + \nu \frac{\partial^2 \overline{u_i}}{\partial x_j \partial x_j} \tag{4.2}$$

where ρ is the fluid density, p is the pressure, and ν the viscosity . Then, the temporally averaged quantity $\overline{u_i}$ is further decomposed into its 'intrinsic' spatial average $\langle \overline{u_i} \rangle (x,y,z)$ and deviations from that average $\overline{u_i}''$. The 'intrinsic' spatial average $\langle \overline{u_i} \rangle \equiv (1/V_f) \int_{V_f} \overline{u_i}\, dV$, where V_f is the fluid volume that is related to the overall volume V_o containing the solid canopy by $V_f = \phi_f V_o$, where ϕ_f is the fluid volume fraction (also known as porosity) that is $\phi_f = 1 - \phi$, with ϕ the usual solid volume fraction (e.g. Whitaker, 1969; Breugem et al., 2006). Thus,

$$\overline{u_i}(x,y,z) = \langle \overline{u_i} \rangle (x,y,z) + \overline{u_i}''(x,y,z) \tag{4.3}$$

and therefore, the local, instantaneous velocity component u_i is given by,

$$u_i(x,y,z,t) = \langle \overline{u_i} \rangle (x,y,z) + u_i'(x,y,z,t) + \overline{u_i}''(x,y,z) \tag{4.4}$$

Substituting (4.3) into (4.2), and averaging over the volume V_o, i.e., $(1/V_o) \int_{V_f} (4.2)\, dV$ along with the use of the transport theorems for spatial averaging (i.e. say for the variable $\overline{p}$ implies $(1/V_o) \int_{V_f} \frac{\partial \overline{p}}{\partial x_i}\, dV = \frac{\partial \phi_f \langle \overline{p} \rangle}{\partial x_i} - (1/V_o) \int_A \overline{p}\, \hat{n}_i\, dA$, where A is the area where the fluid and the solid are in contact and $\hat{n}_i$ is the normal vector pointing from solid towards the fluid region), and the fact that $(1/V_o) \int_{V_f} \overline{u_i}\, \overline{u_j}\, dV = \phi_f \langle \overline{u_i} \rangle \langle \overline{u_j} \rangle + \phi_f \langle \overline{u_i}'' \overline{u_j}'' \rangle$ leads to (e.g. Whitaker, 1969; White & Nepf, 2007),

$$\frac{\partial \left(\phi_f \langle \overline{u_i} \rangle \langle \overline{u_j} \rangle \right)}{\partial x_j} + \frac{\partial \left(\phi_f \langle \overline{u_i}'' \overline{u_j}'' \rangle \right)}{\partial x_j} + \frac{\partial \left(\phi_f \langle \overline{u_i' u_j'} \rangle \right)}{\partial x_j} = -\frac{1}{\rho}\frac{\partial \left(\phi_f \langle \overline{p} \rangle \right)}{\partial x_i} + \nu \frac{\partial}{\partial x_j} \left(\phi_f \left\langle \frac{\partial \overline{u_i}}{\partial x_j} \right\rangle \right) + \frac{1}{V_o} \int_A \left(\frac{\overline{p}}{\rho} \hat{n}_i - \nu \frac{\partial \overline{u_i}}{\partial x_j} \hat{n}_j \right) dA \tag{4.5}$$

Equation (4.5) can be written more succinctly as,

$$\rho\frac{\partial\left(\phi_f\langle\overline{u_i}\rangle\langle\overline{u_j}\rangle\right)}{\partial x_j} = -\frac{\partial\left(\phi_f\langle\overline{p}\rangle\right)}{\partial x_i} + \frac{\partial\left(\phi_f\langle\overline{\tau_{ij}}\rangle\right)}{\partial x_j} + \mu\frac{\partial}{\partial x_j}\left(\phi_f\left\langle\frac{\partial\overline{u_i}}{\partial x_j}\right\rangle\right) - \phi_f\langle\overline{D_i}\rangle \quad (4.6)$$

where the shear stress tensor $\langle\overline{\tau_{ij}}\rangle$ consist of turbulent Reynolds and dispersive stresses, respectively; and the locally averaged drag force $\langle\overline{D_i}\rangle$ represents the resistance due to the obstruction elements, and it is the sum of the form (pressure) drag and the viscous drag over the averaging scale,

$$\langle\overline{\tau_{ij}}\rangle \equiv -\rho\langle\overline{u_i}''\overline{u_j}''\rangle - \rho\langle\overline{u_i'u_j'}\rangle, \quad \text{and} \quad \langle\overline{D_i}\rangle \equiv \frac{1}{V_f}\int_A\left(-\overline{p}\,\hat{n}_i + \mu\frac{\partial\overline{u_i}}{\partial x_j}\hat{n}_j\right)dA.$$

Since the bulk flow is in the x-direction (i.e., $i = 1$), streamwise momentum equation is the most important for modelling purposes. Hence, (4.6) after replacing $u_1,\ u_2$ and u_3 with $u,\ v$ and w respectively, (and neglecting the x-derivative of $\langle\overline{\tau_{xx}}\rangle$ compared to the other stress gradient terms) becomes,

$$\begin{aligned}\rho\frac{\partial\left(\phi_f\langle\overline{u}\rangle^2\right)}{\partial x} + \rho\frac{\partial\left(\phi_f\langle\overline{v}\rangle\langle\overline{u}\rangle\right)}{\partial y} + \rho\frac{\partial\left(\phi_f\langle\overline{w}\rangle\langle\overline{u}\rangle\right)}{\partial z} &= -\frac{\partial\left(\phi_f\langle\overline{p}\rangle\right)}{\partial x} + \frac{\partial\left(\phi_f\langle\overline{\tau_{xy}}\rangle\right)}{\partial y} \\ &+\frac{\partial\left(\phi_f\langle\overline{\tau_{zx}}\rangle\right)}{\partial z} + \mu\frac{\partial}{\partial y}\left(\phi_f\left\langle\frac{\partial\overline{v}}{\partial y}\right\rangle\right) + \mu\frac{\partial}{\partial z}\left(\phi_f\left\langle\frac{\partial\overline{w}}{\partial z}\right\rangle\right) - \phi_f\langle\overline{D_x}\rangle \quad (4.7)\end{aligned}$$

Now, since most practical conveyance calculations in river management use depth-averaged models, in anticipating this application the depth-averaged quantity, hereinafter represented by $\langle\ \rangle_d$, (say for $\langle\overline{u}\rangle$) is defined as,

$$\langle\phi_f\rangle_d\langle\overline{u}\rangle_d = \frac{1}{H}\int_0^H\left(\phi_f\langle\overline{u}\rangle\right)dz, \quad \text{where, } \langle\phi_f\rangle_d \equiv \frac{1}{H}\int_0^H\phi_f\,dz \quad (4.8)$$

Hence, the depth-averaged streamwise momentum equation (4.7), i.e., $1/H\int_0^H(4.7)\,dz$, can be written as,

$$\begin{aligned}\rho\frac{\partial\left(\langle\phi_f\rangle_d\langle\overline{u}\rangle_d^2\right)}{\partial x} + \rho\frac{\partial\left(\langle\phi_f\rangle_d(\langle\overline{v}\rangle\langle\overline{u}\rangle)_d\right)}{\partial y} &= -\frac{\partial\left(\langle\phi_f\rangle_d\langle\overline{p}\rangle_d\right)}{\partial x} + \frac{\partial\left(\langle\phi_f\rangle_d\langle\overline{\tau_{xy}}\rangle_d\right)}{\partial y} \\ &+\mu\frac{\partial}{\partial y}\left(\langle\phi_f\rangle_d\left\langle\frac{\partial\overline{u}}{\partial y}\right\rangle_d\right) - \left(\frac{\mu}{H}\frac{\partial\left(\phi_f\langle\overline{u}\rangle\right)}{\partial z}\bigg|_{z=0} + \langle\phi_f\rangle_d\langle\overline{D_x}\rangle_d\right) \quad (4.9)\end{aligned}$$

where the shear stress $\langle\overline{\tau_{xy}}\rangle_d$ is given by,

$$\langle\overline{\tau_{xy}}\rangle_d \equiv -\rho\langle\overline{u'v'}\rangle_d - \rho\langle(\overline{u}-\langle\overline{u}\rangle)(\overline{v}-\langle\overline{v}\rangle)\rangle_d - \rho\langle(\langle\overline{u}\rangle-\langle\overline{u}\rangle_d)(\langle\overline{v}\rangle-\langle\overline{v}\rangle_d)\rangle_d$$

$$\underbrace{\langle\overline{\tau_{xy}}\rangle_d}_{\substack{\text{total}\\\text{shear}\\\text{stress}}} \equiv -\underbrace{\rho\langle\overline{u'v'}\rangle_d}_{\substack{\text{Reynolds}\\\text{shear}\\\text{stress}}} - \underbrace{\rho\langle\overline{u}''\overline{v}''\rangle_d}_{\substack{\text{dispersive shear stress}\\\text{due to spatial fluctuations}\\\text{in the porous media}}} - \underbrace{\rho\langle\tilde{\overline{u}}\tilde{\overline{v}}\rangle_d}_{\substack{\text{dispersive shear stress}\\\text{due to depth variations}\\\text{in the mean flow}}} \tag{4.10}$$

Without the canopy (4.9) shows the usual balance between the streamwise momentum and pressure gradient terms and the wall-stress. On the other hand, canopy induces additional forces due to mean flow (second left-hand-side (LHS) term in (4.9)), spanwise gradient of turbulent stresses (second right-hand-side (RHS) term in (4.9)) and canopy drag (and to a smaller extent viscous stress due to the spanwise gradient of the streamwise velocity). In the river modelling scenario that uses (4.9) – usually without the first term – the turbulent stress terms need parametrisation, and hence, turbulent stress is one of the focus of this study. Note that although the streamwise momentum in (4.9) is retained (i.e. the first term in the LHS), it is usually neglected compared to other terms when the flow is well-developed. In (4.10), Reynolds shear stress represent the average stress exerted by turbulent fluctuations on the mean flow. Dispersive stress $\langle\overline{u}''\overline{v}''\rangle_d$ arises from the spatial fluctuations of the flow near a porous media (i.e. the canopy patch). In obtaining $\langle\overline{u}''\overline{v}''\rangle_d$, the local spatial averaging to obtain $\langle\overline{u}\rangle$ and $\langle\overline{v}\rangle$ was performed over a 2×2 measured-point window in the cross-sectional plane. Although this average window may overestimate the dispersive stresses (Duman et al., 2021), they were found to be an order of magnitude smaller than the other shear stress components, and consequently relatively small (this will be further discussed in §4.5). Advective dispersive stress $\langle\tilde{\overline{u}}\tilde{\overline{v}}\rangle_d$ appears due to depth variations in the mean flow, which in a partially vegetated channel can be attributed to roughness-induced secondary circulation.

Additionally, to describe the flow behaviour in the spanwise direction, in particular the effect of the roughness-induced secondary circulation, equation (4.7) was laterally averaged (in the y-direction) over the spanwise secondary circulation-scale domain. This domain can be represented by a transverse roughness correlation length (Nikora et al., 2019), which can be also associated with the wavelength of the time-averaged spanwise velocity of the pair of roughness-induced secondary

cells (Wang & Cheng, 2006). Here, the transverse wavelength of $\overline{v}$ denoted by λ_V (further explained in §4.4) was used to define the spatial averaging domain in the y-direction, $\langle\,\rangle_{\lambda_V}$ in a manner similar to the depth averaging in (4.8). Note that this lateral averaging allows to assess the impact of the secondary circulations generated only by the spanwise inhomogeneity caused by the vegetation patch, excluding the cross-sectional rotating cells generated at the flume corners. Thus, the temporally and horizontally (in y) averaged streamwise momentum equation (4.7) can be written as (ignoring the viscous stresses from the edges of the integration domain),

$$\rho\frac{\partial\left(\langle\phi_f\rangle_{\lambda_V}\langle\overline{u}\rangle_{\lambda_V}^2\right)}{\partial x}+\rho\frac{\partial\left(\langle\phi_f\rangle_{\lambda_V}(\langle\overline{w}\rangle\langle\overline{u}\rangle)_{\lambda_V}\right)}{\partial z}=-\frac{\partial\left(\langle\phi_f\rangle_{\lambda_V}\langle\overline{p}\rangle_{\lambda_V}\right)}{\partial x}+\frac{\partial\left(\langle\phi_f\rangle_{\lambda_V}\langle\overline{\tau_{zx}}\rangle_{\lambda_V}\right)}{\partial z}$$
$$+\mu\frac{\partial}{\partial z}\left(\langle\phi_f\rangle_{\lambda_V}\left\langle\frac{\partial\overline{u}}{\partial z}\right\rangle_{\lambda_V}\right)-\langle\phi_f\rangle_{\lambda_V}\langle\overline{D_x}\rangle_{\lambda_V} \tag{4.11}$$

where,

$$\langle\overline{\tau_{zx}}\rangle_{\lambda_V}\equiv-\rho\langle\overline{u'w'}\rangle_{\lambda_V}\;-\rho\langle(\overline{u}-\langle\overline{u}\rangle)(\overline{w}-\langle\overline{w}\rangle)\rangle_{\lambda_V}\;-\rho\langle(\langle\overline{u}\rangle-\langle\overline{u}\rangle_{\lambda_V})(\langle\overline{w}\rangle-\langle\overline{w}\rangle_{\lambda_V})\rangle_{\lambda_V}$$

$$\underbrace{\langle\overline{\tau_{zx}}\rangle_{\lambda_V}}_{\substack{\text{total}\\\text{shear}\\\text{stress}}}\equiv-\underbrace{\rho\langle\overline{u'w'}\rangle_{\lambda_V}}_{\substack{\text{Reynolds}\\\text{shear}\\\text{stress}}}-\underbrace{\rho\langle\overline{u}''\overline{w}''\rangle_{\lambda_V}}_{\substack{\text{dispersive shear stress}\\\text{due to spatial fluctuations}\\\text{in the porous media}}}-\underbrace{\rho\langle\tilde{\overline{u}}\tilde{\overline{w}}\rangle_{\lambda_V}}_{\substack{\text{dispersive shear stress}\\\text{due to spanwise variations}\\\text{in the mean flow}}} \tag{4.12}$$

In the present study, Reynolds and dispersive shear stresses were used to evaluate the impact of secondary cells on the total stress via (4.10) and (4.12).

4.2.2 Shear layer thickness

The spatial extent of the vegetated shear layers can be described by the nominal vegetated shear layer thickness t_{ml}, and the momentum thickness θ (e.g. Ho & Huerre, 1984; Ghisalberti & Nepf, 2004). The former defines the width of the vortices product of the rolling up of vortex sheets, while the latter is a theoretical length scale that quantifies the reduced momentum flux due to the canopy drag near the canopy boundary. A typical time-averaged streamwise velocity profile is characterised by U_1, the mean velocity deep inside the array and U_2 the (con-

stant) high speed flow velocity in the open channel (Ghisalberti & Nepf, 2004). Therefore, the mixing-layer thickness t_{ml} can be defined as the distance between the first positions where U_1 and U_2 occur, denoted in the vertical direction as z_1 and z_2 respectively (i.e. $t_{ml_z} = z_2 - z_1$), as shown in Figure 4.1a. Analogously, given the overall velocity difference $\Delta U = U_2 - U_1$ the momentum thickness in the z-direction, θ_z, (at a fixed y-location) is defined as

$$\theta_z = \int_{-\infty}^{+\infty} \left[\frac{\left(\overline{u}(z) - U_1\right)\left(U_2 - \overline{u}(z)\right)}{\Delta U^2} \right] dz \tag{4.13}$$

The low stream velocity U_1 was estimated as the average of velocities below the shear penetration depth, which corresponds to the elevation at which the vertical Reynolds stress $\overline{u'w'}$ decays to 10% of its maximum value (Nepf & Vivoni, 2000). The velocity U_2 was expected to be close to the water surface, and could not be measured with the ADV-probe as the probe measures velocities about 5 cm below its central head. Instead, U_2 was approximated to be the velocity at the water surface, $U_{z=H}$. This is based on the fact that most mixing layers in fully vegetated flows fully develop for H/h between 3 and 5 (e.g. Ghisalberti & Nepf, 2004; Nepf, 2012) and the distribution of the vertical Reynolds shear stress of the measured profiles. The velocity $U_{z=H}$ was found by fitting the experimental velocity data above the top of the canopy to the modified log-law for canopy flows (Nepf & Vivoni, 2000),

$$\overline{u} = \frac{u_*}{\kappa} \ln \frac{(z - h_d)}{z_b} \tag{4.14}$$

where u_* is the friction velocity, κ is the von-Karman constant equal to 0.41, z_b is the bottom roughness length scale and h_d is the canopy displacement height corresponding to the mean level of momentum absorption (Nepf & Vivoni, 2000). A non-linear least squares fitting procedure was used to determine optimal values of u_*, z_b and h_d.

Although in principle the y-direction momentum thickness θ_y could also be defined for a fixed z-location in a similar way as for (4.13), it was difficult in practice. Velocity profiles outside the vegetation did not reach a constant value, and in-

stead followed an approximately sinusoidal velocity distribution with increasing amplitude due to the presence of roll motions in the cross-sectional plane (Figure 4.1b and further discussed in §4.3.1). This particular velocity distribution made it difficult to choose a representative maximum velocity U_2. Therefore, and with the aim of comparing the momentum thickness in the z-direction with that in the y-direction, the spanwise momentum thickness was calculated only up to the inflection point of the velocity profile, y_0 (Figure 4.1b). Thus, the upper integral limit on (4.13) was taken as y_0 instead of $+\infty$. The representative maximum velocity corresponded to the maximum velocity of a hyperbolic tangent profile fitted to the experimental data, $U_{2_{tanh}}$ (Figure 4.1b). The hyperbolic tangent fit is defined as (e.g. White & Nepf, 2007),

$$\overline{u} = U_1 + U_s\left[1 + \tanh\left(\frac{y - y_0}{\delta_I}\right)\right] \tag{4.15}$$

where $U_s = U_0 - U_1$ is the slip velocity, with U_0 being the velocity at the inflection point. The low stream velocity U_1 was taken as the average of $\overline{u}(y)$ from the flume wall to a measured point closer to the LCWI for which the local lateral Reynolds

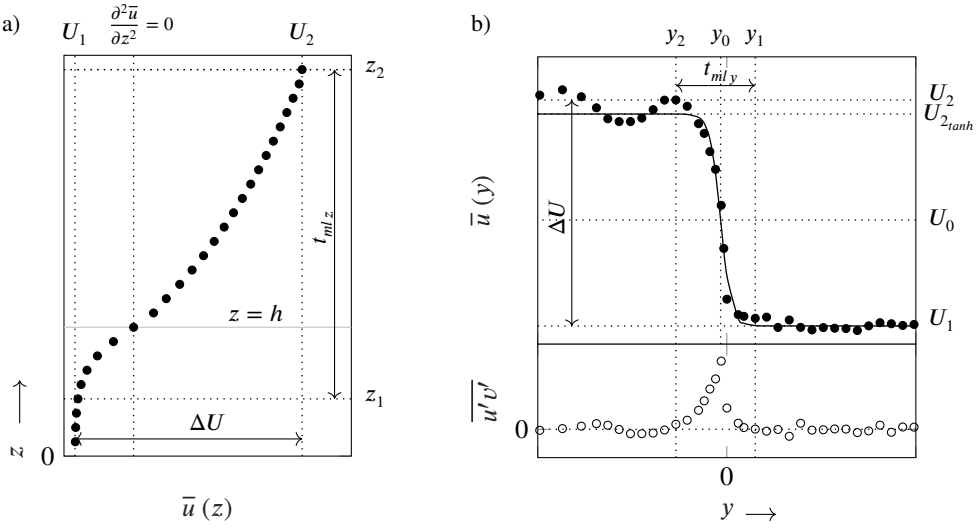


Figure 4.1: Typical vertical and lateral time-averaged streamwise velocity profiles within the patch of vegetation and lateral Reynolds shear stress distribution. a) Representative vertical velocity profile $\overline{u}\,(z)$ with mixing-layer variables defined. b) Lateral velocity profile $\overline{u}\,(y)$ with characteristic mixing-layer variables, and lateral Reynolds shear stress $\overline{u'v'}$. U_1 and U_2 are the low and high stream velocities, respectively, and U_0 is the velocity at the inflection point; t_{ml} is the mixing-layer thickness; and $\Delta U = U_2 - U_1$.

stress $\overline{u'v'}$ inside the patch is equal to zero (Figure 4.1b). The spanwise locations y_0 and y_1 correspond to U_0 and U_1, respectively; and δ_I represents the distance from the inflection point to the location of low constant velocity at the interior of the canopy. Values of δ_I, y_0 and U_s for each measured velocity profile were determined by nonlinear regression. Interestingly, the magnitude of the maximum velocity of the hyperbolic tangent profile coincided with the average of the near-sinusoidal waves seen outside the canopy ($\pm$0.01 cm). The momentum thickness in the y-direction $\theta_{y_{tanh}}$ (at a fixed z-location) can then be defined as,

$$\theta_{y_{tanh}} = \int_{-\infty}^{y_0} \left[\frac{\left(\overline{u}(y) - U_1\right)\left(U_{2_{tanh}} - \overline{u}(y)\right)}{{\Delta U_{tanh}}^2} \right] dy \tag{4.16}$$

where $\Delta U_{tanh} = U_{2_{tanh}} - U_1$. Note that this approach does not embed the effects of the cross-sectional cells in the main channel. Therefore, it will be compared to a vertical momentum thickness $\theta_{z_{tanh}}$ defined in a manner similar to (4.16) but in the z-direction. The upper integral limit corresponded to the velocity inflection point $z_0 = \partial^2\overline{u}/\partial z^2 = 0$ (Figure 4.1a), and $U_{2_{tanh}}$ was taken as the maximum velocity of a hyperbolic tangent profile fitted to experimental data below the canopy top using (4.15), but in the z-direction.

Analogously, the mixing-layer thickness in the y-direction was calculated as $t_{ml_y} = y_2 - y_1$. The spanwise location y_2 was taken as the y-position where the lateral Reynolds stress $\overline{u'v'}$ outside and next to the patch (i.e. in the main channel) became zero (White & Nepf, 2007), which coincides with the first peak of $\overline{u}(y)$ profiles observed adjacent to the canopy (Figure 4.1b). This is further analysed in §4.3.1 where the extent of the mixing-layer is evaluated for densities $\phi = 0.025$ and $\phi = 0.10$ by means of the two parameters defining their characteristic thickness, t_{ml} and θ.

4.2.3 Peclet number and vertical scalar transport

Fully vegetated flows are typically characterised by large-scale shear-induced vortices in which turbulent diffusion is believed to be the dominant process controlling material exchange between the canopy and the open water. However, in flows with strong spanwise variations, this assumption may be challenged if the secondary circulations generated make a non-negligible contribution to transport

by means of vertical advection. Here, the relative contributions of vertical advection and turbulent mixing to vertical scalar transport are quantified through the Peclet number Pe, a ratio between the diffusive time scale ($= {l_z}^2/D_{tz}$) and the advective time scale ($= l_z/W_{lz}$). The vertical characteristic length over which scalar transport is being described l_z is taken as the water depth above the canopy ($H-h$), as large part of the secondary circulation cells is located above the canopy. D_{tz} is the vertical turbulent diffusivity and W_{lz} is a representative time-averaged vertical velocity within l_z. Thus, the Peclet number describing vertical transport above submerged canopies is given by (e.g. Ghisalberti, 2010),

$$Pe = \frac{W_{lz}\ (H-h)}{D_{tz}} \tag{4.17}$$

Here, W_{lz} is taken as the spatially average magnitude of $\overline{w}$ above the canopy. Values of D_{tz} were not experimentally retrieved. Rather, D_{tz} was estimated by making use of the relationship between the turbulent eddy viscosity ν_{tz}, and turbulent diffusivity D_{tz}. This relationship, defined by the turbulent Schmidt number $Sc_{tz} = \nu_{tz}/D_{tz}$ was found to be approximately equal to 0.47 in fully vegetated shear flows (Ghisalberti & Nepf, 2005). Therefore, D_{tz} was calculated as $D_{tz} \approx 2\ \nu_{tz}$, such that the Peclet number can be rewritten as

$$Pe \approx \frac{W_{lz}\ (H-h)}{2\ \nu_{tz}} \tag{4.18}$$

In (4.18), the turbulent eddy viscosity ν_{tz} is determined from experimental measurements of the turbulent stress $-\langle\overline{u'w'}\rangle$ and the mean velocity gradient $\langle\partial\overline{u}/\partial z\rangle$ by using the definition $\nu_{tz} \equiv -\langle\overline{u'w'}\rangle/\langle\partial\overline{u}/\partial z\rangle$. To avoid ambiguity in the terminology, hereinafter the word 'vortex/vortices' is used to refer to the large coherent structures in the shear layer and 'cell/cells' is used to describe the cross-plane roll motions.

4.3 Streamwise flow structure

Colour contours of the time-averaged streamwise velocity $\overline{u}(y,z)$ for the two canopy densities are shown in Figures 4.2a and 4.2b, where length and velocity

scales are normalised by the outer scales H and U_b, respectively. Strong spanwise heterogeneities in the mean flow can be observed. These heterogeneities are represented by large spanwise and vertical undulations of the streamwise velocity contours that increase in magnitude with increasing canopy density. Above the canopy, smooth contours of the streamwise velocity are observed for the sparser array, in contrast with the strong upward bulging of the contours over the denser canopy. In the vegetated zone and above the patch, the streamwise velocity difference between the sparser and the denser canopies is as much as 44% (Figures 4.2a and 4.2b). The magnitude of the streamwise velocity variation above the vegetation patch is $0.48U_b$ for the denser canopy compared to $0.37U_b$ for the sparser array (Figures 4.2a and 4.2b). Next to the vegetation, velocity contours also evince large perturbations with increasing canopy density. A prominent downward distortion of the velocity contours is observed next to the LCWI over the main channel followed by an upward distortion (at $y/H \approx 0.9$) as vegetation density increases. Furthermore, the velocity difference for $z > h$ between the peak above and the peak next to the vegetation (i.e. at $y/H \approx 1.05$ and $y/H \approx -0.95$) for the denser array is on average approximately 1.8 times that for the sparser patch. These results reveal that increasing vegetation density leads to larger perturbations of the mean velocity field structure in contrast to flat velocity contours observed in open-channel flows over smooth beds (e.g. Tominaga & Nezu, 1991).

The in-plane secondary flow indicated by vectors in Figures 4.2a and 4.2b organises into rotating roll motions with a downwelling region that occurs at the LCWI independent of canopy density. This is in contrast with observations over ridge- (e.g. Vanderwel et al., 2017; Hwang & Lee, 2018; Medjnoun et al., 2020) and strip-type roughness flows (Wang & Cheng, 2006; Anderson et al., 2015; Willingham et al., 2014) where downward motions occur over the elevated/rough region (c.f. Figures 1.1d and 1.1e), which suggests a new roughness type characterised by a canopy patch (further analysed in §4.4). Constant streamwise velocity contours bulge upwards (downwards) in regions of upward (downward) flow of the secondary circulation, which demonstrates the link between the streamwise velocity distribution and the cross-plane mean flow structures (Figures 4.2a and 4.2b). The degree of spanwise inhomogeneity in the mean flow leads to a redistribution of streamwise momentum in the cross-plane. The secondary circulation transports low momentum fluid within the canopy to the above non-obstructed region and high momentum fluid to the vegetated and non-vegetated region around the LCWI.

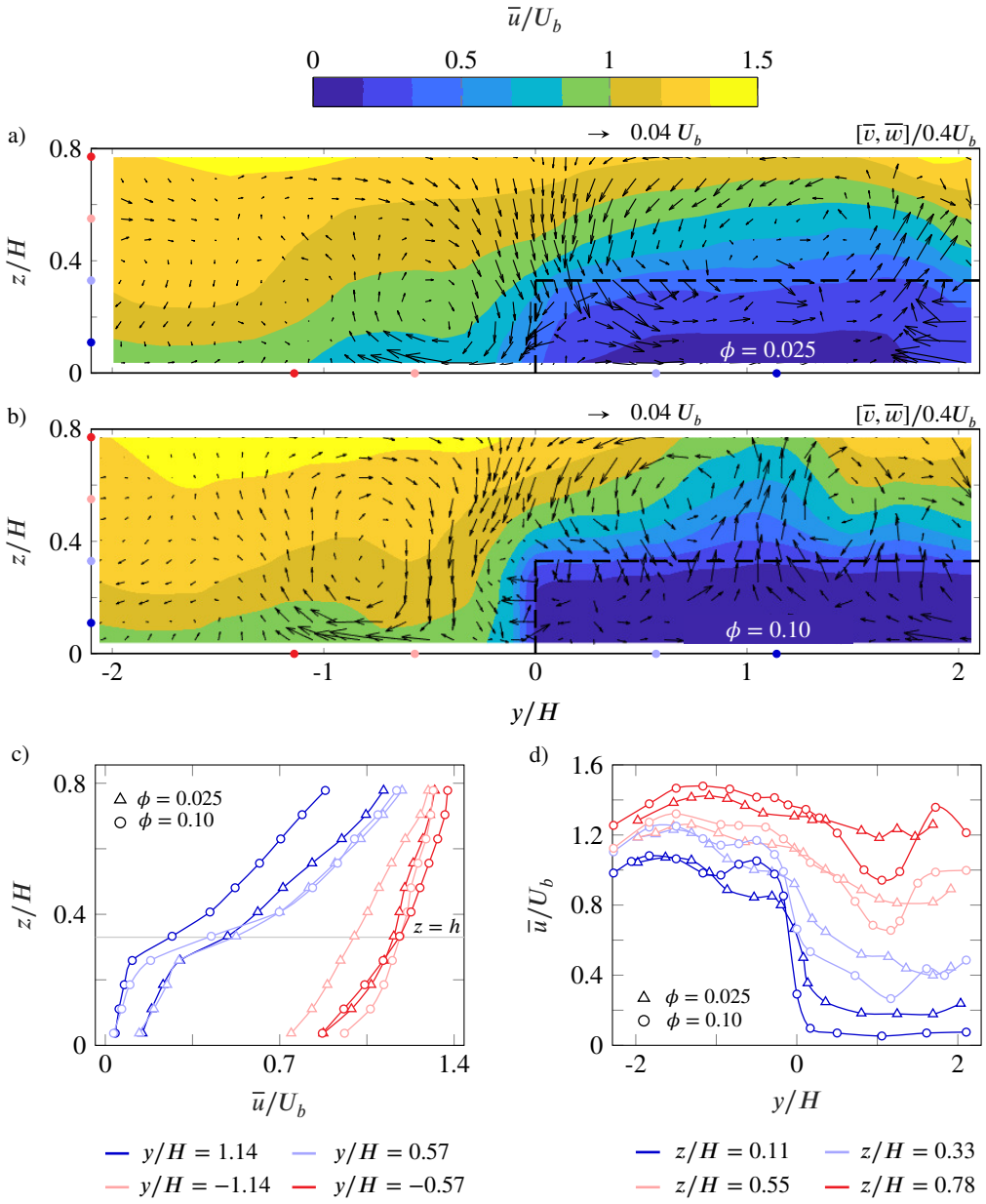


Figure 4.2: Contour maps of the normalised time-averaged streamwise velocity $\overline{u}$ in the cross (yz) plane centred on the lateral edge of the canopy for, a) the sparser ($\phi = 0.025$), and b) denser ($\phi = 0.10$) canopies. Dashed lines represent patch boundaries. The (in plane) secondary flow is indicated by velocity vectors $[\overline{v},\overline{w}]/0.4U_b$. c) Normalised $\overline{u}(z)$ profiles at four spanwise locations. d) Normalised $\overline{u}(y)$ profiles at four depths. Here markers represent only 40% of the data for clarity. Horizontal and vertical locations of profiles in c) and d) are also shown by dots over the x- and y-axis in the top panels. Streamwise velocity contours bulge upwards (downwards) in regions of upward (downward) flow of the secondary circulation. Undulations of the contours become more pronounced with increasing ϕ. Hence, $\overline{u}(y)$ profiles recover uniformity towards the water surface more rapidly in the sparser array. Velocities inside the patch increase with decreasing ϕ.

Vertical distributions of the streamwise velocity at spanwise distances $y = B/2 = 1.14H$, $y = B/4 = 0.57H$ (inside the canopy), and $y = -B/4 = -0.57H$ and $y = -B/2 = -1.14H$ (outside the canopy) are shown in Figure 4.2c. These locations are also highlighted by coloured dots on the abscissas of Figures 4.2a and 4.2b. Profiles within the patch are characterised by a hyperbolic-tangent-like shape with the inflection point near the top of the vegetation as observed in fully vegetated flows (e.g. Raupach et al., 1996). Inside the patch, vertical velocity gradients are larger for the denser canopy than for the sparser array. The gradients are also similar for each canopy density at different y-locations within the patch. This is expected as the magnitude of streamwise velocities inside the array, and below the overflow penetration, is inversely proportional to the resistance that the vegetated patch imposes onto the flow, and so larger streamwise velocities are observed for the sparser array (e.g. Moltchanov et al., 2015).

Above the denser canopy (blue circles in Figure 4.2c), streamwise velocities are lower at mid-patch-width by an average of 40% relative to those present at the LCWI. In contrast, for $\phi = 0.025$, the average differential velocity between the two profiles above $z = h$ is only 10%. This difference in behaviour is due, in part, to the action of the characteristic cross-sectional vortical structures that develop above each vegetated patch. In addition, $\overline{u}(z)$ profiles next to the vegetation gradually change form from a hyperbolic-tangent-like shape to a boundary-layer-like shape (to be discussed further in §4.3.1). Streamwise velocity profiles at $y = -0.57H$ take a form in between these two shapes. Profiles outside the vegetation, at $y = -B/2 = -1.14H$, do not seem to be influenced by the vegetation density as they show similar velocity distributions at low and high canopy densities (c.f. Figure 4.2c).

Lateral distributions of time-averaged streamwise velocity at increasing depths for the two canopy densities are shown in Figure 4.2d. Streamwise velocity averaged over the canopy is less than 0.24 U_b and 0.08 U_b for the sparser and the denser canopies, respectively. The velocity distribution within the patch resembles that of partially vegetated flows with emergent vegetation, i.e. having a hyperbolic-tangent-like shape in the y-direction (e.g. White & Nepf, 2007). The in-canopy velocities remain almost constant and rapidly increase close to the LCWI due to the penetration of lateral shear into the array. Next to the vegetated patch, profiles of velocity follow a sinusoidal-like shape due to the influence of the secondary circulation. This undulation attenuates in proximity to the water surface more

rapidly for the sparser array. Thus, streamwise flow recovers uniformity faster for the lower canopy density. For instance, at $z/H = 0.78$, the highest point measured, the mean absolute velocity difference in the spanwise direction for the sparser array is 21%. However, at the same depth, the distribution of velocity within the canopy for the patch of higher vegetation density is still highly influenced by the secondary flow near the centre of the patch (i.e. at $y/H \approx 1.1$). As a result, the mean absolute velocity difference, at $z/H = 0.78$, in the denser canopy is 44%.

4.3.1 Streamwise velocity scaling and shear layer structure

Finite shear layers develop at the vertical and lateral edges of the canopy patch. These layers are associated with the scale of the shear-induced vortices controlling the interfacial mass and momentum exchange (e.g. Ghisalberti & Nepf, 2002, 2005; White & Nepf, 2007). Normalised vertical profiles of streamwise velocity that is time-averaged and horizontally averaged over the canopy width, $\overline{u}\,|_{y>0}/U_2$, for the two canopy densities are shown in Figure 4.3a. Recall that U_2 is the free stream velocity far above the canopy, close to the free water surface. Above the vegetation, and more specifically above the red circle in Figure 4.3a, the normalised velocity becomes nearly independent of density. This suggests that the patch of vegetation has little influence on the form of the profile structure in the outer flow. Therefore, the vertical distribution of streamwise velocity, and so the shear layer structure, may be predicted by two distinct layers with independent length scales: an inner-layer (of thickness δ_I) over which the momentum penetrates into the canopy, and an outer-layer (of thickness δ_O) over which the shear extends outside the patch (above the red circle in 4.3a). The velocity inflection point near the vertical canopy-water interface suggests the inner-layer can be represented by a mixing-layer profile, while the outer-layer can take a boundary-layer velocity distribution. To probe the validity of this two-layer scaling, all measured velocity profiles within the vegetation in the inner-layer were fitted to a hyperbolic tangent profile using (4.15), but in the z-direction. Values of parameters used in (4.15) are specified in §4.2.2 and can be schematically identified in Figure 4.1a.

In the outer-layer, the modified log-law for canopy flows (Nepf & Vivoni, 2000) given by (4.14) is used to scale the velocity profiles. Unlike fully vegetated flows in

which the velocity profile follows the canopy-log-law at heights larger than twice the canopy height ($z > 2h$) (Ghisalberti & Nepf, 2002), in partially vegetated flows with submerged vegetation the canopy-log-law applies from lower depths above the top of the vegetation, starting at about $z = 1.2h$ (Figure 4.3a). The position z_m of the matching velocity for the hyperbolic-tangent (4.15) and the logarithmic (4.14) velocity profiles, U_{m_z}, defines the limit of the inner and outer layers. Here, z_m was determined as the height at which the relative streamwise velocity between results from (4.15) and (4.14) was of the order of 10^{-4} cm.

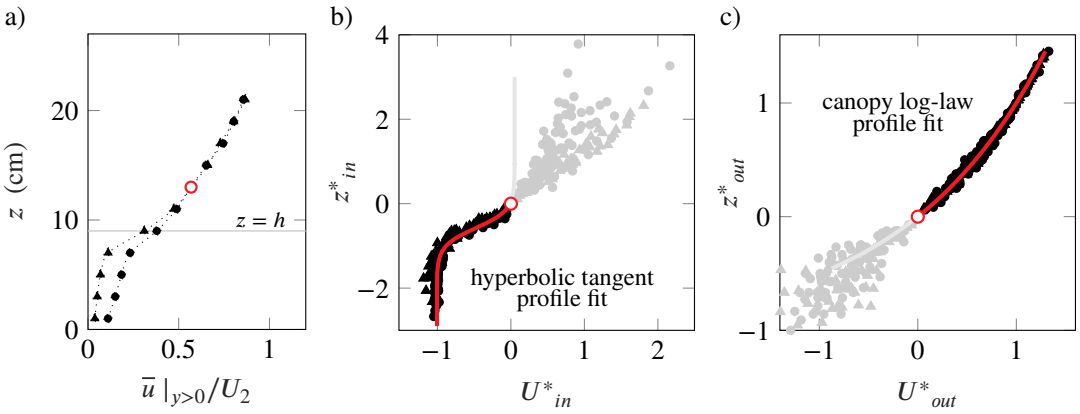


Figure 4.3: Vertical scaling of time-averaged streamwise velocity, within the canopy, for the two solid volume fractions $\phi = 0.025$ (▲) and $\phi = 0.10$ (●). a) Normalised streamwise velocity horizontally-averaged over the canopy width $\overline{u}\,|_{y>0}/U_2$. b) Normalised inner-layer profiles with the hyperbolic tangent profile fit (4.15) for reference (red line). (c) Normalised outer-layer profiles with the canopy-boundary-layer profile fit (4.14) for reference (red line). The red circle indicates the matching point between the inner and outer layers. The vertical velocity distribution in and over submerged vegetation patches, independent of canopy density, is asymmetric and can be described by two length scales: the inner-layer scale $\delta_I = z_m - z_1$ where profiles collapse into a hyperbolic-tangent profile described by (4.15) and the outer-layer scale $\delta_O = z_2 - z_m$ described by (4.14).

Figure 4.3b shows the scaled inner layer velocity profiles for the low and high canopy density. Rescaled velocities in the inner region $U^*_{in} = (\overline{u} - U_{m_z})/(U_{m_z} - U_1)$ are plotted against the coordinate $z^*_{in} = (z - z_m)/(z_m - z_1)$. It can be observed that velocity measurements, for the two solid volume fractions, collapse into a hyperbolic-tangent profile (4.15) shown as a solid red line. This profile resembles the mixing-layer structure observed in canopy flows (e.g. Ghisalberti & Nepf, 2002). However, the velocity distribution in the present study is asymmetric and the measured vertical velocity profiles do not collapse with one single layer scaling as for classic shear layers. Data points diverge from the hyperbolic-tangent form $\approx 0.2 - 0.4h$ above the top of the array, closer to the outer region.

Outer-layer velocity profiles for the two solid volume fractions are shown in Figure 4.3c. Rescaled velocities in the outer region ${U^*}_{out} = (\overline{u} - U_{m_z})/(U_2 - U_{m_z})$ are plotted against the outer-layer coordinate ${z^*}_{out} = (z - z_m)/(z_2 - z_m)$, where z_2 corresponds to the vertical position at which the high-stream velocity U_2 is observed. In the outer-layer, profiles for both canopy densities collapse into a canopy-boundary-layer profile (4.14) denoted by a red line. Figures 4.3b and 4.3c clearly demonstrate that the vertical shear layer in a partially vegetated channel with submerged vegetation is governed by two independent length scales: the inner-layer scale $\delta_I = z_m - z_1$ and the outer-layer scale $\delta_O = z_2 - z_m$. Note that although a simple, yet effective, approach was taken here for fitting the vertical velocity profiles, using the hyperbolic tangent and the modified canopy log-law fits, other models have also been proposed in the literature for the prediction of the distribution of vertical velocity profiles in submerged fully vegetated flows, which usually rely on empirical constants (e.g. Ghisalberti & Nepf, 2004; Defina & Bixio, 2005; Huai et al., 2009). Their applicability on submerged partially vegetated flows remains unexplored and should be addressed in future investigations.

Lateral variation of the streamwise velocity profiles averaged in z over depths below the canopy height, $\overline{u}\,|_{z<h}$, and normalised by the maximum streamwise velocity within $-B < y < B$ in the y-direction, $\overline{u}_{max-y}$, is shown in Figure 4.4a. Profiles for the two experiments collapse well outside the patch of vegetation (Figure 4.4a). The collapse that occurs from around 30 cm off the LCWI ($= 3.33h$) demonstrates that the influence of the vegetation patch on the velocity profile structure outside its boundaries extends further in the spanwise direction than in the vertical direction (which extends approximately $0.3h$ above the canopy). Velocity distributions in the spanwise direction, analogous to the vertical velocity distributions, are not characterised by a single length scale. However, the velocity structure outside the canopy in the y-direction resembles a near-sinusoidal curve, which differs from the logarithmic profiles observed in the z-direction (c.f. Figures 4.3a and 4.4a).

Measured streamwise velocity profiles in the y-direction below the top of the canopy are fitted to a hyperbolic tangent profile using (4.15). As velocity distributions in Figure 4.4a collapse from the sinusoidal curve located farther from the canopy edge, hyperbolic tangent profiles are fitted to data inside the patch and up to the end of the first sinusoidal wavelength (shown by red markers in Figure 4.4a). The influence of the secondary flow that causes waving of the velocity

profiles next to the vegetation is less pronounced in the lower canopy density (c.f. Figure 4.4a). Hence, U_2 almost coincides with the maximum (constant) velocity of the hyperbolic tangent fit. However, for the denser patch the maximum velocity of the hyperbolic tangent closely matches the average between peaks and troughs observed in the main channel.

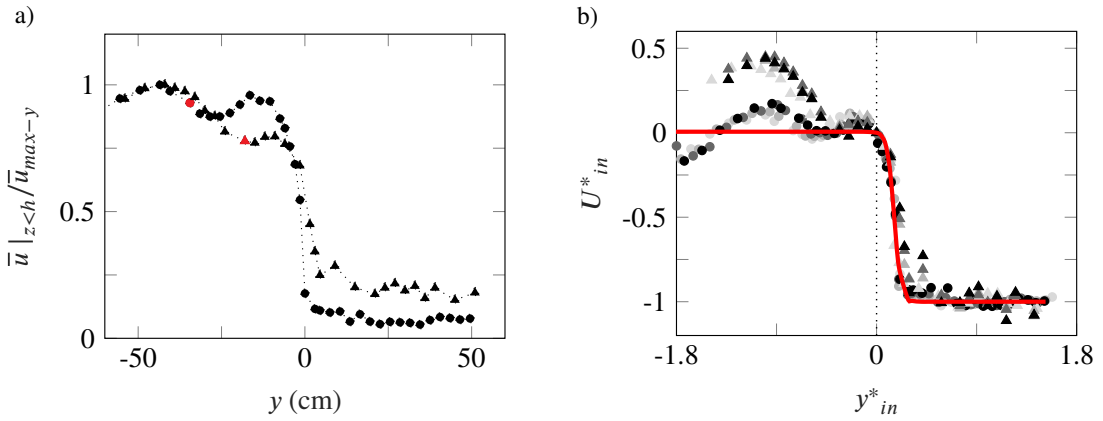


Figure 4.4: Lateral scaling of time-averaged streamwise velocity $\overline{u}$ within the canopy for the two solid volume fractions $\phi = 0.025$ (▲) and $\phi = 0.10$ (●). a) Normalised time-space-averaged streamwise velocity. b) Normalised inner-layer profiles with the fitted hyperbolic tangent profile (4.15) for reference (red line). The use of gray scale indicates z/H values of 0.04 (lighter), 0.11, 0.19, 0.26 and 0.33 (darker). Velocity profiles for different vegetation densities collapse at the second sinusoidal wavelength ($y \approx 30$ cm) demonstrating the little influence of the vegetation on the outer flow structure far from the patch. Inside the canopy, the velocity distribution fits a hyperbolic tangent profile typical of vegetated flows.

Scaled inner-layer velocity profiles in the spanwise direction for the two solid volume fractions are shown in Figure 4.4b. Re-scaled velocity $U^*_{in} = (\overline{u} - U_{m_y})/(U_{m_y} - U_1)$ is plotted against the coordinate $y^*_{in} = (y - y_m)/(y_m - y_1)$. Here, y_m, similar to z_m, is the position at which the velocities from the hyperbolic tangent profile in the inner-layer and velocities describing near-sinusoidal variations associated with the secondary flow outside the canopy, differ by less than 0.01%. The velocity U_{m_y} is the velocity at y_m. Velocity data in the inner-layer collapse to a hyperbolic-tangent curve as seen from the solid line in Figure 4.4b, meaning that the distribution of velocities resembles the mixing-layer structure of canopy flows. The fact that scaled profiles in Figure 4.4b from the same vegetation density measured at different heights within the canopy (represented in gray scale) collapse into a single profile outside the vegetation shows the uniformity of $\overline{u}(y)$ for depths below $z = h$.

4.3.2 Shear layer thickness

The extent of the vertical and lateral shear layers are estimated by using the mixing-layer thickness and the momentum thickness (as per §4.2.2). Figure 4.5 shows these two characteristic lengths for the two canopy densities. The vertical mixing-layer thickness t_{ml_z}, represented by dark red filled markers, decreases by approximately $0.22h$ with the increase in canopy density. This inverse relationship is consistent with results from previous studies in fully vegetated flows (e.g. Ghisalberti & Nepf, 2004). Note that the difference in t_{ml_z} with canopy density in the present study is solely due to the vortex penetration into the canopy, i.e the position at which U_1 is reached, as U_2 was assumed to be the time-averaged streamwise velocity at the water surface. In the spanwise direction, the mixing-layer thickness t_{ml_y} (represented by light red markers in Figure 4.5) also decreases for the denser array, which is in agreement with the observations of White & Nepf (2007) in patchy vegetation with emergent canopies. Interestingly, shear-layer thicknesses in the y-direction are greater than those in the z-direction by $0.80h$ and $0.35h$ for the lower and higher vegetation density, respectively. This suggests that shear layer vortices in the horizontal plane (xy plane) may grow larger than those in the vertical plane, possibly due to the kinematic constraint/boundary condition enforced by the (shallow) water depth in the present study.

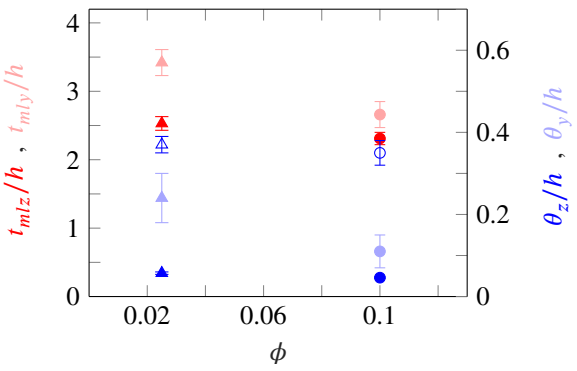


Figure 4.5: Normalised average thickness of the shear layer in the vertical and lateral directions for the two vegetation densities. The mixing-layer thickness t_{ml} is represented by red markers, t_{ml_z} (dark red) and t_{ml_y} (light red), while the momentum thickness in the vertical direction θ_z is represented by hollow dark blue markers. Lateral and vertical momentum thickness calculated up to the inflection point of the velocity profiles $\theta_{z_{tanh}}$ and $\theta_{y_{tanh}}$ are represented by filled dark blue markers and filled light blue markers. Error bars indicate one standard deviation of the mixing layer thickness from all profiles measured within the vegetated patch and take into account the uncertainty in U_2. The error is sometimes smaller than the size of the marker. Mixing-layer thickness increases with decreasing canopy density and is larger in the spanwise direction than in the vertical direction probably due to the shallow conditions here studied.

Increasing canopy density leads to a small decrease in the vertical momentum thickness θ_z of the order of $0.02h$ (Hollow dark blue markers in Figure 4.5). However, the magnitude of θ_z largely depends on the vertical streamwise velocity profiles, in particular on the choice of U_2. A 5% variation in U_2 resulted in a variation in θ_z of $0.03h$. Unfortunately, this range is larger than the difference between momentum thickness for the denser and the sparser canopies making it difficult to draw conclusions on the relationship between θ_z and vegetation density. Yet, the in-canopy vertical momentum thickness (i.e. $\theta_{z_{tanh}}$ calculated from U_1 to U_0, as in §4.2.2) for the sparser canopy was found to be ≈ 1.2 times larger than the momentum thickness for the denser patch. Hence, the momentum thickness inside the array shares an inverse relationship with the canopy density. Similarly, the lateral momentum thickness $\theta_{y_{tanh}}$ (see §4.2.2) for the sparse array was ≈ 2.2 times larger than that for the denser vegetation. This is consistent with the behaviour observed in the z-direction for the two canopy densities. Moreover, the lateral momentum thickness $\theta_{y_{tanh}}$ is larger than the vertical momentum thickness $\theta_{z_{tanh}}$, which may suggest that the canopy drag acting on the lateral and vertical directions is not the same. Moreover, the interaction between large coherent vortices and small-scale turbulence within the canopy elements may play a crucial role in shear layer expansion. In vertical shear layers, the large coherent structures are aligned with the axis of the cylindrical canopy elements, while in the lateral shear layers the vortical structures are perpendicular to it, which may affect the dissipation of large scale vorticity by the stems. Although these results were anticipated knowing the characteristics of shear layers in fully vegetated flows and emergent partially vegetated flows, further studies on flows over patchy-vegetation with larger submergence ratios should be conducted before generalised conclusions can be drawn. Perhaps the mixing-layer characterisation cannot be expressed in terms of the mean canopy drag alone.

4.4 Secondary circulation

Spanwise bed inhomogeneity is known to generate secondary circulations of Prandtl's second kind (e.g. Anderson et al., 2015), with statistical features of the flow field periodically changing with the periodicity of the varying surface. The upper panels in Figures 4.6a and 4.6b show the secondary motion in the yz-plane for the high and low canopy densities. The secondary motion consists of a pair of cells, one above and one next to the patch for both vegetation densities. Downward

motion is observed close to the LCWI and upward motions over the smooth bed and well into the canopy. The secondary cells extend approximately $2.7H$ and $2.4H$ in the spanwise direction for the sparser and denser canopies, respectively. In the bed-normal direction, secondary cells next to both patches of vegetation cover almost the entire water depth; as in several studies of flows over rough-smooth surfaces (e.g. Wang & Cheng, 2006; Vermaas et al., 2011; Hwang & Lee, 2018), their growth is unrestricted by the walls or vegetation. The secondary cell within the vegetation patch fully penetrates the sparser canopy; for the denser array, this cell does not penetrate into the canopy and is mostly confined between the top of the vegetation and the water surface.

The strength of the secondary motion can be deduced from the magnitude of the vertical velocities. Vertical velocities at the LCWI (i.e. around $y = 0$) transport fluid downwards and into the canopy irrespective of vegetation density (see upper panels in Figures 4.6a and 4.6b). The maximum magnitude of the downward flow is larger for the denser canopy ($\approx$ 0.06 U_b) than for the sparser patch, ($\approx$ 0.05 U_b). The upward flow within the vegetation is roughly 0.06 U_b in the denser canopy and 0.04 U_b in the sparser canopy. Upward velocities are nearly twice as large within the vegetation than over the main channel.

As vegetation density increases, a small rotating pair of cells is generated at the lateral canopy-water interface (LCWI), with rotation opposite to that of the secondary flow (identified with "tc" in the upper panel in Figure 4.6b). This cellular flow, termed 'tertiary circulation' has also been observed in flows over strip-type roughness on superhydrophobic surfaces, and can reverse the rotational direction of the vortical motions (Türk et al., 2014; Stroh et al., 2016). An additional cross-sectional rotating cell next to the secondary cell over the denser patch between $y/H = 1$ and $y/H = 1.6$ is also created, which leads to two induced vortical cells compared to just one observed within the sparser patch (as seen in the upper panels in Figures 4.6a and 4.6b). The width (in y) of this additional cell is comparable to the secondary cell above the denser array. Both cells occupy a similar spanwise width as the single secondary cell observed for $\phi = 0.025$. This suggests that the lateral scale of secondary cells within the canopy is controlled by vegetation density. Additional rotating cells may also develop at the recessed region of ridge-type roughness flows once the separation between elevated regions P exceeds the boundary layer thickness, which is the length scale of the rotating cells (Vanderwel & Ganapathisubramani, 2015) (Figure 1.1d). These new rotat-

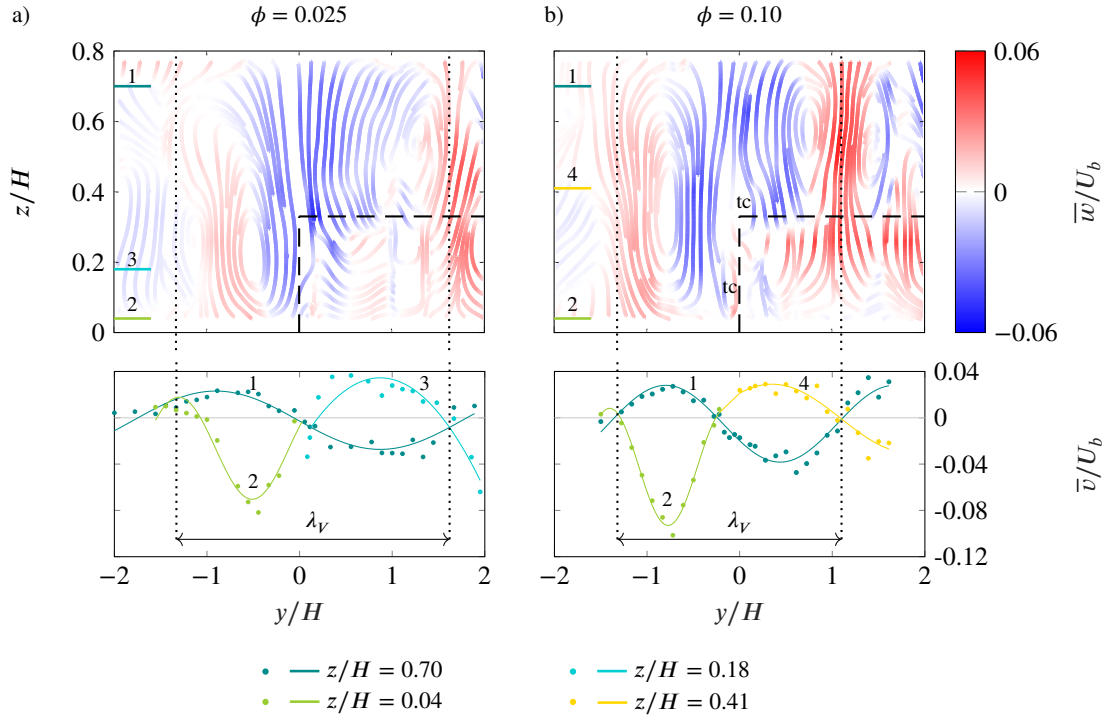


Figure 4.6: Normalised time-averaged velocities in the cross-plane for a) $\phi = 0.025$ and b) $\phi = 0.10$. Upper plots represent streamlines coloured by the normalised time-averaged vertical velocity $\overline{w}/U_b$. Dashed lines represent canopy boundaries. Lower plots show normalised time-averaged spanwise velocities $\overline{v}/U_b$ (dot markers) at the top and bottom of the pair of secondary cells developed close to the LCWI. Solid lines are sinusoidal fits to the data. Curve intersections define the spanwise wavelength used for horizontal averaging, λ_V. Vertical velocities at the LCWI transport fluid downwards into the canopy irrespective of vegetation density. The number of secondary cells above the vegetation increases with increasing ϕ, while the cell next to the patch is of constant size (but is stronger for the denser patch). Maximum spanwise velocities are observed near the bed from the canopy to the main channel and increase in magnitude with increasing ϕ.

ing motions can also be found above the elevated region, when the width of the elevated region S is sufficiently large (Figure 1.1c). The size and strength of the additional cells are enhanced with a further increase of S and can be comparable to the secondary cell (Hwang & Lee, 2018). These results may suggest that additional cells above a vegetated region may develop when the length scale of the cell above the patch is exceeded. Therefore, if the organised vortex structures above the vegetation are thought to be three-dimensional structures, where shear layer vortex streets, of limited growth, travelling out-of-phase of each other are seen to have either positive or negative vorticity (Ikeda & Kanazawa, 1996), thus either flow coming or leaving their cores, then secondary cells may develop in between shear layer vortex streets (Ghisalberti & Nepf, 2002). Consequently, the width (in the spanwise direction) of the rotating secondary cells may scale

with the vertical scale of turbulence-induced vortices, i.e. the vertical shear layer thickness t_{ml_z}.

It appears, therefore, that the number of cells observed for each canopy density will be directly related to the vertical shear-layer thickness t_{ml_z} (§4.3.2). Thus, subtracting the width occupied by the corner secondary circulations to the total patch width, there is a free width of $y/H \approx 1.6$ for the development of the rotating cells above the canopy. For the sparser canopy, one cell develops between two vertical shear layer vortices of thickness $t_{ml_z}/H \approx 0.84$ each, which is observed in the upper panel of Figure 4.6a. For the denser canopy, three shear layer vortices of thickness $t_{ml_z}/H \approx 0.74$ each, may develop creating two cross-plane rotating cells with a combined width of $y/H \approx 1.48$ as seen in the upper panel of Figure 4.6b. This suggest that the cross-sectional cells scale with the vertical shear layer thickness t_{ml_z}.

Towards quantifying the $\overline{v}$-motion, note that, in the upper panel of Figure 4.6a, the flow moving downwards at the LCWI turns to the main open channel near the bed, where it joins the horizontal flow that exits the vegetation. This creates strong spanwise velocities from the patch towards the main channel at the lower depths. This horizontal velocity reaches its maximum near the spanwise centre of the secondary cell located next to the patch, and reaches about $0.08U_b$ for the sparser canopy and $0.1U_b$ for the denser patch of vegetation. Spanwise velocities $\overline{v}$ close to the water surface are approximately $0.036U_b$ and $0.03U_b$ for the lower and higher canopy densities, respectively.

Lower panels in Figures 4.6a and 4.6b show the distribution of the spanwise velocity $\overline{v}$ normalised by U_b. Measurements are presented for three heights to show their distribution at the top and bottom of the pair of secondary cells. For the sparser canopy, these measurements are located well above the canopy at $z/H = 0.70$ (—), around mid-canopy height $z/H = 0.18$ (—) and close to the bed $z/H = 0.04$ (—). As the secondary cells above the canopy for the denser array do not penetrate the patch, the spanwise velocity measurement at mid-canopy height is replaced by measurements above the canopy top at $z/H = 0.41$ (—). The data show the wavelength of the spanwise velocity, which has been shown to be the same as the wavelength of the bedform over strip-type roughness flows comprising a pair of counter rotating cells (e.g. Wang & Cheng, 2006). This spanwise velocity wavelength can serve as the spatial averaging width in the y-direction.

Although for flows over ridge-type roughness the spanwise averaging is done over several geometrical wavelengths where one geometrical wavelength corresponds to one width of the elevated region plus one width of the recessed region (e.g. Vanderwel & Ganapathisubramani, 2015; Hwang & Lee, 2018), this is not possible in this study as the partially vegetated channel comprises just one geometric wavelength (equivalent to twice the vegetation patch width = $2B$). Moreover, the geometrical wavelength here not only includes the secondary circulation induced by the differential roughness, but also the rotating pair generated by corner effects. Hence, to isolate the effects of the turbulence-induced secondary circulations, the spanwise velocity wavelength, denoted hereinafter as λ_V, is used as the horizontal averaging width (see lower panels in Figures 4.6a and 4.6b) as in strip-type roughness flows.

4.5 Turbulent and dispersive shear stresses

As discussed in §4.2.1, mean flow heterogeneity contributions to the total shear stresses are represented by the advective dispersive stresses. Comparative colourmaps of the dispersive, turbulent Reynolds and total shear stresses (in columns) for the two canopy densities (in rows) are presented in Figures 4.7a and 4.7b. The dispersive stresses due to spatial fluctuations (left panels) are large inside the vegetation, in proximity to the top of the canopy; however, they are an order of magnitude smaller than other shear stresses, and consequently negligible. This result from patchy vegetation is consistent with the conclusions reached by other researchers in fully-vegetated flows that dispersive stresses due to spatial fluctuations are significant inside the canopy, but negligible elsewhere (Böhm et al., 2000; Poggi et al., 2004; Coceal et al., 2006). By contrast, advective dispersive stresses (middle-left panels) are non-negligible with respect to the turbulent Reynolds stresses (middle-right panels). In fact, they are present along the spanwise direction with varying intensity and at some locations they are non-zero for most of the water depth. Patterns of turbulent and advective dispersive stresses are not similar; while the Reynolds stresses are maximised on top of the canopy, the advective dispersive stresses are more localised, changing intensity with the motions in the cross-sectional plane.

Advective dispersive stresses are largest in the region of strong upward flow within the canopy as a result of negative $\tilde{\tilde{u}}$ and positive $\tilde{\tilde{w}}$ (see middle-left panels in

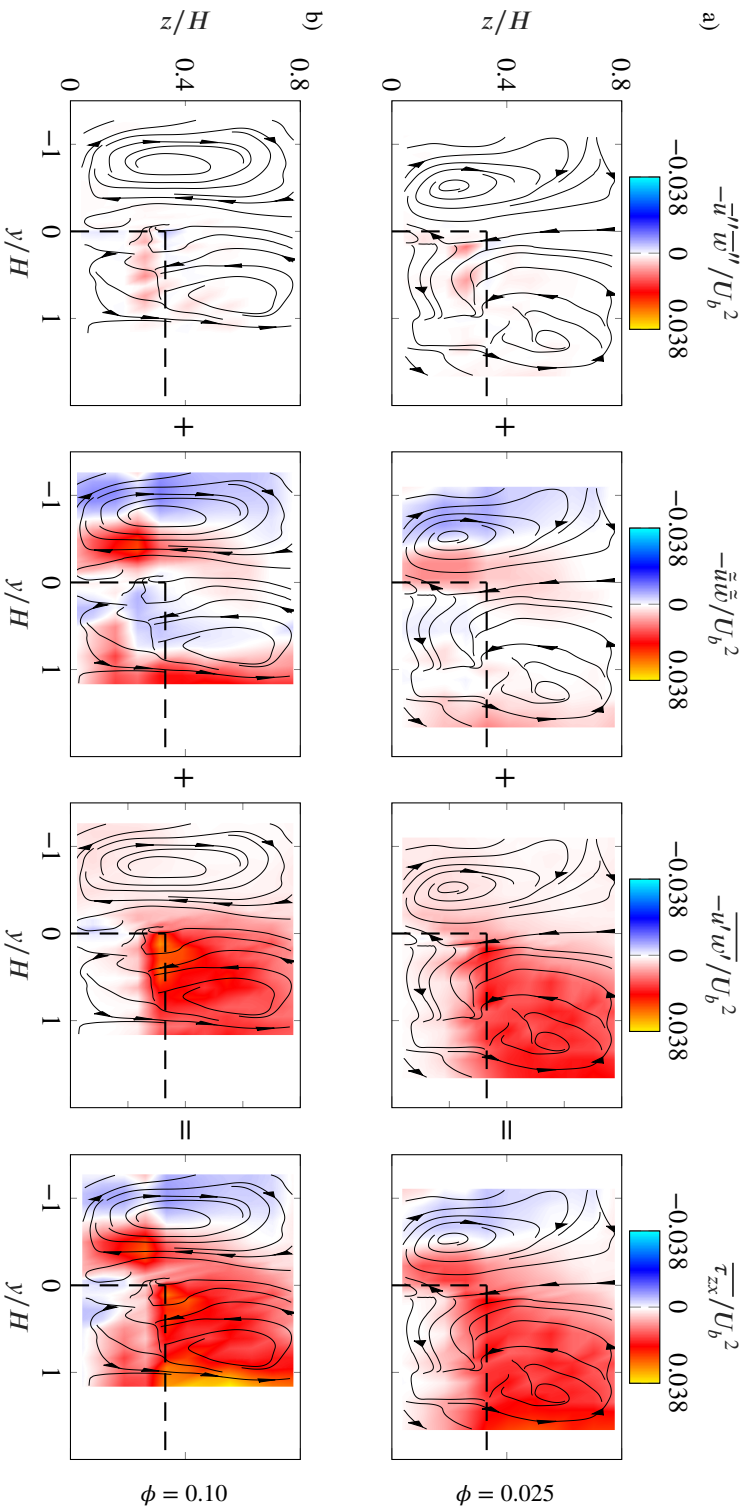


Figure 4.7: Effect of the vegetation patch on the normalised dispersive (left panels), advective dispersive (middle-left panels) turbulent Reynolds (middle-right panels) and total (right panels) shear stresses for a) $\phi = 0.025$ and b) $\phi = 0.10$. Shear stresses increase with canopy density. Advective dispersive stresses can be of the same order of magnitude as Reynolds stresses and contribute significantly to the total shear stress.

Figures 4.7a and 4.7b). This is consistent with the numerical simulations over ridge-type roughness of Medjnoun et al. (2020) where high intensity advective dispersive stresses were observed above the surface elevation in which there is an upward flow. Negative values of $-\tilde{\bar{u}}\tilde{\bar{w}}$ at the vertical interface between the vegetation and the open water are the result of negative $\tilde{\bar{u}}$ and positive $\tilde{\bar{w}}$. Adjacent to the canopy, $\tilde{\bar{u}}$ is positive and $\tilde{\bar{w}}$ is negative leading to advective dispersive stresses that are larger than the turbulent Reynolds stresses. In this region, the highest (positive) intensity of $-\tilde{\bar{u}}\tilde{\bar{w}}$ is observed at one-third below the canopy height. This location of maximum $-\tilde{\bar{u}}\tilde{\bar{w}}$ may be associated with the location of the core of the secondary cell as in the study of Forooghi et al. (2020) over strip-type surfaces. Moving farther away form the vegetation patch in the spanwise direction, strong negative dispersive stresses (resulting from positive $\tilde{\bar{u}}$ and $\tilde{\bar{w}}$) are observed, which are also larger than the Reynolds stress. These negative values of $-\tilde{\bar{u}}\tilde{\bar{w}}$ in the region of upward flow in the main channel (as in the present study) have not been observed in similar flows with spanwise varying roughness. This may be due to the much weaker bed-normal motions observed, for instance, on the recessed regions of ridge-type roughness flows, which lead to positive values of the advective dispersive stress $-\tilde{\bar{u}}\tilde{\bar{w}}$ (e.g. Medjnoun et al., 2020). Additionally, the dispersive stress is shown to vanish in between upward and downward motions, where there is enhanced spanwise and very weak vertical motions.

For the Reynolds stress tensor component $-\overline{u'w'}$ (shown in the middle-right panels in Figures 4.7a and 4.7b), stronger values are observed above the patch of vegetation than next to it. This is due to the strong shear caused by the differential velocity between the canopy and the overlying flow. It can also be observed that maximum values are located at the top of the canopy close to the LCWI. In this region, the vertical Reynolds stress is dominant and an order of magnitude larger than the advective dispersive stress. For the sparser array, the shear stress penetration into the canopy is larger compared with the denser canopy, which is consistent with a larger shear layer thickness for the sparser canopy illustrated in Figure 4.5. The vertical Reynolds stress above the canopy and in the region of upward flow is shown to be larger for the sparser array than for the denser patch. This may be due to the fact that in the region of higher flow (i.e. main channel) there is a weaker secondary flow in the sparser canopy relative to the denser canopy leading to a lower contribution to the advective dispersive stress and consequently a slightly higher Reynolds stress. The peak value of the Reynolds stress is, as expected, higher in magnitude for the denser compared to

the sparser canopy. Maps of total shear stress (right panels in Figures 4.7a and 4.7b) show that increases in canopy density result in the rise in magnitude of the total shear stress $\overline{\tau_{zx}}$, but do not necessarily affect its spatial distribution. Moreover, the increase in the magnitude of $\overline{\tau_{zx}}$ is mainly attributed to advective dispersive stresses that increase with increasing vegetation density.

The overall distribution of vertical stresses is shown by horizontally averaging stresses in Figure 4.7 over the spanwise velocity wavelength λ_V (see Figure 4.6 for reference), normalised by the 'friction velocity' $U_{m_z} - U_1$ squared . Results are shown in Figure 4.8a. Below $z = h$, dispersive stresses due to spatial fluctuations are negligible for most of the canopy height, but are about 17% of the total shear stresses just below the top of the canopy. Advective dispersive stresses inside the canopy and for the denser vegetation are larger than Reynolds stresses. Instead, for the sparser array, vertical advective dispersive stresses reach about 20% of the vertical Reynolds stresses. These shear stress distributions inside the canopy show the high impact of the vegetation on the stresses (c.f. Figure 4.8a). At the top of the patch of vegetation, Reynolds stresses are an order of magnitude larger than other shear stresses. Dispersive stresses due to spatial fluctuations above the vegetation are negligible. This finding agrees with observations in fully vegetated flows where the dispersive stress due to spatial fluctuations is an order of magnitude smaller than the Reynolds stress and becomes smaller with increasing vegetation density (Poggi et al., 2004). Similar conclusions regarding this dispersive stress were reached by e.g. Cheng & Castro (2002); Coceal et al. (2006) in urban-like roughness systems. Contributions of the advective dispersive stresses to the total shear stresses above the canopy are about 21% for the denser patch and 4% for the sparser vegetation.

The behaviour of the vertical advective dispersive stresses within the patch of vegetation is examined by horizontally averaging results in Figures 4.7a and 4.7b over the part of the wavelength λ_V (see Figure 4.6) that lies within the canopy denoted by λ_{Vc}, i.e. $-\langle\tilde{\tilde{u}}\tilde{\tilde{w}}\rangle_{\lambda_{Vc}} \equiv -\langle(\overline{u} - \langle\overline{u}\rangle_{\lambda_V})\,(\overline{w} - \langle\overline{w}\rangle_{\lambda_V})\rangle_{\lambda_{Vc}}$. Similarly, the vertical dispersive and turbulent Reynolds stresses are horizontally averaged over λ_{Vc} and normalised by $(U_{m_z} - U_1)^2$, allowing the comparison of the contributions of all shear stresses to the total shear stress. Results are shown in Figure 4.8b. Deep inside the canopy and close to the bed, the advective dispersive stress is negative for both canopy densities and increases to reach a maximum at $z/h \approx 0.78$. At this location, vertical advective dispersive stresses become very large, being

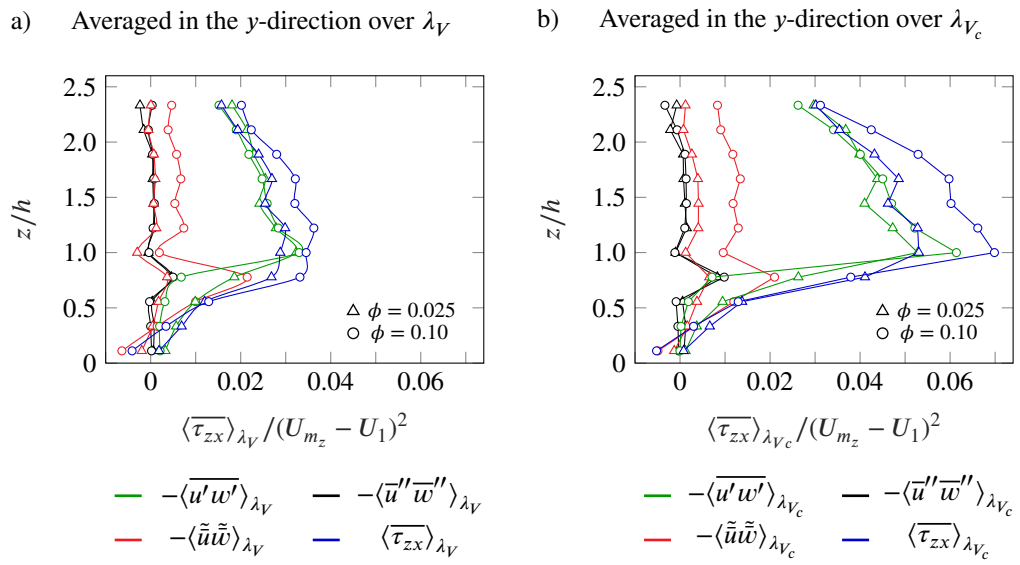


Figure 4.8: Normalised vertical dispersive $-\langle\overline{\tilde{u}}''\overline{\tilde{w}}''\rangle$, advective dispersive $-\langle\tilde{\tilde{u}}\tilde{\tilde{w}}\rangle$, turbulent Reynolds $-\langle\overline{u'w'}\rangle$ and total $-\langle\overline{\tau_{zx}}\rangle$ shear stresses for the two canopy densities $\phi = 0.025$ (△) and $\phi = 0.10$ (○). The spanwise average was done over a) the spanwise velocity wavelength λ_V, and b) part of the wavelength λ_V that lies within the canopy denoted as λ_{Vc}. Vertical advective dispersive stresses are non-negligible compared to the vertical Reynolds stresses and their contribution to the total shear stress increases with increasing vegetation density.

one-fourth and three times the vertical Reynolds stresses for the denser and the sparser array, respectively. At the top of the canopy, the advective dispersive stress becomes around 13% of the total turbulent stress for both canopy densities. Above the denser canopy patch, normalised values of the vertical advective dispersive stress are about 20% to 27% of the total stress, as shown in Figure 4.8b. This relative importance of advective dispersive stresses decreases with the decrease in canopy density. For the sparser patch, the advective dispersive stress is about 9% of the total stress close to the canopy top and decreases to about 4% in proximity to the water surface. Dispersive stresses due to spatial fluctuations are less than 2% of the total shear stresses for both canopy densities above the canopy. Total vertical shear stresses, represented by blue markers in Figure 4.8b, are larger for the denser canopy mainly due to the higher contribution of advective dispersive stresses. Results from this study demonstrate that vertical advective dispersive stresses should be taken into account when calculating total vertical shear stresses in partially vegetated channels.

Normalised depth-averaged lateral shear stresses are shown in Figure 4.9. The maximum value of $\langle\overline{u'v'}\rangle_d$ is found just outside the LCWI for the denser array (at

$y/H = -0.055$), but it is shifted into the canopy (at $y/H = 0.06$) for the sparser vegetation. This peak of the lateral Reynolds stress at the LCWI shows the significance of the interaction between the vegetated and non-vegetated regions suggesting that horizontal vortices are generated here. The Reynolds stress in the main channel is zero or very close to zero for both patches of vegetation (Figure 4.9). The advective dispersive stress is large on both sides of the LCWI indicating the presence of mean horizontal motions. The peak of $\langle\tilde{\overline{u}}\tilde{\overline{v}}\rangle_d$ next to the patch is located further from the LCWI for the denser canopy (at $y/H = -0.83$) than for the sparser array (at $y/H = -0.55$), in accordance with the positions of the secondary cells (Figures 4.6a and 4.6b). Within the canopy, advective dispersive stresses are larger for the sparser canopy than for the denser canopy. A change of sign is observed for dispersive stresses within the patch of higher vegetation density at the meeting line between the two cross-sectional cells developed above the canopy (see Figure 4.6b for reference). In the vegetated region, and for $\phi = 0.10$, the magnitude of the Reynolds stress compared to the advective dispersive stress differs by less than 6%, where the latter is larger than the former, but with their signs inverted. For the sparser patch, the advective dispersive stress is up to 34 times larger than the Reynolds stress within the region $0.78 \leq y/H \leq 1.22$. This highlights the three-dimensionality of the flow and suggests the interaction of horizontal shear layer vortices in the xy-plane. Looking closer at the LCWI, it can be observed that the advective dispersive stress distribution for $\phi = 0.10$ peaks at $y/H \approx 0$ and then reaches a minimum at $y/H = -0.055$. This suggests the presence of a small rotating cell at the LCWI, which is also seen in the

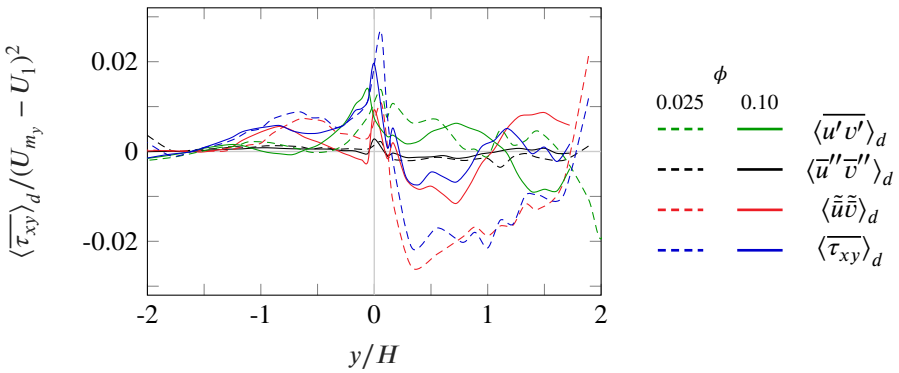


Figure 4.9: Normalised depth-averaged lateral dispersive $\langle\overline{u}''\overline{v}''\rangle_d$, advective dispersive $\langle\tilde{\overline{u}}\tilde{\overline{v}}\rangle_d$, turbulent Reynolds $\langle\overline{u'v'}\rangle_d$ and total $\langle\overline{\tau_{xy}}\rangle_d$ shear stresses for the two vegetation densities $\phi = 0.025$ (△) and $\phi = 0.10$ (○). Markers are down-sampled for clarity. The lateral Reynolds stress predominates at the LCWI but it is of lesser importance or negligible elsewhere, where the advective dispersive stress is the main shear stress contributor.

upper panel of Figure 4.6b. Total lateral shear stresses, represented by blue markers in Figure 4.9, peak at the LCWI where the Reynolds stresses are the main contributors. Far from the interface, total stresses take the form of advective dispersive stresses that are, in general, larger than the Reynolds stresses.

4.6 Impact of flow structure on vertical scalar transport

The strength of the vertical motions observed within the vegetation patch and acting on the vertical scale $(H-h)$ (see Figures 4.6a and 4.6b for reference) is used to determine the importance of the contribution of advection to vertical scalar transport within the canopy. This is done by making use of the Peclet number as defined in §4.2.3. For the sparser canopy, the average advective velocity above the canopy $(z/h < 1)$ is $W_{lz} = 0.12$ cm/s, acting over a vertical length scale of $H - h = 18$ cm. In the denser array, the average vertical flow of the secondary circulation above the patch is $W_{lz} = 0.15$ cm/s.

The vertical turbulent diffusivity D_{tz} was approximated as twice the vertical eddy viscosity within the mixing-layer (e.g. Ghisalberti & Nepf, 2005). Figure 4.10 presents the vertical profiles of turbulent eddy viscosity within the shear layer. Normalised eddy viscosity profiles show a similar distribution for both canopy densities and follow the universal form characteristic of vegetated shear layers seen in Ghisalberti & Nepf (2004). From measured data, averaged turbulent

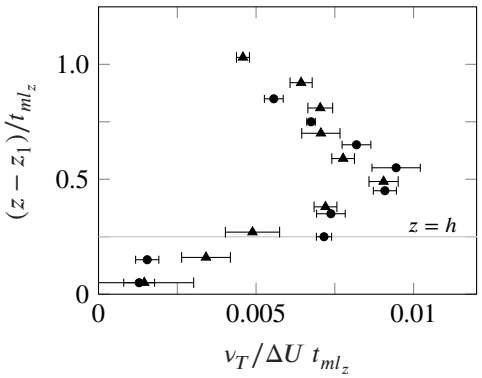


Figure 4.10: Normalised vertical profile of horizontally-averaged eddy viscosity within the mixing layer for the two densities, $\phi = 0.025$ (▲) and $\phi = 0.10$ (●). The standard error in each data point is represented by horizontal error bars and indicates the uncertainty between profiles measured within the vegetation patch.

eddy viscosities of $\nu_{tz} = 0.92$ cm^2/s and $\nu_{tz} = 1.56$ cm^2/s, are obtained for the less and more dense canopies, respectively. These lead to estimates of Pe ≈ 3.0 for $\phi = 0.025$ and Pe ≈ 1.4 for $\phi = 0.10$. Recall that without any secondary flow $Pe = 0$ in open-channel flows, and mixing is only due to turbulence (i.e., via ν_{tz}) rather than via secondary circulation. These results demonstrate that within the vegetation patch the cross-sectional coherent structures and turbulent mixing can contribute about equal amounts to vertical scalar transport.

4.7 Discussion

The hydrodynamics presented here provide a description of the three-dimensional flow characteristic of the interaction between a porous obstruction (i.e. a patch of vegetation) and the surrounding flow. The characterisation focuses on the structures mainly created due to three direct effects of the canopy array on the flow: (i) the drag discontinuity at the patch boundaries generates large-scale shear which leads to the creation of coherent vortices, (ii) the vegetation resistance enhances interfacial turbulent shear by limiting the penetration of the coherent vortices, and (iii) the array creates a spanwise bed inhomogeneity that generates potentially strong cross-sectional circulations of Prandtl's second kind, and the impact of such structures on mass and momentum exchange. The experimental data describes the flow over a partially vegetated channel for canopy densities relevant to aquatic systems.

Results presented here highlight the dependence of flow properties such as vertical and lateral shear layers on vegetation density. Unlike fully vegetated flows where vertical streamwise velocity distributions are symmetric (e.g. Ghisalberti & Nepf, 2006, 2004), in patchy vegetation (considered in this study) velocity profiles were found to be asymmetric. Therefore, vertical shear layers here are predicted by two distinct layers with independent length scales (c.f. Figure 4.11). The inner-layer is characterised by a hyperbolic tangent profile typical of a vegetated mixing-layer, and so the thickness is set by the resistance of the porous obstruction. The outer-layer, where velocity profile scales with the modified log-law for canopy flows, has a width set by the water depth and bottom (i.e. bed) friction. Lateral velocity distributions, analogous to the vertical velocity distributions, are characterised by two independent length scales. The inner-layer thickness is set by the canopy resistance to the flow, as in partially vegetated flows with emergent vegetation

(e.g. White & Nepf, 2007). The outer-layer is described by near-sinusoidal velocity distributions that bulge upward or downward with the vertical velocity of the cross-plane secondary circulation, which is in contrast to the boundary layer profile observed in emergent patchy vegetation (e.g. White & Nepf, 2007). These results have implications for the delimitation of turbulent mixing layers where vegetation plays a key ecological role in controlling nutrient uptake.

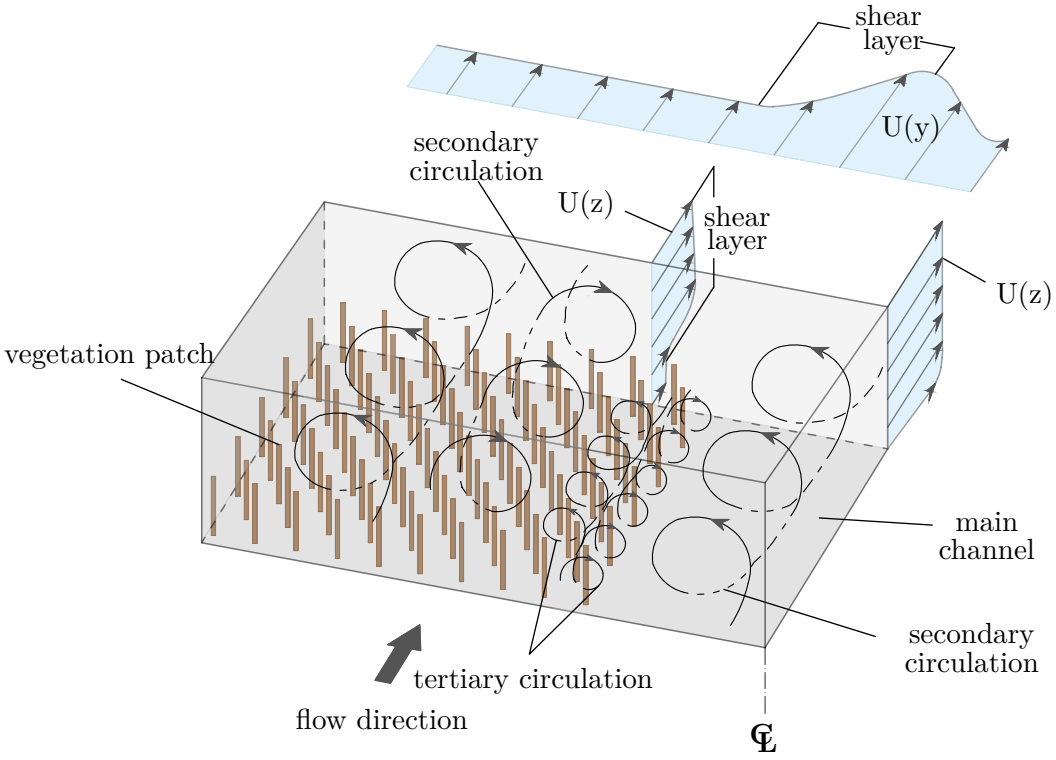


Figure 4.11: The three-dimensional flow structure in a partially vegetated channel.

Cross-sectional coherent structures are generated due to the spanwise inhomogeneity of the bed with patchy vegetation. Secondary motions in the form of large-scale rollers on the plane perpendicular to the streamwise direction are created close to the lateral canopy-water interface LCWI (c.f. Figure 4.11). Previous studies on secondary circulation over ridge and strip-type roughness surfaces have shown that the spanwise wavelength, and the width of the elevated/rough region are relevant parameters for the presence of secondary circulation (Nezu & Onitsuka, 2001; Wang & Cheng, 2006; Hwang & Lee, 2018; van Rooijen et al., 2018). However, the present study highlights the importance of an additional surface feature for patchy vegetation represented by the canopy density. Comparing the present work with previous studies over strip- and ridge-type roughness flows,

some differences are identified. The direction of rotation of the pair of secondary cells is opposite to that observed over ridge-type and strip-type roughness flows (Figures 1.1d and 1.1e). For ridge-type roughness flows, secondary motions manifested in rollers flanking the ridge with upward flow at the ridge edge (Tominaga & Nezu, 1991; Wang & Cheng, 2006; Hwang & Lee, 2018) (Figure 1.1d). In the case of strip-type roughness flows, the upwash and downwash motions occurred above the rough and smooth surfaces, respectively (Wang & Cheng, 2006; Türk et al., 2014; Willingham et al., 2014; Anderson et al., 2015; Stroh et al., 2016) (Figure 1.1e). This suggests a different distribution of the secondary cells when the flow encounters a canopy patch.

Tertiary circulations were also observed at the LCWI for the patch of high vegetation density. The size and strength of these tertiary cells were smaller than that of the secondary flow and had opposite rotational direction to that of the secondary circulation (Figure 4.11). The appearance of the new pair of cells has been previously observed over flows with varying roughness. The pair manifests when two parameters, the rough strip/elevated region width S and the pitch P (the separation between consecutive rough strips/elevated steps), increase above threshold values. On strip-type roughness flows, an incremental increase in S and P lead to the growth of a new pair of cross-sectional cells displacing (and eventually replacing) existing secondary circulation structures (Türk et al., 2014; Stroh et al., 2016). By contrast, results from ridge-type roughness flows (e.g. Hwang & Lee, 2018) have shown that although tertiary flows are observed, by increasing S and P, the rotational sense is invariant due to the weak nature of the tertiary circulation. In the present study, neither the spanwise wavelength nor the vegetation patch width S were varied, yet the tertiary flow was still apparent. Further analysis of the cross-sectional structures in a partially vegetated channel is required to understand the driving mechanisms of the secondary (and tertiary) flows and their behaviour under changes in relevant submerged patchy-vegetation systems characteristics such as vegetation density, canopy patch width and flow shallowness. Additionally, the well-organised transition of the rotational directions of the secondary motions, when varying the spanwise wavelength and the low shear-stress width on strip-type roughness flows shown by, for instance, Stroh et al. (2016) suggested that high and low roughness can produce thicker or thinner boundary layers, which represent the scale of secondary flow. The consideration of a single length scale is therefore not sufficient in characterising the surface heterogeneity. In the present experiments, cross-sectional secondary circulations

above the canopy were shown to scale with the vertical shear layer thickness t_{ml_z}, which is inversely proportional to the vegetation density. This scaling explains why two rotating cells were observed over the high density patch compared to the single cell seen above the low density patch. This further confirms that vegetation density is a key parameter for flow characterisation in patchy vegetation.

The spanwise inhomogeneity, caused by the vegetation patch, introduces dispersive stresses both at the secondary circulation scale and the porous medium i.e. canopy scale, contributing to the total shear stress and consequently to the streamwise momentum transport. Results from this study confirm that dispersive stresses can be significantly larger than the Reynolds stresses inside the canopy, as also seen in fully vegetated flows (Böhm et al., 2000; Poggi et al., 2004; Coceal et al., 2006). The vertical advective dispersive stresses were also found to be of importance above the canopy, increasing for the higher canopy density and contributing up to 20% of the total shear stress for the denser vegetation patch. This is in agreement with the studies of e.g. Vanderwel et al. (2019); Medjnoun et al. (2020) over ridge-type roughness flows, where advective dispersive stresses contribute up to 28%, and between 15% and 55% of the total shear stress, respectively. Contrary to the conclusions of previous studies on emergent patchy vegetation (e.g. White & Nepf, 2007), the submerged partially vegetated channel caused non-negligible lateral advective dispersive stresses, which can be even larger than the lateral Reynolds stresses. This result is in line with the observations made by Vermaas et al. (2011) that secondary circulations and mixing-layer vortices can both contribute significantly to streamwise momentum exchange. Therefore, understanding and evaluating advective dispersive stresses in submerged patchy vegetation is required for correctly modelling riverine and coastal flows. Although quantifying advective dispersive stresses in natural environments requires detailed velocity measurements, more laboratory experiments and numerical simulations should be performed to improve existing models that describe the effects of patchy vegetation on fluvial and coastal dynamics.

4.8 Conclusions

Laboratory experiments were performed to characterise the flow through patchy vegetation, representative of river flows with riparian vegetation. Experimental results clearly demonstrate the three-dimensionality of the flow. The inhomogene-

ity of the streamwise velocity field in the cross-sectional plane occurs as a consequence of the spanwise bed heterogeneity caused by the canopy patch. Smoother contours of streamwise velocity are observed for the sparser canopy, while large undulations of the contour lines, extending almost the full water depth, are seen for the patch of higher vegetation density. Negative and positive deviations of the streamwise velocity from horizontal averages are associated with upward and downward motions of the cross-plane secondary circulations, respectively. The interaction between the patch of vegetation and the open channel region creates a sharp velocity gradient resulting in the development of vertical and lateral mixing-layers controlling mass and momentum exchange. Both mixing-layers are found to possess two distinct regions: The inner-layer with streamwise velocity distributions that have a hyperbolic tangent shape, and the outer-layer that resembles a boundary-layer in the vertical direction, but exhibits sinusoidal-like variations in the spanwise direction due to the action of the secondary circulation. The mixing-layer thickness is found to be larger in the lateral direction than in the vertical direction, and decreases with increasing vegetation density.

Secondary flow structures consisting of a pair of counter-rotating cells are seen in the yz plane, with vertical and horizontal velocities of (respectively) up to 6% and 12% of the bulk velocity U_b. Strong downwelling occurs at the LCWI irrespective of canopy density. Upwelling is observed well into the canopy and within a region extending the equivalent of one water depth from the lateral edge of the patch. The size of the secondary cells above the patch scales with the mixing layer thickness, which is smaller for denser arrays. Hence, two rotating cells are observed above the denser array, with only one seen for the sparser patch.

Advective dispersive stresses represent significant components of total shear stresses in flows through patchy vegetation. The vertical dispersive stress above the canopy is 20-27% of the total shear stress for the more dense vegetation, and up to 9% for the sparser patch. Lateral dispersive stresses are the main contributors to the total lateral shear stress inside, and adjacent to, the canopy patch. Reynolds stresses are largest at the canopy-water interfaces where dispersive stresses are of lesser magnitude. These results indicate that understanding and evaluating the dispersive stresses and their contribution to the total shear stress is required for correctly modelling submerged partially vegetated flows.

Finally, vertical scalar transport due to turbulence and cross-sectional structures

is compared through the consideration of the Peclet number Pe. The vertical flow above the canopy makes a non-negligible contribution to mass exchange by means of vertical advection, which is demonstrated to be of the same order of turbulent diffusion. This result shows that cross-plane structures generated by patchy vegetation can promote the exchange and retention of various types of matter including, but not limited to nutrients, particulate, sediments and heavy metals between a patch of vegetation and the overlying water, playing a key role in ecosystem function. Therefore, models used to study biological processes, such as vertical scalar transport and residence times of biological species in aquatic vegetation should include diffusive and advective processes to estimate productivity in patchily-vegetated flows.

Chapter 5

Effects of vegetation density and shallowness on the flow structure

Abstract

Knowing the three-dimensional flow structure in riverine submerged patchy vegetation is of primary importance to understanding river bank stability, sediment transport processes and particulate transport. Riparian vegetation comprises different plant species and consequently is of varying density, and may or may not be submerged as water levels fluctuate throughout the year due to, for instance, periods of intense rainfall. Here, the effects of these two parameters: vegetation density and relative water depth levels on the three-dimensional flow structure are experimentally investigated. Three-component point velocity measurements in the cross-sectional plane are used to investigate the flow field. In general, the cross-sectional streamwise velocity distribution becomes less heterogeneous at lower densities and the less submergence conditions (where submergence is described by water depth to canopy height ratio). A symmetric vertical shear layer resembling one formed in fully vegetated flows is developed for the less deep flow studied, while asymmetric shear layers form at the vegetation patch boundaries for deeper flows. Secondary cells form at the lateral canopy-water interface with downward flow at the change in roughness. The direction of the vertical flow at this location changes due to the growth of a new pair of counter-rotating cells for denser vegetation patches and the less submergence conditions. The strength of

the cross-plane rotating motions at the lateral interface increases with decreasing water depth. In the three-dimensional shallow flow investigated in all cases, the lateral advective dispersive stress can significantly contribute to the total shear stress, being (in some cases) even greater than the lateral Reynolds shear stress. These results show that vegetation density and shallowness are critical parameters for the occurrence and importance of the secondary motions that define a three-dimensional flow.

5.1 Introduction

The inhomogeneity of a surface consisting of a submerged patch of vegetation in an open-channel impacts the organisation of the mean and turbulent structure in a way that seems to be different from similar flows over other heterogeneous beds such as strip- and ridge-type roughness flows (see Figure 1.1 and Chapter 4). However, various system length scales can play a key role in structure re-organisation. In this chapter, the effects of (i) vegetation density, which is characterised by the array resistance $(C_D a)^{-1}$, and (ii) shallowness conditions (i.e. water depth to canopy height ratio) on the mean and secondary flow, as well as the shear layers developing at the vegetation boundaries and turbulent stresses are investigated. Changes in bed heterogeneity consist of a patch of vegetation, occupying approximately one-third of the channel width, of different densities defined by solid volume fractions ranging from $\phi = 0.0125$ to $\phi = 0.20$ and $\phi = 1$ (i.e. a solid *step* replaced for the canopy). These varying ϕ induce varying flow resistance. Shallowness conditions were changed from $H/h = 3.0$, $H/h = 2.5$ to $H/h = 2.0$, where H and h are respectively the water and canopy height.

5.2 Methodology

5.2.1 Shear stress over heterogeneous beds

Due to the bed inhomogeneity in the spanwise direction, statistical features of the flow field are expected to vary with the surface topography. Thus, momentum transport also occurs due to bed inhomogeneities through the so-called advective dispersive stresses (in addition to the usual turbulent stresses), arising from mean flow variations in the spanwise direction (e.g. White & Nepf, 2007; Nikora et al., 2019). The definition of advective dispersive stresses is based on the spatial averaging of the double-averaged (in time and over a small volume of interstitial

fluid which includes some canopy elements) flow (which were explained in detail in §4.2.1). This averaging concept has been widely used to assess flows over spanwise heterogeneous beds. In this framework, the expression for the total momentum flux, in index notation, can be written as,

$$\underbrace{\langle \overline{u_i}\,\overline{u_j} \rangle}_{\substack{\text{total} \\ \text{momentum flux}}} = \underbrace{\langle \overline{u}_i \rangle \langle \overline{u}_j \rangle}_{\substack{\text{mean flow} \\ \text{flux}}} + \underbrace{\langle \overline{u}_i{}' \overline{u}_j{}' \rangle}_{\substack{\text{turbulent} \\ \text{flux}}} + \underbrace{\langle \overline{u_i}'' \overline{u_j}'' \rangle + \langle \tilde{\overline{u}}_i \tilde{\overline{u}}_j \rangle}_{\substack{\text{dispersive} \\ \text{stress}}} \tag{5.1}$$

In (5.1), the total dispersive stress is represented as the sum of the dispersive stress due to spatial fluctuations in the porous medium $\langle u_i{}'' u_j{}'' \rangle$ and the advective dispersive stress due to potential correlations of spatial variations in time-averaged velocity fields $\langle \tilde{\overline{u}}_i \tilde{\overline{u}}_j \rangle$. Therefore, defining the time-, spatially- and depth-averaged flow, the total shear stress is composed by turbulent Reynolds, dispersive shear stress due to spatial fluctuations in the porous medium and advective dispersive stresses as in (4.10). In addition to the usual dominant momentum sink, i.e. the Reynolds shear stress, the advective dispersive stress can play a major role in the transport of momentum flux, having a significant impact on the organisation of the turbulent structure (§4.5). Note that a flow without spanwise inhomogeneity would exhibit zero advective dispersive stresses. Depth-averaged shear stresses will be evaluated and linked to the mean flow features observed for a canopy with increasing vegetation density and under three shallowness conditions.

5.2.2 Shear layer thickness

Due to the drag discontinuity in a submerged partially vegetated channel, there is a large gradient of shear at the vegetation boundaries characterised by the formation of large coherent structures that enhance interfacial mass and momentum exchange. A measure of the width, in the y- and z- directions, of these coherent vortices is given by the shear/mixing layer thickness t_{ml_y} and t_{ml_z}, respectively. As the flow through vegetation is understood to resemble a finite free shear layer flow (Ghisalberti & Nepf, 2004), the velocity profile is characterised by a high constant velocity U_2 in the free-flow, located at a distance y_2 or z_2, and a low constant velocity U_1 inside the canopy, at y_1 or z_1, which are separated by a confined region of shear where the vortices reside. Thus, the mixing layer thickness is given by $t_{ml_y} = y_2 - y_1$ and $t_{ml_z} = z_2 - z_1$.

The vertical position z_2 of the high constant vertical velocity was assumed to be the water depth, H. The position z_1 of the low constant vertical velocity was evaluated as the location of the streamwise velocity at which the vertical turbulent Reynolds stress $-\overline{u'w'}$ decayed to 10% of its maximum value (Nepf & Vivoni, 2000). In the spanwise direction, the position of the velocity U_1, y_1, was calculated as in the vertical direction. However, the lateral streamwise velocity profile in a partially vegetated channel does not reach a constant high velocity in the non-vegetated region, instead it takes a nearly sinusoidal shape with increasing amplitude (Figure 4.1b). Thus, the spanwise location y_2 was taken as the y-position at which the Reynolds stress $\overline{u'v'}$ crosses zero close to the vegetation patch in the non-vegetated region (see Chapter 4 for further details of the mixing layer thickness definitions).

5.2.3 Secondary circulation strength

Swirling strength λ_{ci} is used to illustrate the cores of the rotating cell structures in the cross-sectional plane which, unlike vorticity, enables the analysis of the cells without contamination from shear (Tomkins & Adrian, 2003). The swirl is computed as the imaginary part of the complex eigenvalue of the two-dimensional (spanwise and bed-normal) velocity gradient of the time-space averaged velocity gradient tensor (e.g. Willingham et al., 2014; Medjnoun et al., 2020),

$$D_{23} = \begin{bmatrix} \dfrac{\partial\langle\overline{v}\rangle}{\partial y} & \dfrac{\partial\langle\overline{v}\rangle}{\partial z} \\ \dfrac{\partial\langle\overline{w}\rangle}{\partial y} & \dfrac{\partial\langle\overline{w}\rangle}{\partial z} \end{bmatrix} \tag{5.2}$$

The swirling strength, a scalar, is the imaginary part of the swirling motions represented by the plane described by the complex pair of eigenvectors (derivation and further physical interpretation of the swirling strength can be found in Zhou et al. (1999)). The direction of rotation of the swirling motions are recovered by multiplying λ_{ci} by the mean streamwise vorticity $\Omega_x/|\Omega_x|$, where $\Omega_x \equiv \partial\langle\overline{w}\rangle/\partial y - \partial\langle\overline{v}\rangle/\partial z$.

Furthermore, the circulation ϵ of the streamwise vorticity is used to investigate the overall trend of secondary circulation strength with varying vegetation density. The circulation ϵ is evaluated as the magnitude of streamwise vorticity within the cross-sectional area enclosing the pair of secondary cells developed at the lateral

canopy-water interface for each canopy density as in the study of Medjnoun et al. (2020). The quantity ϵ is defined as,

$$\epsilon = \int_0^H \int_{-\lambda_V/2}^{\lambda_V/2} |\Omega_x| \tag{5.3}$$

where H is the water depth and λ_V is one wavelength of the spanwise velocity $\overline{v}$ that forms in between the upward flows of the secondary circulation pair where $\overline{v} \approx 0$ as shown in Figure 4.6. Note that the integral limits $-\lambda_V/2$ and $\lambda_V/2$ comprise a pair of secondary cells and not only one individual cell.

Vegetation densities ϕ and shallowness conditions H/h studied in this Chapter are presented in Table 5.1. Different symbols were used for each vegetation density and will be used in graphical representations throughout this Chapter.

Table 5.1: Summary of vegetation densities and shallowness conditions studied.

Vegetation density	**Shallowness**			**Patch width**	**Symbol**
ϕ	H/h			B [cm]	
0.0125	3.0			61.5	■
0.025	3.0		2.0	61.5	▲
0.05	3.0			61.5	★
0.10	3.0	2.5	2.0	61.5	●
0.20	3.0	2.5	2.0	61.5	♦
0.20	3.0			123	◊
1.00 (*step*)	3.0			61.5	+

5.3 Impact of varying vegetation density ϕ on streamwise velocity structure

Maps of the time-averaged streamwise flow field demonstrate strong spanwise heterogeneities that depend on the vegetation density and the canopy patch width. These non-homogeneities are clearly observable in the contour maps of the mean streamwise velocity plotted in Figure 5.1(a-g). As vegetation density increases, the amount of undulations above the patch of vegetation increases, and the spanwise variations of the velocity contours become more pronounced. For the sparser cases, $\phi = 0.0125$, $\phi = 0.025$ and $\phi = 0.05$, the spanwise variations over the canopy are similar, although velocities inside the patch decrease with increasing

ϕ (Figure 5.1(a-c)). For $\phi = 0.10$, a strong upward bulging of the velocity contours is observed above the canopy at mid-patch width, and a smaller upward bulge is seen at $y/H \approx 1.7$ (Figure 5.1d). Instead, for the denser patch, $\phi = 0.20$, two similar (in size) upward undulations are observed (Figure 5.1e). Next to the vegetation patches, the downward undulation of the velocity contours, followed by an upward undulation, becomes more pronounced with increasing canopy density. For instance, the mean streamwise velocity for $\phi = 0.025$ exhibits a maximum peak-to-trough variation of 7.8% of U_b (comparing streamwise velocities at $y/H = -0.30$ and $y/H = -0.74$). This difference is smaller than the difference for $\phi = 0.05$ for which the maximum peak-to-trough variation is 9.8% of U_b, at $y/H = -0.48$ and $y/H = -0.81$. The maximum peak-to-trough variation for $\phi = 0.10$ is 12% of U_b, comparing the flow at locations $y/H = -0.61$ and $y/H = -0.94$, and 8.8% of U_b for $\phi = 0.20$ at $y/H = -0.56$ and $y/H = -1.23$. These results suggest that the patch of density $\phi = 0.10$ presents the largest heterogeneities within the vegetated and non-vegetated region. Presumably, as ϕ increases from $\phi = 0.0125$ to $\phi = 0.10$ the pressure drop deep inside the canopy keeps increasing, which continues to strengthen the secondary flow coming inside the canopy. However, for $\phi = 0.20$, the flow blockage is very high and the mean flow field starts resembling that of a solid *step* (Figures 5.1e and 5.1f). Here, the canopy density $\phi = 0.10$ seems to represent a transition in the mean flow pattern.

The mean secondary circulation is shown in Figure 5.1(a-g) as in-plane vectors of $\overline{v}$ and $\overline{w}$ (time-averaged spanwise and bed-normal velocity, respectively). In regions of upward flow, positive $\overline{w}$ locally coincides with the upward bulging of the velocity contours, whereas in regions of downward flow, negative $\overline{w}$ drives the flow towards the bed, corresponding to a local downward undulation of the velocity contours. As expected, the number of secondary cells observed above the patch of vegetation increases with increasing canopy density, as the width of the secondary cells scales with the vertical mixing layer thickness, which in turn decreases for increasing ϕ (as previously seen in §4.4). A strong region of downwelling, $\overline{w} < 0$, is seen at the lateral edge of the vegetation patch for densities $\phi = 0.0125, 0.025, 0.05$ and 0.10. However, a switch in the vertical velocity direction occurs for $\phi = 0.20$, where an upwelling $\overline{w} > 0$ is instead observed. This upward flow is shared by the small counter-clockwise (CCW) cell located adjacent to the vegetation patch, and the clockwise (CW) cell located at the top-left corner of the canopy, which is not clearly visible from the in-plane vectors in Figure 5.1e but easily identifiable in Figure 5.6e (where the swirl strength is

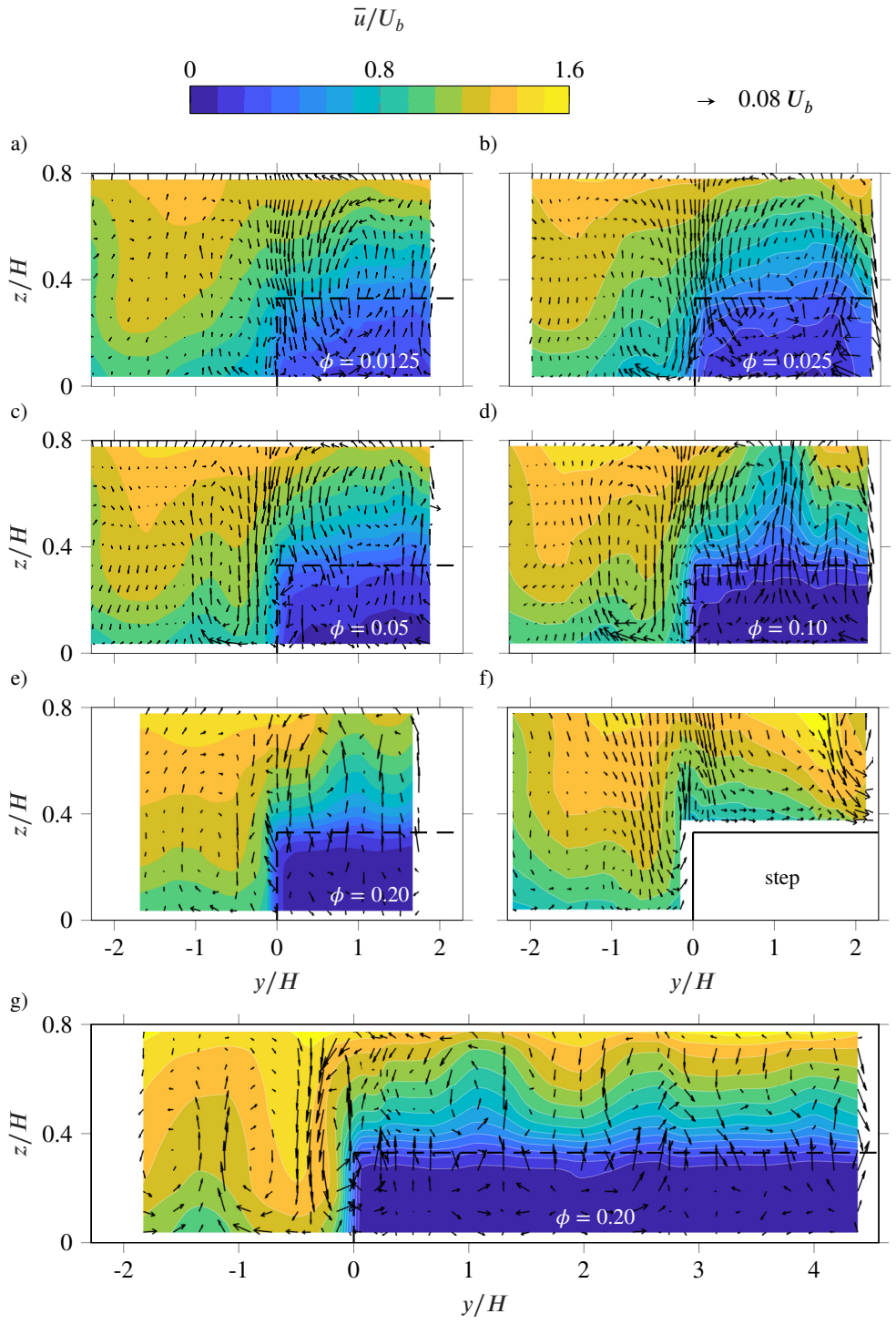


Figure 5.1: Contour maps of the normalised time-averaged streamwise velocity $\overline{u}$ in the cross (yz) plane. Note that here the lateral right edge of the canopy or flume wall is at 61.5 cm $\approx 2.28\ y/H$. a) $\phi = 0.0125$ b) $\phi = 0.025$, c) $\phi = 0.05$, d) $\phi = 0.10$, and e) $\phi = 0.20$. f) Velocity contours over a solid *step* representing the densest case possible, and g) represents the flow over a patch of density $\phi = 0.20$ of double the canopy width B for cases (a-e), it is $B \approx 4.56\ y/H$. Dashed lines represent patch boundaries. The (in-plane) secondary flow is indicated by velocity vectors $[\overline{v}, \overline{w}]$ at each measurement location.

shown). These results suggest that the downward flow at the lateral canopy-water interface is characteristic of partially vegetated channels at lower ϕ, and the direction of the flow at this location is inverted with increasing ϕ. Thus, one would expect that the densest condition would lead to flow characteristics similar to those observed over ridge-type roughness flows (Wang & Cheng, 2006; Hwang & Lee, 2018) or compound channels (e.g. Shiono & Knight, 1991; Tominaga & Nezu, 1991; Omran, 2005), where there is a strong upward flow at the lateral change in elevation. To test this hypothesis, the flow distribution passing over a *step* (the densest condition possible) of the same width as the canopy patch was also studied. Results are presented in Figure 5.1f. As hypothesised, the secondary circulation pair is characterised by an upward flow at the lateral canopy-water interface. On the *step*, the flow tries to recover local homogeneity. Note that the *step* is at $y/H = 2.28$ from the flume wall and therefore slight corner effects can be seen in the undulations of the velocity contours as one approaches the wall. (For corner effects, see also e.g. Naot & Rodi, 1982).

Although it is observed that the direction of rotation of the secondary circulation at the lateral edge of the canopy patch changes from downwelling to upwelling for $\phi = 0.20$, the CW rotating cell above the denser patch and at the lateral canopy-water interface, is of smaller size compared with other rotating cells within the vegetation. Instead, this roll motion is confined to near the top of the canopy, occupying a smaller spanwise width (Figure 5.1e). To explore the behaviour of the pair of rotating cells developing at the lateral interface in a less confined spanwise space above the canopy, cross-sectional velocity measurements were also taken for a dense (i.e. $\phi = 0.20$) patch of vegetation of twice the initial width, i.e. $2B = 123$ cm (Figure 5.1g). Note that the right flume wall is at $y/H \approx 4.5$ and the left flume wall is at $y/H \approx -2.3$. Results show that the pair of rotating cells at the lateral interface occupy a larger space in the vertical direction compared to the case of $B = 61.5$ cm, leading to an upward flow that occupies almost the entire water depth (as observed by comparing Figure 5.1g with Figure 5.1e). The width (in the y-direction) of the CW rotating cell at the lateral interface is smaller in size to the adjacent cells above the canopy. However, its size is the same as the CW roll motion observed at the edge of the *step* case studied (Figure 5.1f). The width (in the y-direction) of the rotating motions in the main channel between $y/H = 0$ and $y/H \approx -1$ is not significantly altered by the widening of the vegetation patch. Although augmenting the width of the patch of higher density leads to a slightly bigger CW cell at the lateral canopy-water interface,

the rotational sense at the interface is invariant to changes in vegetation patch width. This suggests that the majority of cases studied here using $B = 61.5$ cm is sufficient to investigate the secondary flows.

Contours of streamwise velocity above the patch of larger width (Figure 5.1g) bulge upwards at $y/H \approx 1$ and $y/H \approx 2.5$, where the upward secondary flows are present. Downward flows are observed in between the upward flows and at $y/H \approx 3.0$. Velocity contours for spanwise distances larger than $y/H = 3.0$ flatten, leading to a bulk homogeneous region that becomes heterogeneous close to the flume wall due to corner effects. In the main channel, a CW rotating cell is observed next to the secondary circulation pair developed at the lateral canopy-water interface, which spans the full water depth. This cell is common to all cases with varying vegetation density and develops due to corner effects.

5.3.1 Streamwise velocity profiles and shear-layer structure

Time-averaged velocity profiles in submerged canopies develop an inflection point at the top of the canopy due to drag discontinuity, leading to the generation of Kelvin-Helmholtz (KH) vortices that enhance interfacial mass and momentum exchange (e.g. Ghisalberti & Nepf, 2002, 2005; White & Nepf, 2007). These vortices reside in-between areas of low constant streamwise velocity inside the canopy, U_1, and high constant velocity close to the water surface, U_2 (Figure 4.1a). From the contours represented in Figure 5.1(a-e), it can be observed that the region of low constant velocity inside the canopy becomes thicker (in the z-direction) for denser canopies, which is also associated with the reduction of the penetration of the secondary circulation into the vegetation patch. Normalised (by the high constant streamwise velocity U_2) time-averaged and spatially averaged within the vegetated region ($y > 0$) streamwise velocity profiles, for all canopy densities, are shown in Figure 5.2a. Inside the canopy, velocities decrease with increasing ϕ. Profiles for all canopy densities collapse for $z/h \gtrsim 1.44$, where the vegetation has little influence on the profile form. Thus, vertical streamwise velocity profiles can be predicted by two layers of different scales: an inner-layer scale to which the KH vortices penetrate into the canopy, δ_I, and an outer layer scale to which vortices extend above the common point between velocity profiles of different canopy densities, δ_O (i.e. red circle in Figure 5.2a, as in §4.3.1).

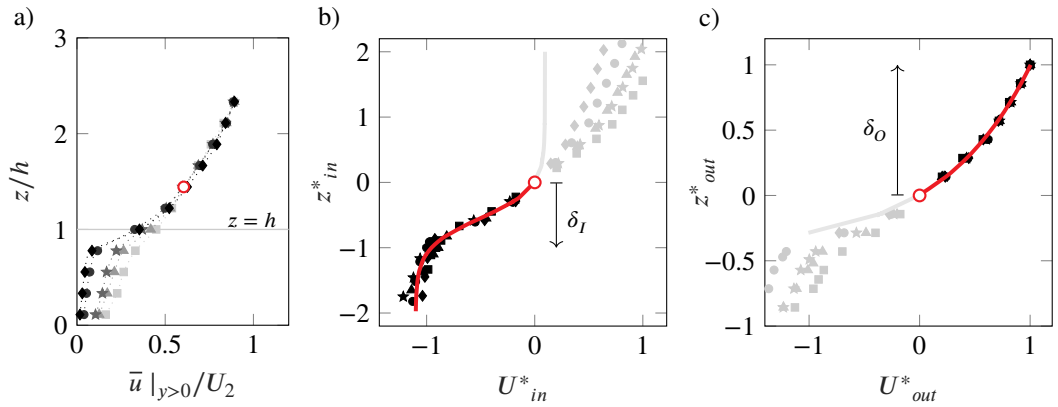


Figure 5.2: Vertical scaling of streamwise velocity profiles for varying densities represented by symbols as in Table 5.1. a) Normalised time-averaged and horizontally averaged within the canopy ($y > 0$) streamwise velocity $\overline{u}|_{y>0}/U_2$. b) Normalised inner-layer profiles with the hyperbolic tangent profile fit (4.15) for reference (red line). c) Normalised outer-layer profiles with the canopy-boundary-layer profile fit (4.14) for reference (red line). The red circle indicates the matching point between the inner and outer layers. The vertical velocity distribution in and over submerged vegetation patches, independent of canopy density, is asymmetric and can be described by two length scales: the inner-layer scale $\delta_I = z_m - z_1$ where profiles collapse into a hyperbolic-tangent profile described by (4.15) and the outer-layer scale $\delta_O = z_2 - z_m$ described by (4.14).

The inner-layer can be represented by a hyperbolic-tangent profile (4.15) as in fully vegetated flows (Ghisalberti & Nepf, 2004). Scaled inner-layer profiles for all canopy densities are illustrated in Figure 5.2b using the rescaled velocity $U^*_{in} = (\overline{u} - U_{m_z})/(U_{m_z} - U_1)$ and coordinate $z^*_{in} = (z - z_m)/(z_m - z_1)$. The collapse of measured velocities into the hyperbolic tangent profile (red line) confirms that the inner-layer scale is given by $\delta_I = z_m - z_1$. In this instance, z_m (corresponding to velocity U_{z_m}) is the last common point to all canopy density profiles, and is also the common point between the hyperbolic tangent profile (4.15), and the canopy log-law profile (4.14); and z_1 corresponds to the vertical position of U_1. Outer-layer profiles for all canopy densities are shown in Figure 5.2c. Rescaled velocities, $U^*_{out} = (\overline{u} - U_{m_z})/(U_2 - U_{m_z})$, are plotted against rescaled coordinates $z^*_{out} = (z - z_m)/(z_2 - z_m)$, where z_2 is the location of $U_2 = U_{z=H}$ in the z-direction, i.e. $z = H$. All velocity profiles collapse into a canopy boundary layer profile described by (4.14), which is represented by a red line in Figure 5.2c. Therefore, the outer-layer scale is given by $\delta_O = z_2 - z_m$. This two-layer scaling of the streamwise velocity profiles confirms that vertical shear layers in submerged partially vegetated channels scale with $\delta_I = z_m - z_1$ and $\delta_O = z_2 - z_m$ for a wide range of canopy densities varying from $\phi = 0.0125$ to $\phi = 0.20$.

Lateral distribution of time-averaged and spatially averaged within the canopy

height ($z < h$) streamwise velocity $\overline{u}|_{z<h}$ for all canopy densities are shown in Figure 5.3a. Velocity profiles present low velocities inside the canopy that rapidly increase at the lateral canopy-water interface (LCWI), and follow different waving patterns in the non-vegetated region. Velocities collapse for all canopy densities at $y/H \approx -1.5$, suggesting this y-location as the termination point of influence of the vegetation patch on the streamwise velocity profiles' form. Inside the canopy, velocities increase with decreasing canopy density. Next to the vegetation, and within the region $y/H = 0$ to $y/H \approx -1.5$, velocity profiles take different forms for each canopy density.

The profile of the lower vegetation density $\phi = 0.0125$, shown in Figure 5.3b, presents velocities that slowly increase well within the canopy and start to rapidly increase around the LCWI. Near the LCWI, an inflection point is observed, changing the concavity of the velocity distribution curve. Outside the vegetation, the velocity increases further, reaching a peak, then descending into a trough, and forming a sinusoidal-like shape. This suggests that the lateral streamwise velocity profile for $\phi = 0.0125$ can be described by two independent shear layers with different length scales. Velocities within the canopy can be described by a hyperbolic-tangent profile (4.15) (red dashed line in Figure 5.3b), while velocities next to the canopy follow a sinusoidal curve (red line in Figure 5.3b). Hence, the inner-layer scale is given by $\delta_I = y_m - y_1$ and the outer-layer scale by $\delta_O = y_2 - y_m$. Analogous to the vertical velocity profile scaling, y_1 corresponds to the y location of the constant low velocity well inside the canopy U_1, and y_m is the matching point between the inner- and outer-layer profiles; y_2 corresponds to the y location of the maximum velocity next to the canopy $\overline{u}_{max-y}$, given by the peak of the sinusoidal distribution (Figure 5.3b).

Interestingly, this two-layer scaling of the lateral streamwise velocity profiles does not apply to all canopy densities. Lateral velocity profiles, for all vegetation densities, are fitted to a hyperbolic tangent profile (4.15). Rescaled velocities $U^*{}_{in} = (\overline{u} - U_{m_y})/(U_{m_y} - U_1)$ are plotted against the coordinates $y^*{}_{in} = (y - y_m)/(y_m - y_1)$ in Figure 5.3c. The low constant streamwise velocity inside the canopy U_1, and the velocity at the last common point between measured data and the hyperbolic tangent profile fit U_{m_y} are used for the rescaled velocities. The location of U_{m_y} in the y-direction y_m, and the y position at which the velocity becomes constant inside the canopy y_1 are used for the rescaled y coordinates. The collapse into a hyperbolic tangent profile inside all vegetation patches suggests

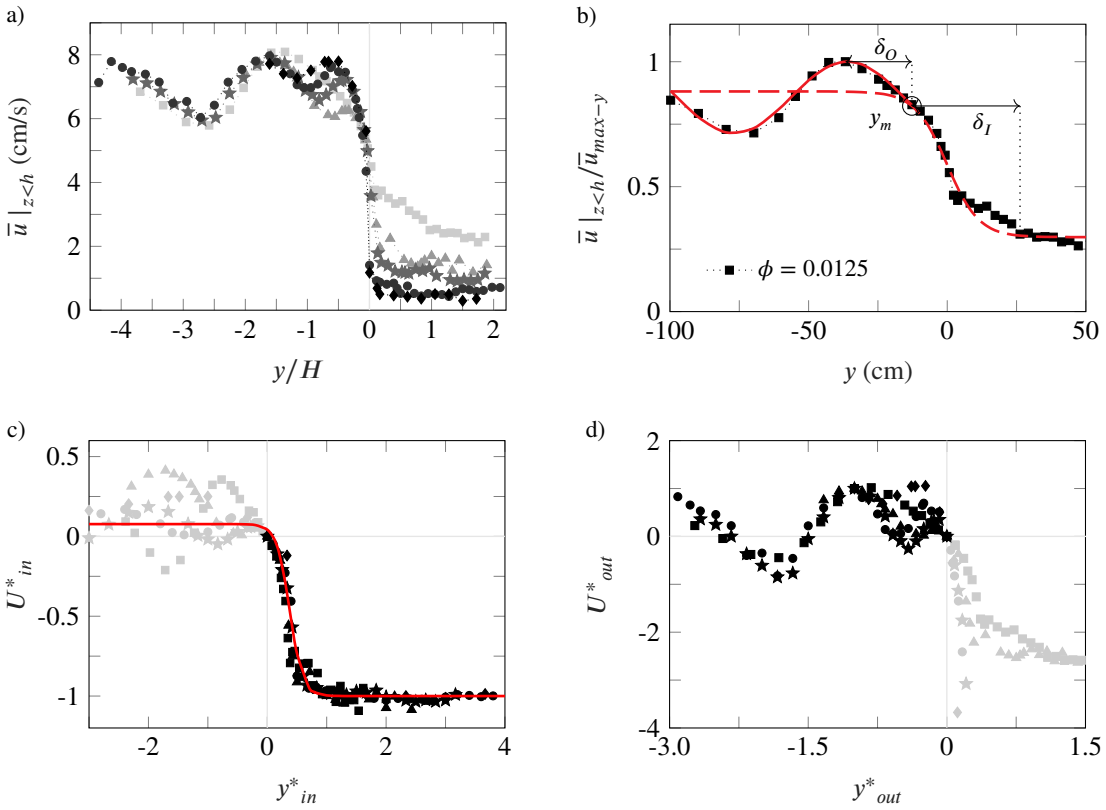


Figure 5.3: Lateral scaling of streamwise velocity profiles for varying densities represented by symbols as in Table 5.1. a) Lateral time-averaged and vertically-averaged over heights $z < h$ streamwise velocity profiles $\overline{u}|_{z<h}$. b) Normalised lateral streamwise velocity with inner- and outer-layers for $\phi = 0.0125$. The inner-layer profile scales with a hyperbolic-tangent profile described by (4.15). The outer layer profile scales with a sinusoidal function. c) Normalised inner-layer profiles with the hyperbolic-tangent profile fit (4.15) for reference (red line). d) Normalised outer-layer profiles.

that velocities inside the vegetation can be described by an inner-layer $\delta_I = y_m - y_1$. However, velocities outside the vegetation cannot be described by a sinusoidal function due to the varying velocity distributions in the region $y/H = 0$ to $y/H \approx -1.5$ (Figure 5.3a). A graph of rescaled outer velocities, $U^*{}_{out} = (\overline{u} - U_{m_y})/(U_2 - U_{m_y})$, against rescaled outer coordinates, $y^*{}_{out} = (y - y_m)/(y_2 - y_m)$, is presented in Figure 5.3d, where U_2 is the maximum velocity in the unobstructed region. An upward undulation of the velocity profile develops next to the vegetation, and becomes more pronounced with increasing vegetation density. For $\phi = 0.20$ the peak of this upward undulation, located at $y^*{}_{out} = 0.2$, is of the same magnitude as the peak in the outer flow, U_2, at $y^*{}_{out} = 1.0$ (Figure 5.3d). This suggests that, for $\phi = 0.20$, the (new) emergent counter-rotating cell next to the vegetation is of comparable strength to the secondary circulation cell for a dense patch where

$\phi = 0.20$ (further analysed in §5.4).

Lateral streamwise velocity profiles within the vegetation height, $\overline{u}\,|_{z<h}$, of the two cases with dense canopy but of different patch width and the *step* are shown in Figure 5.4. Although the peak next to the vegetation patch associated with a downward flow is larger for the wider canopy, it is located at the same spanwise location as that of the two other cases. The same occurs for the trough, at $y/H \approx -1.2$, associated with an upward flow. In fact, the canopy array of width B and the *step* have very similar velocity profiles. These observations suggest that a vegetation patch of $\phi = 0.20$ causes the same effects on the lateral streamwise velocity profiles, and so dictates the location of upward and downward flows in the main channel, as a solid step. However, the mean velocity structure above a dense patch of vegetation is different from that seen on a *step* (c.f. Figure 5.1(e-g)). The higher velocities observed in the main channel for the wider patch are due to the reduction of the cross-section (width) of the main channel.

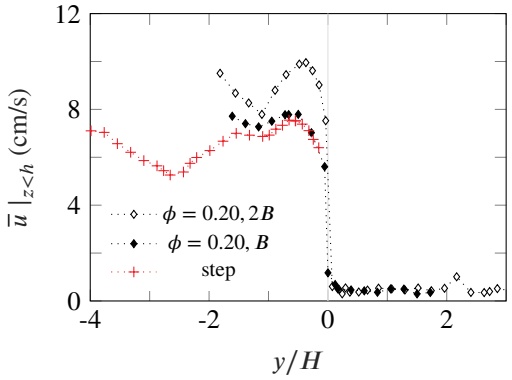


Figure 5.4: Lateral streamwise velocity profiles for the denser patch of vegetation ($\phi = 0.20$) of widths B and $2B$ and a *step*. A dense patch of vegetation causes the same effects on the lateral streamwise velocity profiles in the main channel near the drag discontinuity as a solid step.

5.3.2 Shear layer thickness

The vertical extent of the vegetated shear layers is estimated by the nominal mixing layer thickness, $t_{ml_z} = z_2 - z_1$ (§4.2.2). The thicknesses t_{ml_z} normalised by the water depth H for all canopy densities are shown by black markers in Figure 5.5. The shear layer thickness reduces with increasing canopy density as turbulence-induced vortices penetrate less into denser canopies (c.f. Figure 5.1(a-e)). This inverse relationship between vegetation density and mixing layer thickness is consistent with previous studies in fully vegetated flows (Ghisalberti

& Nepf, 2004). In the spanwise direction, the shear layer thickness also decreases with increasing canopy density (red markers in Figure 5.5). This is in agreement with lateral shear layers seen in partially vegetated flows with emergent vegetation (White & Nepf, 2007). Shear layers in the spanwise direction are larger than vertical shear layers. However, the growth in the outer-layer of the vertical shear layer, in a shallowness condition of $H/h = 3$, may be restricted by the water depth; hence, larger water depth to canopy height ratios should be studied before making generalised conclusions on the difference in magnitude between vertical and lateral shear layers in submerged partially vegetated flows.

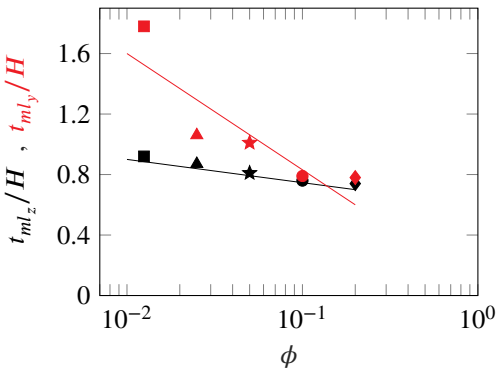


Figure 5.5: Vertical and lateral mixing layer thickness, t_{ml_z} and t_{ml_y}, respectively, normalised by the water depth (H). The black solid line represents the linear regression to t_{ml_z}/H ($R^2 = 0.98$). The red solid line represents the linear regression to t_{ml_y}/H ($R^2 = 0.78$). Markers as in Table 5.1. The mixing layer in the z-direction decreases with increasing ϕ, owing to the reduction of the shear penetration into the canopy as vegetation density increases. Larger mixing layer thicknesses are observed in the spanwise direction than in the vertical direction for $H/h = 3.0$.

5.4 Impact of varying vegetation density on the structure of Secondary circulation

The vectors of time-averaged spanwise ($\overline{v}$) and bed-normal ($\overline{w}$) velocity components in Figure 5.1(a-g) illustrate the secondary circulation for all ϕ cases. These rotating motions are now identified through the signed swirl strength (§5.2.3). Figure 5.6(a-g) shows the signed swirl strength, λ_{ci}, normalised by the water depth, H, and the bulk streamwise velocity, U_b, for each canopy density. In-plane vectors correspond to measured transverse and vertical velocities. Clockwise (CW) rotating cells are represented by blue-filled contours, while counter-clockwise cells (CCW) are in red. The differential roughness between the patch of vegetation and the main channel next to it induces a secondary circulation

that appears as a pair of counter-rotating cells formed at both sides of the lateral canopy-water interface (LCWI), indicated with the symbol (s). This secondary circulation pair consists of a major CCW cell within the canopy and a major CW cell next to the vegetation patch for all canopy densities (Figure 5.6(a-g)). The CW cell in the main channel scales with the water depth in the vertical and spanwise directions, independent of canopy density. The CCW cell size depends on the vegetation density. For $\phi = 0.0125$, $\phi = 0.025$ and $\phi = 0.05$, one big CCW cell (s) is observed within the vegetation, but its extension in the z-direction reduces as vegetation density increases (Figure 5.6(a-c)). For $\phi = 0.10$, a new CW rotating cell appears next to the CCW cell (s) in the vegetated region, whereas for the densest vegetation studied, a third cell appears next to the CCW cell observed for $\phi = 0.10$, with the opposite sense of rotation (Figures 5.6d and 5.6d, respectively). These observations suggest that the size of the rotating motions within the canopy decrease with increasing canopy density and scale with the vertical shear layer thickness t_{ml_z}. This is in contrast to observations in other differential roughness flows such as strip and ridge-type roughness flows, where the secondary cells scale with the boundary layer thickness in both the y- and z-direction (Wang & Cheng, 2006; Willingham et al., 2014; Hwang & Lee, 2018; D. D. Wangsawijaya et al., 2020). However, larger submergence conditions should be studied before generalising these results.

The swirl strength of the major CCW cell ((s) within the vegetation in Figure 5.6(a-e)) appears to increase with increasing canopy density. For $\phi = 0.10$, the swirl strength of the CW cell located between $y/H \approx 1$ and $y/H \approx 1.7$ is about the same as that of the CCW secondary cell next to it (indicated by (s) above the canopy in Figure 5.6. Moreover, the strength of the major secondary CW cell ((s) next to the vegetation patch) of the densest canopy, $\phi = 0.20$ (Figure 5.6e), is an order of magnitude less than the ones observed for other canopy densities. This decrease in strength of the secondary cell is most likely associated with the increasing amount of rotating motions and their sizes compared to less dense canopies.

In between the major pair of cross-sectional cells at the LCWI, a small pair of rotating motions is generated, known as tertiary flow (indicated by (t) in Figure 5.6(a-g)). Contrary to the secondary circulation pair that brings the high speed fluid from the free stream towards the bed, at the LCWI, the tertiary flow attempts to propel the low-speed fluid away from the bed. This tertiary flow

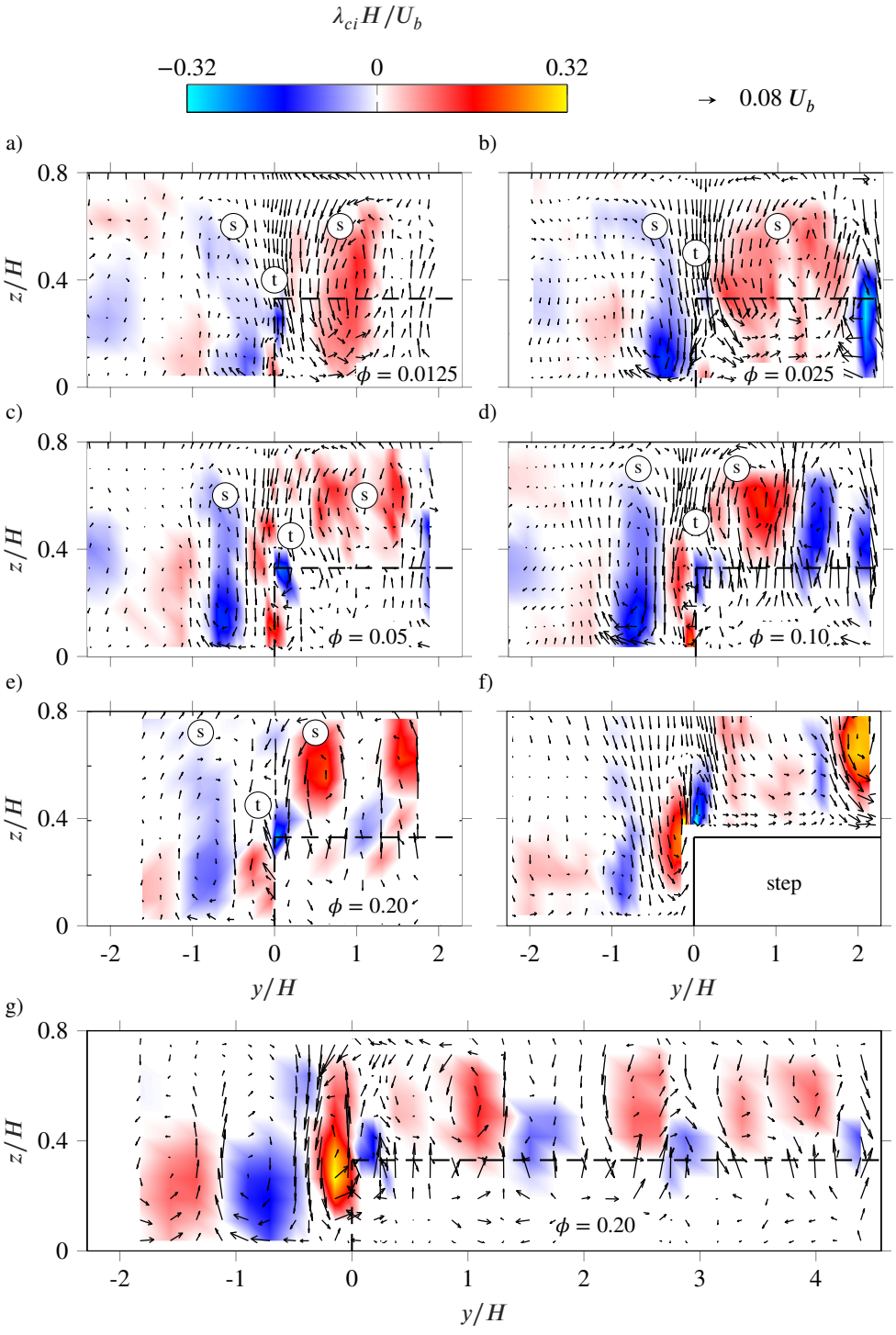


Figure 5.6: Secondary circulation illustrated by the normalised swirl strength multiplied by the sign of vorticity for a) $\phi = 0.0125$ b) $\phi = 0.025$, c) $\phi = 0.05$, d) $\phi = 0.10$, and e) $\phi = 0.20$. f) a *step* and g) a wider (i.e. double the width for cases (a-e)) patch of density $\phi = 0.20$. Dashed lines represent patch boundaries. The (in-plane) flow is indicated by velocity vectors $[\overline{v}, \overline{w}]$ at each measurement location. Red indicates a counter-clockwise roll and blue clockwise motion. Secondary flow is identified by (s) and tertiary flow by (t).

is stronger but smaller than the pair of secondary cells for the sparser canopy, $\phi = 0.0125$, and reduces in size and strength for $\phi = 0.025$ (c.f. Figures 5.6a and 5.6b). For denser canopies (i.e. $\phi = 0.05$, $\phi = 0.10$, and $\phi = 0.20$), the tertiary flow generated increases in size with increasing canopy density, becoming a predominant feature for the densest case. Therefore, for $\phi = 0.20$ the vertical velocity at the LCWI is no longer negative, but positive pointing towards the free surface, coinciding with the direction of rotation of the tertiary flow (Figure 5.6(c-e)). As the tertiary motion becomes a strong feature of the flow, it can be considered as the 'new' secondary motion. This indicates that vegetation density is a key parameter that determines the direction of rotation of the secondary circulation in partially vegetated flows. A change of the vertical flow direction due to the growth of a tertiary flow has been also observed in turbulent flows with hydrophobic surfaces (e.g. Türk et al., 2014; Stroh et al., 2016). The normalised strength, $\lambda_{ci}H/U_b$, of the tertiary CCW motion increases for increasing canopy densities $\phi = 0.0125$, $\phi = 0.05$ and $\phi = 0.10$. This cell is weak for the patch of higher density, $\phi = 0.20$, but of comparable strength to the secondary circulation cell in the main channel (Figure 5.6e). This suggests that changes in the strength and size of the secondary circulation for the highest density are due to an imbalance caused by the tertiary flow, which ultimately ends up balancing the strength of all roll motions in the cross-sectional plane. The CW tertiary cell is stronger for $\phi = 0.05$ and $\phi = 0.20$ (Figures 5.6c and 5.6e, respectively).

Furthermore, the pair of rotating cells flanking the LCWI for $\phi = 0.20$ (Ⓣ in Figure 5.6f) and the *step* (Figure 5.6f) rotate in the same direction, illustrating an upward flow at the lateral boundary of the vegetation patch. However, the largest strength of the tertiary CW cell above the vegetated patch is only 34% of the CW cell at the *step* corner. The CCW cell adjacent to the obstructions (i.e. *step* and densest vegetation patch), is also stronger for the *step* than the canopy patch. The largest strength of the cell next to the vegetation is only 20% of that of the *step*. This can be explained by the fact that no other rolling motions are seen above the *step*, besides those due to corner effects, whereas three additional roughness-induced cells are observed above the vegetation patch. Size-wise, the pair of cells for both obstructions extend equally in the y- and z-directions, suggesting that their growth is limited, independent of density after a 'solid' state is achieved. However, augmenting the width (in the y-direction) of the densest canopy patch, leads to thicker (in the vertical direction) rotating cells at the LCWI, although no size changes can be observed in the spanwise

direction (Figures 5.6e and 5.6g). This is in contrast with observations on ridge-type roughness flows, where the cells reduce their size for wider (in the y-direction) elevated regions (e.g. Vanderwel & Ganapathisubramani, 2015; Hwang & Lee, 2018; Medjnoun et al., 2020). The CCW cell at the LCWI for the wider-densest case, shown in Figure 5.6g, is the strongest among all cases studied. The largest strength of the CW cell is of the same magnitude as that for $\phi = 0.10$ with the original patch width of $B = 61.5$ cm (Figure 5.6g). The results regarding strength are similar for this experimental study and some studies over ridge-type roughness flows, which show this tertiary flow grow stronger for wider ridges (Hwang & Lee, 2018; Medjnoun et al., 2020). This suggests that the canopy width has an impact on the strength of the pair of cells at the LCWI as in ridge-type roughness flows. Also, the distance between 'walls', which for the wider patch are the LCWI and the flume side wall, could also reorganise the flow as has been observed in other roughness-induced secondary flow studies (e.g. Stroh et al., 2016; Medjnoun et al., 2018; Hwang & Lee, 2018). Therefore, further studies should be undertaken to draw conclusions on the characteristics of the secondary circulation in submerged partially vegetated flows with varying patch width and adjacent vegetation patches.

Following the above observations, it is interesting to further investigate the relationship between the secondary circulation strength, in an overall sense, and canopy density. Therefore, the strength of the mean secondary circulation is also evaluated as the amount of streamwise vorticity, $|\Omega_x|$, produced within the area comprising the major pair of rotating cells at the LCWI (i.e. the major CCW cell above the canopy and the major CW cell next to the patch identified previously by (s)), which also encompasses the emergent tertiary flow denoted previously with the symbol (t) (§5.2.3). The normalised circulation of streamwise vorticity $\epsilon^* = \epsilon/HU_b$ for all canopy densities is shown in Figure 5.7. An almost positive-linear variation of ϵ^* is seen for increasing density. However, a limit for this relation exists. A detailed comparison of ϵ^* with the flow swirling strength and in-plane mean velocity vectors in Figure 5.6 reveals that the circulation of streamwise vorticity of the secondary circulation increases until the secondary cells are dominant over the tertiary flow. However, the newly emerging pair of cells (i.e. tertiary flow) becomes the new secondary circulation, switching the direction of the vertical flow at the LCWI for the densest canopy, and ϵ^* significantly decreases reaching about the same magnitude as that for the sparser canopy, $\phi = 0.0125$. This behaviour is consistent with the observations of Stroh

et al. (2016, 2020) on strip-type roughness flows as the results from the Direct Numerical Simulations (DNS) showed the link between a minimum of the circulation of streamwise vorticity and the reversal of the secondary flow direction.

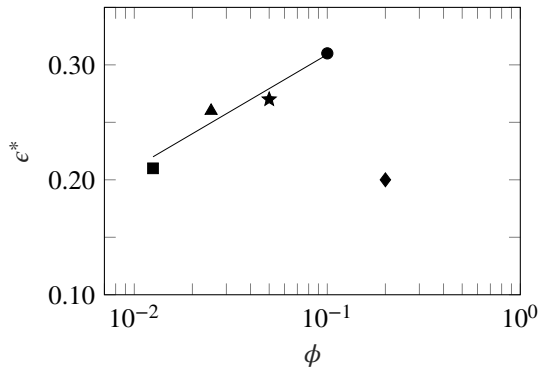


Figure 5.7: Variation of the normalised circulation of streamwise vorticity with vegetation density. Markers as in Table 5.1. The solid line represents the linear regression ($R^2 = 0.86$). The streamwise circulation increases in an approximately linear fashion within the range of vegetation densities studied herein.

5.5 Impact of varying vegetation density - relationship between shear stress and secondary circulation

In turbulent flows over spanwise strip- and ridge-type roughness, the upwash and downwash motions of the secondary circulation have been associated with "low momentum pathways" (LMPs) and "high momentum pathways" (HMPs), respectively, alternating in the y-direction (Anderson et al., 2015; Willingham et al., 2014; Barros & Christensen, 2014; Vanderwel & Ganapathisubramani, 2015). These pathways, in turn, are closely related to the spanwise distribution of the vertical shear stress (Wang & Cheng, 2006; Willingham et al., 2014; Hwang & Lee, 2018). In Figure 5.8(a-g), contours of the vertical Reynolds stress $-\overline{u'w'}$ normalised by the bulk velocity squared, ${U_b}^2$, are plotted against vegetation density. In each figure, the spanwise location of upward and downward motions are indicated with the symbols (u) and (d), respectively. These upwelling and downwelling movements, representing LMP and HMP patterns, are flanking the swirling motions illustrated in Figure 5.6(a-g). Above the vegetation patch, downward motions are observed in spanwise regions of high vertical Reynolds shear stress, independent of canopy density (although it becomes clearer with increasing ϕ) (Figure 5.8(a-e)). This is consistent with patterns observed on strip-type

roughness flows (Willingham et al., 2014; Anderson et al., 2015; Chung et al., 2018), but also over ridge-type roughness flows where the spacing between consecutive elevated regions is more than twice the boundary layer thickness (e.g. Awasthi & Anderson, 2018; Yang & Anderson, 2018). In the non-vegetated region next to the vegetation patch, the location of HMPs and LMPs varies in the spanwise direction with increasing vegetation density. For the less dense canopies, i.e. $\phi = 0.0125$ and $\phi = 0.025$, HMPs and LMPs are located above regions of relatively high and low shear stress, respectively (Figures 5.8a and 5.8b). Further increments in canopy density lead to a reorganisation of the flow, illustrating an exchange of the HMPs and LMPs, which now occur over low and high vertical Reynolds shear stress zones, respectively (Figure 5.8(c-e)). The location of HMPs (LMPs) over low (high) shear stress is consistent with the studies over ridge-type roughness flows by Vanderwel & Ganapathisubramani (2015); Vanderwel et al. (2019); Hwang & Lee (2018).

However, at the LCWI, the vertical turbulent shear stress sharply changes due to the discontinuity; thus above the vegetation corner, the shear stress is much larger than over the smooth bed (just off the vegetation) (Figure 5.8(a-e)). This is in line with the experimental study by Medjnoun et al. (2020) and the numerical simulations of Hwang & Lee (2018) in turbulent boundary layer flows with alternating elevated-recessed regions, where they observed maximum values of the wall shear stress always occurring at the crest ends and small values of the wall shear stress at the bottom wall near the elevation. In fact, for canopy densities where $\phi > 0.0125$, the vertical Reynolds shear stress $-\overline{u'w'}$ changes sign, i.e. it is negative, at the LCWI below the top of the canopy, which also corresponds to the sign of $\partial U/\partial z$. This change in sign has also been observed in compound channels, i.e. a type of ridge-type roughness flow representing a main channel and elevated floodplain, (e.g. Tominaga & Nezu, 1991). The differences in the spanwise distribution of HMPs above either large or low drag regions as vegetation density increases suggests that the generation of the secondary circulation is not simply due to the downward motions created by vertical Reynolds shear stress, but may also be as a result of the heterogeneity of transverse shear stress, and/or turbulent transport as in the ridge-type roughness flow studied by Hwang & Lee (2018).

The growth of the tertiary cells at the LCWI (seen and discussed in §5.4), which reverses the sense of rotation (in this region) for the denser canopy of $\phi = 0.20$,

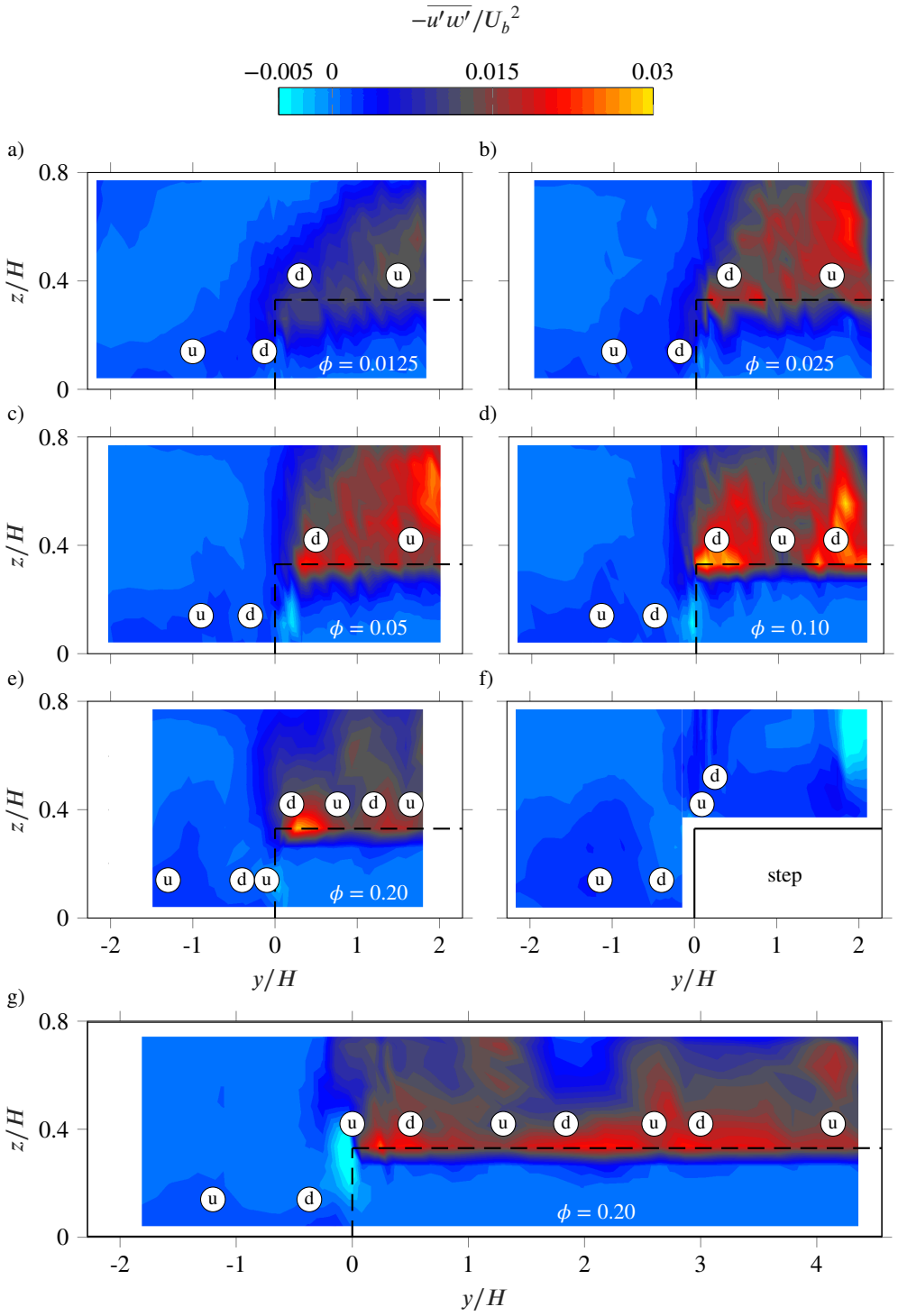


Figure 5.8: Normalised vertical shear stress distribution in the cross-sectional plane with the locations of upward (u) and downward (d) motions. Dashed lines represent canopy patch boundaries. Within the canopy, HMPs are located above regions of relatively high drag, while in the main channel HMPs are located over relatively low drag regions.

does not alter the vertical shear stress distribution of the zone. Hence, the new observed upwelling motion at the LCWI is present within a LMP above a region of relatively low vertical shear stress. This was also observed by Hwang & Lee (2018) in the recessed region of a ridge-type roughness flow where the separation between consecutive elevated surfaces was relatively large with respect to the boundary layer thickness. In the *step* case illustrated in Figure 5.8f, HMPs and LMPs, are present above low and high vertical shear stress zones, which is consistent with previous findings over ridge-type roughness flows (Vanderwel & Ganapathisubramani, 2015; Medjnoun et al., 2018; Vanderwel et al., 2019). For the dense patch of vegetation ($\phi = 0.20$) of width $2B$ (Figure 5.8g), the shear stress distribution and the location of HMPs and LMPs is the same as observed for the narrower patch of the same density (c.f. Figure 5.8e).

The total depth-averaged lateral shear stress, $\langle\overline{\tau_{xy}}\rangle_d$, includes a significant contribution from the advective dispersive stress, arising from mean flow fluctuations, and takes its form within the vegetated region §4.5. Thus, $\langle\overline{\tau_{xy}}\rangle_d$ profiles (gray profiles in Figure 5.9a) resemble the pattern of secondary circulation with zero-crossings at regions of strong upward and downward flow (c.f. Figure 5.6). However, lateral depth-averaged turbulent shear stress $\langle\overline{u'v'}\rangle_d$ also resembles the periodicity of the cross-sectional cells (Figures 5.9a and 5.9b). In fact, next to the canopy, the first zero-crossing off the vegetation patch of the depth-averaged turbulent shear stress coincides with a peak of the depth-averaged streamwise velocity (dashed blue vertical line in Figure 5.9a and Figure 5.9b); which is, in turn, the spanwise location of a strong downward flow (c.f. Figure 5.1c and 5.1d). Farther away from the vegetation patch (in the y-direction), there is another zero-crossing of the Reynolds stress $\langle\overline{u'v'}\rangle_d$, this time associated with a trough of the depth-averaged streamwise velocity profile, and consequently an upward flow (dashed green vertical line in Figure 5.9a and Figure 5.9b). The second peak of $\langle\overline{u'v'}\rangle_d$, in the non-vegetated region, also coincides with a zero-crossing of the lateral Reynolds stress, which is associated with another downward flow (dashed red line in Figure 5.9a and Figure 5.9b). At this location, the total stress $\langle\overline{\tau_{xy}}\rangle_d$ also becomes zero. These observations agree with the study of Anderson et al. (2015) who highlighted the importance of the lateral turbulent shear stress as being responsible for sustaining the interfacial spanwise momentum transport over beds with spanwise differential roughness, resulting in Prandtl's secondary circulation of the second kind.

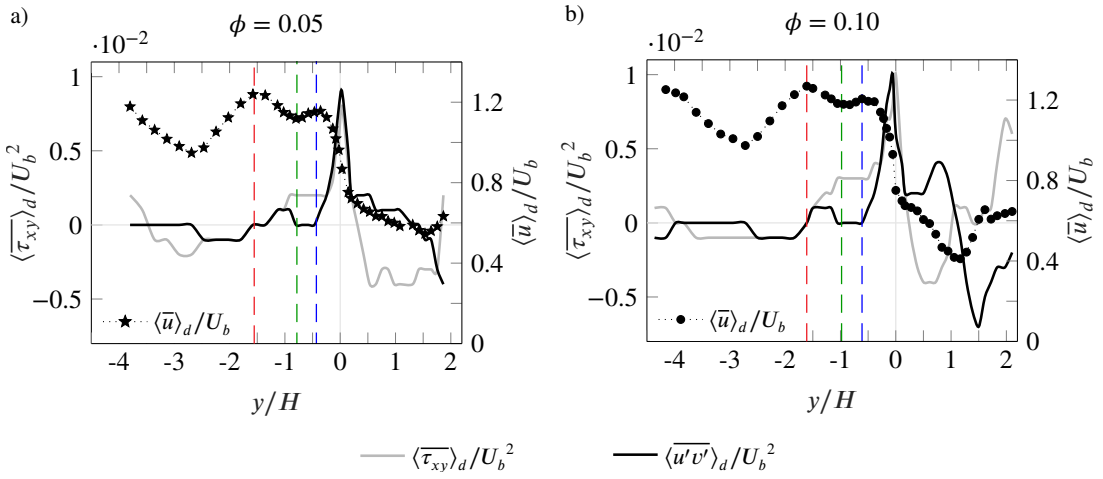


Figure 5.9: Shear stresses and their relationship with upward and downward flows. Normalised depth-averaged streamwise velocity, total lateral shear stress, and lateral Reynolds shear stress for a) $\phi = 0.05$ and b) $\phi = 0.10$. Dashed red and blue lines represent zero-crossings of the Reynolds shear stress, which coincide with peaks of the streamwise velocity profile in regions of strong downward flow. The dashed green line passes through a zero-crossing of the lateral Reynolds stress, and a trough of the streamwise velocity profile, associated with an upward flow.

5.6 Impact of shallowness H/h on the streamwise velocity structure

The impact of shallowness (i.e. water depth to canopy height ratio, H/h) on the mean flow, for three canopy densities ($\phi = 0.025$, $\phi = 0.10$, $\phi = 0.20$), was investigated by decreasing the water depth for a constant canopy patch height. Time-averaged streamwise velocity contours for the various cases are illustrated in Figure 5.10(a-h). Upward and downward undulations of the velocity contours occur at regions of upward and downward flow of the secondary circulation, respectively. However, the undulations above the patches of vegetation gradually flatten as H/h decreases. For the denser patch, $\phi = 0.20$, the two upward undulations of the streamwise velocity contours observed above the vegetation patch at $H/h = 3.0$ (Figure 5.10a) remain at $H/h = 2.5$ (Figure 5.10b), which does not occur for the less dense patch of $\phi = 0.10$ (Figures 5.10d and 5.10e). This may be due to the fact that secondary circulation structures scale with the shear-layer thickness (§4.4), which is thinner (in the z-direction) for the denser patch of vegetation. Thus, there is enough space for such structures to develop, even at a lower water depth. Velocity contours for $H/h = 2.0$ above all vegetation patches have smoother undulations that seem truncated by the water surface, suggesting that no cross-channel cells reside there.

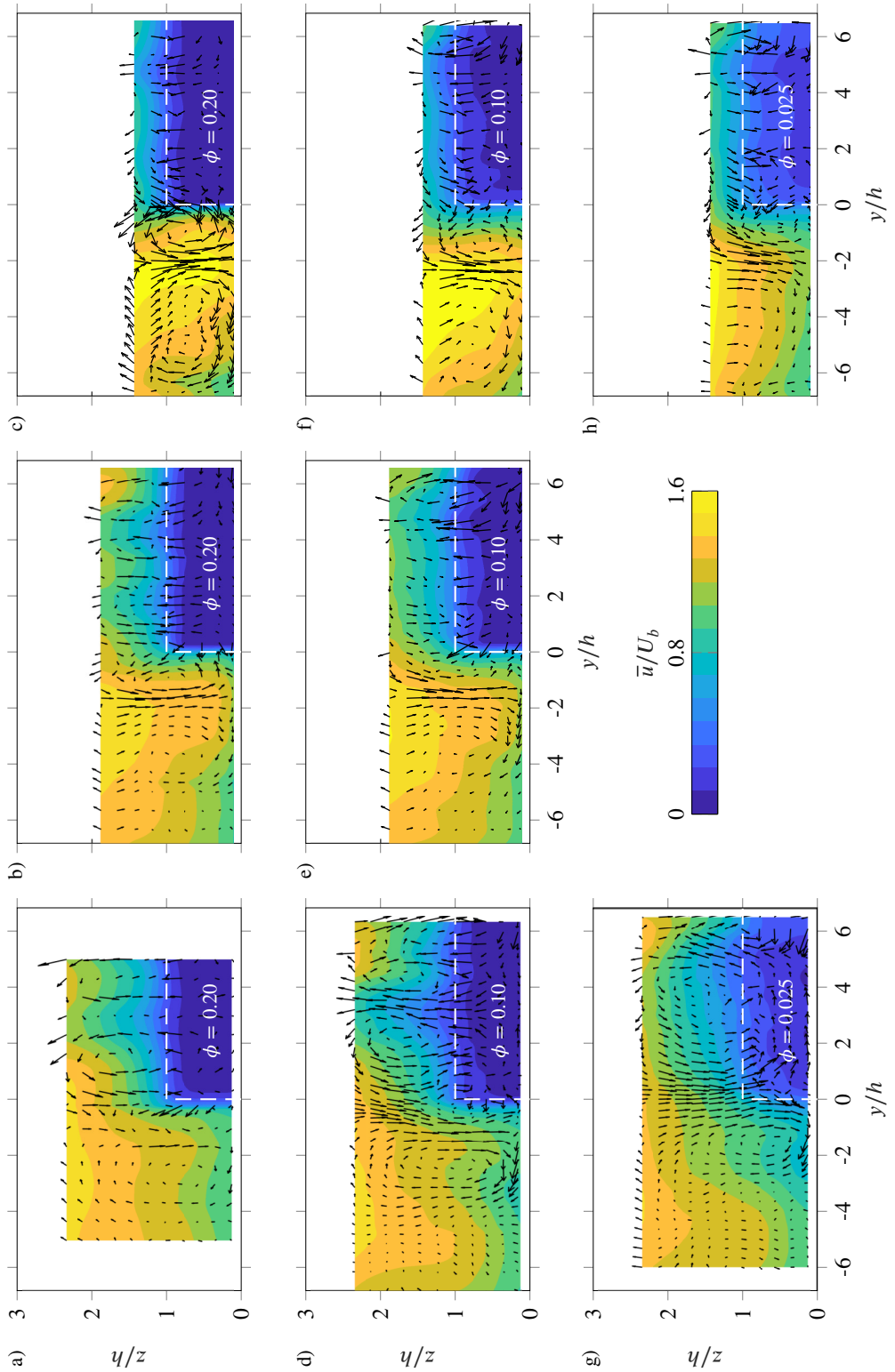


Figure 5.10: Contour maps of the normalised time-averaged streamwise velocity $\overline{u}$ in the cross (yz) plane centred on the lateral canopy-water interface for shallowness conditions of $H/h = 3.0$, $H/h = 2.5$, and $H/h = 2.0$ (in columns) and canopy densities $\phi = 0.025$, $\phi = 0.10$, and $\phi = 0.20$ (in rows). Dashed lines represent patch boundaries. The (in plane) secondary flow is indicated by scaled overlying velocity vectors $[\overline{v}, \overline{w}]/0.15U_b$. Decreasing H/h reverts the direction of the vertical flow observed at the lateral-canopy water interface, and suppress secondary circulations above the canopy.

In the main channel, and for $H/h = 2.0$, velocity contours tend to flatten (i.e. become more uniform across the span) for the less dense canopy (comparing Figures 5.10c, 5.10f, and 5.10h). This can be associated with the blockage effect imposed by the canopy patches on the flow that accentuates as vegetation density increases, which, in turn, tends to reduce the main channel width, changing the distribution of the cross-sectional rotating cells. The reorganisation of the secondary cells with changes in aspect ratio, i.e. channel width to water depth ratio, in open-channel flows, has been investigated by e.g. Naot & Rodi (1982). The downward bulging of the velocity contours adjacent to the patch of vegetation (for all canopy densities) becomes more pronounced as H/h decreases (Figure 5.10(a-h)). The magnitude of the corresponding downwelling motion, represented by scaled velocity vectors $[\overline{v},\ \overline{w}]/0.15U_b$, increased with decreasing H/h. This downward flow moves away from all vegetation patches with decreasing water depth. For the patches of densities $\phi = 0.025$ and $\phi = 0.10$, a new emerging cross-plane rotating motion can be seen just off the vegetation patch at lower water depths. This new rotating motion inverts the direction of the strong downward flow observed at the LCWI at the higher water depth (i.e. $H/h = 3.0$) (Figures 5.10d and 5.10g) to an upward flow (Figures 5.10e, 5.10f and 5.10h). The denser patch of vegetation ($\phi = 0.20$) is characterised by an upward flow at the LCWI for the highest water depth (i.e. $H/h = 3.0$) (Figures 5.10a), which appears to be stronger at lower water depths (Figures 5.10b and 5.10c).

The CW rotating cell in the main channel observed for all canopy densities at $H/h = 3.0$ (Figures 5.10a, 5.10d, and 5.10g), appears to be displaced away from the canopy patch at lower water depths by a new CCW cell created at the LCWI over the smooth bed. It can be observed that this CW cell scales with water depth for all cases. When comparing the CCW cross-sectional rotating motion adjacent to the vegetation patches of different densities at $H/h = 2.0$, it can be observed that the cell occupies approximately the same cross-sectional space of $\approx 2h = H$, indicating that it scales with water depth rather than canopy properties (Figures 5.10c, 5.10f, and 5.10h).

5.6.1 Streamwise velocity profiles and shear layer structure

Time-averaged streamwise velocity profiles at $H/h = 2.0$ developed an inflection point known to trigger KH instabilities in fully vegetated flows (Ikeda &

Kanazawa, 1996; Ghisalberti & Nepf, 2002) and qualitatively resembled the hyperbolic tangent profile of a mixing layer. Therefore, mixing layer parameters may define the mean velocity profiles. Figure 5.11a shows the profiles with velocities and z-locations shifted by U_{mean}, the arithmetic mean of U_1 and U_2, and z_{mean}, the height at which $\overline{u} = U_{mean}$, and normalised by the mixing layer parameters ΔU and θ_z defined in §4.2.2. The collapse of the velocity profiles for the three vegetation densities ($\phi = 0.025$, $\phi = 0.10$ and $\phi = 0.20$) (Figure 5.11a) suggests that profiles of the mixing layers generated at the top of the vegetation patches, in low shallow conditions, can be estimated by knowing U_1, U_2, t_{ml_z} and z.

However, as water levels increase, the velocity profiles can no longer be fully described by mixing layer parameters. For $H/h = 2.5$, time-averaged streamwise velocity profiles resemble those of the deeper flow, $H/h = 3.0$, and therefore may be predicted by two layers of different scales: an inner-layer δ_I represented by a hyperbolic tangent profile (4.15), and an outer layer δ_O described by a boundary layer profile (4.14) (as in §5.3.1). Scaled inner-layer profiles for $H/h = 2.5$ are

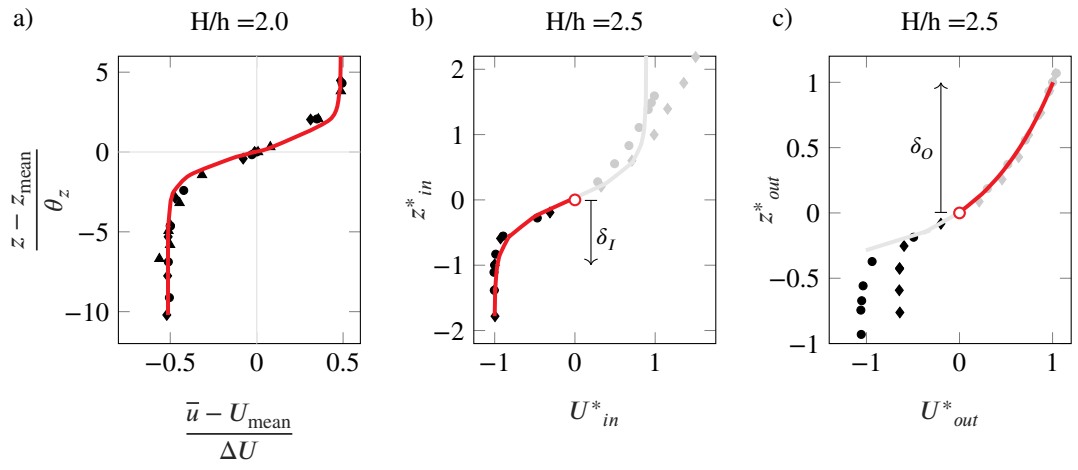


Figure 5.11: Vertical scaling of time-averaged streamwise velocity within the canopy for various shallowness conditions. a) Streamwise velocity profiles for $H/h = 2.0$ normalised by mixing layer parameters, with the hyperbolic tangent profile fit for reference (red line). b) Normalised inner-layer profiles for canopies in a submerged condition of $H/h = 2.5$. The hyperbolic tangent profile appears in red for reference. c) Normalised outer-layer profiles at $H/h = 2.5$ with the canopy-boundary-layer profile fit for reference (red line). Markers as in Table 5.1. The red circle indicates the matching point between the inner and outer layers. The vertical velocity distribution for $H/h = 2.0$ is symmetric described by the mixing layer profile (4.15). For $H/h = 2.5$, velocity profiles are asymmetric and can be described by two length scales: the inner-layer scale $\delta_I = z_m - z_1$ where profiles collapse into a hyperbolic-tangent profile described by (4.15) and the outer-layer scale $\delta_O = z_2 - z_m$ described by (4.14).

shown in Figure 5.11b, using the rescaled velocity $U^*_{in} = (\overline{u} - U_{m_z})/(U_{m_z} - U_1)$ and height ${z^*}_{in} = (z - z_m)/(z_m - z_1)$. Profiles for all canopy densities collapse into the hyperbolic tangent profile confirming the validity of the inner-layer scale $\delta_I = z_m - z_1$ for $H/h = 2.5$. Outer-layer profiles are shown in Figure 5.11c, where rescaled velocities ${U^*}_{out} = (\overline{u} - U_{m_z})/(U_2 - U_{m_z})$ are plotted against rescaled heights ${z^*}_{out} = (z - z_m)/(z_2 - z_m)$. Velocities collapse into a boundary layer profile, thus the outer layer scale is given by $\delta_O = z_2 - z_m$ for canopies at $H/h = 2.5$.

Lateral profiles of time-averaged streamwise velocity for the region below the canopy top $\overline{u}\,|_{z<h}$ at $H/h = 2.0$ and for densities $\phi = 0.025$, $\phi = 0.10$ and $\phi = 0.20$ are shown in Figure 5.12a. Low velocities are observed within the canopy and rapidly increase at the LCWI to reach a maximum in the main channel, next to the patch of vegetation. Then, they decrease and follow a waving pattern. Inside the canopy velocities get smaller as vegetation becomes denser. Next to canopy patch, the streamwise velocity reaches a maximum, which is larger for the denser cases of $\phi = 0.10$ and $\phi = 0.20$ than for $\phi = 0.025$. In fact, for these two densities the velocity profiles are qualitatively similar (Figure 5.12a). Velocities for the three densities collapse at $y/h \approx -6.5$ ($y = 58.5$ cm) indicating that the mean flow structure beyond this point is not affected by the vegetation patch. This spanwise distance of 58.5 cm is 18 cm larger than the point of collapse of streamwise velocity profiles of various densities at $H/h = 3.0$, suggesting major flow disturbances in a partially vegetated flow at lower submergence conditions. As velocity profiles present an inflection point near the LCWI, velocities within the canopy can be described by a mixing layer profile (4.15) as shown in Figure 5.12b.

Analysing the lateral velocity profiles for $\phi = 0.10$ at the three different shallowness conditions (Figure 5.12c), it can be observed that the profile at $H/h = 3.0$, in the region between $y/h = 0$ and $y/h \approx -4$, changes its form with decreasing H/h. The near sinusoidal profile seen at the higher water depth becomes a convex upward curve with an increasing peak that moves towards the main channel at lower water depths. This translates into a sign reversal at the LCWI as the peak (and so the downward flow) moves away from the canopy, and a stronger downward flow as the peak increases (c.f. in-plane vectors in Figure 5.10(d-f)).

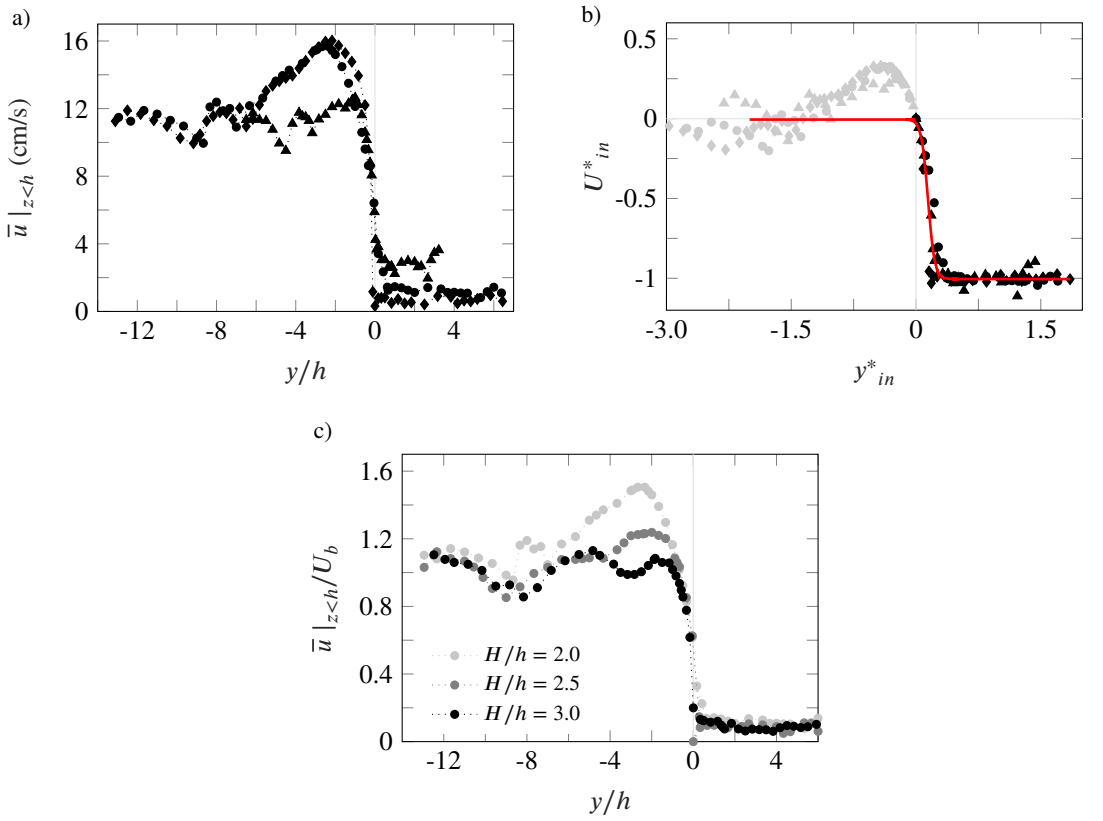


Figure 5.12: Lateral distribution of streamwise velocity profiles below the canopy top. a) Time-averaged and vertically-averaged over $z < h$ streamwise velocity profiles for three canopy densities at $H/h = 2.0$. b) Normalised inner-layer profiles for canopies in a submerged condition of $H/h = 2.0$. The inner-layer profile scales with a hyperbolic-tangent profile (red line) described by (4.15) c) Time-averaged and vertically-averaged over $z < h$ streamwise velocity profiles of the patch of density $\phi = 0.10$ for the three submergence conditions. The change in concavity of profiles near the LCWI as water depth decreases reflects the sign reversal of the vertical flow at the lateral drag discontinuity. Markers as in Table 5.1.

5.6.2 Shear layer thickness

Vertical shear layers are generated due to the submergence of the vegetation patches, growing only to a finite thickness where rapid vertical mixing occurs between the vegetation and the overlying flow (Ghisalberti & Nepf, 2004). For the less deep conditions, the free surface may restrict the shear layer growth (Nepf & Vivoni, 2000). Thus, the vertical mixing layer thickness t_{ml_z} is expected to be directly proportional to the submergence ratio H/h. Results shown by black markers in Figure 5.13 confirm that the vertical shear layer thickness increases with increasing H/h. However, water levels have a greater influence in the thickness size than vegetation density, as t_{ml_z} differences between different ϕ at the same H/h are smaller than differences for a single ϕ at different H/h. In

sufficiently submerged canopies, the vertical mixing layer thickness is no longer restricted by water depth and the effects of vegetation density will prevail (§5.3.2).

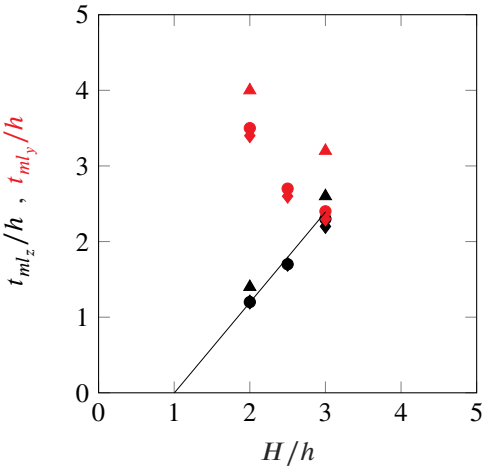


Figure 5.13: Vertical, t_{mlz}, and lateral, t_{mly}, mixing layer thickness normalised by the array height h. The solid line represents the linear regression for t_{mlz} ($R^2 = 0.97$). Markers as in Table 5.1. The mixing layer in the z-direction increases with increasing H/h, as the shear layer growth is not limited by the water surface. By contrast, spanwise mixing layers increase at lower water depths. Note that some markers are overlapping.

The effects of shallowness on the lateral shear layer thickness t_{ml_y} are opposite to those of shallowness on the vertical shear layer thickness t_{ml_z}. Reduced water levels lead to thicker lateral shear layers (red markers in Figure 5.13). The influence of shallowness conditions and vegetation density are now comparable, and lateral mixing layer thicknesses are dominated by these two parameters. Thus, the gradient of mean streamwise velocity is smaller for a sparse patch of vegetation (e.g. $\phi = 0.025$) with a submergence ratio of $H/h = 2.0$, drawing a larger exchange area that spans deeper into the canopy and further away from the lateral vegetation edge.

5.7 Impact of shallowness - characteristics of secondary circulation

Following the changes observed in the mean flow structure, changes in the generated mean streamwise vorticity are to be expected. Time-averaged cross-plane rotating cells were identified through the vorticity-signed swirling strength λ_{ci}. Results are shown in Figure 5.14(a-h), indicating swirling motions in the cross-sectional plane of the different canopy densities (in rows) at various shallow-

ness conditions (in columns). The secondary circulation pair of counter-rotating cells (indicated by (s)) formed at either side of the lateral canopy water interface (LCWI) for $H/h = 3.0$ does not prevail at reduced water levels. Instead, the small CCW cell of the tertiary flow (red cell, indicated by (t)), gets bigger and stronger as water depth drops (compare Figure 5.14a with Figures 5.14b and 5.14c, and Figure 5.14d with Figures 5.14e and 5.14f). However, distinctive qualitative features and swirl magnitude are seen across cases. At $H/h = 3$, the spatial extent of the CW (blue) secondary cell (s) is qualitatively similar for all vegetation densities, although their swirl magnitude is affected by vegetation density. This cell is the strongest for $\phi = 0.10$ and the weakest for the densest canopy patch (Figures 5.14a, 5.14d, and 5.14g). On the contrary, the CCW (red) secondary cell (s) shrinks for increasing vegetation density, which confirms that this rotating motion scales with canopy properties.

As water depth reduces, the secondary cell (s) located above the densest canopy reduces in size (as the water surface hinders its growth) and swirl strength by about 70% of the maximum λ_{ci} at $H/h = 3.0$ (Figure 5.14(a-c)). For $\phi = 0.10$, the maximum magnitude of the CCW secondary motion (s) decreases by 50% from $H/h = 3.0$ to $H/h = 2.5$ getting to $\lambda_{ci}h/U_b \approx 0.03$ (Figures 5.14d and 5.14e). In contrast, the swirl strength of the CW secondary cell ((s) located in the main channel), for all cases except for $\phi = 0.025$, increases as water levels move towards the channel bed. This CW secondary rotating cell extends further into the main channel for H/h=2.5 and H/h=2.0, and its width (in the y-direction) does not scale with the water depth for the most confined flow studied. Wider cross-sectional rotating cells in the main channel are not uncommon in wide channels (Naot & Rodi, 1982; Rodríguez & García, 2008) and have also been observed in compound channels (e.g. Tominaga & Nezu, 1991).

Remarkable differences in the streamwise vorticity occur for the tertiary circulation (t) as water level is reduced (Figure 5.14(a-h)). When the vegetation patch is very dense (i.e. $\phi = 0.20$), the CCW tertiary cell, located in the main channel next to the canopy array, extends towards the water surface as water depth is reduced. For $H/h = 3.0$, this rotating motion occupies approximately one third of the water depth, but it is as tall as the water column at the less deep conditions (Figure 5.14(a-c)). Interestingly, its extent in the y-direction is of $\approx 2h$ and does not seem to be affected by changes in shallowness. This highlights the importance of the blockage effect that the patch of $\phi = 0.20$ imposes on the flow

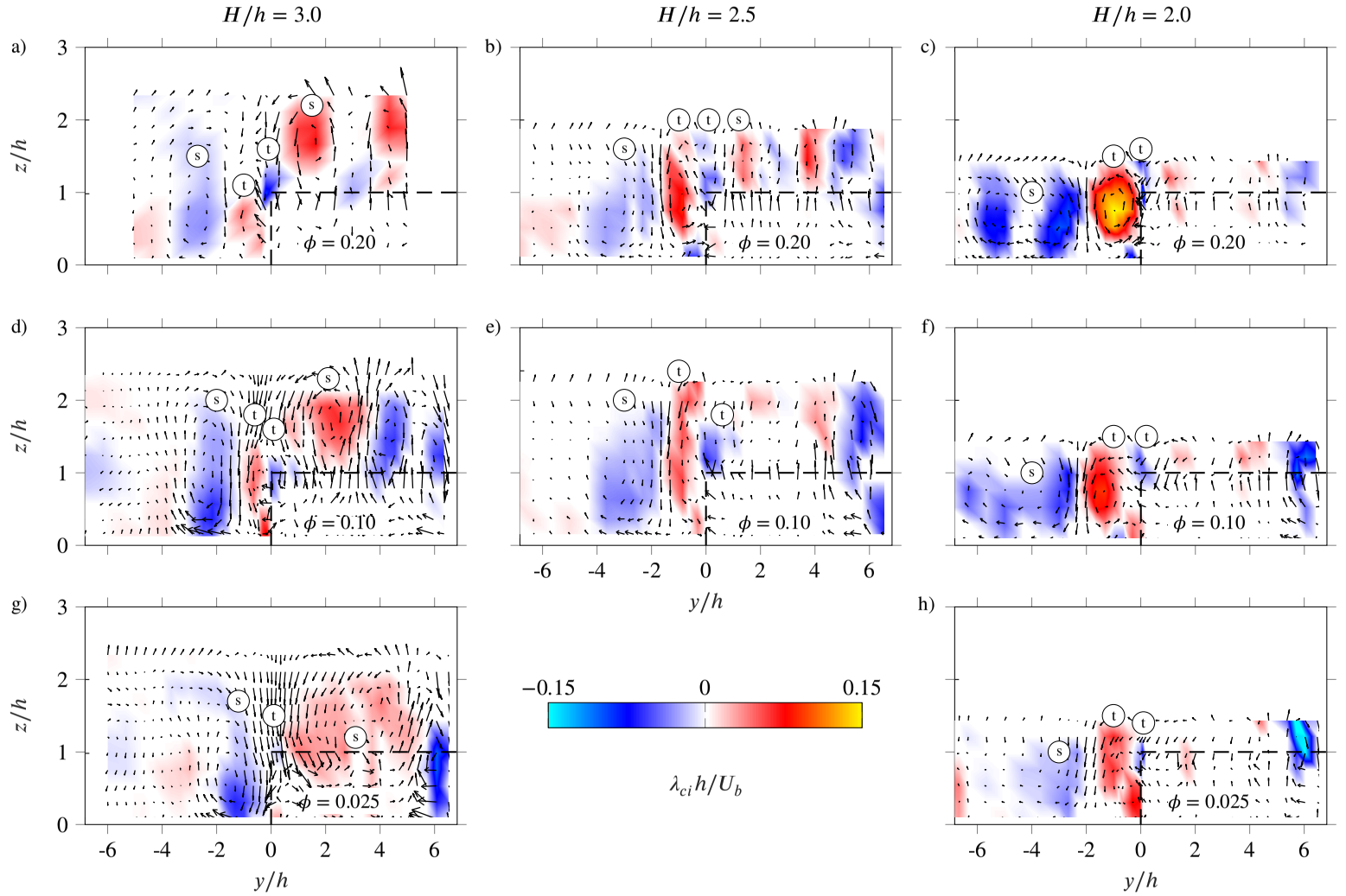


Figure 5.14: Normalised swirl strength multiplied by the sign of streamwise vorticity illustrating the secondary circulation for shallowness conditions of $H/h = 3.0$, $H/h = 2.5$, and $H/h = 2.0$ (in columns) and canopy densities $\phi = 0.025$, $\phi = 0.10$, and $\phi = 0.20$ (in rows). Lower water depths strengthen the counter clockwise cell next to the patch of vegetation, changing the direction of the vertical flow at the LCWI. Secondary flow is indicated by (s) and tertiary flow by (t).

where the mean flow structure next to the patch may be also highly influenced by the patch width as occurs with the growth of horizontal shear layer vortices in high-blockage emergent canopies (Rominger & Nepf, 2011). For the patches of densities $\phi = 0.10$ and $\phi = 0.025$, the CCW tertiary cell also changes in size at lower water depths, expanding in both the vertical and the spanwise directions (Figure 5.14(d-h)). In the less submerged case, $H/h = 2.0$, the CCW tertiary cell extends in the vertical and spanwise directions a length equal to the water depth ($H = 2h$) for all canopy densities, as secondary flows in compound channels (Figures 5.14c, 5.14f and 5.14h) (e.g. Tominaga & Nezu, 1991; Shiono & Knight, 1991; Omran, 2005). The CW (blue) tertiary cell, on the other hand, is not massively affected by changes in density or shallowness. It is confined to the corner of the vegetation patches for $H/h = 3.0$ and slightly grows as water depth is reduced (Figure 5.14(a-h)).

A more general view of the relationship between the strength of the swirling motions in the cross-sectional plane and shallowness has been investigated through the normalised circulation of streamwise vorticity $\epsilon^* = \epsilon/hU_b$. Results are presented in Figure 5.15. Similar to previous results for $H/h = 3.0$ in a range of vegetation densities varying from $\phi = 0.0125$ to $\phi = 0.10$, ϵ^* also increases linearly with increasing density for $H/h = 2.0$. However, for $H/h = 2.0$, the circulation of streamwise vorticity seen for the densest vegetation patch is larger than all less dense canopies. This is in contrast with results for $H/h = 3.0$, where the densest patch of vegetation has an ϵ^* comparable to that of the sparser canopy, $\phi = 0.0125$. However, it is consistent with the observations by Stroh et al. (2016) who showed that a minimum ϵ^* is reached only at the point of transition where the reversal of the secondary circulation direction occurs due to the growth of the emerging tertiary circulation. Once the tertiary pair of cells is established as the new secondary flow, ϵ^* grows as the rotating motions grow. In this case ϵ^* increases with increasing ϕ.

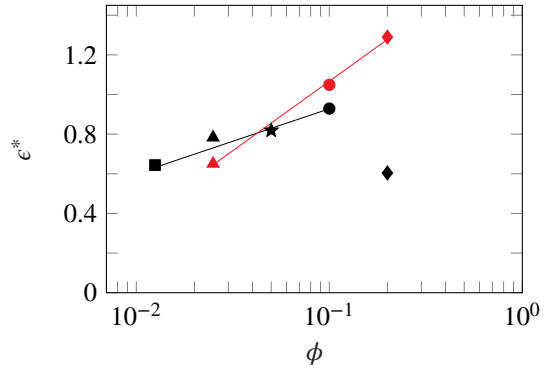


Figure 5.15: Variation of the normalised circulation of streamwise vorticity with shallowness. Black markers represent a submergence condition of $H/h = 3.0$, while red markers correspond to $H/h = 2.0$. Markers as in Table 5.1. The black solid line represents the linear regression for $H/h = 3.0$ ($R^2 = 0.96$). The red solid line represents the linear regression for $H/h = 2.0$ ($R^2 = 0.99$). The streamwise circulation increases in an approximately linear fashion within the range of vegetation densities studied for both shallowness conditions.

5.8 Impact of shallowness - relationship between shear stress and secondary circulation

The vertical shear stress distribution not only changes with the presence of surface heterogeneity but also with changes in water depth. Figures 5.16a and 5.16b show colourmaps of the vertical shear stress for vegetation patches of densities $\phi = 0.10$ and $\phi = 0.20$ at $H/h = 2.5$. Above the canopies, it can be observed that the maximum vertical shear stress $-\overline{u'w'}$ is located slightly away from the LCWI on top of the vegetation patch and it is no longer located at the vegetation corner as in the more submerged canopies (c.f. Figures 5.8d and 5.8f). At the LCWI near the channel bed, the region of negative $-\overline{u'w'}$ becomes bigger and extends in both the vertical and the lateral direction towards the main channel for both canopy densities (comparing colourmaps in Figures 5.16a and 5.16b with Figures 5.8d and 5.8f, respectively). This flow reorganisation can be explained by the relationship between the distribution of the vertical shear stress and the HMPs and LMPs created by the secondary circulation, which dictate the spanwise location of the upward and downward motions (e.g. Barros & Christensen, 2014; Vanderwel & Ganapathisubramani, 2015). Thus, the reversal of the vertical direction of the flow at the LCWI also comes with changes in the spanwise distribution of the vertical Reynolds shear stresses. The upwelling and downwelling movements seen above the two denser vegetation patches at $H/h = 2.5$ are located within regions

of low and high vertical Reynolds shear stress, respectively (Figures 5.16a and 5.16b). This is consistent with observations at $H/h = 3.0$, therefore, the upward flow at the vegetation corner, at $H/h = 2.5$, coincides with a low vertical shear stress.

Furthermore, the transverse distribution of the vertical shear stress above the denser patch is clearly periodic in accordance with the direction of the vertical flow of the secondary circulation, $\overline{w}$ (Colourmaps in Figure 5.16b). However, although the amount of rotating cells seen above the denser canopy array at this lower submergence condition is the same at $H/h = 3.0$, their spanwise extent is more symmetric at $H/h = 2.5$. This may be due to the smaller shear layer thickness at lower water depths, which is believed to be the length scale of the secondary circulations. For the canopy of density $\phi = 0.10$ and $H/h = 2.5$ (Figure 5.16a), there is a small CW rotating cell near the vegetation corner, extending from $y/h \approx 0$ to $y/h \approx 0.66$, and a pair of cells extending from the mid-canopy width to the flume wall, whilst no rotating cells can be clearly identified in the region between $y/h \approx 0.66$ and $y/h \approx 3.4$. This shows that the amount of cells above the canopy and their spanwise distribution at $H/h = 2.5$ differs from observations at $H/h = 3.0$ (c.f. Figure 5.8). In the main channel, the location of HMPs and LMPs is observed above high and low vertical Reynolds shear stress, respectively, which is also consistent with results shown at $H/h = 3.0$ for the two densities, $\phi = 0.10$ and $\phi = 0.20$.

Lateral Reynolds shear stresses are also analysed for changes in shallowness as large coherent structures also develop in the spanwise direction due to shear heterogeneity, contributing to lateral scalar and momentum transport. In shallow flows, one would expect substantial contributions from these coherent structures to lateral mass and momentum exchange (e.g. Truong et al., 2019). However, in a three-dimensional shallow flow, there are at least three mechanisms that contribute to lateral exchange of streamwise momentum, including the advection by the mean depth-averaged velocity due to secondary circulation effects, $\langle\tilde{\tilde{u}}\tilde{\tilde{v}}\rangle_d$, transfer due to the spatial fluctuations in the porous medium (i.e. the canopy patch), $\langle\overline{u}''\overline{v}''\rangle_d$, and exchange due to the action of the lateral Reynolds stress mainly generated by the large coherent structures, but also due to 3D small-scale turbulence, $\langle\overline{u'v'}\rangle_d$ (§5.2.1) (Uijttewaal, 2014).

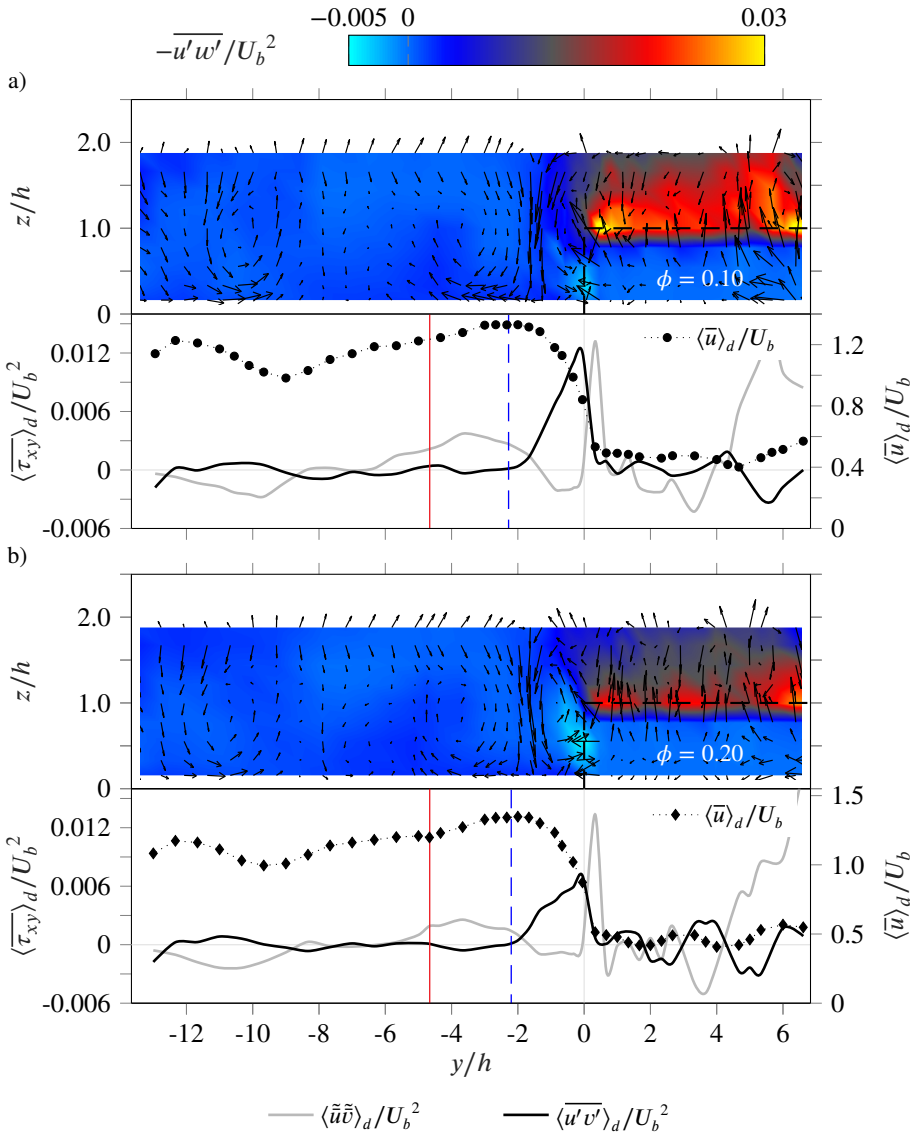


Figure 5.16: Colourmaps of the normalised vertical shear stress, $-\overline{u'w'}/{U_b}^2$, and profiles of the normalised depth-averaged lateral shear stress, $\langle\overline{u'v'}\rangle_d/{U_b}^2$, and dispersive stress due to mean flow fluctuations, $\langle\tilde{\overline{u}}\tilde{\overline{v}}\rangle_d/{U_b}^2$, at $H/h = 2.5$ for densities a) $\phi = 0.10$, b) $\phi = 0.20$. The in-plane secondary circulation is represented by scaled overlying velocity vectors $[\overline{v}, \overline{w}]/0.1U_b$.

The lateral depth-averaged shear Reynolds stress, $\langle\overline{u'v'}\rangle_d$, for canopies at $H/h = 2.5$ is maximum at the canopy edge where there is a large change in drag (Figures 5.16a and 5.16b). The zero-crossings of the lateral Reynolds stress, which are a good estimate of the extent of the lateral shear layer (White & Nepf, 2007) occur close to the LCWI inside the vegetation and in the main channel in the region of downward flow at $y/h \approx 2$ (dashed blue vertical lines in Figures 5.16a and 5.16b).

The lateral dispersive stress due to mean flow fluctuations is negative for the CCW rotating cell next to the canopy and positive for the CW cell next to it, with zero-crossings in the regions of downward and upward flow of the secondary circulation. The dispersive shear stress between $y/h = 0$ and $y/h \approx -2$ contributes to less than 5% to the total lateral shear stress with major contributions given by the lateral Reynolds shear stress. However, further into the main channel and until $y/h \approx -5$ the lateral dispersive shear stress, $\langle \tilde{\bar{u}}\tilde{\bar{v}} \rangle_d$, greatly contributes to the total stress with negligible $\langle \overline{u'v'} \rangle_d$ (Figures 5.16a and 5.16b). The dispersive stress due to porous medium fluctuations are an order of magnitude smaller than the other two stresses and consequently negligible.

Figure 5.17(a-c) shows colourmaps of the vertical Reynolds stress for $H/h = 2.0$. The vertical Reynolds stress is maximum at the top of the canopy and more or less constant along the patch width (except close to the flume wall) independent of vegetation density. This confirms that no secondary circulations due to surface heterogeneity are present above the patch at low water depths. The negative $-\overline{u'w'}$ at the LCWI continues expanding towards the water surface and the main channel and occupies almost the entire cross-sectional area of the CCW rotating cell next to the vegetation patch for $\phi = 0.20$ at $H/h = 2.0$ (Figure 5.17c). However, in the vicinity of the lateral edge of the vegetation patch above the canopy, $-\overline{u'w'}$ attains a positive peak. This vertical Reynolds shear stress distribution resembles that of a compound channel where a negative peak of $-\overline{u'w'}$ has been observed in the main channel below the outflow at the junction and a positive peak on the floodplain (Tominaga & Nezu, 1991). This implies that there is a momentum exchange from the main channel towards the patch of vegetation.

Profiles of lateral Reynolds shear stress at $H/h = 2.0$ shown by black lines in Figure 5.17(a-c) present a peak at the LCWI for all canopy densities. The stress decays to zero at the spanwise location of strong downward flow in the main channel, next to the vegetation patch (dashed blue vertical lines in Figure 5.17(a-c)). This is consistent with observations for the aforementioned deeper flows. In the region between $y/h = 0$ and $y/h = -2$, the dispersive shear stress, $\langle \tilde{\bar{u}}\tilde{\bar{v}} \rangle_d$, is negative for the less dense canopy, $\phi = 0.025$, approximately zero for $\phi = 0.10$ and becomes positive for the densest patch of vegetation, $\phi = 0.20$ (gray profiles in Figure 5.17(a-c)). This shows that the largest lateral shear stresses next to a vegetation patch occur for a dense patch of vegetation at the lower water depth.

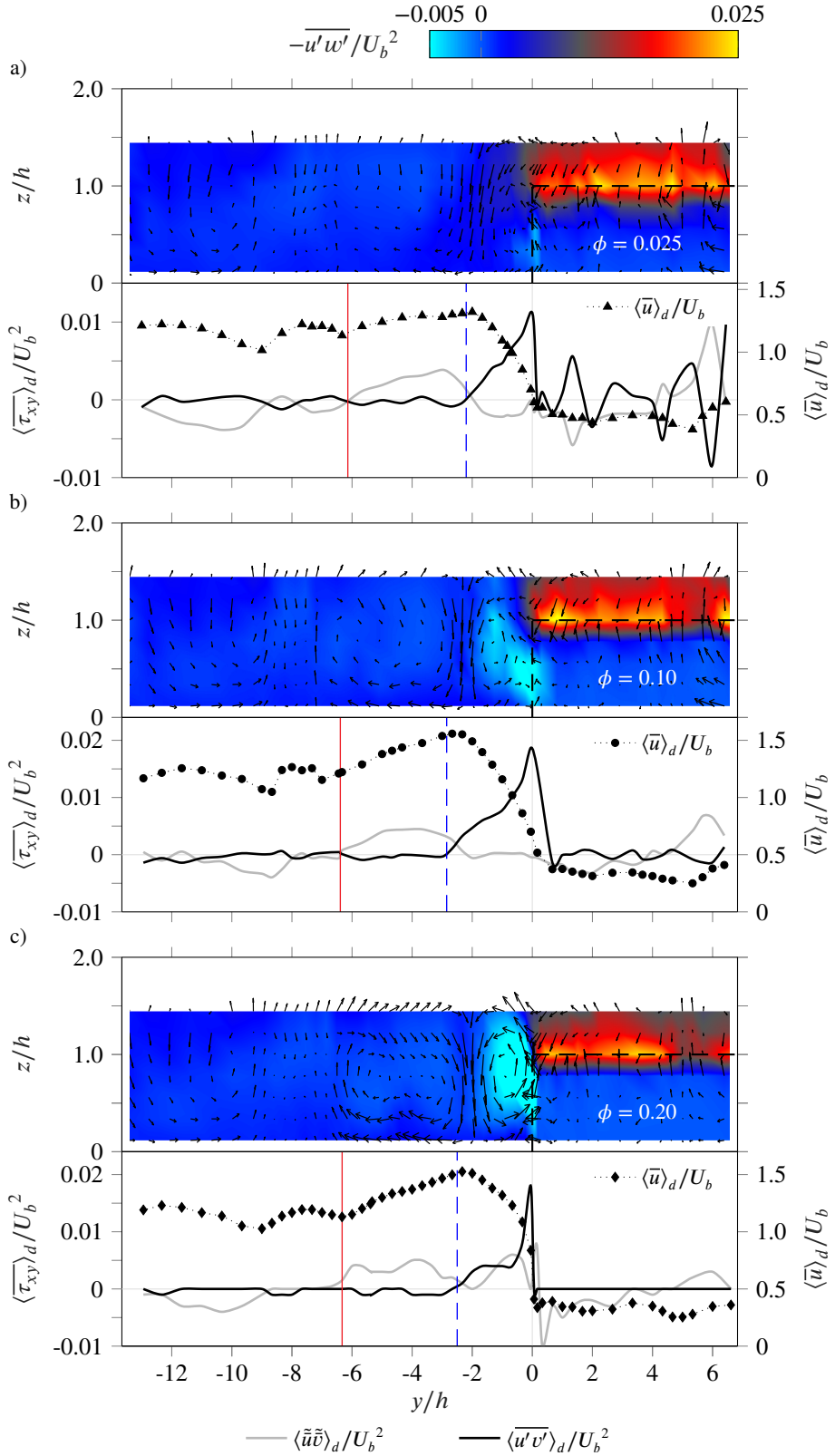


Figure 5.17: Colourmaps of the normalised vertical shear stress, $-\overline{u'w'}/{U_b}^2$, and profiles of the normalised depth-averaged lateral shear stress, $\langle\overline{u'v'}\rangle_d/{U_b}^2$, and dispersive stress due to mean flow fluctuations,$\langle\tilde{\overline{u}}\tilde{\overline{v}}\rangle_d/{U_b}^2$, at $H/h = 2.0$, for densities a) $\phi = 0.025$, b) $\phi = 0.10$, and c) $\phi = 0.20$. The in-plane secondary circulation is represented by scaled overlying velocity vectors $[\overline{v}, \overline{w}]/0.2U_b$.

The depth-averaged dispersive shear stress is positive in the region between $y/h = -2$ and $y/h \approx -6$ for all canopy densities, where there is a CW rotating cell and becomes zero at the y-location of the upward flow.

Interestingly, the location of upward flow in the main channel (close to $y/h \approx -6$ in Figure 5.17(a-c)) coincides with longitudinal sediment streaks formed on the bed with deposited seeding particles, after several hours of experimental runs on an undisturbed flow (Figure 5.18). The curves of gathered particles start at the corner of the canopy leading edge and get farther away from the canopy patch (i.e. in the y-direction) in the main direction of the flow. Their spanwise location is represented by red lines in Figures 5.17a and 5.17b for cases at $H/h = 2.5$ and 5.16(a-c) for partially vegetated channels at $H/h = 2.0$. Although the red lines are located in the region of upward flow for both shallowness conditions, they only coincide with the zero-crossing of $\langle\tilde{\tilde{u}}\tilde{\tilde{v}}\rangle_d$ for cases at $H/h = 2.0$. The lines also become more visible with increasing canopy density. These sediment streaks were not observed for the more submerged cases (i.e. $H/h = 3.0$).

Although there is also an upward flow at the LCWI (at $y/h \approx 0$), sediment streaks were not visibly identified at this spanwise location for any of the shallowness conditions and densities studied. However, for observational purposes only, a patch of vegetation density $\phi = 0.13$ and width B was placed in the channel with an imposed shallowness condition of $H/h = 1.6$. Results from this experiment are illustrated in Figure 5.18(right). In the picture, two streaks are observed, one at approximately 5.8 cm of the LCWI ($y/h \approx 0.3$) and another at 49 cm far from the lateral canopy edge ($y/h \approx 5.4$). Velocity measurements above the sediment streaks showed that both coincide with an upward flow. The streak closer to the vegetation patch, does not seem to be related to the lateral Reynolds stress. Instead, results suggest that it is formed due to the upward flow of the cross-sectional rotating cells. These results are particularly important, not only in the context of vegetation colonisation and morphological changes in rivers, but also for aquatic ecosystem services and should be investigated in future studies.

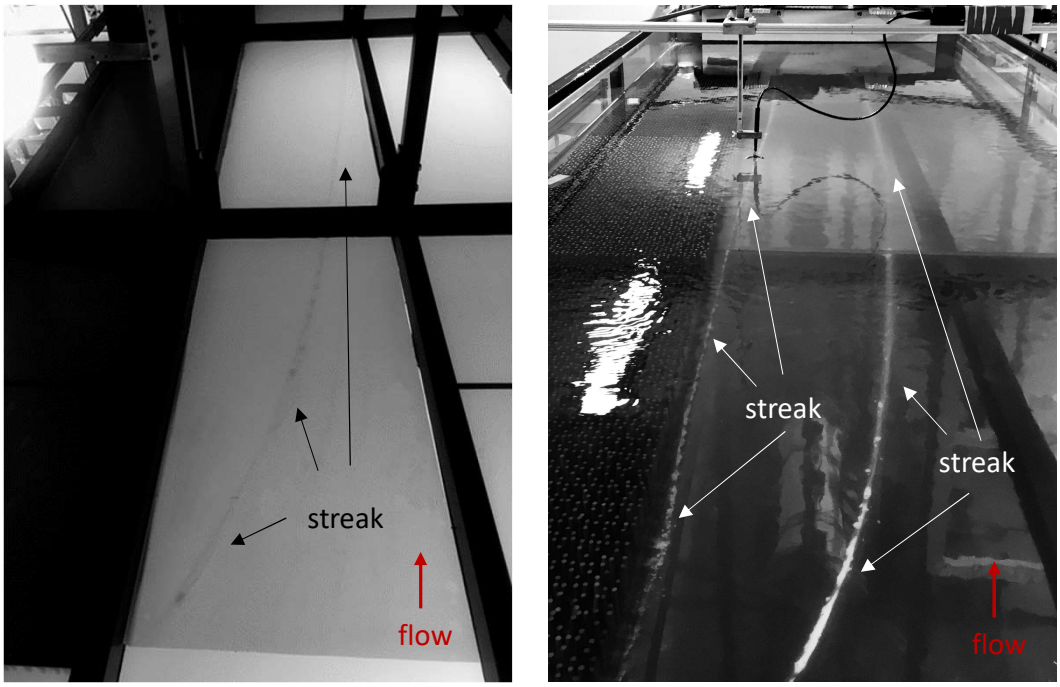


Figure 5.18: Pictures of the longitudinal sediment strikes seen during experiments with a patch of density $\phi = 0.20$ at $H/h = 2.0$ (left picture), and $\phi = 0.13$ at 1.6 (right picture).

5.8.1 Conclusions

Unprecedented measurements of the three-dimensional flow in a partially vegetated channel under changes in vegetation density and shallowness conditions are presented. The predominant effect of the sharp change in drag (in the spanwise direction) due to the presence of a submerged patch of vegetation is the generation of cross-sectional rotating cells travelling in the streamwise direction, which makes the flow highly three-dimensional. The presence of these roll motions were observed for a wide range of canopy densities, $\phi = 0.0125$, 0.025, 0.05, 0.10 and 0.20, and water depths, H, of 2.0, 2.5 and 3.0 times the canopy height, h. The mean streamwise velocity contours become increasingly heterogeneous with predominant upward and downward undulations coinciding with the upwash and downwash of the vertical velocity of the secondary flow as vegetation density and H/h increase. At the highest submergence condition, $H/h = 3.0$, the number of cells observed above the vegetation increases with increasing canopy density, as the width of the secondary cells scales with the vertical mixing layer thickness, which in turn decreases for increasing ϕ. At low water depths, $H/h = 2.0$, the flow above the patch of vegetation recovers uniformity and cross-sectional cells are absent.

An interesting feature of the submerged partially vegetated flow is the strong downwash at the lateral canopy-water interface (LCWI), which differs from observations in other roughness-varying flows (i.e. strip- and ridge-type roughness flows). However, as vegetation density increases, and water depth decreases, there is a change in the direction of this vertical flow due to the growth of a new counter-rotating pair of cells with opposite direction of rotation. This new pair of cross-sectional cells replaces the secondary flow at the lateral canopy-water interface for $\phi = 0.20$ at all shallowness conditions and at $H/h = 2.0$ for all canopy densities. The upward flow at the LCWI for the densest canopy is also present for a dense ($\phi = 0.20$) wider patch, double the initial width, and for a solid *step* change, highlighting the transition from a porous obstruction to an impermeable (solid) obstruction.

Vertical and lateral mixing layers controlling mass and momentum transport develop at the boundaries of all vegetation patches. Both mixing layers are found to scale differently within the canopy and in the outer flow. In the inner-layer, both vertical and lateral streamwise velocity profiles are characterised by an inflection point near the canopy-water interfaces and have a hyperbolic tangent shape. In the outer-layer, the mean velocity distribution resembles a boundary-layer in the vertical direction but takes different shapes in the spanwise direction. However, at $H/h = 2.0$, the vertical distribution of the streamwise velocity within the canopy can be fully described by mixing layer parameters as in fully vegetated flows. The thickness of the vertical and lateral mixing layers decrease with increasing vegetation density, however, reduced water levels lead to thicker (thinner) lateral (vertical) mixing layers.

The overall strength of the secondary motion at the LCWI, evaluated by the circulation of streamwise vorticity ϵ, increases with increasing ϕ. The streamwise counter-rotating circulation of the secondary flow is located within spanwise-alternating 'low momentum pathways' LMPs and 'high momentum pathways' HMPs associated with upward and downward motion, respectively. For the less dense canopies, i.e. $\phi = 0.0125$ and $\phi = 0.025$, HMPs (LMPs) are located above regions of relatively high (low) vertical shear stress. Denser canopies present HMPs over low vertical Reynolds shear stress zones. These results are not altered by changes in water depth.

Lateral advective dispersive stresses (resulting from mean flow fluctuations) are

the main lateral shear stress contributors outside the mixing layer, where the lateral Reynolds shear stress is dominant. The largest lateral shear stress next to the vegetation patch occurs for the densest patch and at the lower water level. An interesting feature observed during the experimental work was the formation of sediment streaks developing from the canopy leading edge and expanding (in the spanwise direction) in the streamwise direction. This feature was associated with upward flows of the vertical velocity of the secondary flow. Results from this parametric study indicate the importance of the three-dimensional flow structure in partially vegetated channels, stressing the key role of the secondary flow in mass and momentum exchange, which should be included in predictive models.

Chapter 6

Turbulent kinetic energy production and transport, and energy spectra

Secondary circulations are investigated in this chapter through the analysis of the imbalance between production, dissipation and advective velocity terms within the turbulent kinetic energy (TKE) equation in the cross-sectional plane. Inspection of the turbulent kinetic energy budget reveals that TKE transport terms contribute as much as TKE production terms to the local imbalance of energy. The imprint of the secondary circulation on the nature of turbulence in the streamwise direction is investigated by looking at the 1D energy spectra of the streamwise turbulent velocity fluctuations. The 1D energy spectra demonstrates that there is an interplay between turbulent fluctuations and secondary circulation. The latter manifests as an additional burst of energy, concentrated in the vertical direction, far from the bed or the top of the canopy.

6.1 Introduction

Velocity measurements in the cross-sectional plane of the dense canopy, $\phi = 0.10$, at the submergence condition of $H/h = 3.0$ are used to examine the turbulent kinetic energy budget to identify the TKE terms that significantly contribute to the energy balance and to infer the direction of rotation of the secondary cells

above the patch of vegetation. Furthermore, 1D energy streamwise spectrograms are analysed for all canopy densities at $H/h = 3.0$, and for $\phi = 0.20$ at the three different shallowness conditions of $H/h = 3.0$, $H/h = 2.5$ and $H/h = 2.0$ to explore the impact of the secondary circulation on turbulence in the streamwise direction.

6.1.1 Energy balance within the secondary circulation

The rotational sense of the secondary cells over ridge-type roughness flows is opposite to that seen over strip-type roughness flows (e.g. Wang & Cheng, 2006; Anderson et al., 2015; Hwang & Lee, 2018) but they both differ from observations on partially vegetated flows as the one studied here. The Reynolds-averaged turbulent kinetic energy (TKE) equation has been used to investigate the physical mechanisms that drive the secondary circulation on ridge- and strip-type roughness flows (Hinze, 1967; Anderson et al., 2015; Hwang & Lee, 2018). Although analysing all terms in the TKE equation is not possible with the measurements taken in the present partially vegetated flows, it is worth investigating the behaviour of key TKE terms and comparing the results with those reported for strip- and ridge-type roughness flows. The Reynolds-averaged (i.e., only time-averaged and no subsequent in-canopy or depth average used in the previous chapters) TKE transport equation is,

$$\frac{\partial \mathcal{K}}{\partial t} + \overline{u_j}\frac{\partial \mathcal{K}}{\partial x_j} = -\frac{\partial}{\partial x_j}\frac{\overline{pu_j'}}{\rho} + 2\nu\frac{\partial \overline{s_{ij}u_i'}}{\partial x_j} - \underbrace{\frac{\partial}{\partial x_j}\frac{\overline{u_i'u_j'u_j'}}{2}}_{\mathcal{T}} - \underbrace{\overline{u_i'u_j'}\frac{\partial \overline{u_i}}{\partial x_j}}_{\mathcal{P}} - \varepsilon \tag{6.1}$$

where $\mathcal{K}$ is the turbulent kinetic energy, ρ is the water density, p is pressure and ν is the kinematic viscosity. The second term on the left-hand-side (LHS) is the advection of TKE by the mean flow. Terms on the right-hand-side (RHS) correspond to the transport of TKE due to pressure work, viscous stresses, and turbulent fluctuations $\mathcal{T}$, TKE production $\mathcal{P}$, and TKE dissipation $\varepsilon \equiv 2\nu\overline{s_{ij}s_{ij}}$, respectively; $s_{ij} = (\partial\overline{u_i'}/\partial x_j + \partial\overline{u_j'}/\partial x_i)/2$ is the rate of strain tensor. Viscous stresses were found to be significant only very close to the bed/wall in flows over alternating spanwise rough-smooth strips (Hinze, 1967; Anderson et al., 2015) but more relevant over ridge-type roughness flows. Transport due to turbulent fluctuations plays a key role over spanwise heterogeneous surfaces with elevated

regions (Hwang & Lee, 2018) but are less significant on strip-type roughness flows (Anderson et al., 2015) presumably due to the absence of change in surface elevation.

Assuming a steady and uniform flow in the x-direction ($\partial(\cdot)/\partial t = 0$ and $\partial(\cdot)/\partial x = 0$), Anderson et al. (2015) (for a strip-type roughness flow) and Hwang & Lee (2018) (for a ridge-type roughness flow) reduced equation (6.1) to key TKE terms as follows,

$$\underbrace{\overline{v}\frac{\partial \mathcal{K}}{\partial y}}_{\mathcal{C}_y} + \underbrace{\overline{w}\frac{\partial \mathcal{K}}{\partial z}}_{\mathcal{C}_z} \approx \underbrace{-\frac{1}{2}\left(\frac{\partial u'u'v'}{\partial y} + \frac{\partial v'v'v'}{\partial y} + \frac{\partial w'w'v'}{\partial y} + \frac{\partial u'u'w'}{\partial z} + \frac{\partial v'v'w'}{\partial z} + \frac{\partial w'w'w'}{\partial z}\right)}_{\mathcal{T}} - \underbrace{\overline{u'v'}\frac{\partial \overline{u}}{\partial y}}_{\mathcal{P}_{u'v'}} - \underbrace{\overline{u'w'}\frac{\partial \overline{u}}{\partial z}}_{\mathcal{P}_{u'w'}} - \underbrace{\overline{v'v'}\frac{\partial \overline{v}}{\partial y}}_{\mathcal{P}_{v'v'}} - \underbrace{\overline{w'w'}\frac{\partial \overline{w}}{\partial z}}_{\mathcal{P}_{w'w'}} - \varepsilon \tag{6.2}$$

For flows over spanwise heterogeneous roughness, terms on the RHS in (6.2) are locally imbalanced on the cross-sectional plane, but are expected to achieve balance with the TKE advection terms on the LHS, which represent the mean streamwise circulation of the secondary flow (Hinze, 1967). In (6.2), the total production term is the sum of all production terms, i.e. $\mathcal{P} = \mathcal{P}_{u'v'} + \mathcal{P}_{u'w'} + \mathcal{P}_{v'v'} + \mathcal{P}_{w'w'}$. These production terms for $\phi = 0.10$ and $H/h = 3.0$ are shown in Figure 6.1(a-d). The magnitude of $\mathcal{P}_{u'v'}$ and $\mathcal{P}_{u'w'}$ is more significant compared to the magnitude of the other production terms. The former dominates the total production at the LCWI (Figure 6.1a), while the latter is dominant at the top of the canopy patch and significant above the vegetation (Figure 6.1b). Variations of $\mathcal{P}_{u'w'}$ at the top of the canopy reflect the location of HMPs and LMPs previously discussed in §5.5. In Figure 6.1b at $y/H \approx 1$, $\mathcal{P}_{u'w'}$ is higher at $z/H \approx 0.6$ than at the top of the canopy $z/H \approx 0.3$. The spanwise location of this local peak corresponds to an upward flow. Patterns of $\mathcal{P}_{u'w'}$ agree well with the observations of Anderson et al. (2015) and Hwang & Lee (2018) over strip- and ridge-type roughness flows, respectively. The magnitude of $\mathcal{P}_{v'v'}$ and $\mathcal{P}_{w'w'}$ is roughly eight times less than that of the other two production terms. The occurrence of the large magnitude of $\mathcal{P}_{v'v'}$ at the corner of the canopy, indicates that the instantaneous spanwise velocity is strongly deflected due to the elevation represented by the canopy height, leading to enhanced spanwise fluctuations at

the vegetation corner. At the LCWI, the enhanced production is mainly due to the gradient $\partial\overline{u}/\partial y$.

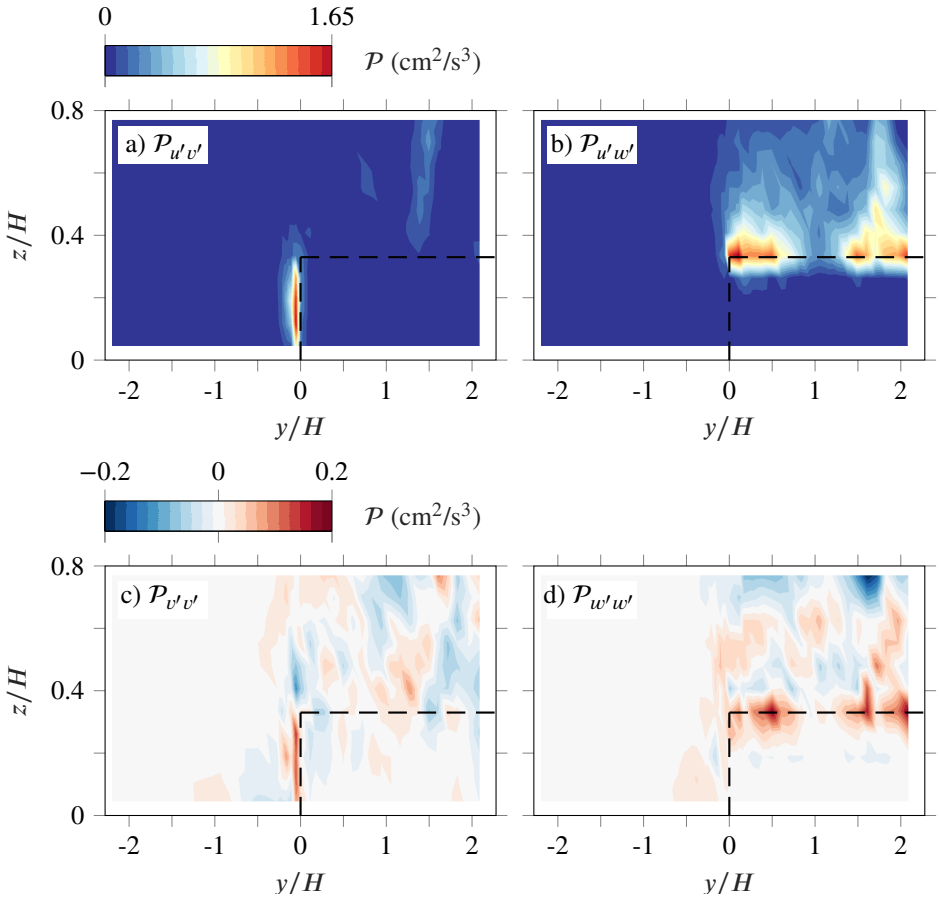


Figure 6.1: Colourmaps of the production terms a) $P_{u'v'}$, b) $P_{u'w'}$, c) $P_{v'v'}$ and d) $P_{w'w'}$ for the patch of density $\phi = 0.10$ and $H/h = 3.0$. Production terms $P_{u'v'}$ and $P_{u'w'}$ are dominant and larger at the canopy patch boundaries. Note that colourbars are different for colourmaps in the first row and the second row.

The sum of all the production terms is illustrated in Figure 6.2a and shows the dominance of the production terms $\mathcal{P}_{u'v'}$ and $\mathcal{P}_{u'w'}$. Anderson et al. (2015) and Hwang & Lee (2018) stressed the importance of the role of the spanwise gradients of shear stresses on the circulation of secondary cells, which were interpreted as Prandtl's secondary flows of the second kind. The similarity of the behaviour of the spanwise gradients of shear stresses in the present study with those reported by Anderson et al. (2015) and Hwang & Lee (2018) support this interpretation. Furthermore, the sum of the transport terms is shown in Figure 6.2b. It is evident that the turbulent transport term $\mathcal{T}$ significantly contributes to the local imbalance of TKE, not only close to the top of the vegetation but also above it. This is in agreement with the findings of Hwang & Lee (2018) who reported

relatively large values of $\mathcal{T}$ up to $z/\delta = 0.6$. Note that in open-channel flows the boundary layer thickness δ is approximately equal to the water depth H. The sum of the turbulent transport and production terms is shown in Figure 6.2c and reflects the significant contributions of both, with $\mathcal{P}$ being more relevant at the patch boundaries and $\mathcal{T}$ away from them. However, it is important to highlight the fact that $\mathcal{T} > 0$ close to the LCWI (from $y/H \approx -0.2$ to $y/H \approx -0.5$) where a strong downward flow is observed in partially vegetated flows. This differs from results over ridge-type roughness flows where $\mathcal{T} < 0$ at the change in elevation where an upward flow has been reported (Hwang & Lee, 2018).

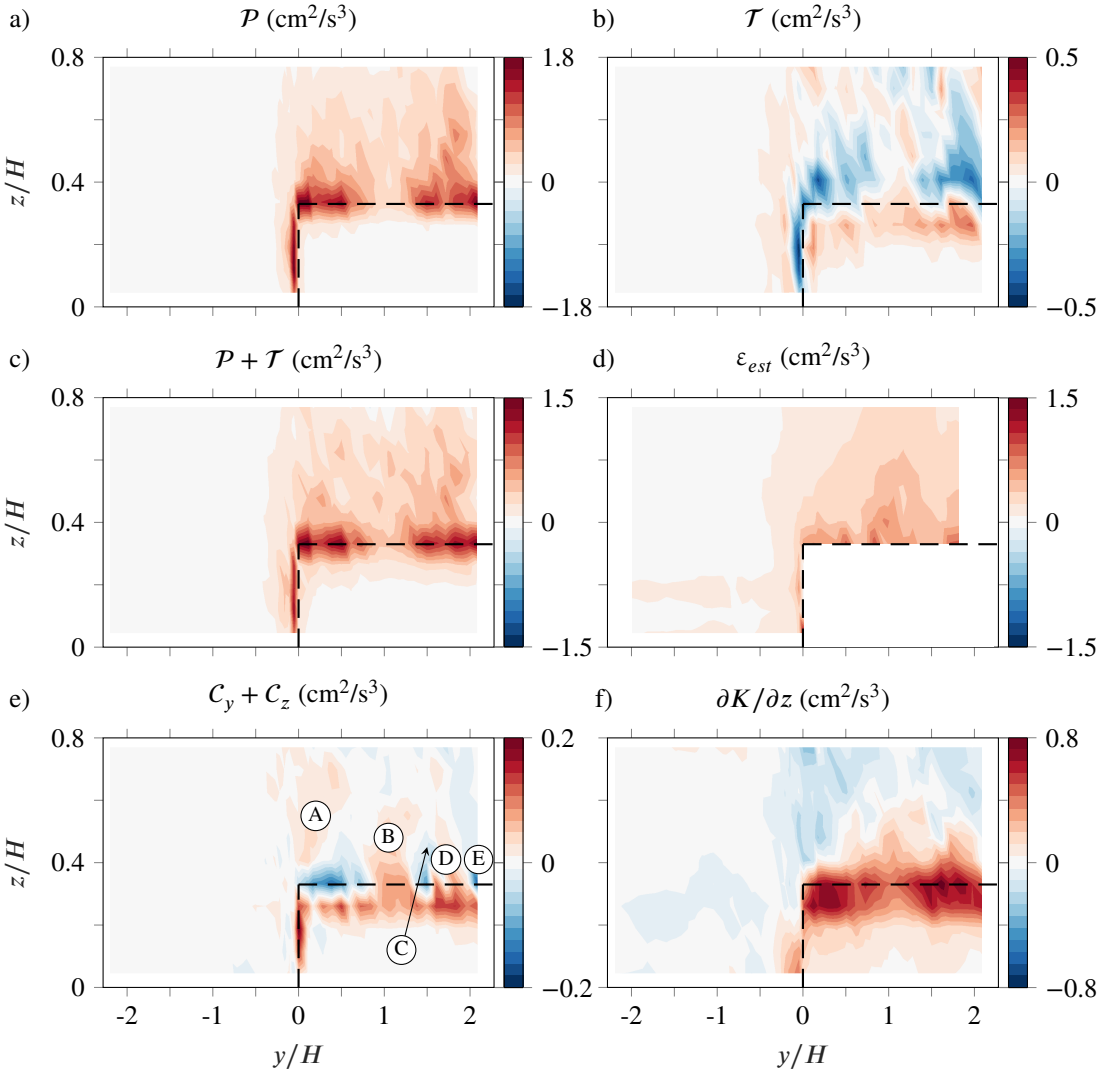


Figure 6.2: Colourmaps of TKE transport equation terms for a patch of density $\phi = 0.10$ and $H/h = 3.0$: a) $\mathcal{P}$, b) $\mathcal{C}_y + \mathcal{C}_z$, c) $\mathcal{T}$, d) $P + T$ and e) $-\varepsilon_{est}$; and f) the vertical gradient of TKE.

The TKE dissipation term ε can be severely underestimated if calculated with the

measurements taken in the partially vegetated flow due to the spatial resolution of the measurements and the lack of measurements in the streamwise direction (e.g. Xu & Chen, 2013; D. Wangsawijaya et al., 2019). However, ε can be also estimated assuming homogeneous isotropic turbulence. Thus, ε can be calculated from the velocity gradient (Wang et al., 2021)

$$\varepsilon \approx 15\nu \overline{\left(\frac{\partial u'}{\partial x}\right)^2} \tag{6.3}$$

The spatial information required for (6.3) can be retrieved using time-series, assuming Taylor's frozen flow hypothesis such that,

$$\varepsilon_{est} \approx \frac{15\nu}{\overline{u}^2} \overline{\left(\frac{\partial u'}{\partial t}\right)^2} \tag{6.4}$$

Figure 6.2d shows the estimated dissipation of TKE, ε_{est}. Although the magnitude of ε_{est} is more or less the same as $\mathcal{P}+\mathcal{T}$, it should be noted that (6.4) only holds for homogeneous isotropic turbulence, which does not necessarily apply to the flow investigated here; however it is a good approximation which gives an overall idea of the distribution of ε. The sum of the TKE advection terms $\mathcal{C}_y+\mathcal{C}_y$ in (6.2) is presented in Figure 6.2e. It is positive in the regions marked by (A), (B) and (D). Above the vegetation and near the LCWI, in region (A), positive $\mathcal{C}_y+\mathcal{C}_z$ ($\mathcal{P}+\mathcal{T} > \varepsilon_{est}$) can be seen. If the mean spanwise velocity is approximately zero at that point, $\mathcal{C}_z = \overline{w}(\partial\mathcal{K}/\partial z) > 0$. Since $(\partial\mathcal{K}/\partial z) < 0$ in (A) (c.f. Figure 6.2f), the vertical velocity $\overline{w}$ should also be negative; thus a downward flow may be observed in (A). In (B) and (D), the sum of the advection terms is also positive indicating that the production and transport terms dominate over the dissipation term. If $\overline{v} \approx 0$ in these two regions, the value of $(\partial\mathcal{K}/\partial z)$ helps determining the direction of the vertical flow. As $(\partial\mathcal{K}/\partial z) > 0$ (Figure 6.2f), an upward flow is expected to occur at regions (B) and (D). Similarly, in regions (C) and (E), negative $\mathcal{C}_y+\mathcal{C}_z$ ($\mathcal{P}+\mathcal{T} < \varepsilon$) is observed. There, the vertical rate of change of $\mathcal{K}$ is positive; hence, if $\overline{v} \approx 0$ is assumed, these two regions should be identified with a downward flow. These predictions of upward and downward flow for regions A to E coincide with experimental observations illustrated by velocity vectors in Figure 5.1d.

Moreover, the transport of TKE due to viscous stresses may be significant in partially vegetated flows as found over ridge-type roughness flows by Hwang & Lee (2018). In their study, the viscous diffusion term was of the same order of magnitude as the transport term but the former was confined close to the wall. Unfortunately, the viscous diffusion term could not be accurately calculated with the spatial resolution of the velocity measurements taken for the present study. Furthermore, the transport of TKE due to pressure fluctuations may also be important due to the porous nature of the vegetation patch, although it is of lesser importance over ridge-type roughness flows (Hwang & Lee, 2018). The analysis of these two terms remains unexplored and worthy of further investigation.

6.2 1D streamwise turbulence energy spectra

Energy spectrograms constructed from ADV three-dimensional point velocity measurements are used to explore the length scale distribution of turbulent energy (u variance) under the imposed porous obstruction in the channel. The 1D power spectral density of the streamwise turbulent velocity fluctuation $\Phi_{u'u'}$ in the longitudinal direction is defined as,

$$\overline{u'u'} = \int_0^\infty \Phi_{u'u'} d(k_x) \tag{6.5}$$

where $k_x \equiv 2\pi/\lambda_x$ is the streamwise wavenumber and $\lambda_x \equiv \overline{u}(y,z)/f_s$ is the streamwise wavelength; f_s is the sampling frequency (= 25 Hz), and $\overline{u}(y,z)$ is the local mean velocity at a specific spanwise-vertical measurement point. Taylor's frozen flow hypothesis is used to estimate spatial turbulence characteristics from single-point time-series, assuming $\overline{u}(y,z)$ as the convection velocity U_c, thus, $\Delta x = -U_c \Delta t \approx \overline{u}\Delta t$. The accuracy of Taylor's hypothesis on projected streamwise distances has not been investigated in vegetated flows. However, Dennis & Nickels (2008) confirmed the accuracy of the hypothesis for projected distances up to 6δ on turbulent boundary layers, which are in the range of observations on partially vegetated flows (e.g. Ikeda & Kanazawa, 1996; White & Nepf, 2007). Furthermore, although distortions may arise from the use of Taylor's hypothesis when passing from frequency to wavenumber, as in turbulent boundary layer flows, it is a useful method to provide a picture of the energy distribution at different scales and to infer the scaling of large-scale structures.

Figure 6.3(a-d) shows the normalised premultiplied energy spectra of the streamwise velocity fluctuations and the normalised turbulence profiles for the canopy density $\phi = 0.10$ and $H/h = 3.0$, at different spanwise locations. In the main channel, at $y/H = -0.5$ (Figure 6.3a), the peak in turbulence is located close to the smooth bed due to the presence of near-bed streaks over smooth surfaces

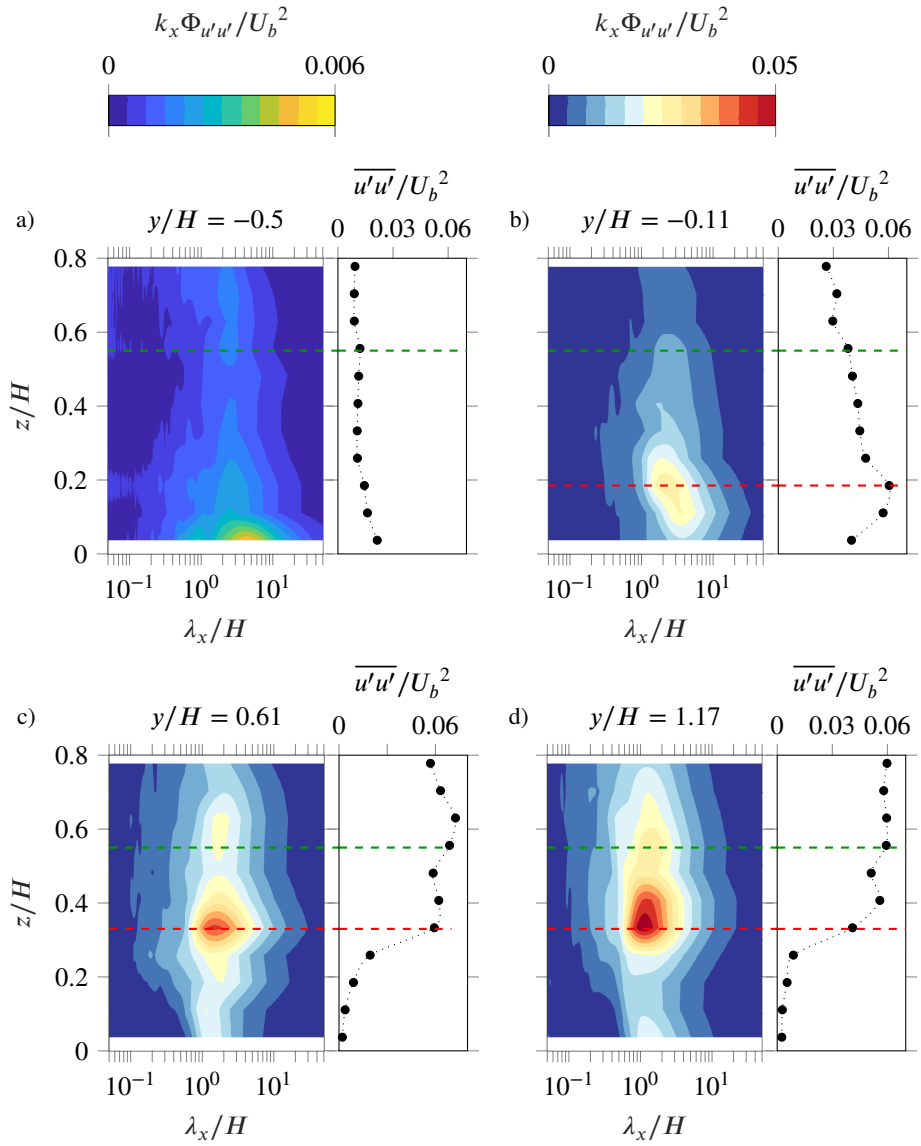


Figure 6.3: Premultiplied streamwise energy spectrograms for a canopy patch of $\phi = 0.10$ and $H/h = 3.0$ in the main channel at a) $y/H = -0.5$ and b) $y/H = -0.11$; and within the vegetation at c) $y/H = 0.61$ and $y/H = 1.17$. Turbulence intensity profiles are presented next to the spectrograms. The red dashed lines mark the height at which maximum energy is observed. In c) and d), the red dashed line also coincides with the top of the canopy. The green line represents a point of large energy level above the canopy, at $z/H = 0.55$. Note that the colorbar for a) is different from that of (b-d)

(e.g. Medjnoun et al., 2018). Closer to the vegetation patch, at $y/H = -0.11$ (Figure 6.3b), the peak is an order of magnitude larger than that at $y/H = -0.5$. However, the peak is no longer located near the bed but at $z/H \approx 0.18$, presumably due to the effect of the secondary circulation on the streamwise velocity structure. Above the canopy, the peak of $k_x\Phi_{u'u'}$ is located at the top of the vegetation patch (indicated by a red dashed line in Figures 6.4c and 6.4d), and it is larger well inside the patch than near the lateral canopy-water interface (LCWI) (comparing Figures 6.4c and 6.4d). The length scale of the energetic peak outside the vegetation is larger than the one within the vegetation, being $\lambda_x \approx 4$ and $\lambda_x \approx 2$, respectively. At $z/H \approx 0.55$ (the green dashed line in Figure 6.4(a-d)), a large energy-containing region also appears, which is more or less constant in the vertical location within the canopy and in the main channel. The quantity of energy contained within this region is larger in the vegetated zone than in the main channel, and it is presumed to be related to the secondary flows formed.

Energy spectrograms for vegetation densities $\phi = 0.0125$, $\phi = 0.025$, $\phi = 0.05$, $\phi = 0.20$ and the *step*, and for the shallowness condition of $H/h = 3.0$ are shown in Figure 6.4. The figures show spectrograms at the measurement location closest to $y = B/2$ (first row) and at approximately one-quarter of the canopy width measured from the LCWI towards the main channel ($y = -B/4$) (second row). Comparison of the spectra within the vegetation patch (first row) across different canopy densities indicates that in the region close to the top of the canopy (i.e. at $z/H = 0.33$) the flow becomes more energetic with increasing canopy density. Interestingly, this point of maximum energy has a wavelength of $\lambda_x/H \approx 2$ for all canopy densities. The densest vegetation patch starts taking the form of the *step* case. However, the energy content of the smooth *step* is an order of magnitude smaller than that over the densest canopy, $\phi = 0.20$. For the canopy densities $\phi = 0.025$ and $\phi = 0.05$ a local 'upper' peak at $z/H \approx 0.63$ and $z/H \approx 0.55$, respectively, can be observed (indicated by a black '+' sign in Figure 6.4), which does not seem to be present in the other cases. Furthermore, the 'upper' peak appears at roughly the same streamwise wavelength at which the dominant 'lower' (at the canopy top) peak appears. This suggests that at intermediate canopy densities, the porous canopy allows a streamwise meandering mode both at the edge of the canopy as well as slightly above the canopy. When ϕ is too small, the top region appears less 'constrained' to form another meandering mode, and for very large ϕ, like in the step, the flow is not constrained in forming an upper meandering mode.

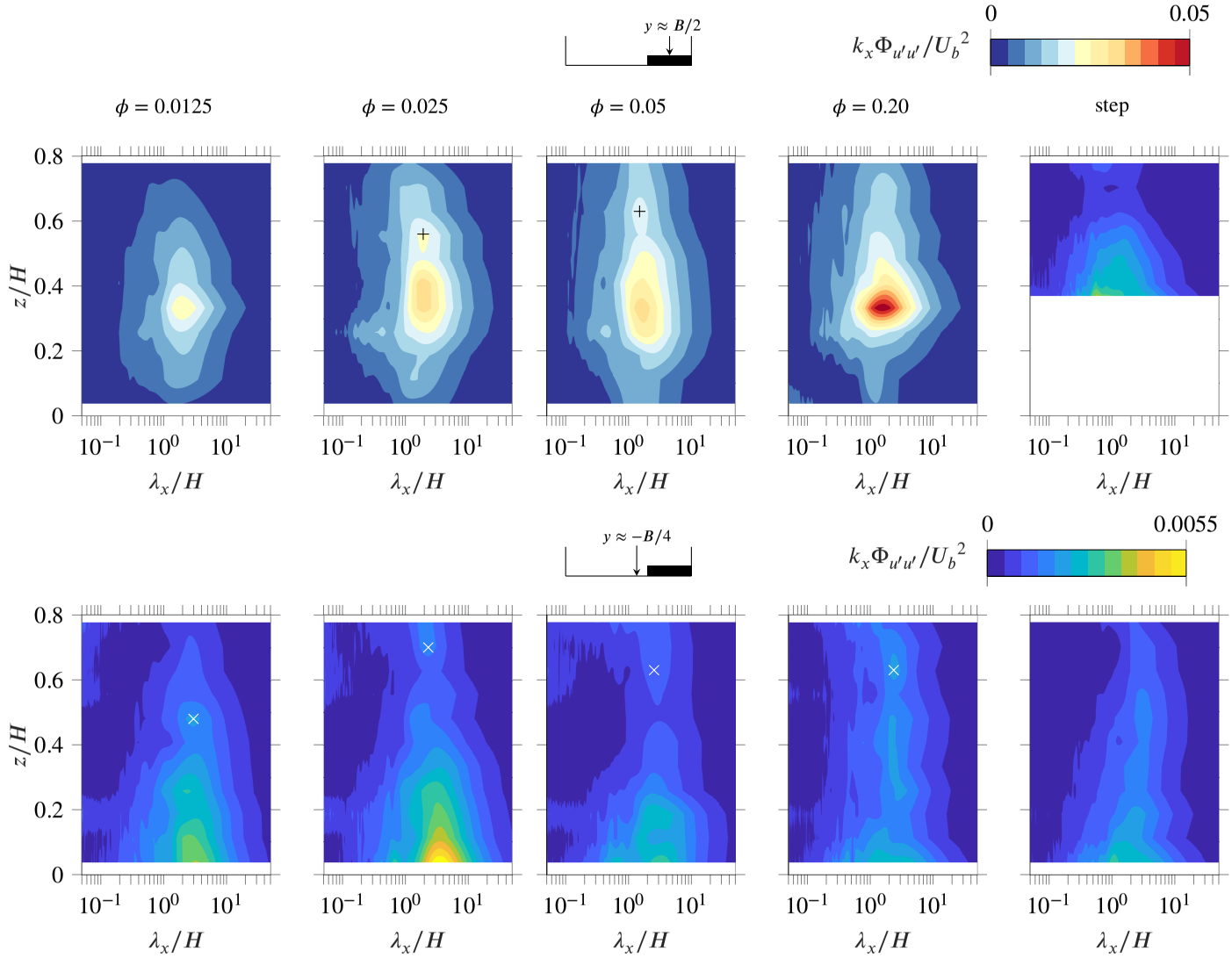


Figure 6.4: Premultiplied 1D streamwise energy spectra $k\Phi_{u'u'}/{U_b}^2$ as a function of streamwise wavelength λ_x and vertical location z of all canopy densities (in columns) at $H/h = 3.0$. Cases on the first row are spectrograms at the centre of the patch width (i.e. $y = B/2$). The second row illustrates spectrograms in the main channel, next to the vegetation patch at $y = -B/4$. Note that the colorbar of the *step* in the first row corresponds to the colorbar of the second row for practical purposes.

Next to the vegetation patch (second row of Figure 6.4), the peak of energy is concentrated near the smooth bed, representing the large coherent structures developed due to the differential roughness between the vegetated and non-vegetated regions. Note that these structures change in size and strength when canopy density is varied, therefore, the peak is larger for the canopy density $\phi = 0.025$ at that particular spanwise location. Furthermore, this y-location approximately coincides with the centre of the secondary cell of the sparse patch, $\phi = 0.025$, as shown by the swirl strength in Figure 5.6b. The wavelength where the maximum $k_x\Phi_{u'u'}$ is located slightly increases or is approximately constant with increasing canopy density for $\phi = 0.0125$, $\phi = 0.025$ and $\phi = 0.05$ being $\lambda_x/H \approx 3.2$, $\lambda_x/H \approx 3.6$ and $\lambda_x/H \approx 3.6$, respectively (Figure 6.4 (second row)). Interestingly, the point of maximum energy for both the densest canopy and the *step* have a wavelength of $\lambda_x/H \approx 1.6$. Far away from the bed, in the vertical direction, a local peak is also observed (marked with a white 'x' in Figure 6.4 (second row)). These additional energetic regions are presumed to be related to secondary circulation effects. As vegetation increases, this additional region of energy is pushed outwards from $z/H \approx 0.48$ to $z/H \approx 0.63$.

Spectrograms for the densest canopy patch, $\phi = 0.20$, at the three different submergence conditions, i.e. $H/h = 3.0$, $H/h = 2.5$ and $H/h = 2.0$, are illustrated in Figure 6.5(a-c). The most energetic region is located at the top of the vegetation. The peak of maximum energy decreases in magnitude and wavelength as water depth is reduced. The wavelengths of the peak of energy are $\lambda/h \approx 5$ ($=\lambda/H \approx 1.6$), $\lambda/h \approx 3$ ($=\lambda/H \approx 1.2$) and $\lambda/h \approx 2$ ($=\lambda/H \approx 1$) for decreasing H/h. This trend is directly linked to the characteristics of the large coherent structures developed due to the vertical differential roughness between the vegetated and non-vegetated regions, the growth of which is restricted at lower water depths. Furthermore, the energy inside the vegetation (i.e. for $z/h < 1$) decreases as water depth decreases. For the $H/h = 3.0$ case (Figure 6.5a), a strong additional energetic site can be observed near the bed at wavelengths ranging from $\lambda_x/h \approx 0.05$ to $\lambda_x/h \approx 0.1$, which corresponds to small scale turbulence close to the bed and in proximity to the LCWI.

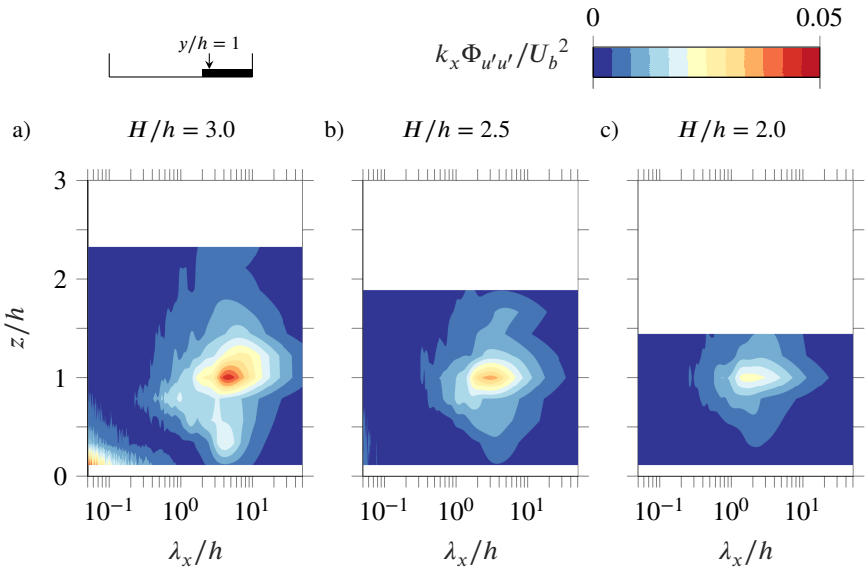


Figure 6.5: Premultiplied 1D streamwise energy spectra $k_x\Phi_{u'u'}/U_b{}^2$ as a function of streamwise wavelength λ_x and vertical location z for a dense canopy, $\phi = 0.20$, at a) $H/h = 3.0$, b) $H/h = 2.5$, and c) $H/h = 2.0$.

6.3 Conclusions

The origin of the rotation sense of the secondary circulation was analysed using the Reynolds-averaged TKE transport equation. It was shown that the local imbalance of TKE turbulent transport, production and dissipation resulting from the spanwise heterogeneity caused by the patch of vegetation is consistent with the TKE advective velocities on the cross-sectional plane. Consequently, it can be said that the secondary flow generated in partially vegetated channels is Prandtl's secondary flow of the second kind, and it is consistent with the anisotropy of turbulence observed. The distinctive strong downward flow observed at the LCWI in partially vegetated flows, which differs from the direction of the vertical flow at the change in roughness on strip- and ridge-type roughness flows, is mainly attributed to the significant contribution of the TKE transport due to turbulent fluctuations to the energy budget.

The 1D streamwise energy spectra revealed that energy peak is located close to the smooth bed in the main channel and at the top of the canopy within the vegetated region. In the vegetated zone, the peak of energy becomes larger with increasing vegetation density and at higher submergence conditions. An additional local peak of energy was also observed far from the bed and the canopy

top. Above the canopy, this additional peak becomes more prominent for $\phi = 0.025$ and $\phi = 0.025$, suggesting a streamwise meandering mode. The streamwise wavelength of this additional periodicity in the flow is in the range $\lambda_x \approx 1.9 - 2.5H$. Results from the 1D streamwise energy spectra could be further supported by 2D energy spectra, co-spectra and/or 2-point correlation coefficient, which can be analysed in future investigations for which accurate measurements in the streamwise direction are available.

Chapter 7

Modelling spanwise depth-averaged velocity distributions in submerged partially vegetated channels[†]

Abstract

Accurate estimation of flow conveyance in natural rivers, commonly characterised by a main channel and a riparian vegetation zone, is essential for river restoration and management, and flood related studies. The presence of vegetation significantly modifies the lateral distribution of streamwise velocities by augmenting the velocity difference between the vegetated and non-vegetated regions, creating large shear layers at the vegetation boundaries and strong secondary circulations in the cross-sectional plane. The velocity distribution, in turn, affects the discharge and consequently the river conveyance. Here, physical and numerical simulations of open-channel flow over a patchily vegetated bed are investigated. The detailed and systematic three-component velocity measurements, taken in the cross-sectional plane, show the dominant effect of the vegetation on local shear stress distributions, which in turn, impact the mean flow structure, and

[†]Results from this chapter have been submitted for publication in the *Journal of Hydraulic Engineering.*

consequently momentum exchange. The quasi-2D Shiono and Knight method (SKM), based on the depth-mean momentum equation, was employed to model the lateral distribution of the depth-averaged streamwise velocity in a partially vegetated channel. The combined physical and numerical approach gives an insight into the flow structure and provides a basis for modelling flow conveyance, as the SKM successfully predicts streamwise velocity distributions.

7.1 Introduction

Although efforts have been made towards predicting depth-averaged velocities in channels with emergent vegetation, it is unknown if velocities in submerged patchily vegetated channels can be successfully predicted by 'simple' two dimensional models, as the flow in such systems is highly three-dimensional (see §4). This chapter investigates the capabilities of the Shiono-knight model (SKM) to accurately predict depth-averaged streamwise velocities in submerged partially vegetated channels for various canopy densities. A physical model was used for the validation of the numerical model (i.e. SKM), which allowed for conclusions on the feasibility of predicting lateral velocity distributions in submerged patchy vegetation.

7.2 Physical modelling

7.2.1 Velocity distribution and Reynolds shear stress

The distribution of the normalised streamwise velocity in the cross-plane $\overline{u}/U_b$ is represented by contour maps overlayed with the secondary circulation (depicted by in-plane $[\overline{v}, \overline{w}]$ vectors), for canopies of densities $\phi = 0.0125$, $\phi = 0.05$ and $\phi = 0.10$, in Figure 7.1(a-c). Contour lines of streamwise velocity present large undulations, that extend almost to the water surface, compared to the flat contours seen over smooth beds (c.f. Tominaga & Nezu, 1991). These undulations are indicative of cross-plane roll motions which cause the contours to bulge upwards (downwards) in regions of upward (downward) flow (Figure 7.1(a-c)). The effect of increasing vegetation density leads to increasingly marked rising and falling forms of the streamwise velocity contours. The relatively smooth contours seen above the vegetation patch for $\phi = 0.0125$ and $\phi = 0.05$ bulge upwards at $\approx B/2$ for $\phi = 0.10$, indicating the presence of an additional cross-sectional secondary cell (Figure 7.1(a-c)). This occurs as the size of the secondary circulation above

the canopy is limited, determined by their length scale which is comparable to the vertical mixing layer thickness (§4.4). Near the lateral canopy-water interface, there is a relatively strong downward flow for all canopy densities (Figure 7.1(a-c)). In this region, momentum is transported towards the canopy and the main channel bed. This downward flow is indicative of the vegetation patch characteristics and the submergence conditions here studied, as illustrated in §4.

The cross-flow cells next to the wall in the main channel, for $\phi = 0.0125$, are characteristic of corner-induced secondary flow (e.g. Rodríguez & García, 2008). One of the cells of the secondary flow pair is located below the free-surface and

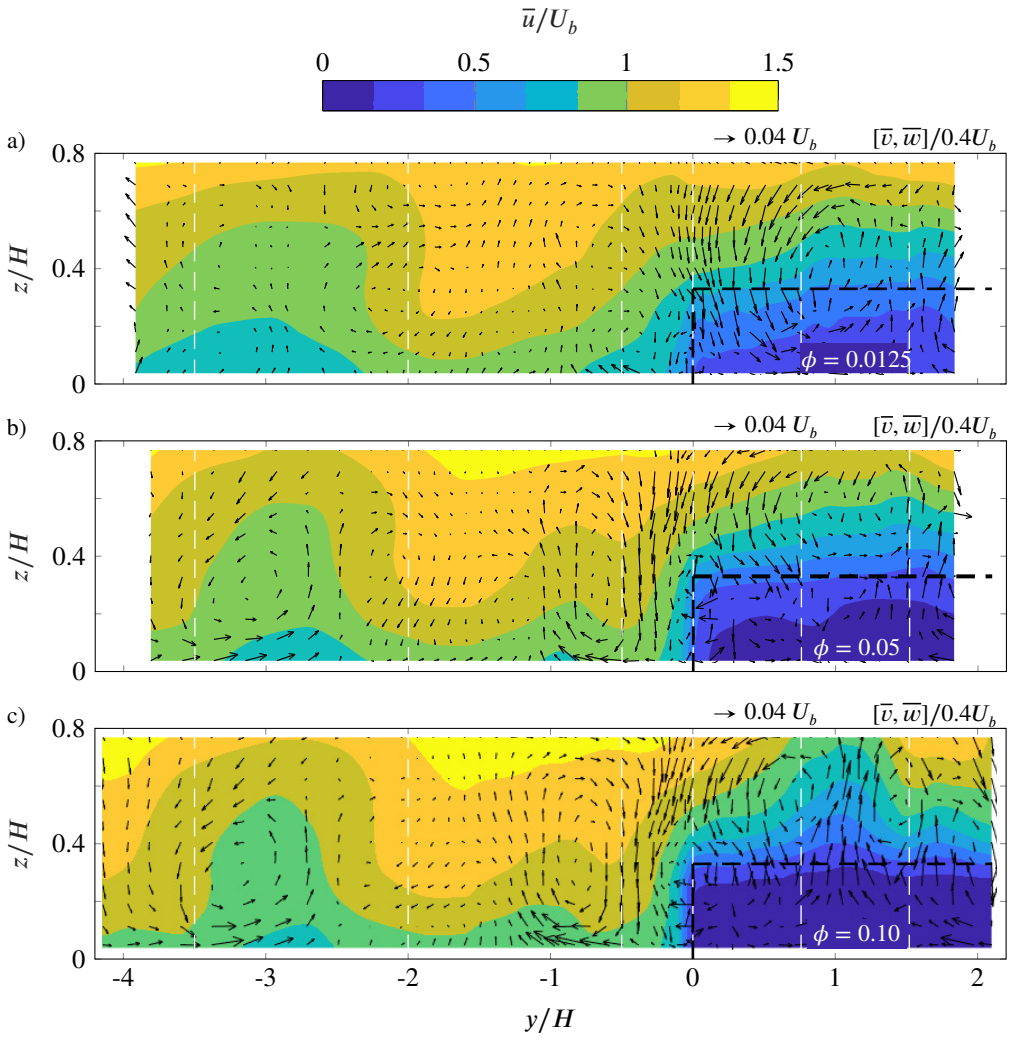


Figure 7.1: Distribution of normalised time-averaged streamwise velocity $\overline{u}$ in the cross (yz) plane for a) $\phi = 0.0125$, b) $\phi = 0.05$, and c) $\phi = 0.10$. The (in plane) secondary flow is indicated by velocity vectors $[\overline{u},\overline{w}]/0.4U_b$. Black dashed lines represent patch boundaries. Locations of channel subdivisions for the SKM panels are shown by vertical white dashed lines.

the other near the bed. The free-surface cell transports energy and momentum from the wall towards the centre of the main channel, near the water surface. However, with increasing vegetation density (i.e. for $\phi = 0.05$ and $\phi = 0.10$) the bottom cell becomes bigger (Figure 7.1(a-c)) likely due to changes in the aspect ratio B_{ch}/H as a consequence of the increasing flow blockage.

The spanwise heterogeneity of the vertical turbulent Reynolds shear stress $-\overline{u'w'}$, where u' and w' represent time velocity fluctuations in the streamwise and vertical directions, has also been linked to the secondary circulations created due to bed heterogeneity (Wang & Cheng, 2006; Willingham et al., 2014; Vanderwel & Ganapathisubramani, 2015). In the partially vegetated channel of the present study, the maximum shear occurs close to the top of the canopy due to the sudden change in drag. The Reynolds stress increases with increasing canopy density. However, the magnitude of $-\overline{u'w'}$ at the vertical interface is not constant along the patch width, at least for $\phi = 0.05$ and $\phi = 0.10$. For these two canopy densities, the vertical turbulent stress $-\overline{u'w'}$ at the top of the canopy is larger in regions of downward flow than in regions of upward flow (Figures 7.2b and 7.2c). This behaviour has also been observed in studies on alternating smooth-rough longitudinal strips (e.g. Willingham et al., 2014; Anderson et al., 2015). The maximum vertical Reynolds stress, excluding wall effects, is observed at the top of the vegetation, near the edge flanking the main channel (Figure 7.2(a-c)). By contrast, small Reynolds stress values are seen near the bed at two locations: inside the vegetation, and towards the flume wall opposite the canopy patch. Shear penetration into the canopy decreases with increasing canopy density. The magnitude of the Reynolds shears stress above the patch is more than twice that of the Reynolds stress observed in the main channel. Large values of the shear stress in the main channel are observed next to the vegetation patch, near the bed (Figure 7.2(a-c)).

The spanwise distribution of the depth-averaged lateral shear stress, $\langle \tau_{xy} \rangle_d$, in the partially vegetated channel also reflects the three-dimensionality of the flow. Due to the porous nature of the canopy and the mean velocity fluctuations caused by the secondary circulation, the total shear stress $\langle \tau_{xy} \rangle_d$ is not mainly due to lateral turbulent shear, $\langle \overline{u'v'} \rangle$, but has an additional contribution from the spatial fluctuations of the flow near the porous medium, known as dispersive stress $\langle \overline{u}''\overline{v}'' \rangle_d$, and a contribution from the secondary circulation as advective dispersive stress, $\langle \tilde{\overline{u}}\tilde{\overline{v}} \rangle_d$ (§7.3). The latter is significantly large, sometimes even larger than

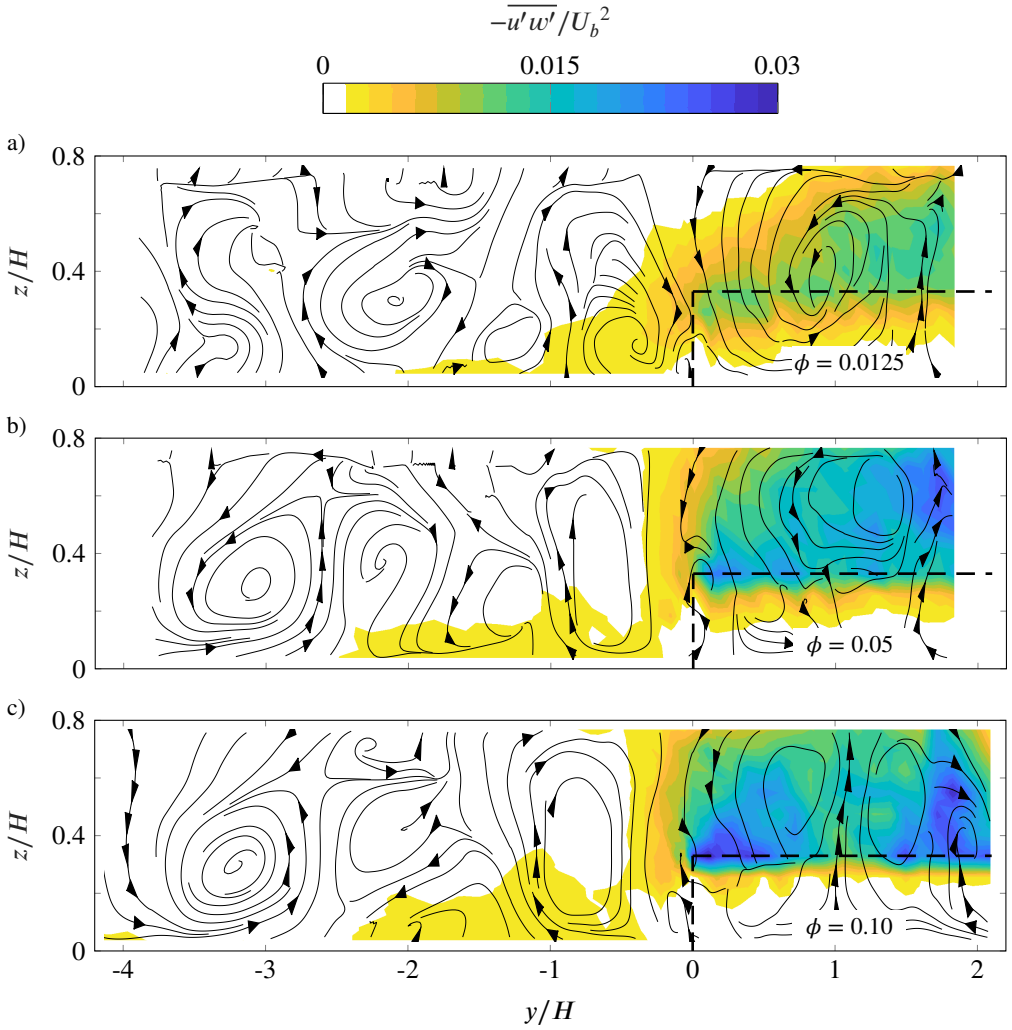


Figure 7.2: Normalised time-averaged vertical turbulent Reynolds stress for a) $\phi = 0.0125$, b) $\phi = 0.05$, and c) $\phi = 0.10$. Secondary circulations are represented by in-plane streamlines. Black dashed lines represent patch boundaries. The maximum shear occurs at the top of the canopies, being larger in regions of downward flow than in those of upward flow. Be aware that the white space in the figure does not represent zero vertical Reynolds stress but it is much smaller than the stress caused by the vegetation patch.

the Reynolds stress, but of the opposite sign as shown in Figure 7.3a. Dispersive stress $\langle \overline{u}''\overline{v}'' \rangle_d$ is relatively small, and its contribution is slightly bigger in the vegetated zone than in the main channel. Within the vegetation, the advective dispersive stress and turbulent Reynolds stress both change sign near $y/H = 1$, where there is an upward flow shared by the two secondary cells developed above the canopy patch for $\phi = 0.10$ (c.f. Figure 7.1c, and Figure 7.2c). The largest magnitude of the lateral Reynolds stress occurs at the lateral canopy-water interface where other stress components are less significant.

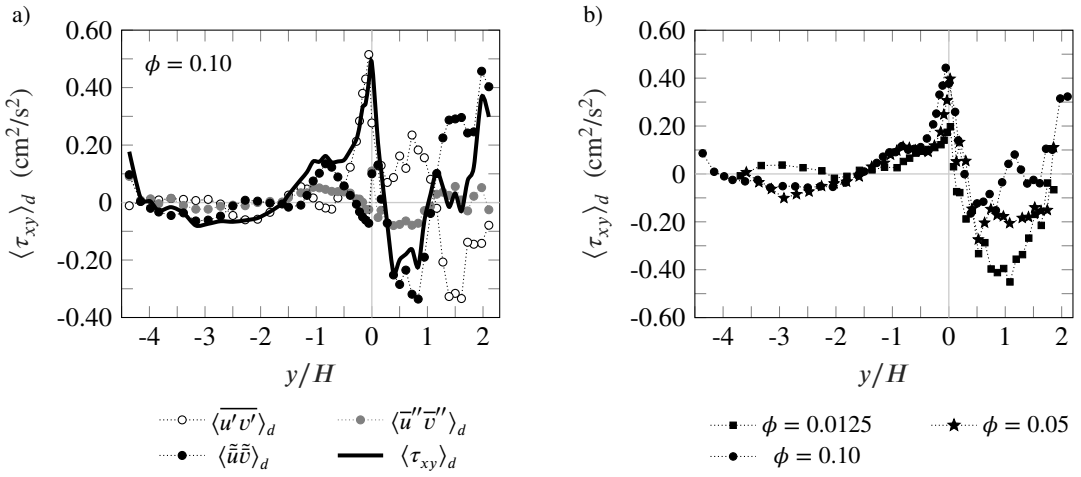


Figure 7.3: a) Contributions of turbulent Reynolds, dispersive and advective dispersive stresses to the depth-averaged lateral shear stress for $\phi = 0.10$. b) Total depth-averaged lateral shear stress for the three canopy densities. Contributions of the secondary circulation through the advective shear stress are significant and should be taken into account when considering the depth-average lateral shear stress.

Comparative distributions of the total lateral shear stresses for the three canopy densities are illustrated in Figure 7.3b. In the main channel, the total lateral shear stress is larger close to the lateral interface and changes sign at $y/H \approx 1.5$ for all canopy densities. Total stresses in the vegetated region include a significant contribution from the advective dispersive stresses. The magnitude of $\langle \tau_{xy} \rangle_d$ within the canopy, decreases with increasing canopy density due to a larger contribution from the turbulent Reynolds stresses that have the opposite sign.

7.3 Predicting depth-averaged velocities using the Shiono-Knight Method

The SKM is a lateral distribution model based on the depth-averaged form of the Reynolds Averaged Navier Stokes (RANS) momentum equation. The advantage of the SKM model, over other lateral distribution models, is the incorporation of an advective term that accounts for the secondary flow effects in three-dimensional flows. In partially vegetated channels, due to the inhomogeneity of the velocity in the spanwise direction, a double averaging procedure (in time and space) of the Navier Stokes momentum equation should be employed prior to depth-averaging (White & Nepf, 2007). The spatial averaging is done over the interstitial fluid, which is related to the average within a space including the canopy elements (or

flow obstructions), through the porosity $\phi_f = 1 - \phi$ (see e.g. Whitaker, 1969; Breugem et al., 2006, and §4.2.1). The governing equation, combines the x-momentum equation with the continuity equation for the streamwise motion, which upon depth-averaging (i.e. integrating over the water depth), for a uniform steady flow and neglecting viscosity results in (Rameshwaran & Shiono, 2007),

$$\underbrace{\rho \frac{\partial (H \langle \phi_f \rangle_d \langle \overline{u} \rangle_d \langle \overline{v} \rangle_d)}{\partial y}}_{\text{I}} = \underbrace{\rho g H \phi_f S_0}_{\text{II}} + \underbrace{\frac{\partial (H \langle \phi_f \rangle_d \langle \tau_{xy} \rangle_d)}{\partial y}}_{\text{III}} - \underbrace{\tau_b}_{IV} - \underbrace{\langle \overline{D_x} \rangle_d}_{\text{V}} \tag{7.1}$$

where the lateral shear stress $\langle \overline{\tau_{xy}} \rangle_d$ is given by (4.10). The expression in (7.1) is similar to the depth-averaged x-momentum equation for uniform steady flow in prismatic channels (2.9) proposed by Shiono & Knight (1991), but it has an additional term that accounts for the vegetation drag force, and terms in (7.1) are premultiplied by the porosity parameter, ϕ_f. However, $\phi_f = 1$ for depth-averaged velocities next to the canopy, which leads to the same mathematical expression for the momentum equation given by Shiono & Knight (1991). In (7.1), the overline $\overline{\ }$ indicates the time average of the instantaneous velocities over the length of the velocity record and angle brackets $\langle\ \rangle$ are used for the spatial average. The subscript d next to the angle brackets indicate a depth-averaged quantity, i.e. average in the z-direction. In the depth-mean-averaged momentum equation (7.1), ρ represents the water density, g is the acceleration of gravity, and S_0 is the bed slope, which is assumed to be equal to the water surface slope. The bed shear stress τ_b is the force exerted by the bed on the fluid, which using the Darcy-Weisbach equation results in, $\tau_b \equiv (f/8)\ \rho\ (\langle \overline{u} \rangle_d^{\,2}/2)$, where f is the friction coefficient. The drag force $\langle D_x \rangle_d$ is that caused by the vegetation per unit fluid volume. If the vegetation is seen as a rough surface, $\langle D_x \rangle_d$ may be given by $\equiv c_f \rho A(\overline{u}^2/2)$, where c_f is the Fanning friction factor and A is the projection of the bed roughness on the plane normal to the main flow direction. Thus, in the depth-averaged flow, it can be assumed that $\langle D_x \rangle_d \equiv (f_v/8)\ \rho\ (\langle \overline{u} \rangle_d^{\,2}/2)$, where $f_v = 4c_f$ is the friction coefficient for the vegetated region (further discussed in §7.3.1) (Katopodes, 2018). Term I is the advection term also referred to as Γ, which represents the momentum exchange due to the averaged secondary flow structures; Term II is the gravity term; Term III accounts for the effects of the transverse shear stress, Term IV represents the bed friction and Term V corresponds to the drag force exerted by the vegetation on the flow

per unit fluid volume.

For modelling purposes it was decided that the analytical solution to (7.1) would be the one proposed by Shiono & Knight (1991) for uniform steady flow in prismatic channels, with a drag force in the vegetated region represented by an empirical friction coefficient for vegetated flows (further discussed in §7.3.1). For flows with a constant depth domain, i.e. flows over a flat bed, the analytical solution of the differential equation (7.1) for the time-depth-averaged streamwise velocity is given by (2.13) as $\langle \overline{u} \rangle_d = [A_1 e^{\gamma y} + A_2 e^{-\gamma y} + k]^{1/2}$, where constants γ and k are defined as,

$$\gamma = \left(\frac{2}{\lambda}\right)^{1/2} \left(\frac{f}{8}\right)^{1/4} + \frac{1}{H} \tag{7.2}$$

$$k = \frac{8 g S_0 H}{f} \left(1 - \frac{\Gamma}{\rho g S_0 H}\right) \tag{7.3}$$

Wherein the friction coefficient f is determined by the Darcy-Weisbach equation (2.10) and the dimensionless eddy viscosity λ is given by,

$$\lambda = \frac{\langle \tau_{xy} \rangle_d}{\rho H u_* \dfrac{\partial \langle \overline{u} \rangle_d}{\partial y}} \tag{7.4}$$

where u_* is the friction velocity. Furthermore, the unknown constants $A1$ and $A2$ in the solution for $\langle \overline{u} \rangle_d$ can be determined assuming appropriate boundary conditions. One of the assumptions of the SKM is that a cross-section of a prismatic channel may be discretised by a series of panels with an even bed to improve the predictive capabilities of the model (Shiono & Knight, 1988, 1991). Thus, a series of linear simultaneous equations based on (**??**) can be solved to obtain A_1 and A_2 for each panel. Omran (2005) demonstrated that an appropriate boundary condition applicable to the inner panels in compound channels was,

$$\left(\mu_{bc} \frac{\partial U_d}{\partial y}\right)^i = \left(\mu_{bc} \frac{\partial U_d}{\partial y}\right)^{i+1} \quad \text{with} \quad \mu_{bc} = \lambda \sqrt{f/8} \tag{7.5}$$

where superscript i refers to the number of an individual panel. The no-slip condition, i.e. $\langle\overline{u}\rangle_d = 0$, can be applied to the outermost boundaries. The boundary condition in (7.5) has also been successfully applied in open-channels with differential roughness (e.g. Jesson et al., 2013c) and compound channels with emergent vegetated floodplains (e.g. Rameshwaran & Shiono, 2007; Tang & Knight, 2009). This means that there is precedent for the boundary condition in (7.5) to be applied to the current experimental set-up. The number of panels and spacing for the present study were defined based upon a process of trial and success, adding the necessary panels to ensure a reasonable distribution of $\langle\overline{u}\rangle_d$ while limiting the complexity of the model.

7.3.1 Input model parameters

Modelling the depth-averaged velocity distribution depends on the appropriate quantification of γ, Γ and f. Γ values were evaluated using measured data. For the distribution of γ, the friction velocity u_* was calculated using the logarithmic law of the wall in the main channel, while the canopy logarithmic law was used within the vegetation patch (Nepf & Vivoni, 2000). Central differences were used for the discrete approximation of gradients. The skin friction f of the smooth bed was evaluated using the friction velocity for the bed shear stress $\tau b = -\rho\, u_*^2$ along with measured depth-averaged streamwise velocities $\langle\overline{u}\rangle_d$ using (2.10). However, within the vegetation, the friction coefficient f_v was calculated from two different equations, the generic form of which resembles the original Darcy-Weisbach equation (2.10). The first equation used for calculating f_v was proposed by Poggi et al. (2009),

$$f_v = 4\left(\frac{L_D}{h}\right)^{-1}\left[1+\left(1-\frac{h}{H}\right)\frac{\Delta U}{U_v}\right]^{-2} \tag{7.6}$$

where $L_D = (C_D a)^{-1}$ is the canopy drag length scale with C_D being the drag coefficient calculated using the formula of van Rooijen et al. (2018); ΔU is the velocity difference between the bulk velocity inside the canopy U_v and the bulk velocity in the overlying flow. The second equation for f_v was formulated by Wang et al. (2019),

$$f_v = 4C_D \left(\frac{U_v}{U_b} \right)^2 \tag{7.7}$$

where the drag coefficient was calculated using the equation proposed by the authors and U_b is the weighted averaged of the bulk velocities inside and above the canopy patch (Wang et al. 2019). Expressions for f_v in (7.6) and (7.7) are based on a force balance between the drag exerted by the vegetation and the gravity force associated with the water weight, where it is assumed that the canopy drag is much larger than the bed skin friction.

7.3.2 Modelling depth-average streamwise velocity

The modelled depth-average streamwise velocity profile depends on the distribution of λ and Γ within the cross-section of the channel. An initial approximation of these parameters is calculated from the experimental results and the subdivision of the channel cross-section is inferred from their distribution and the characteristic flow and bed structures. Final values are reported after a sensitivity analysis of the parameters and the discretisation of the channel cross-section. Distributions of λ, using (7.4), for $\phi = 0.0125$, $\phi = 0.05$ and $\phi = 0.10$ are shown in Figures 7.4(a-c), respectively. Large values of the non-dimensional eddy viscosity are observed in the vegetated region for $\phi = 0.0125$ and $\phi = 0.05$, as lateral shear stresses are large and the contours of the time-averaged streamwise velocity are relatively smooth. Spikes in λ within the main channel are a result of the use of central differences for the calculation of the velocity gradient. The dimensionless eddy viscosity $\lambda \propto 1/(\partial \langle \overline{u} \rangle_d / \partial y)$, thus $\lambda \to \infty$ as $\partial \langle \overline{u} \rangle_d / \partial y \to 0$. However, a local maximum or minimum will not be captured by the central differences unless the differential velocity, $\langle \overline{u} \rangle_{d(y_{i+1})} \approx \langle \overline{u} \rangle_{d(y_{i-1})}$. Average values of λ within the vegetated area are 0.026, 0.070, and 0.046, for increasing vegetation density. The dimensionless eddy viscosity for the denser canopy, $\phi = 0.10$, is smaller as the spanwise distribution of the lateral shear stress is small and the velocity gradient is large. In the main channel, values of λ oscillate between 0.040 and 0.078 for the various canopies (disregarding the large spikes), with an average of $\lambda = 0.060$. This value is close to the standard value for smooth open-channels $\lambda = 0.067 \approx 0.07$ ($= \kappa/6$, where κ is the von Karman constant) (Omran, 2005).

The distribution of the secondary flow term Γ is either positive or negative de-

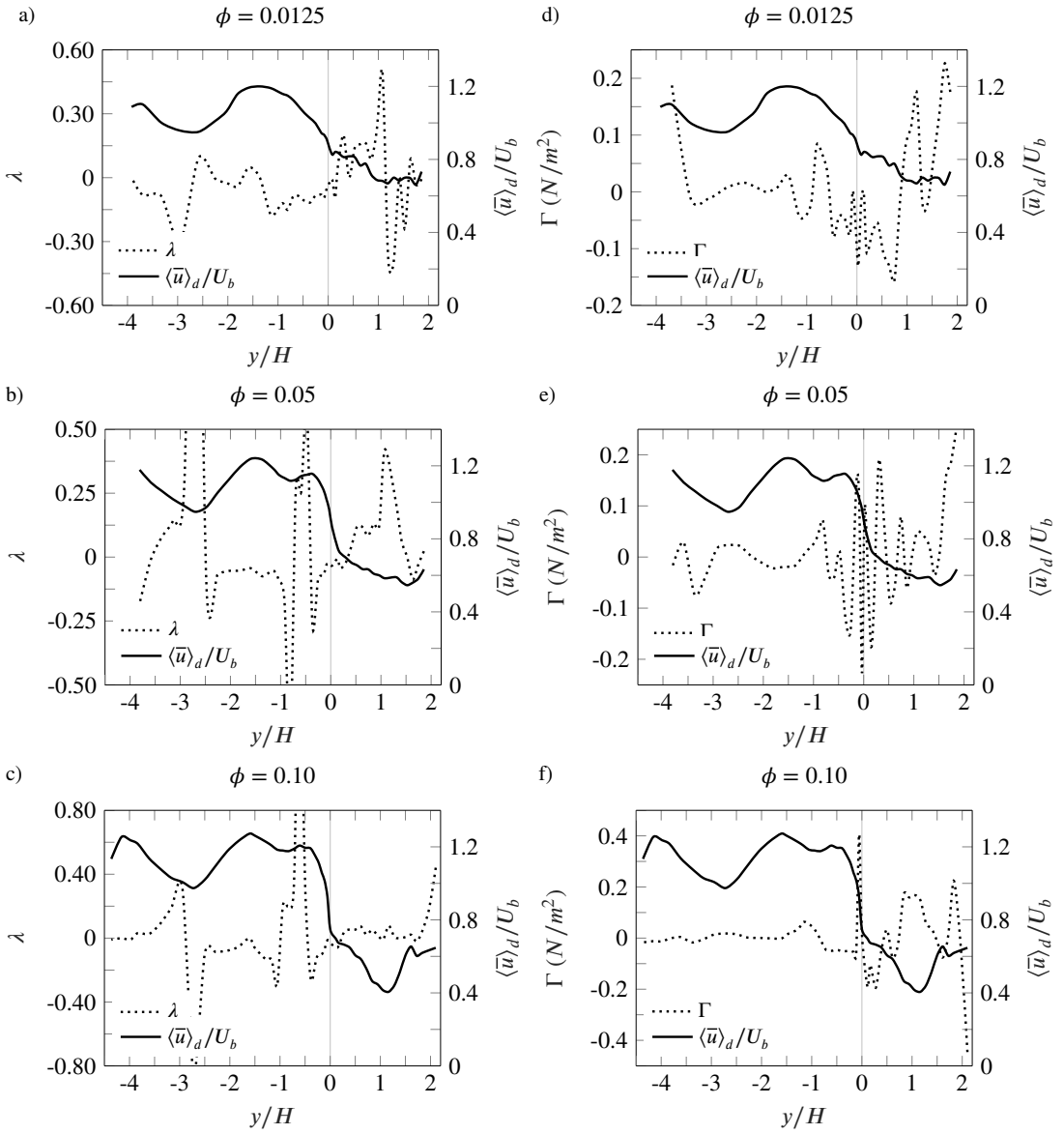


Figure 7.4: Distribution of the non-dimensional eddy viscosity λ (a-c) and secondary circulation term Γ (d-f) across the partially vegetated channel for three canopy densities $\phi = 0.0125$, $\phi = 0.05$, and $\phi = 0.10$. Large variations in lambda are observed close to the lateral canopy-water interface (i.e. $y/H = 0$) with increasing canopy density as momentum transport is enhanced there. Positive peaks of Γ occur at locations of strong upward flow while negative peaks are associated to downward flows.

pending on the vertical distribution of the time-averaged transverse velocity $\overline{v}(z)$, which indicates the rotational direction of the secondary circulation. Since $\overline{v} \approx 0$ at the edge of the rotational cell, the magnitude of $\langle\overline{u}\rangle_d\langle\overline{v}\rangle_d$ in Γ is maximum at the centreline of the cross-sectional cell. Therefore, $\langle\overline{u}\rangle_d\langle\overline{v}\rangle_d$ is positive for a clockwise cell and negative for an anticlockwise cell (for further details see Knight et al. (2007)). In submerged patchy-vegetation, large values of Γ are seen to occur

in regions of strong downward and upward flow. For instance, large values of Γ are observed at the lateral canopy-water interface for all canopy densities (figure Figures 7.4(d-f)), where there is a strong flow towards the channel bed (c.f. Figure 7.1(a-c)). Peaks of Γ in regions where the cross-flow goes from the bed to the water surface are seen, for example, at $y/H \approx 1.7$ for $\phi = 0.0125$ and $\phi = 0.05$, and at $y/H \approx 1$ for $\phi = 0.10$ (Figures 7.4(d-f)). A peak is also observed next to the vegetation patch around $y/H = -1$ for all canopy densities, indicating the strong upward flow of the secondary circulation cell (c.f. Figure 7.1(a-c)).

The average friction coefficient f determined by (2.10) in the main channel was 0.034, 0.044 and 0.045 for $\phi = 0.0125$, $\phi = 0.05$ and $\phi = 0.10$, with standard deviations of 0.012, 0.009 and 0.014, respectively. Friction coefficients in the main channel were observed to increase close to the vegetation patch. Within the canopy, values of f_v calculated using (7.6) were, for increasing vegetation density, 0.400, 0.490, and 0.670, which are more than 10 times larger than the values over the respective smooth beds (i.e. the main channel). This indicates that friction coefficients in the vegetated region, similar to the non-vegetated region, increase with increasing canopy density (i.e. $f_v \propto \phi$). Using (7.7), instead of (7.6), to calculate friction coefficients in the vegetated zone leads to smaller f_v values than the ones obtained by applying (7.6). For increasing vegetation densities, friction coefficients were $f_v = 0.33$, $f_v = 0.17$ and $f_v = 0.10$, suggesting an inverse relationship between f_v and ϕ (i.e. $f_v \propto 1/\phi$). This contrasts with the results obtained for (7.6). However, f_v has been found to change with two dimensionless parameters, one based on canopy attributes L_D/h and the submergence ratio given by H/h (Tsihrintzis & Madiedo, 2000; Järvelä, 2002; Green, 2005; Huthoff et al., 2007). Thus, for a given H/h (as in the present study), f_v should decrease with increasing L_D/h. This relationship is found to be true for f_v values obtained via (7.6) and not when using (7.7). Furthermore, the expression in (7.7) uses the bed shear stress calculated from the bed slope. This method is appropriate for their study on a fully vegetated flow, but less accurate for local estimates or small-scale estimates of the variation of the shear stress (Dey, 2014) as in the present study (i.e. in a submerged partially vegetated flow). Therefore, the equation proposed by Poggi et al. (2009) (i.e. (7.6)) was chosen for the SKM.

Distributions of λ, Γ and f within the partially vegetated channel previously illustrated are complex. However, accounting for their complexity may hinder the simplicity of the SKM. Therefore, simplifications that lead to acceptable depth-

averaged velocity predictions, yet capture the physics of the flow, are evaluated. As the secondary circulation distribution (Figure 7.1) is related to the turbulent Reynolds shear stress distribution (§ 7.2.1) and consequently to the friction velocity f, channel subdivisions were chosen to be as close as possible to the centres of the secondary cells and at the lateral canopy-water interface, where there is a large change in f. Within the vegetation two partitions were made at $B/3$ intervals, which roughly coincide with the centres of secondary cells for $\phi = 0.10$ (Figure 7.1c). Another subdivision was done at the lateral canopy-water interface, where there is a large change in f. Additionally, it can be observed from Figure 7.1(a-c) that there is a secondary cell just off the canopy patch in the main channel for all canopy densities. Its width (in the spanwise direction) scales with the water depth §4.4, thus a subdivision was made at $H/2$ from the lateral canopy water interface towards the main channel. Although the latter subdivision almost coincide with the centre of the cell next to vegetation patch for $\phi = 0.0125$, this does not occur for higher vegetation densities due to the appearance of a new pair of cells at the lateral canopy-water interface §4.4. Another channel subdivision was taken at H from the wall opposite the vegetation patch as the corner secondary flow for a channel with aspect ratio B_{ch}/H between 6.3 and 8.5 occupies a spanwise distance of $2H$ (Rodríguez & García, 2008). A last division was placed in the middle of the two subdivisions in the main channel. The 7-panel partition is indicated by vertical white dashed lines in Figure 7.1(a-c).

As the undulations of the time-averaged streamwise velocity are closely related to the secondary circulations and, in turn, to the friction coefficient, either (or both) Γ and f should vary between the panels for the SKM to closely replicate the bending in the depth-average velocity profile. Thus, reducing the number of panels leads to less accurate representations of the velocity profiles. The expressions for the friction coefficient in channels with submerged vegetation, (7.6) and (7.7), could, in principle, be used to evaluate a f_v varying for each panel. On the other hand, distributions of Γ in the cross-plane are sometimes complex and measurements within each panel lead to fluctuating Γ values for which the standard deviation can be larger than the maximum differences between average Γ values at each panel (Figure 7.5(a-c)). Therefore, and to keep with the simplicity of the model, the decision was to keep the 7-panel subdivision, take an average f for the main channel and an average f for the vegetated zone (f_v), and to have Γ as a tuning parameter (found via non-linear regression) changing for each panel but with the sign that corresponds to the observed rotation at each panel. A

measured λ-averaged value was used for panels within the vegetated patch. In the main channel, a sensitivity analysis for λ was performed using measured λ-averaged values and the typical value of $\lambda = 0.07$. Differences in the relative error of depth-averaged streamwise velocity profiles, measured and simulated, were of less than 1%, thus $\lambda = 0.07$ was used for panels in the main channel. The value of λ used over the smooth bed in the present work is consistent with previous stud-

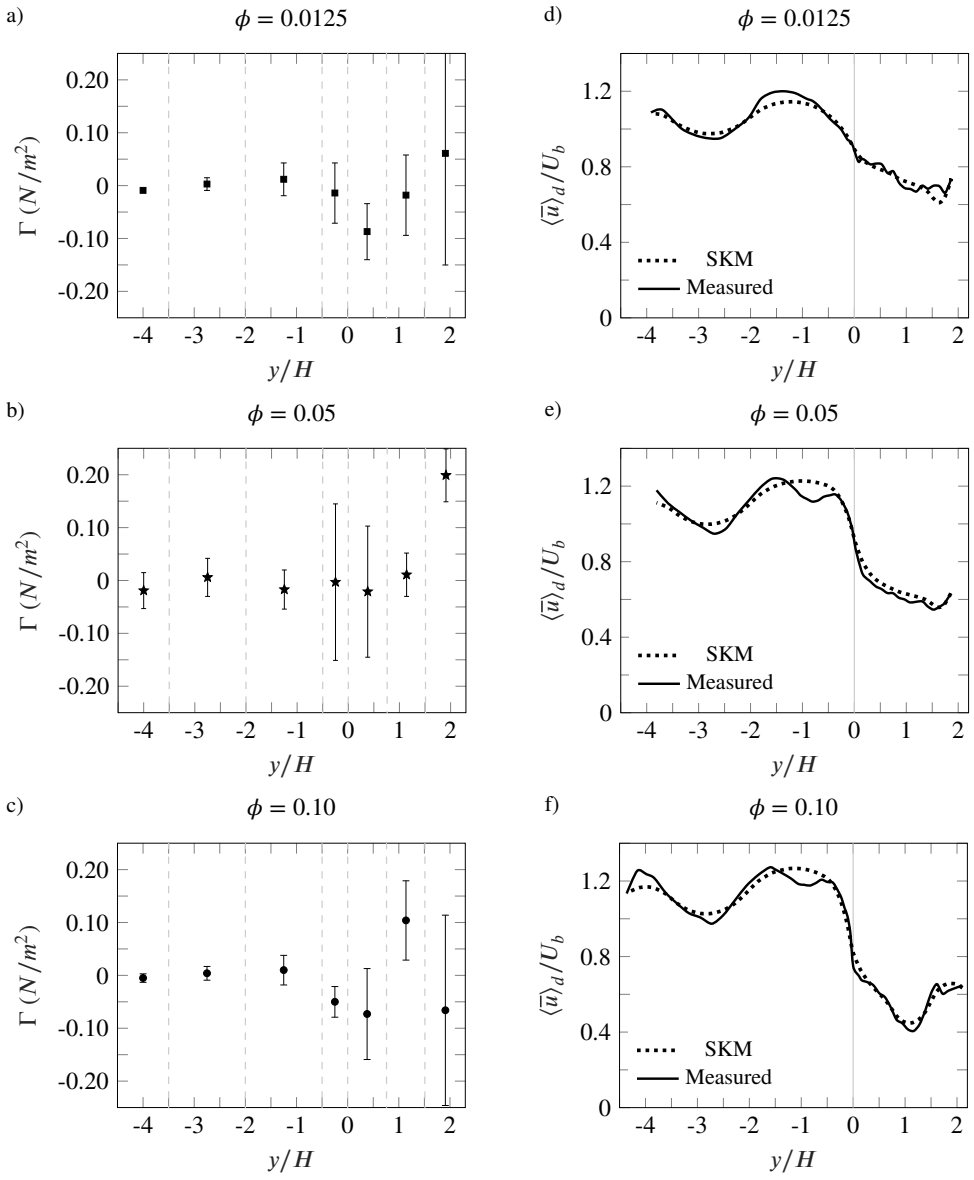


Figure 7.5: Panel-averaged secondary circulation term Γ (a-c) and lateral distribution of the depth-averaged streamwise velocity (d-f) across the partially vegetated channel for three canopy densities $\phi = 0.0125$, $\phi = 0.05$, and $\phi = 0.10$. Error bars represent the standard deviation of measured Γ values within each panel. The standard deviation of Γ is sometimes larger than the maximum difference between averaged Γ values in the channel. Modelled depth-averaged velocities agree well with experimental data.

ies (e.g. Rameshwaran & Shiono, 2007; Tang & Knight, 2009; Tang et al., 2011; Jesson et al., 2013c). Values of λ, f and Γ used in the SKM are given on Table 7.1.

Table 7.1: Values of the SKM parameters λ, f and Γ used in the model. The first three rows correspond to panels within the vegetated patch, while the last four rows represent panels in the main channel.

Panel	$\phi = 0.0125$			$\phi = 0.05$			$\phi = 0.10$		
	λ	f	Γ	λ	f	Γ	λ	f	Γ
$2.27 \geq y/H \geq 1.51$			0.000			0.000			-0.170
$1.50 \geq y/H \geq 0.76$	0.026	0.400	-0.093	0.070	0.490	-0.060	0.046	0.670	0.015
$0.75 \geq y/H \geq 0$			-0.119			-0.072			-0.094
$0.01 \leq y/H \leq 0.50$			0.000			-0.034			-0.052
$0.51 \leq y/H \leq 2.00$	0.070	0.034	0.000	0.070	0.044	0.000	0.070	0.045	0.004
$2.01 \leq y/H \leq 3.50$			0.020			0.028			0.034
$3.51 \leq y/H \leq 4.51$			-0.004			-0.014			-0.012

Measured and predicted (by the SKM) depth-averaged streamwise velocity profiles are in good agreement, with Root-Mean-Square-Errors (RMSEs) of 0.035, 0.0028, and 0.0029 for increasing vegetation density (Figure 7.5(d-f)). These RMSEs are comparable to the ones obtained by Tang & Knight (2009) for compound channels with vegetated floodplains. Relative $\langle \overline{u} \rangle$ errors within the canopy are less than 11%, while in the main channel the maximum relative error is 7%. However, a sensitivity analysis was carried out to test how predictions changed due to the uncertainty in the bulk velocity above the canopy, which changes the velocity difference ΔU in the expression for the canopy friction coefficient (7.6). These uncertainties in the bulk velocity come from the lack of measurements in the upper 6 cm of the flow and the extrapolation of data in this region. Therefore, a $\pm$ 10% variation in the bulk velocity above the canopy leads to f_v values that differ by up to 0.07 from the initial adopted value on Table 7.1. These variations in f_v lead to changes in the local relative errors between measured and predicted $\langle \overline{u} \rangle$ profiles within the canopy. However, the maximum relative error for all vegetation densities increase by less than 4%, resulting in maximum relative errors of 14%, 8% and 13% for increasing vegetation densities.

As a simple validation of this approach, the subdivisions and SKM parameters for $\phi = 0.0125$ and $\phi = 0.05$ (Table 7.1) were used to estimate λ, f and Γ for

$\phi = 0.025$ via linear interpolation. Predicted depth-averaged streamwise velocities were compared to measured velocities for $\phi = 0.025$ taken within a spanwise width of $2B$, at the nodes of the same space grid used for $\phi = 0.0125$ (Figure 7.1a). Results of the numerical model of depth-averaged streamwise velocity with the experimental data are presented in Figure 7.6. The maximum relative error within the canopy is 10%, being the largest error close to the flume wall. In the main channel, the maximum relative error is 12%. In this region, errors increase from the centre of the flume towards the channel wall opposite the vegetation patch. These errors are within the limits seen for the other vegetation densities studied, which suggests that depth-averaged streamwise velocities were also successfully predicted for $\phi = 0.025$. Although the parameters and panel subdivision suggested seem to be valid for intermediate densities in the range $\phi = 0.0125 - 0.10$, these are not necessarily generalisable for other submergence conditions apart from $H/h = 3.0$, densities outside the range studied and wider or narrower patches as these parameters (and the panelling) are highly dependent on the size and distribution of the cross-sectional structures in the yz-plane, which, in turn, directly affect the distribution of the depth-averaged streamwise velocity. Therefore, more studies need to be done, exploring different configurations that lead to effective rules or relationships that facilitate the choice of panelling and parameter values for specific cases.

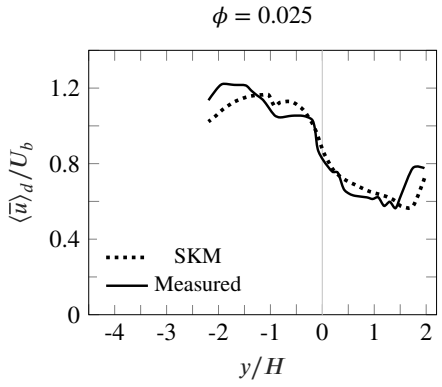


Figure 7.6: Distribution of the depth-averaged streamwise velocity for $\phi = 0.025$. Predicted velocities represent measured data with a maximum relative error of 12%.

7.4 Conclusions

A quasi-2D analytical model based on the depth-volume-averaged Navier-Stokes equation was used for predicting the depth-averaged streamwise velocity of a submerged partially vegetated channel, with increasing canopy density (for solid

volume fractions $\phi = 0.0125$, $\phi = 0.025$, $\phi = 0.05$ and $\phi = 0.10$). Vegetation was modelled as a flow resistance using a friction coefficient based on the canopy drag exerted by the vegetation; its generic form resembles the original Darcy-Weisbach equation for skin friction. Detailed-systematic 3D point velocity measurements in the cross-sectional plane were used to calculate the input parameters for the model. Numerical modelling illustrated that the friction factor and the secondary circulation parameter are key to accurately representing the bending of the depth-averaged velocity profiles generated due to the appearance of differential roughness-induced large-scale secondary circulation in the cross-plane. The distribution of the secondary circulation parameter Γ is complex and exhibits relatively large fluctuations (mostly) within the canopy patch. The friction coefficient f and the dimensionless eddy viscosity λ present a more organised distribution within the canopy and in the main channel. Results from the numerical simulations show that for appropriate values of Γ, f and λ, a seven-panel subdivision of the cross-section is a good approximation to predict the spanwise distribution of depth-averaged streamwise velocities. Modelled velocities agree with the experimental data reasonably well. The conclusions stated can only be made for the cylinder array studied here with densities ranging from $\phi = 0.0125$ to $\phi = 0.010$; results are required from a wider range of porous-layer geometries, higher densities and larger submergence conditions before a generalization on the use of the SKM in partially vegetated channels can be confirmed.

Chapter 8

Conclusions and future work

8.1 Conclusions

The aim of this study is to investigate the secondary circulation as a key feature of the three-dimensionality of the flow in a submerged partially vegetated channel. In particular, it seeks to provide an insight into the current understanding of the contribution of secondary flows to mass and momentum transport in such systems. This study is unique as the experimental approach allowed for the analysis of: (i) flow features simultaneously developing in both the vertical and spanwise directions, such as shear layers, which in the literature have been studied separately; (ii) roughness-induced secondary circulation developed by the presence of a porous medium (i.e. patch of vegetation). Additionally, the modelling section set a precedent in how to model such systems using a simple but informative depth-averaged model, the Shiono-Knight Method.

From the analysis of the secondary circulation and perturbed mean and turbulent flow distributions observed in the cross-sectional 3D velocity field resulting from the presence of vegetation patches of solid fraction densities, $\phi = 0.0125$, 0.025, 0.05, 0.10, 0.20 and $1(step)$, and submerged conditions $H/h = 2.0$, 2.5 and 3.0, it can be concluded that,

Addressing objectives 1.2.1 and 1.2.2: Characterisation of the three-dimensional flow in submerged partially vegetated channels and the impact of vegetation density and shallowness on the flow structure.

(a) The bed heterogeneity caused by the canopy patch leads to a heterogeneous streamwise velocity field in the cross-sectional plane, with undulations of the contour lines that accentuate as vegetation density increases and water depth decreases. Upward (downward) undulations of the streamwise velocity contour lines were associated with positive (negative) vertical velocities of the cross-plane secondary circulation.

(b) The sharp velocity gradient between the flow inside the vegetation and the free-flow outside results in the development of mixing layers in the vertical and lateral directions, controlling mass and momentum exchange between different flow domains. Both mixing layers possess two distinct regions, an inner layer δ_I with a streamwise velocity distribution that has a hyperbolic tangent shape, and an outer layer δ_O that resembles a boundary layer in the vertical direction but takes a sinusoidal-like shape in the lateral direction due to the effects of the secondary circulation. There is an exception for $H/h = 2.0$, where the vertical streamwise velocity distribution can be fully described by mixing layer parameters as in fully vegetated flows. The mixing layer thickness is inversely proportional to the vegetation density. However, the reduction of the water depth leads to thicker lateral mixing layers and thinner vertical mixing layers.

(c) The size and strength of the time-averaged secondary circulation are functions of vegetation density ϕ and the submergence condition H/h. The size of the cross-sectional cells above the patch of vegetation is approximately limited by the mixing layer thickness, which in turn is a function of the vegetation density. Thus, the number of cells developed above the vegetation increase with increasing (decreasing) canopy density (mixing layer thickness). In the main channel their size is capped by the water depth. The strength of the vortical structures is maximum for $\phi = 0.10$, but decreases for denser canopies due to the growth of an emerging tertiary pair of cells at the lateral canopy-water interface. Lowering the water depth hinders the development of cross-sectional cells above the canopy and strengthens the secondary circulation in the main channel.

(d) The rotational sense of the secondary circulation differs from that observed in strip- and ridge-type roughness flows (Wang & Cheng, 2006; Anderson et al., 2015; Hwang & Lee, 2018, also see Figure 1.1), and it is characterised by a strong downward flow at the lateral canopy-water interface (Figure 4.11). However, for very dense canopies (i.e. $\phi = 0.20$), the direction of rotation of the secondary cells resembles that of ridge-type roughness flows. This was confirmed by the experiment with a *step* replacing the vegetation patch (i.e. resembling $\phi \approx 1$). The origin of the opposite rotational sense of secondary flows between the submerged partially vegetated flow and strip- and ridge-type roughness flows was attributed to the distribution and significant contribution of turbulent fluctuations to the transport of turbulent kinetic energy (TKE).

(e) In a submerged partially vegetated channel, the secondary circulation driven by turbulence anisotropy can significantly contribute to momentum exchange through shear stress caused by mean flow fluctuations, known as advective dispersive stress. In the vertical direction, the advective dispersive stress increases with increasing canopy density, being about 23% of the total shear stress for $\phi = 0.10$ at $H/h = 3.0$. Lateral dispersive stresses are the main contributors to the total lateral shear stress within the vegetated area and in the region adjacent to the vegetation patch, outside the mixing layer where the Reynolds shear stress is dominant. These results highlight the importance of understanding and evaluating advective dispersive shear stresses to accurately model submerged partially vegetated flows.

(f) The vertical flow above the canopy can actively contribute to vertical scalar transport by means of vertical advection, which was demonstrated to be of the same order of magnitude as turbulent diffusion. This means that the cross-sectional cells developed in a submerged partially vegetated channel can promote the exchange and retention of various types of matter between the vegetation and the overlying flow. Therefore, models used to study biological processes should consider advective processes as much as diffusive processes for accurate representations in patchily-vegetated flows.

(g) Observations of the formation of sediment streaks on the main channel, associated with upward flows, highlight the importance of points (e) and (f), and, in general, of the three-dimensionality of submerged patchy vegetation.

(h) The characteristic downward flow observed at the lateral canopy-water interface of the submerged patchy vegetation, which differs from the vertical flow direction at the change in elevation (roughness) in ridge- (strip-) type roughness flows, was mainly attributed to the significant contribution of the TKE transport due to turbulent fluctuations to the Reynolds-averaged TKE transport equation. Additionally, the 1D streamwise energy spectra revealed that the peak of energy within the vegetation is located at the top of the canopy. However, an additional local peak associated with the cross-sectional cells, with wavelength $\lambda_x \approx 1.9 - 2.5H$ was also observed. This additional peak became more energetic with increasing vegetation density presumably due to the secondary circulation strength.

Addressing objective 1.2.3: Modelling the spanwise depth-averaged velocity distribution in submerged partially vegetated channels

The SKM was customised to successfully predict the depth-averaged streamwise velocity distribution in a submerged partially vegetated flow. Values of the friction coefficient f for the vegetated region were calculated from experimental data. Calculation of the non-dimensional eddy-viscosity λ from the experimental data had little influence on the final results compared with the results obtained using the 'standard' value of $\lambda = 0.07$. The parameter representing secondary flow Γ was used as a tuning parameter. However, knowledge of the location of the secondary cells in the cross-sectional plane was found to be essential for the panel subdivision and consequently for accurate depth-averaged streamwise velocity predictions. Based on the above, and acknowledging that more studies should be carried out before generalising this conclusion, the following scheme is recommended for applying the SKM in submerged partially vegetated flows (see Chapter 7 for more details): i) a seven-panel subdivision (three sections within the vegetated region); ii) f constant on each side using the Darcy-Weisbach equation in the main channel and the equation proposed by Poggi et al. (2009) in the vegetated zone; iii) $\lambda = 0.07$; and iv) Γ is used as a tuning parameter.

8.2 Future work

Secondary circulation induced by surface roughness has recently gained intensive attention due to the many possible applications in flow control, sediment trans-

port, flood risk, etc. Nonetheless, the study of aquatic vegetated flows has also gained momentum in recent years due to emerging climate change issues. This means that the understanding of submerged partially vegetated flows is currently a topic of great relevance yet relatively new, and consequently in need of investigation.

Studies on secondary circulation in turbulent boundary layer flows have identified the ratio of elevated/rough region S to boundary layer thickness δ as a key parameter defining the size and strength of the secondary cells (e.g. Wang & Cheng, 2006; Willingham et al., 2014; Vanderwel & Ganapathisubramani, 2015; Hwang & Lee, 2018; D. D. Wangsawijaya et al., 2020). This has allowed them to use the ratio S/δ as a simple predictive tool to avoid the effects of unwanted strong, meandering secondary flows for certain applications, but also to locally promote mixing or heat transfer. In partially vegetated flows, the effects of the **submerged** vegetation patch dimensions on the secondary circulation are yet to be studied. This may have important implications for mass and momentum exchange and will help in identifying the key parameters of the system. Furthermore, the location of the patch of vegetation within the channel may also play a key role in the size/strength of the secondary circulation. Thin (in the spanwise direction) vegetation patches located in the middle of the channel may strengthen secondary cells growing at both corners of the vegetation patch in a similar way to which mixing layer vortices were found to get stronger for narrow emergent patchy vegetation (White & Nepf, 2007).

In terms of engineering design, the predictive power of the present study is limited by the vegetation densities ϕ and shallowness conditions H/h studied here. In the future, denser patches, and a broader range of shallowness conditions, different vegetation patch geometries and flow conditions (i.e. Reynolds number) should be investigated. The use of the secondary circulation parameter Γ as a tuning parameter in the SKM is somewhat unsatisfactory; alternatives to ADV measurements should be considered to allow for the mapping out of the entire flow depth and to further study the behaviour of Γ. Although the use of $\lambda = 0.07$ gives satisfactory results, additional datasets are required to analyse the behaviour of this parameter. Finally, the empirical equations available to calculate the friction coefficient in submerged vegetation are very limited and their use is yet to be extensively validated. Thus, further studies on the friction coefficient in submerged vegetation (derived from or linked to the Darcy-Weisbach equation) may provide

other mathematical expressions that could be used for a sensitivity analysis and improvement of the model. In the long term, numerical models such as LES may also facilitate the study of Γ.

Moreover, it is important to note that there are other questions that remain unanswered for the system of the present study, such as how the flow develops in the streamwise direction from the canopy leading edge, and how important pressure fluctuations are for the transport of TKE. Although the validity of the Taylor's frozen Hypothesis is expected to hold for the flows analysed here, results from the 1D streamwise energy spectra could be further supported by 2D energy spectra, co-spectra or 2-point correlation coefficient by having high resolution velocities in the streamwise direction. There is also the possibility of analysing the secondary circulation by means of the vorticity fluxes, which may give a hint at the possibility of predicting mean vertical and spanwise velocities in partially vegetated flows.

References

Abril, J., & Knight, D. (2004). Stage-discharge prediction for rivers in flood applying a depth-averaged model. *J. Hydraul. Res.*, *42*(6), 616–629.

Anderson, W., Barros, J. M., Christensen, K. T., & Awasthi, A. (2015). Numerical and experimental study of mechanisms responsible for turbulent secondary flows in boundary layer flows over spanwise heterogeneous roughness. *J. Fluid Mech.*, *768*, 316-347.

Asaeda, T., Fujino, T., & Manatunge, J. (2005). Morphological adaptations of emergent plants to water flow: a case study with typha angustifolia, zizania latifolia and phragmites australis. *Freshw. Biol.*, *50*(12), 1991–2001.

Awasthi, A., & Anderson, W. (2018). Numerical study of turbulent channel flow perturbed by spanwise topographic heterogeneity: amplitude and frequency modulation within low-and high-momentum pathways. *Phys. Rev. Fluids*, *3*(4), 044602.

Bal, K. D., Brion, N., Woulé-Ebongué, V., Schoelynck, J., Jooste, A., Barron, C., ... Bouma, T. J. (2013). Influence of hydraulics on the uptake of ammonium by two freshwater plants. *Freshw. Biol.*, *58*(12), 2452–2463.

Barros, J. M., & Christensen, K. T. (2014). Observations of turbulent secondary flows in a rough-wall boundary layer. *J. Fluid Mech.*, *748*.

Benifei, R., Solari, L., Vargas-Luna, A., Geerling, G., & Van Oorschot, M. (2015). Effect of vegetation on floods: The case of the river magra. In *E-proceedings of the 36th iahr world congress. june.*

Bertoldi, W., Drake, N. A., & Gurnell, A. M. (2011). Interactions between river flows and colonizing vegetation on a braided river: exploring spatial and temporal dynamics in riparian vegetation cover using satellite data. *Earth Surf. Process. Landf.*, *36*(11), 1474–1486.

Böhm, M., Finnigan, J., & Raupach, M. (2000). Dispersive fluxes and canopy flows: Just how important are they?

Bousmar, D., & Zech, Y. (1999). Momentum transfer for practical flow computation in compound channels. *J. Hydraul. Eng.*, *125*(7), 696–706.

Breugem, W., Boersma, B., & Uittenbogaard, R. (2006). The influence of wall permeability on turbulent channel flow. *J. Fluid Mech.*, *562*, 35–72.

Carollo, F., Ferro, V., & Termini, D. (2005). Flow resistance law in channels with flexible submerged vegetation. *J. Hydraul. Eng.*, *131*(7), 554–564.

Caroppi, G., Västilä, K., Gualtieri, P., Järvelä, J., Giugni, M., & Rowiński, P. M. (2021). Comparison of flexible and rigid vegetation induced shear layers in partly vegetated channels. *Water Resour. Res.*, *57*(3), e2020WR028243.

Cheng, H., & Castro, I. P. (2002). Near wall flow over urban-like roughness. *Bound.-Layer Meteorol.*, *104*(2), 229–259.

Chlebek, J., & Knight, D. (2006). *A new perspective on sidewall correction procedures, based on skm modelling.[w:] f. alves, l. cardoso (red.). river flow 2006, t. 1.* Taylor & Francis, Lisbon.

Chung, D., Monty, J. P., & Hutchins, N. (2018). Similarity and structure of wall turbulence with lateral wall shear stress variations. *J. Fluid Mech.*, *847*, 591–613.

Coceal, O., Thomas, T., Castro, I., & Belcher, S. (2006). Mean flow and turbulence statistics over groups of urban-like cubical obstacles. *Bound.-Layer Meteorol.*, *121*(3), 491–519.

Colombini, M. (1993). Turbulence-driven secondary flows and formation of sand ridges. *J. of Fluid Mech.*, *254*, 701–719.

Colombini, M., & Parker, G. (1995). Longitudinal streaks. *J. Fluid Mech.*, *304*, 161–183.

Cornacchia, L., Licci, S., Nepf, H. M., Folkard, A., van der Wal, D., van de Koppel, J., ... Bouma, T. J. (2019). Turbulence-mediated facilitation of resource uptake in patchy stream macrophytes. *Limnol. Oceanogr.*, *64*(2), 714–727.

Defina, A., & Bixio, A. C. (2005). Mean flow and turbulence in vegetated open channel flow. *Water Resources Research*, *41*(7).

Dennis, D. J., & Nickels, T. B. (2008). On the limitations of taylor's hypothesis in constructing long structures in a turbulent boundary layer. *Journal of Fluid Mechanics*, *614* , 197–206.

Dey, S. (2014). *Fluvial hydrodynamics* (Vol. 818). Springer.

Duman, T., Bohbot-Raviv, Y., Moltchanov, S., & Shavit, U. (2021). Error estimates of double-averaged flow statistics due to sub-sampling in an irregular canopy model. *Bound.-Layer Meteorol.*, *179*(3), 403–422.

Einstein, H. A., & Li, H. (1958). Secondary currents in straight channels. *Eos, Trans. AGU*, *39*(6), 1085–1088.

Folorunso, O. P. (2015). *Physically and numerically modelling turbulent flow in a patchy vegetated open channel* (Unpublished doctoral dissertation). University of Birmingham.

Forooghi, P., Yang, X. I., & Abkar, M. (2020). Roughness-induced secondary flows in stably stratified turbulent boundary layers. *Phys. Fluids*, *32*(10), 105118.

Ghisalberti, M. (2010). The three-dimensionality of obstructed shear flows. *Environ. Fluid Mech.*, *10*(3), 329–343.

Ghisalberti, M., & Nepf, H. M. (2002). Mixing layers and coherent structures in vegetated aquatic flows. *J. Geophys. Res. Oceans*, *107*(C2), 3–1.

Ghisalberti, M., & Nepf, H. M. (2004). The limited growth of vegetated shear layers. *Water Resour. Res.*, *40*(7).

Ghisalberti, M., & Nepf, H. M. (2005). Mass transport in vegetated shear flows. *Environ. Fluid Mech.*, *5*(6), 527–551.

Ghisalberti, M., & Nepf, H. M. (2006). The structure of the shear layer in flows over rigid and flexible canopies. *Environ. Fluid Mech.*, *6*(3), 277–301.

Goring, D. G., & Nikora, V. I. (2002). Despiking acoustic doppler velocimeter data. *J. Hydraul. Eng.*, *128*(1), 117–126.

Green, J. C. (2005). Modelling flow resistance in vegetated streams: review and development of new theory. *Hydrol. Process: An International Journal*, *19*(6), 1245–1259.

Hinze, J. (1967). Secondary currents in wall turbulence. *Phys. Fluids*, *10*(9), S122–S125.

Ho, C.-M., & Huerre, P. (1984). Perturbed free shear layers. *Annu. Rev. Fluid Mech.*, *16*, 365–424.

Hopkinson, L., & Wynn, T. (2009). Vegetation impacts on near bank flow. *Ecohydrology: Ecosystems, Land and Water Process Interactions, Ecohydrogeomorphology*, *2*(4), 404–418.

Huai, W., Zeng, Y., Xu, Z., & Yang, Z. (2009). Three-layer model for vertical velocity distribution in open channel flow with submerged rigid vegetation. *Advances in Water Resources*, *32*(4), 487–492.

Huang, Y. H., Saiers, J. E., Harvey, J. W., Noe, G. B., & Mylon, S. (2008). Advection, dispersion, and filtration of fine particles within emergent vegetation of the florida everglades. *Water Resour. Res.*, *44*(4).

Huthoff, F., Augustijn, D. C., & Hulscher, S. J. (2007). Analytical solution of the depth-averaged flow velocity in case of submerged rigid cylindrical vegetation. *Water Resour. Res.*, *43*(6).

Hwang, H. G., & Lee, J. H. (2018). Secondary flows in turbulent boundary layers over longitudinal surface roughness. *Phys. Rev. Fluids*, *3*(1), 014608.

Ikeda, S., & Kanazawa, M. (1996). Three-dimensional organized vortices above flexible water plants. *J. Hydraul. Eng.*, *122*(11), 634–640.

Järvelä, J. (2002). Flow resistance of flexible and stiff vegetation: a flume study with natural plants. *J. Hydrol.*, *269*(1-2), 44–54.

Jesson, M. A. (2012). *The effect of heterogeneous roughness on conveyance capacity and application to the shiono-knight method* (Unpublished doctoral dissertation). University of Birmingham.

Jesson, M. A., Bridgeman, J., & Sterling, M. (2015). Novel software developments for the automated post-processing of high volumes of velocity time-series. *Advances in Engineering Software*, *89*, 36–42.

Jesson, M. A., Sterling, M., & Bridgeman, J. (2013a). Despiking velocity time-series—optimisation through the combination of spike detection and replacement methods. *Flow Measurement and Instrumentation*, *30*, 45–51.

Jesson, M. A., Sterling, M., & Bridgeman, J. (2013b). An experimental study of turbulence in a heterogeneous channel. In *Proceedings of the institution of civil engineers-water management* (Vol. 166, pp. 16–26).

Jesson, M. A., Sterling, M., & Bridgeman, J. (2013c). Modeling flow in an open channel with heterogeneous bed roughness. *J. Hydraul. Eng.*, *139*(2), 195–204.

Kang, H., & Choi, S.-U. (2006). Reynolds stress modelling of rectangular open-channel flow. *Int. J. Numer. Methods Fluids*, *51*(11), 1319–1334.

Kara, S., Stoesser, T., & Sturm, T. W. (2012). Turbulence statistics in compound channels with deep and shallow overbank flows. *J. Hydraul. Res.*, *50*(5), 482–493.

Katopodes, N. D. (2018). *Free-surface flow:: Shallow water dynamics*. Butterworth-Heinemann.

Katul, G., & Vidakovic, B. (1998). Identification of low-dimensional energy containing/flux transporting eddy motion in the atmospheric surface layer using wavelet thresholding methods. *Journal of the atmospheric sciences*, *55*(3), 377–389.

Knight, D. W., Omran, M., & Tang, X. (2007). Modeling depth-averaged velocity and boundary shear in trapezoidal channels with secondary flows. *J. Hydraul. Eng.*, *133*(1), 39–47.

K. van Wesenbeeck, B., Van De Koppel, J., MJ Herman, P., & J. Bouma, T. (2008). Does scale-dependent feedback explain spatial complexity in salt-marsh ecosystems? *Oikos*, *117*(1), 152–159.

Leonard, L. A., & Luther, M. E. (1995). Flow hydrodynamics in tidal marsh canopies. *Limnol. Oceanogr.*, *40*(8), 1474–1484.

López, F., & García, M. (1998). Open-channel flow through simulated vegetation: Suspended sediment transport modeling. *Water Resour. Res.*, *34*(9), 2341–2352.

Luhar, M., Rominger, J., & Nepf, H. M. (2008). Interaction between flow, transport and vegetation spatial structure. *Environ. Fluid Mech.*, *8*(5), 423–439.

Mazda, Y., Magi, M., Ikeda, Y., Kurokawa, T., & Asano, T. (2006). Wave reduction in a mangrove forest dominated by sonneratia sp. *Wetl Ecol Manag*, *14*(4), 365–378.

Mazda, Y., Wolanski, E., King, B., Sase, A., Ohtsuka, D., & Magi, M. (1997). Drag force due to vegetation in mangrove swamps. *Mangroves and salt marshes*, *1*(3), 193–199.

McGahey, C., Samuels, P., & Knight, D. (2006). A practical approach to estimating the flow capacity of rivers–application and analysis. In *River flow* (Vol. 2006, pp. 303–312).

McKinney, J. P. (1993). A method for locating spikes in a measured time series. In *Ocean wave measurement and analysis* (pp. 388–393).

McLean, S. (1981). The role of non-uniform roughness in the formation of sand ribbons. In *Developments in sedimentology* (Vol. 32, pp. 49–74). Elsevier.

McLelland, S. J., Ashworth, P. J., Best, J. L., & Livesey, J. R. (1999). Turbulence and secondary flow over sediment stripes in weakly bimodal bed material. *J. Hydraul. Eng.*, *125*(5), 463–473.

Medjnoun, T., Vanderwel, C., & Ganapathisubramani, B. (2018). Characteristics of turbulent boundary layers over smooth surfaces with spanwise heterogeneities. *J. Fluid Mech.*, *838*, 516–543.

Medjnoun, T., Vanderwel, C., & Ganapathisubramani, B. (2020). Effects of heterogeneous surface geometry on secondary flows in turbulent boundary layers. *J. of Fluid Mech.*, *886*, 1–36.

Mejia-Alvarez, R., & Christensen, K. T. (2013). Wall-parallel stereo particle-image velocimetry measurements in the roughness sublayer of turbulent flow overlying highly irregular roughness. *Phys. Fluids*, *25*(11), 115109.

Moltchanov, S., Bohbot-Raviv, Y., Duman, T., & Shavit, U. (2015). Canopy edge flow: a momentum balance analysis. *Water Resour. Res.*, *51*(4), 2081–2095.

Moltchanov, S., Bohbot-Raviv, Y., & Shavit, U. (2011). Dispersive stresses at the canopy upstream edge. *Bound.-Layer Meteorol.*, *139*(2), 333–351.

Moore, K. A. (2004). Influence of seagrasses on water quality in shallow regions of the lower chesapeake bay. *J. Coast. Res.*(10045), 162–178.

Morse, A., Gardiner, B., & Marshall, B. (2002). Mechanisms controlling turbulence development across a forest edge. *Bound.-Layer Meteorol.*, *103*(2), 227–251.

Murray, A., Knaapen, M., Tal, M., & Kirwan, M. (2008). Biomorphodynamics: Physical-biological feedbacks that shape landscapes. *Water Resour. Res.*, *44*(11).

Murray, R. M., Li, Z., & Sastry, S. S. (2017). *A mathematical introduction to robotic manipulation*. CRC press.

Naot, D., Nezu, I., & Nakagawa, H. (1996). Hydrodynamic behavior of partly vegetated open channels. *J. Hydraul. Eng.*, *122*(11), 625–633.

Naot, D., & Rodi, W. (1982). Calculation of secondary currents in channel flow. *J. of the Hydraul. Division*, *108*(8), 948–968.

Nepf, H. M. (2011). Flow over and through biota. *Elsevier Reference Collection in Earth Systems and Environmental Sciences*.

Nepf, H. M. (2012). Hydrodynamics of vegetated channels. *J. Hydraul. Res.*, *50*(3), 262–279.

Nepf, H. M., & Vivoni, E. (2000). Flow structure in depth-limited, vegetated flow. *J. Geophys. Res. Oceans*, *105*(C12), 28547–28557.

Neumeier, U., & Amos, C. L. (2006). The influence of vegetation on turbulence and flow velocities in european salt-marshes. *Sedimentology*, *53*(2), 259–277.

Nezu, I., & Nakagawa, H. (1984). Cellular secondary currents in straight conduit. *J. Hydraul. Eng.*, *110*(2), 173–193.

Nezu, I., & Nakagawa, H. (1993). *Turbulence in open-channel flows*. Routledge.

Nezu, I., & Onitsuka, K. (2001). Turbulent structures in partly vegetated open-channel flows with lda and pi v measurements. *J. Hydraul. Res.*, *39*(6), 629–642.

Nikora, V., & Roy, A. G. (2012). Secondary flows in rivers: Theoretical framework, recent advances, and current challenges. *Gravel-Bed Rivers: Processes, Tools, Environments*, 1–22.

Nikora, V., Stoesser, T., Cameron, S. M., Stewart, M., Papadopoulos, K., Ouro, P., ... Falconer, R. A. (2019). Friction factor decomposition for rough-wall

flows: theoretical background and application to open-channel flows. *J. Fluid Mech.*, *872*, 626–664.

Omran, M. (2005). *Modelling stage-discharge curves, velocity and boundary sheer stress distributions in natural and artificial channels using a depth-averaged approach* (Unpublished doctoral dissertation). University of Birmingham.

Omran, M., & Knight, D. (2006). Modelling the distribution of boundary shear stress in open channel flows. In *River flow* (Vol. 1, pp. 397–404).

Osorio, A. F., Urrego, L. E., et al. (2019). Wave dissipation across a rhizophora mangrove patch on a colombian caribbean island: An experimental approach. *Ecol. Eng.*, *130*, 271–281.

Ozeren, Y., Wren, D., & Wu, W. (2014). Experimental investigation of wave attenuation through model and live vegetation. *J. Waterw. Port Coast. Ocean Eng.*, *140*(5), 04014019.

Perucca, E., Camporeale, C., & Ridolfi, L. (2007). Significance of the riparian vegetation dynamics on meandering river morphodynamics. *Water Resour. Res.*, *43*(3).

Pezzinga, G. (1994). Velocity distribution in compound channel flows by numerical modeling. *J. Hydraul. Eng.*, *120*(10), 1176–1198.

Poggi, D., Katul, G., & Albertson, J. (2004). A note on the contribution of dispersive fluxes to momentum transfer within canopies. *Bound.-layer Meteorol.*, *111*(3), 615–621.

Poggi, D., Krug, C., & Katul, G. G. (2009). Hydraulic resistance of submerged rigid vegetation derived from first-order closure models. *Water Resour. Res.*, *45*(10).

Prandtl, L. (1952). *Essentials of fluid dynamics: With applications to hydraulics aeronautics, meteorology, and other subjects.* Hafner Publishing Company.

Rameshwaran, P., & Shiono, K. (2007). Quasi two-dimensional model for straight overbank flows through emergent. *J. Hydraul. Res.*, *45*(3), 302–315.

Raupach, M. R., Finnigan, J. J., & Brunet, Y. (1996). Coherent eddies and turbulence in vegetation canopies: the mixing-layer analogy. In *Bound.-layer meteorology 25th anniversary volume, 1970–1995* (pp. 351–382). Springer.

Raupach, M. R., & Shaw, R. (1982). Averaging procedures for flow within vegetation canopies. *Bound.-Layer Meteorol.*, *22*(1), 79–90.

Rodi, W., Constantinescu, G., & Stoesser, T. (2013). Large-eddy simulation in hydraulics.

Rodríguez, J. F., & García, M. H. (2008). Laboratory measurements of 3-d flow patterns and turbulence in straight open channel with rough bed. *J. Hydraul. Res.*, *46*(4), 454–465.

Rominger, J. T., & Nepf, H. M. (2011). Flow adjustment and interior flow associated with a rectangular porous obstruction. *J. Fluid Mech.*, *680*, 636–659. doi: 10.1017/jfm.2011.199

Roy, M., Kumar, V. R., Kulkarni, B., Sanderson, J., Rhodes, M., & Stappen, M. v. (2000). Simple denoising algorithm using wavelet transform. *arXiv preprint nlin/0002028*.

Schoelynck, J., De Groote, T., Bal, K., Vandenbruwaene, W., Meire, P., & Temmerman, S. (2012). Self-organised patchiness and scale-dependent bio-geomorphic feedbacks in aquatic river vegetation. *Ecography*, *35*(8), 760–768.

Sharifi, S., Sterling, M., & Knight, D. (2009). A novel application of a multi-objective evolutionary algorithm in open channel flow modelling. *J. Hydroinform.*, *11*(1), 31–50.

Shiono, K., & Knight, D. (1988). Two-dimensional analytical solution for a compound channel. In *Proc., 3rd int. symp. on refined flow modelling and turbulence measurements* (pp. 503–510).

Shiono, K., & Knight, D. W. (1991). Turbulent open-channel flows with variable depth across the channel. *J. of Fluid Mech.*, *222*, 617–646.

SonTek. (2001). *Sontek/ysi advfield/hydra acoustic doppler velocimeter (field) technical documentation* (Tech. Rep.). San Diego, CA: Author.

Stroh, A., Hasegawa, Y., Kriegseis, J., & Frohnapfel, B. (2016). Secondary vortices over surfaces with spanwise varying drag. *J. Turbul*, *17*(12), 1142-1158.

Stroh, A., Schäfer, K., Frohnapfel, B., & Forooghi, P. (2020). Rearrangement of secondary flow over spanwise heterogeneous roughness. *J. Fluid Mech.*, *885*.

Tal, M., & Paola, C. (2007). Dynamic single-thread channels maintained by the interaction of flow and vegetation. *Geology*, *35*(4), 347–350.

Tang, X., Knight, D., & Sterling, M. (2011). Analytical model for streamwise velocity in vegetated channels. *Proc. Inst. Civ. Eng.: Eng. Comput. Mech.*, *164*(2), 91–102.

Tang, X., & Knight, D. W. (2008). A general model of lateral depth-averaged velocity distributions for open channel flows. *Adv. Water Resour.*, *31*(5), 846–857.

Tang, X., & Knight, D. W. (2009). Lateral distributions of streamwise velocity in compound channels with partially vegetated floodplains. *Sci. China Technol. Sci.*, *52*(11), 3357–3362.

Tanino, Y. (2012). Flow and mass transport in vegetated surface waters. *Fluid mechanics of environmental interfaces*, 369–394.

Thom, A. (1971). Momentum absorption by vegetation. *Q. J. R. Meteorol. Soc.*, *97*(414), 414–428.

Tominaga, A., & Nezu, I. (1991). Turbulent structure in compound open-channel flows. *J. Hydraul. Eng.*, *117*(1), 21–41.

Tominaga, A., Nezu, I., Ezaki, K., & Nakagawa, H. (1989). Three-dimensional turbulent structure in straight open channel flows. *J. Hydraul. Res.*, *27*(1), 149–173.

Tomkins, C. D., & Adrian, R. J. (2003). Spanwise structure and scale growth in turbulent boundary layers. *J. Fluid Mech.*, *490*, 37–74.

Truong, S., Uijttewaal, W., & Stive, M. (2019). Exchange processes induced by large horizontal coherent structures in floodplain vegetated channels. *Water Resour. Res.*, *55*(3), 2014–2032.

Tsihrintzis, V. A., & Madiedo, E. E. (2000). Hydraulic resistance determination in marsh wetlands. *Water Resour. Manag.*, *14*(4), 285–309.

Türk, S., Daschiel, G., Stroh, A., Hasegawa, Y., & Frohnapfel, B. (2014). Turbulent flow over superhydrophobic surfaces with streamwise grooves. *J. of fluid Mech*, *747*, 186.

Uijttewaal, W. S. (2014). Hydrodynamics of shallow flows: application to rivers. *J. Hydraul. Res.*, *52*(2), 157–172.

Vanderwel, C., & Ganapathisubramani, B. (2015). Effects of spanwise spacing on large-scale secondary flows in rough-wall turbulent boundary layers. *J. Fluid Mech.*, *774*.

Vanderwel, C., Placidi, M., & Ganapathisubramani, B. (2017). Wind resource assessment in heterogeneous terrain. *Philos. Trans. Royal Soc. A: Mathematical, Physical and Engineering Sciences*, *375*(2091), 20160109.

Vanderwel, C., Stroh, A., Kriegseis, J., Frohnapfel, B., & Ganapathisubramani, B. (2019). The instantaneous structure of secondary flows in turbulent boundary layers. *J. Fluid Mech.*, *862*, 845–870.

Vanoni, V. A. (1946). Transportation of suspended sediment by water. *Trans. Am. Soc. Civil Eng.*, *111*(1), 67–102.

Van Prooijen, B. C., Battjes, J. A., & Uijttewaal, W. S. (2005). Momentum exchange in straight uniform compound channel flow. *J. Hydraul. Eng.*, *131*(3), 175–183.

van Rooijen, A., Lowe, R., Ghisalberti, M., Conde-Frias, M., & Tan, L. (2018). Predicting current-induced drag in emergent and submerged aquatic vegetation canopies. *Front. Mar. Sci.*, *5*, 449.

Vermaas, D. A. (2008). *Mixing layers in open channel flow with abrupt bed roughness changes* (Unpublished doctoral dissertation). Delft University of Technology.

Vermaas, D. A., Uijttewaal, W., & Hoitink, A. (2011). Lateral transfer of streamwise momentum caused by a roughness transition across a shallow channel. *Water. Resour. Res.*, *47*(2).

Vivoni-Gallart, E. R. (1998). *Turbulence structure of a model seagrass meadow* (Unpublished doctoral dissertation). Massachusetts Institute of Technology.

Wahl, T. L. (2000). Analyzing adv data using winadv. In *Building partnerships* (pp. 1–10).

Wahl, T. L. (2003). Discussion of "despiking acoustic doppler velocimeter data" by derek g. goring and vladimir i. nikora. *J. Hydraul. Eng.*, *129*(6), 484–487.

Wang, G., Yang, F., Wu, K., Ma, Y., Peng, C., Liu, T., & Wang, L.-P. (2021). Estimation of the dissipation rate of turbulent kinetic energy: A review. *Chem. Eng. Sci.*, *229*, 116133.

Wang, W.-J., Peng, W.-Q., Huai, W.-X., Katul, G. G., Liu, X.-B., Qu, X.-D., & Dong, F. (2019). Friction factor for turbulent open channel flow covered by vegetation. *Sci*, *9*(1), 1–16.

Wang, Z. Q., & Cheng, N. S. (2006). Time-mean structure of secondary flows in open channel with longitudinal bedforms. *Adv. Water Resour.*, *29*(11), 1634–1649.

Wangsawijaya, D., Kevin, K., Chung, D., Marusic, I., & Hutchins, N. (2019). Time-varying secondary flows in turbulent boundary layers over surfaces with spanwise heterogeneity. In *Aps division of fluid dynamics meeting abstracts* (pp. H42–001).

Wangsawijaya, D. D., Baidya, R., Chung, D., Marusic, I., & Hutchins, N. (2020). The effect of spanwise wavelength of surface heterogeneity on turbulent secondary flows. *J. Fluid Mech.*, *894*.

Whitaker, S. (1969). Advances in theory of fluid motion in porous media. *J. Ind. Eng. Chem.*, *61*(12), 14–28.

White, B. L., & Nepf, H. M. (2007). Shear instability and coherent structures in shallow flow adjacent to a porous layer. *J. Fluid Mech.*, *593*, 1.

Willingham, D., Anderson, W., Christensen, K. T., & Barros, J. M. (2014). Turbulent boundary layer flow over transverse aerodynamic roughness transitions: induced mixing and flow characterization. *Phys. Fluids*, *26*(2), 025111.

Worcester, S. (1995). Effects of eelgrass beds on advection and turbulent mixing in low current and low shoot density environments. *Mar. Ecol. Prog.*, *126*, 223–232.

Wormleaton, P., & Merrett, D. (1990). An improved method of calculation for steady uniform flow in prismatic main channel/flood plain sections. *J. Hydraul. Res.*, *28*(2), 157–174.

Xu, D., & Chen, J. (2013). Accurate estimate of turbulent dissipation rate using piv data. *Experimental Thermal and Fluid Science*, *44*, 662–672.

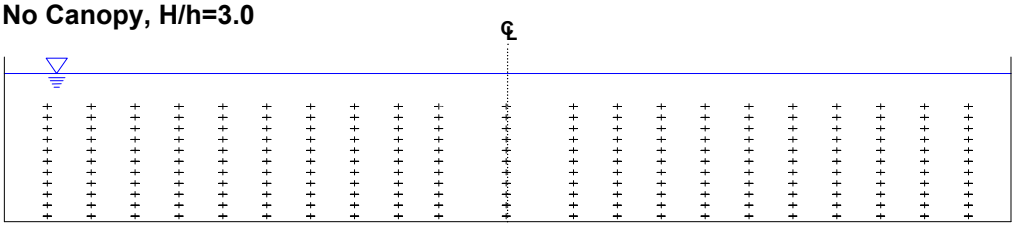
Yang, J., & Anderson, W. (2018). Numerical study of turbulent channel flow over surfaces with variable spanwise heterogeneities: topographically-driven secondary flows affect outer-layer similarity of turbulent length scales. *Flow, Turbul. and Combust.*, *100*(1), 1–17.

Zhou, J., Adrian, R. J., Balachandar, S., & Kendall, T. (1999). Mechanisms for generating coherent packets of hairpin vortices in channel flow. *J. Fluid Mech.*, *387*, 353–396.

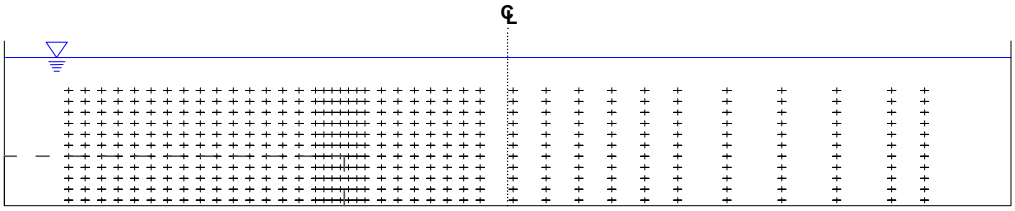
Appendix A

Grid points for all experiments in the present study

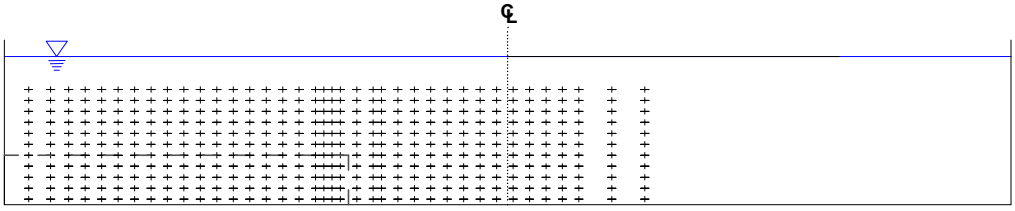
No Canopy, H/h=3.0

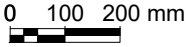


ϕ=0.0125, H/h=3.0



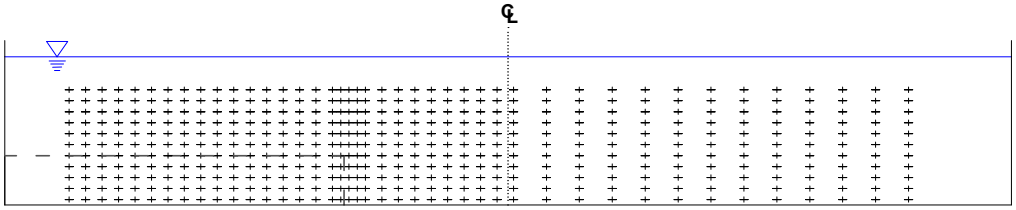
ϕ=0.025, H/h=3.0



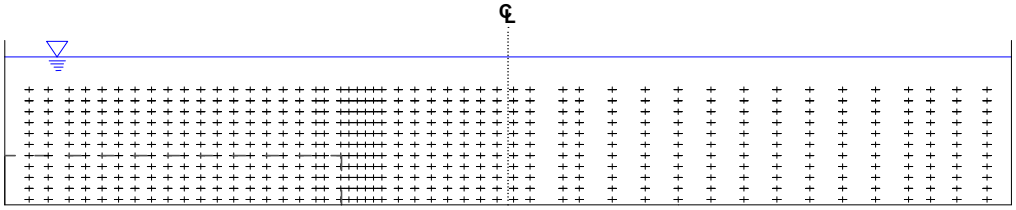


- **All measurements are in millimeters.**
- **Measurements in depth were taken every 20mm starting from 10mm above the bed.**
- **Dashed lines represent the boundaries of the canopy.**

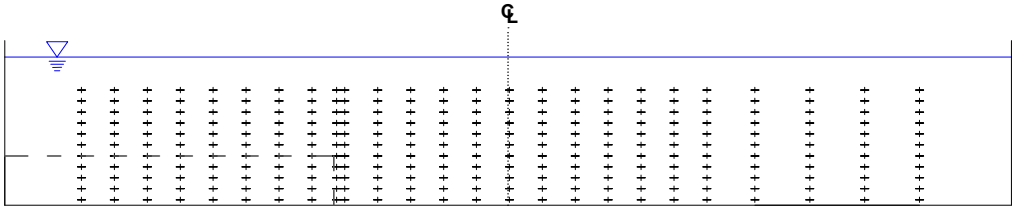
ϕ=0.05, H/h=3.0



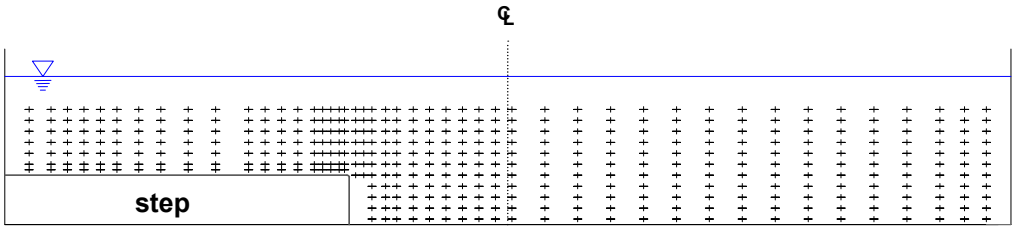
ϕ=0.10, H/h=3.0



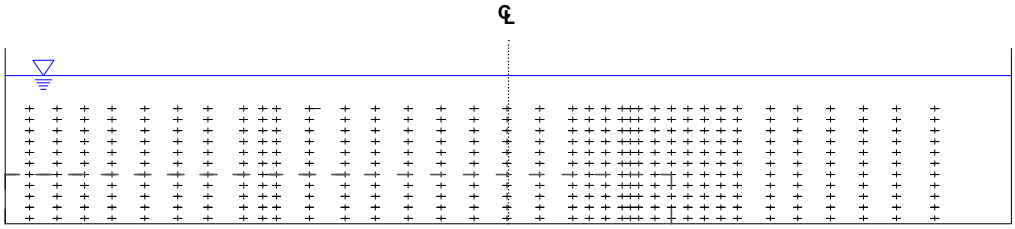
ϕ=0.20, H/h=3.0



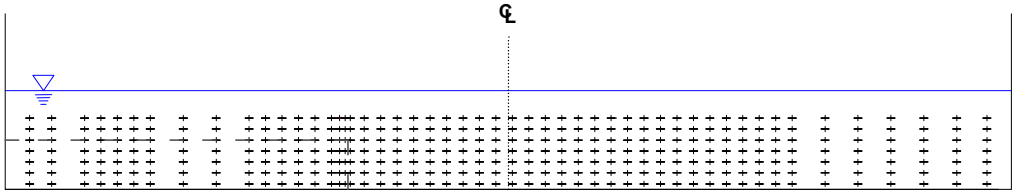
step, H/h=3.0



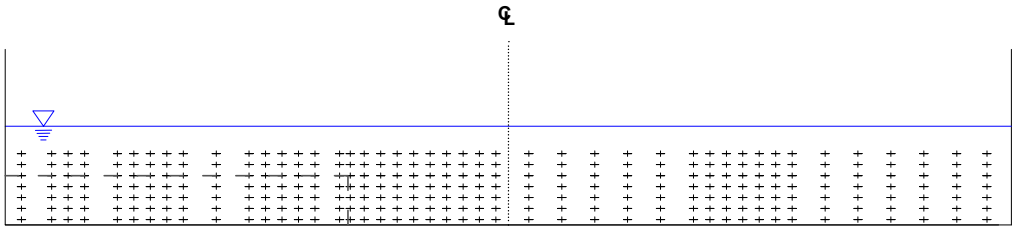
ϕ=0.20, H/h=3.0, 2B



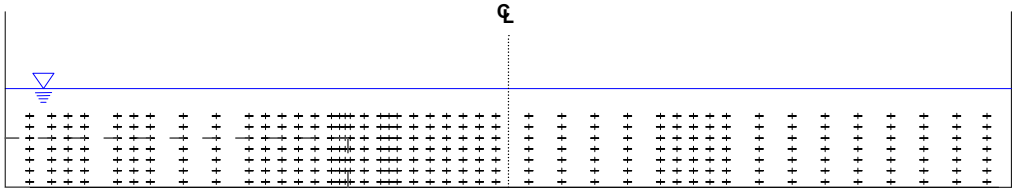
ϕ=0.20, H/h=2.0



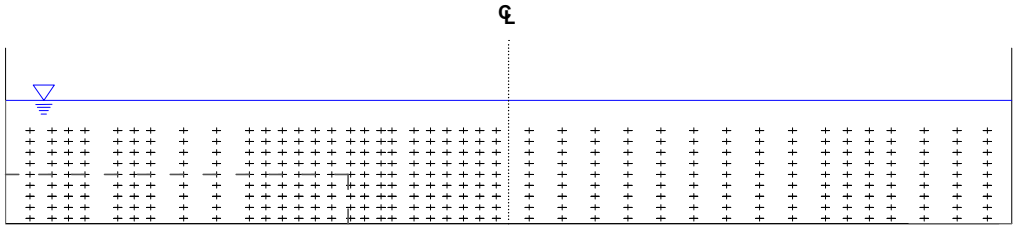
ϕ=0.10, H/h=2.0



ϕ=0.025, H/h=2.0



ϕ=0.10, H/h=2.5



ϕ=0.20, H/h=2.5

